Signal Processing for Airborne Passive Radar : Interference Suppression and Space Time Adaptive Processing Techniques for Transmissions of Opportunity

Danny Kai Pin Tan

N° d'ordre : 2012-21-TH

THÈSE DE DOCTORAT

DOMAINE : STIC

SPECIALITE : Traitement du signal

Ecole Doctorale « Sciences et Technologies de l'Information des Télécommunications et des Systèmes »

Présentée par :

Danny Kai Pin TAN

Sujet :

Traitement du signal pour le radar aéroporté passif : suppression d'interférences et techniques STAP adaptées à des émissions d'opportunité

Signal Processing for Airborne Passive Radar: Interference Suppression and STAP Techniques for Transmissions of Opportunity

Soutenue le 22 novembre 2012 devant les membres du jury :

M. CHERNIAKOV Mikhail	University of Birmingham	Rapporteur
M. GARELLO René	Institut Mines-Telecom Telecom Bretagne	Examinateur
M. LESTURGIE Marc	ONERA/SONDRA	Directeur de thèse
Mme MARCOS Sylvie	CNRS/LSS/SUPELEC	Examinateur
M. RAOUT Jacques	EMAA	Examinateur
M. SUN Hong Bo	Nanyang Technological University	Examinateur
M. UGUEN Bernard	Université de Rennes 1	Rapporteur

Acknowledgements

I would like to express my total appreciation to the people for their support and for guiding me along in completing this thesis. Very special thanks to my thesis director, who is also the director of SONDRA, Marc Lesturgie, for his invaluable time, guidance and supervision on this thesis throughout the tough four years. Sincere thanks must also go to Hongbo Sun from Temasek Laboratories @ Nanyang Technological University. He is a great source of technical guidance and motivation throughout this effort. Appreciation must also go to Hongchuan Feng for his logistical support in conducting the ground-based moving passive radar experimental trials. Next, I would like to express my gratitude to Temasek Laboratories @ Nanyang Technological University for funding this Ph.D. degree where I have this opportunity to spend most of the candidature duration in SONDRA Laboratory in Paris.

I had spent a life enriching and unforgettable three years in Paris and of course this would not be possible without the wonderful people in SONDRA Laboratory and others in Supélec. I would like to thank especially Anne Hélène Picot for her administrative support that she had given me throughout my stay. Sincere thanks must also go to my helpful colleagues in SONDRA Laboratory for their constant physical and mental support. A big and sincere thank you to everyone for these memorable years! Of course not forgetting my helpful colleagues back in Temasek Laboratories @ Nanyang Technological University as well. Thanks you all so much!

Finally, I would also like to express my utmost appreciation to my dearest parents and two sisters for their encouragement throughout my whole educational life. I could not have completed this Ph.D. degree without their continuous and immeasurable support. Their love and support have helped me through difficult times and challenges of completing this work.

Contents

Contents

Contents

Acronyms and Abbreviations

ADC	Analog to Digital Converter
AF	Ambiguity Function
BPF	Band-Pass Filter
CIT	Coherent Integration Time
CNR	Clutter-to-Noise Ratio
COTS	Commercial-Off-The-Shelf
CW	Continuous Wave
DAB	Digital Audio Broadcast
DDC	Digital Down-Converter
DFT	Discrete Fourier Transform
DNR	Direct path-to-Noise Ratio
DOA	Direction Of Arrival
DOF	Degree Of freedom
DPCA	Displaced Phase Center Antenna
DVB-T	Digital Video Broadcast Terrestrial
EM	Electromagnetic
FIR	Finite Impulse Response
FM	Frequency Modulation
GSM	Global System for Mobile communication
ICM	Intrinsic Clutter Motion
IF	Intermediate Frequency
IID	Independent and Identically Distributed
INR	Interference-to-Noise Ratio
JDL	Joint Domain Localized
LFMCW	Linear Frequency Modulated Continuous Wave
LMS	Least Mean Square
LNA	Low Noise Amplifier
LO	Local Oscillator
LOS	Line-Of-Sight
LS	Least Squares
MDV	Minimum Detectable Velocity
MTI	Moving Target Indication
MVDR	Minimum Variance Distortionless Response
NLMS	Normalized Least Mean Square
PC	Principal Components
PCI	Peripheral Component Interconnect
PRI	Pulse Repetition Interval
RCS	Radar Cross Section
RF	Radio Frequency
RLS	Recursive Least Square
RMS	Root Mean Square
SCM	Sample Covariance Matrix
SINR	Signal-to-Interference-plus-Noise Ratio
SMI	Sample Matrix Inversion

SNR	Signal-to-Noise Ratio
STAP	Space-Time Adaptive Processing
ULA	Uniform Linear Array
UDSF	Usable Doppler Space Fraction
UMTS	Universal Mobile Telecommunications System
WiMAX	Worldwide interoperability for Microwave Access

List of Figures

Chapter 4 – Simulations on Airborne Passive Radar Signal Processing

Chapter 5 – Ground-Based Moving Passive Radar Experimental Trials

List of Tables

List of Publications

Journals

- H.B. Sun, **D.K.P. Tan**, Y.L. Lu and M. Lesturgie, "Applications of Passive Surveillance Radar System using Cell Phone Base Station Illuminators", *IEEE Aerospace and Electronic Systems Magazine*, Volume 25, Issue 3, pp. 10 – 18, March 2010
- **D.K.P. Tan**, M. Lesturgie, H.B. Sun and Y.L. Lu, "Interference Spectral Analysis and Suppression for Airborne Passive Radar Using Transmissions of Opportunity", *IEE Proceedings Radar, Sonar & Navigation* (Submitted), 2012.

Conferences

- **D.K.P. Tan**, M. Lesturgie, H.B. Sun and Y.L. Lu, "Target Detection Performance Analysis for Airborne Passive Bistatic Radar", *IEEE International Geoscience and Remote Sensing Symposium*, Honolulu, Hawaii, USA, 25-30 July, 2010.
- **D.K.P. Tan**, M. Lesturgie, H.B. Sun and Y.L. Lu, "Signal Analysis of Airborne Passive Radar using Transmissions of Opportunity", *International Conference on Radar*, Chengdu, China, 24-27 October, 2011.
- **D.K.P. Tan**, M. Lesturgie, H.B. Sun and Y.L. Lu, "Random Range Sidelobes Analysis and Suppression in Airborne Passive Radar", *International Conference on Radar Systems*, Glasgow, UK, 22-25 October, 2012.

Résumé

I Introduction

I.1. Radar passif et radar passif aéroporté

Durant la dernière décennie, de nombreux intérêts ont émergé des possibilités offertes par le radar passif d'exploiter des émetteurs non coopératifs (opportunistes) différents du radar comme sources d'illumination; les avantages potentiels de ces techniques sont aujourd'hui bien connus [7-9]. Les principaux radars passifs destinés à la surveillance de cibles mobiles à des fins militaires ou civiles, actuellement en service ou en développement sont des systèmes statiques au sol dont les opérations et les traitements du signal associés pour le MTI sont bien documentés [8]. L'utilisation du radar passif monté sur une plateforme aéroportée est un concept innovant permettant une véritable percée dans la technologie du radar passif. Le principe de base du radar passif aéroporté est d'utiliser de multiples réseaux de radar passif en réception (configuration en visée latérale et en visée avant) couvrant un angle solide de 4π steradian centré autour de la plateforme aéroportée du radar susceptible d'utiliser une station fixe au sol comme illuminateur opportuniste (Figure I.1). Les applications du radar passif aéroporté pourraient porter sur la surveillance localisée (plus de 10 Km) par une plateforme aéroportée (drone, hélicoptère, cargo, etc).

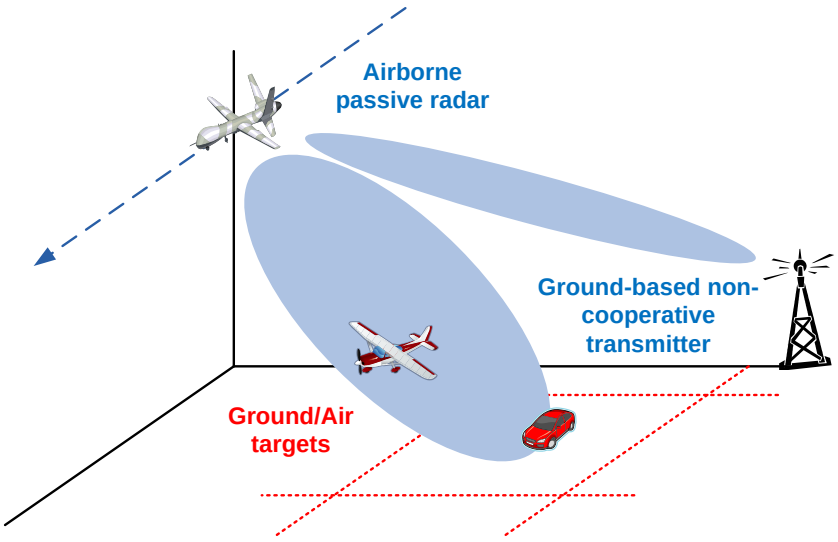

Fig. I.1: Concept de base du radar passif aéroporté.

Le radar passif aéroporté présente néanmoins de nombreuses difficultés pour atteindre des performances satisfaisantes et rendre sa mise en œuvre possible. Les performances du radar passif aéroporté, tout comme celles du radar passif statique au sol, dépendent fortement de la configuration géométrique [5] ainsi que des propriétés du signal non coopératif [7, 41]. Les émetteurs non coopératifs, de diffusion (radio ou TV) et de communication ont des modulations qui changent en fonction du temps, ce qui entraine de grandes variations dans les propriétés du signal passif (corrélation, bande de fréquence, etc. …). La puissance d'émission

des signaux non coopératifs fixe les performances en distance du radar passif. Le signal provenant directement de l'émetteur étant le signal prédominant, cela induit un problème de dynamique importante entre signaux utiles et signaux interférents et l'influence des propriétés de signal non coopératif est dimensionnante vis-à-vis des performances de détection du radar passif aéroporté.

Le principe de base de la détection de cibles par un radar passif est de convoluer le signal provenant de la propagation directe avec les signaux échos des cibles mobiles. L'outil mathématique utilisé est le filtrage adapté qui permet la détection optimale du signal émis dans un bruit blanc Gaussien [42, 43]. Cette idée peut paraitre évidente mais la nature CW, aléatoire et apériodique de signaux passifs amène des difficultés techniques sur les couplages entre le signal direct et le fouillis de forte intensité ce qui dégrade les performances du MTI [45]. Etant donné que la puissance du signal direct et du fouillis de forte intensité est élevée, les couplages via les lobes secondaires aléatoires en distance de ces signaux interférents influencent grandement la détection et l'estimation de la cible.

Quand le radar passif aéroporté utilise un émetteur stationnaire au sol, les décalages Doppler des diffuseurs sont seulement causés par le déplacement de la plateforme du radar. Ainsi, le fouillis de sol reçu par le radar passif est non seulement étendu en distance et en angle mais également en Doppler. En configuration à visée latérale, le spectre bidimensionnel de la puissance du fouillis est distribué sur une ligne diagonale dans le domaine angle-Doppler. Un filtre conventionnel à 1-D (spatial ou Doppler) peut être appliqué pour supprimer le fouillis, néanmoins une cible lente risque de tomber dans la bande de suppression du filtre et être ainsi supprimée. Le fouillis étant localisé dans un domaine bidimensionnel angle-Doppler, peut être supprimé en utilisant un filtre bidimensionnel, i.e. filtre spatio-temporel. Les traitements spatio-temporels exploitent la relation linaire entre l'angle d'arrivée du fouillis et sa fréquence Doppler. Un filtre spatio-temporel possède un nœud étroit qui permet de rejeter le fouillis tout en préservant la puissance des cibles lentes. L'avantage principal du STAP est ainsi d'améliorer la détection des cibles lentes par une meilleure suppression du lobe principal du fouillis et donc aussi d'améliorer la détection de cible à faible puissance cachée par les lobes secondaires du fouillis. Comme nous l'avons écrit précédemment, les deux principales difficultés que représentent les couplages de lobes secondaires aléatoires en distance du signal direct et du fouillis de forte intensité et le fouillis dans le domaine spatial-Doppler, doivent être entièrement formulées et analysées en termes de performances pour rendre réalisable pratiquement le radar passif aéroporté.

Cette thèse "Signal Processing for Airborne Passive Radar" (Traitement du signal pour le radar passif aéroporté) est consacrée à l'étude de méthodes efficaces pour la suppression des interférences et l'amélioration de la détection de cibles mobiles. Nous commencerons par identifier et analyser les difficultés majeures rencontrées par le radar passif aéroporté pour la détection de cibles mobiles. Il est important de développer des modèles des signaux passifs reçus en prenant en compte les différents effets indésirables des interférences pour la détection d'une cible dans la case distance sous test. La compréhension de ces effets permet ensuite de développer des méthodes de traitements applicables au radar passif aéroporté pour réduire les interférences et augmenter les performances de détection de cibles mobiles.

II Modélisation du signal du radar passif

II.1. Radar passif aéroporté et géométrie bistatique des diffuseurs

On considère pour le radar passif aéroporté, une géométrie bistatique à 3 dimensions dans laquelle l'émetteur non coopératif se situe au sol (i.e. émetteurs FM, DVB-T, DAB, etc…) et le radar passif sur une plateforme aéroportée. La Figure II.1 illustre cette géométrie

bistatique. Le diffuseur s peut être une cible mobile ou un élément du fouillis stationnaire. La distance entre le diffuseur et l'émetteur et celle entre le diffuseur et le radar passif sont notées R_{Ts} et R_{Rs} respectivement. Nous définissons la distance bistatique $R_{sum} = R_{Ts} + R_{Rs}$. Le triangle formé par l'émetteur, le radar passif et le diffuseur est appelé l'angle bistatique β_s. L'orientation du diffuseur est caractérisée par ses angles en azimut et en élévation notés ϕ_{Ts} et θ_{Ts} par rapport à l'émetteur et par ses angles en azimut et en élévation notés ϕ_{Rs} and θ_{Rs} par rapport au radar passif.

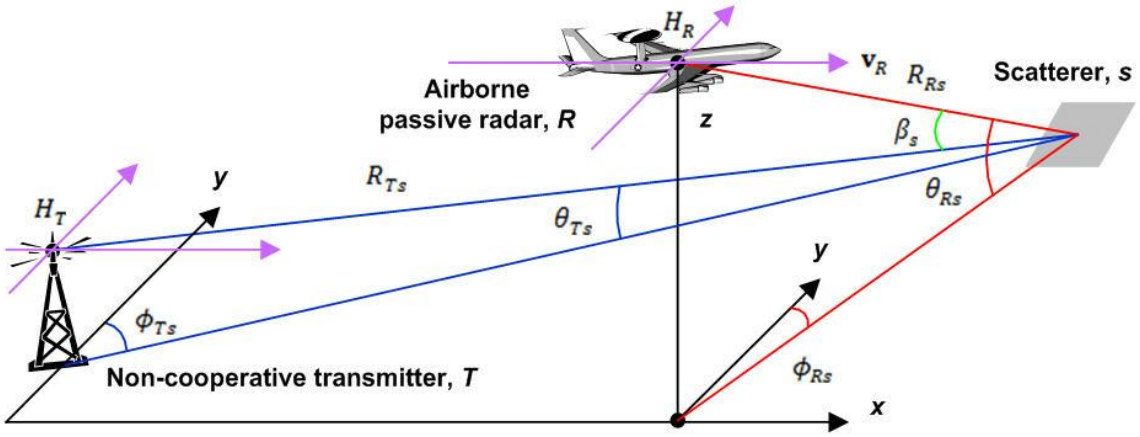

Fig. II.1: Géométrie bistatique du radar passif aéroporté.

II.2 Cube de données du radar passif pour un temps d'intégration cohérente

Le radar passif aéroporté est un système CW localisé sur une plateforme aéroportée. Son réseau d'antennes est composé de N ULA, chacune ayant son canal de réception. Les prétraitements convertissent le signal passif RF reçu par chaque élément de l'antenne en échantillons complexes en bande de base. La durée pendant laquelle le signal passif est reçu est appelé CIT. Pour chaque élément/canal, la durée CIT est divisée en M sous-CIT où M est le nombre total de sous-CIT. Chaque sous-CIT a une durée T_{sub} et une fréquence de répétition de sous-CIT égale à $f_{sub} = 1/T_{sub}$. Pour chaque sous-CIT, nous avons $L = T_{sub} \times f_{BW}$ cases distance, L étant le nombre total de cases distance et f_{BW}la fréquence complexe d'échantillonnage. Les données multidimensionnelles destinées au traitement du signal MTI sont donc représentées par un cube de dimension $N \times M \times L$ d'échantillons complexes en bande de base [49]. Le profil en distance est obtenu par filtrage adapté sur la dimension distance (corrélation en distance). Dans le cas du radar passif aéroportée, nous supposons que le signal direct (propagation directe) est disponible (formateur de faisceaux ou reçu via des antennes auxiliaires) ; par conséquence il peut être également divisé en M sous-CIT comme le cube de données. Ainsi la corrélation en distance (propagation directe et signal reçu) se fait séparément pour chaque sous-CIT et on note par $\mathbf{r}$ la fonction de corrélation de dimension $1 \times L$ pour chaque sous-CIT. La matrice de fonction de corrélation $\boldsymbol{\mathcal{R}}$ de dimensions $M \times L$ dont les colonnes sont les différentes fonctions de corrélation $\mathbf{r}$ pour chaque sous-CIT est définie pour chaque élément tel que $\boldsymbol{\mathcal{R}} = [\mathbf{r}_0; \mathbf{r}_2; \cdots; \mathbf{r}_{M-1}]$. Le cube de données passives CIT [48] est schématisé sur la Figure II.2.

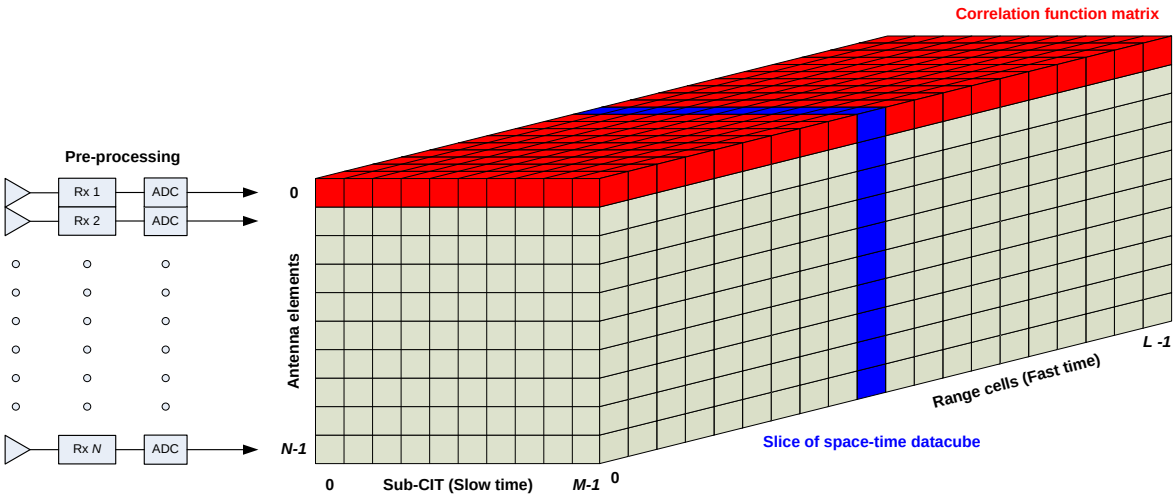

Fig. II.2: Schéma du cube de données.

II.3 Modèle du signal passif

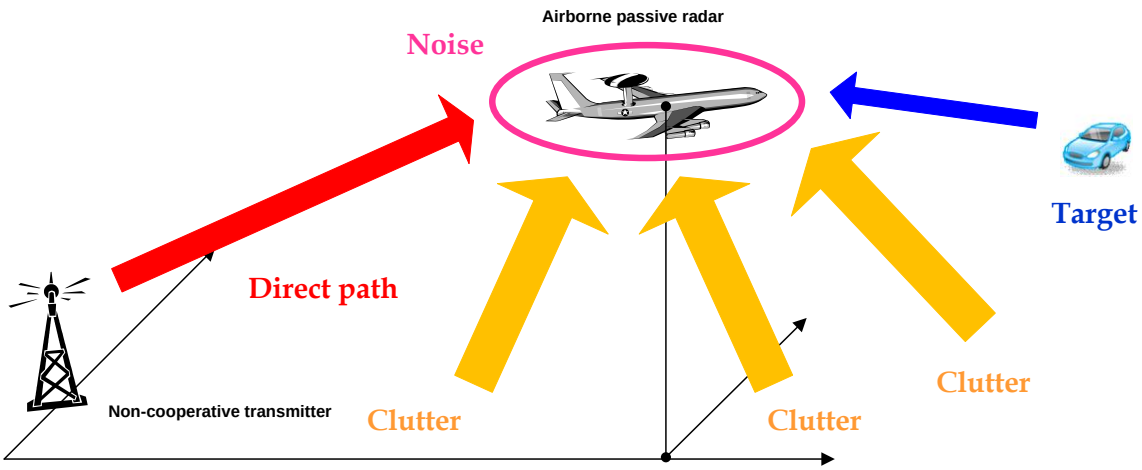

Fig. II.3: Scenario typique d'interférences pour le radar passif aéroporté.

Pour le radar passif aéroporté, la détection de cible rapide en dehors de la bande Doppler du fouillis peut aisément s'effecteur par un traitement classique Doppler. Le principal défi est donc la détection de cibles lentes et de petites dimensions. La détection de cible par un radar passif aéroporté est gênée par des interférences fortes et par une réponse faible de la cible mobile par rapport à la puissance du bruit thermique. Ce milieu très interférent est généralement composé de réponses fortes provenant du trajet direct et de la réponse du fouillis de sol. A cause des propriétés du signal passif, les lobes secondaires aléatoires en distance de ces réponses interférentes se manifestent par des couplages dans les autres cases distances d'intérêt [51]. La Figure II.3 illustre un scenario d'interférence pour le radar passif aéroporté. Notre but est d'apporter des solutions pour supprimer ces interférences afin d'améliorer les performances de détection de cibles localisées dans la bande Doppler des interférences.

II.3.1 Analyse statistique du signal passif

Le spectre électromagnétique est abondant en émissions provenant de diverses sources comme la télévision et les stations de radio, les communications satellites et d'autres systèmes de communication et de diffusion. La majorité de ces émissions a la particularité d'être des signaux CW, aléatoires et apériodiques. En général, les signaux passifs peuvent considérés non corrélés entre eux quand ils sont retardés en temps et décalés en fréquence ce qui peut être amélioré par des techniques de modulation. Ce type de signal a une fonction d'ambiguïté en punaise et présente des propriétés intéressantes [42]. La réponse approximative et échantillonnée (discrète) du signal passif CW provenant d'un émetteur non coopératif peut être modélisée par un processus aléatoire processus $s(n)$ de moyenne nulle et de variance σ^2. La fonction d'autocorrélation de ce processus complexe aléatoire s'écrit de la manière suivante:

$$r(\tau) = \frac{1}{\mathcal{N}} \sum_{n=1}^{N} s(n) s^*(n+\tau)$$

où $\mathcal{N} = BT$ est le nombre d'échantillons du signal passif. On peut montrer également que

$$E[|r(\tau)|^2] = \begin{cases} \left(1 + \frac{1}{BT}\right)\sigma^4, \text{pour } \tau = 0 \\ \frac{1}{BT}\sigma^4, \text{sinon} \end{cases}$$

où T est la durée du signal aléatoire. En normalisant l'équation ci-dessus, on obtient un pic unité à $\tau = 0$, i.e. $|r(0)|^2 = 1$, et une valeur seuil autour du pic

$$E[|r(\tau)|^2] = \frac{\frac{1}{BT}\sigma^4}{\left(1 + \frac{1}{BT}\right)\sigma^4} = \frac{1}{1+BT} \approx \frac{1}{BT}, \text{pour } BT \gg 1 \text{ et } \tau \neq 0.$$

Ces valeurs moyennes du signal aléatoire sont vérifiées par simulation. Pour cela, nous générons un signal aléatoire modulé en fréquence afin de reproduire les émissions de diffusion à savoir ceux d'un émetteur DBV-T pour lequel l'énergie de l'information aléatoire est étalée sur la bande de fréquence du signal de 8 MHz. La Figure II.4 présente la matrice de la fonction d'autocorrélation $\boldsymbol{\mathcal{R}}$ de dimensions $M \times L$ du signal aléatoire avec B = 8 MHz, T_{sub} = 2.5 ms, M = 20 et f_{BW} = 10 MHz pour un seul élément (CIT = 0.05 s). Nous définissons le vecteur colonne $\mathbf{r}_l$ qui représente les coefficients de la fonction de corrélation pour tous les M sous-CIT pour la case distance l avec $\mathbf{r}_0$ le vecteur colonne représentant les coefficients de la fonction de corrélation pour la première case distance i.e. $\boldsymbol{\mathcal{R}} = [\mathbf{r}_0, \mathbf{r}_1, \cdots, \mathbf{r}_{L-1}]$. La fonction d'autocorrélation pour chaque sous-CIT (d'une durée T_{sub} et de bande de fréquence B) montre un pic à l'origine ($l = 0$) avec une valeur de seuil (lobes secondaires aléatoires en distance) de valeur moyenne d'environ –43 dB, ce qui correspond exactement à la valeur calculée. On voit clairement que la fonction d'autocorrélation possède des niveaux significatifs de lobes secondaires en distance (pour $l \neq 0$) qui sont incohérents de sous-CIT à sous-CIT. Les propriétés de la matrice de la fonction d'autocorrélation peuvent se résumer comme suit,

$$E[|\boldsymbol{\mathcal{R}}(m,l)|^2] = \begin{cases} 1, \text{pour } l = 0 \text{ et pour tout } m \\ \frac{1}{BT_{sub}}, \text{sinon} \end{cases}.$$

Pour chaque sous-CIT, la fonction d'autocorrélation du signal aléatoire peut être considérée comme un pic à l'origine avec une valeur plancher moyenne $1/(BT_{sub})$ inférieure à la valeur du pic [42].

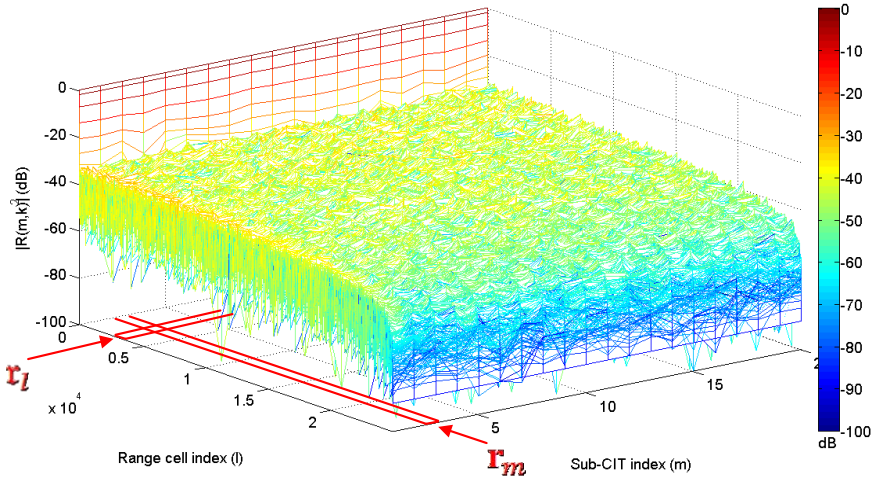

Fig. II.4: Fonction d'autocorrélation du signal aléatoire.

II.3.2 Modèles de la cible et du fouillis

On considère une case distance dans laquelle une seule cible est présente. La réponse de la cible $\boldsymbol{\chi}_t \in C^{MN\times 1}$ pour cette case distance s'écrit directement de la manière suivante :

$$\boldsymbol{\chi}_t = \alpha_t\big(\mathbf{b}(\varpi_t)\otimes\mathbf{a}(\vartheta_t)\big)$$

où α_t, ϖ_t et ϑ_t sont respectivement l'amplitude complexe, la fréquence Doppler normalisée et la fréquence spatiale de la cible; nous avons $\vartheta_t = (d/\lambda)\cos\theta_{Rt}\sin\phi_{Rt}$ et $\varpi_t = (v_t/\lambda)\cos\theta_{Rt}\sin\phi_{Rt}\,T_{sub}$ où ϕ_{Rt} et θ_{Rt} sont respectivement les angles en azimut et en élévation entre la cible et le radar passif. Le vecteur directionnel de dimension $MN\times 1$ de la cible s'écrit alors :

$$\mathbf{v}(\vartheta_t,\varpi_t) = \mathbf{b}(\varpi_t)\otimes\mathbf{a}(\vartheta_t) = \mathbf{v}_t$$

et $\boldsymbol{\chi}_t = \alpha_t\mathbf{v}_t$. L'amplitude complexe de la cible α_t s'exprime à partir de la puissance de la cible $P_t = \alpha_t^2$ qui peut être directement calculée en utilisant l'équation radar. Plus précisément, la puissance de la cible s'exprime comme $P_t = \alpha_t^2 = P_n\xi_t$. α_t est généralement très faible, même pour de grandes cibles; leurs SNR sont très inférieurs comparés aux valeurs de DNR et CNR.

Pour le radar passif aéroporté, la surface de la Terre est la principale source du fouillis. Plusieurs caractéristiques majeures sont importantes à prendre en compte dans la modélisation du fouillis. Premièrement, le fouillis est distribué en même temps en angle et en distance, il est également étalé sur les fréquences Doppler. Deuxièmement, en supposant que la surface terrestre est stationnaire, l'unique décalage induit en Doppler est dû au déplacement relatif de la plateforme du radar passif par rapport au patch du fouillis. Par conséquent, le fouillis bistatique de sol est analysé à une distance constante (case distance) autour de l'émetteur et récepteur. La case distance est divisée en N_c patches de fouillis, indépendants et identiquement distribués en azimut; chaque patch est contenu dans la cellule de résolution en distance et à une vitesse constante par rapport à la plateforme du radar passif dans une CIT. En supposant aucune contrainte de couverture LOS, la réponse du fouillis $\boldsymbol{\chi}_c \in C^{MN\times 1}$ pour une case distance (non-ambigüe) s'écrit tel que

$$\boldsymbol{\chi}_c = \sum_{i=1}^{N_c}\alpha_i\mathbf{b}(\varpi_i)\otimes\mathbf{a}(\vartheta_i) = \sum_{i=1}^{N_c}\alpha_i\mathbf{v}(\vartheta_i,\varpi_i)$$

où $\mathbf{v}_i = \mathbf{v}(\vartheta_i,\varpi_i)$ est le vecteur directionnel du fouillis pour le $i^{ième}$ patch. α_i, ϖ_i et ϑ_i sont respectivement l'amplitude complexe et aléatoire, la fréquence Doppler normalisée et la

fréquence spatiale du $i^{ième}$ patch du fouillis; de plus $\vartheta_i = (d/\lambda)\sin\phi_{Ri}\cos\theta_{Ri}$ et $\varpi_i = (v_R/\lambda)\sin\phi_{Ri}\cos\theta_{Ri}\,T_{sub}$ où ϕ_{Ri} et θ_{Ri} sont respectivement les angles d'azimut et d'élévation entre le patch de fouillis et le radar passif. Les amplitudes complexes et aléatoires α_i des patches de fouillis sont statistiquement décorrélées et ont une valeur moyenne égale à par $E[|\alpha_i|^2] = P_i$. La puissance du $i^{ième}$ patch s'exprime comme $P_i = E[|\alpha_i|^2] = P_n\xi_i$. A cause de l'irrégularité du fouillis, les réponses de différents patches sont supposées décorrélées tel que $E\left[\alpha_i\alpha_{i'}^*\right] = P_n\xi_i\delta_{i-i'}$. En utilisant les propriétés de ces valeurs moyennes, la matrice de covariance du fouillis $\mathbf{R}_c \in C^{MN\times MN}$ peut s'écrire comme suit

$$\mathbf{R}_c = E[\boldsymbol{\chi}_c\boldsymbol{\chi}_c^H] = E\left[\left(\sum_{i=1}^{N_c}\alpha_i\mathbf{b}(\varpi_i)\otimes\mathbf{a}(\vartheta_i)\right)\left(\sum_{i'=1}^{N_c}\alpha_{i'}\mathbf{b}(\varpi_{i'})\otimes\mathbf{a}(\vartheta_{i'})\right)^H\right]$$
$$= P_n\sum_{i=1}^{N_c}\xi_i(\mathbf{b}_i\mathbf{b}_i^H)\otimes(\mathbf{a}_i\mathbf{a}_i^H) = P_n\sum_{i=1}^{N_c}\xi_i\mathbf{v}_i\mathbf{v}_i^H$$

où $\mathbf{b}_i = \mathbf{b}(\varpi_i)$, $\mathbf{a}_i = \mathbf{a}(\vartheta_i)$ et $\mathbf{v}_i = \mathbf{v}(\vartheta_i, \varpi_i)$.

II.3.3 Modélisation des lobes secondaires aléatoires en distance

En plus de la cible (si elle est présente), du fouillis et du bruit, nous considérons pour la case distance sous test les forts effets de couplage des lobes secondaires aléatoires en distance de la propagation directe et de la réponse forte du fouillis. La réponse de la propagation directe $\boldsymbol{\chi}_{dp} \in C^{MN\times 1}$ à l'origine ($l = 0$) est donnée par

$$\boldsymbol{\chi}_{dp} = \alpha_{dp}\mathbf{b}(\varpi_{dp} = 0)\otimes\mathbf{a}(\vartheta_{dp}) = \alpha_{dp}\mathbf{1}\otimes\mathbf{a}(\vartheta_{dp})$$

où α_{dp} et ϑ_{dp} sont respectivement l'amplitude complexe et la fréquence spatiale du signal direct avec $\vartheta_{dp} = (d/\lambda)\cos\theta_{TR}\sin\phi_{TR}$. Le signal direct ne dépend pas de la fréquence Doppler qui est donnée par le vecteur colonne temporel $\mathbf{1} = \text{ones}(M, 1)$; le décalage en Doppler est nul et s'explique par le filtrage adapté avec le signal direct de référence qui a une fréquence Doppler identique. Par conséquent, le signal direct $\boldsymbol{\chi}_{dp_{sl}} \in C^{MN\times 1}$ s'écrit

$$\boldsymbol{\chi}_{dp_{sl}} = \alpha_{dp}(\mathbf{r}_{dp_{sl}}\odot\mathbf{1})\otimes\mathbf{a}(\vartheta_{dp})$$

où $\mathbf{r}_{dp_{sl}}$ de dimension $M \times 1$ représente les coefficients d'autocorrélation complexe sur tous les M sous-CIT pour cette case distance. La puissance du signal de la propagation directe s'exprime tel que $P_{dp} = \alpha_{dp}^2 = P_n\xi_{dp}$ où l'amplitude du signal de la propagation direct est donnée par $\alpha_{dp} = \sqrt{P_n\xi_{dp}}$. Les coefficients $\mathbf{r}_{dp_{sl}}$ des différents sous-CIT sont considérés comme aléatoires et décorrrelés; de plus on suppose également par soucis de simplicité la stationnarité du signal direct sur un CIT. Ainsi on fait l'approximation suivante

$$E\left[\mathbf{r}_{dp_{sl}}\mathbf{r}_{dp_{sl}}^H\right] = \frac{1}{BT_{sub}}\mathbf{I}_M.$$

En utilisant les propriétés de ces valeurs moyennes, la matrice de covariance des lobes secondaires aléatoire en distance du signal direct $\mathbf{R}_{dp_{sl}} \in C^{MN\times MN}$ s'écrit

$$\mathbf{R}_{dp_{sl}} = E\left[\boldsymbol{\chi}_{dp_{sl}}\boldsymbol{\chi}_{dp_{sl}}^H\right] = E\left[\left(\alpha_{dp}(\mathbf{r}_{dp_{sl}}\odot\mathbf{1})\otimes\mathbf{a}(\vartheta_{dp})\right)\left(\alpha_{dp}(\mathbf{r}_{dp_{sl}}\odot\mathbf{1})\otimes\mathbf{a}(\vartheta_{dp})\right)^H\right]$$
$$= P_nE\left[\xi_{dp}(\mathbf{r}_{dp_{sl}}\mathbf{r}_{dp_{sl}}^H)\otimes(\mathbf{a}_{dp}\mathbf{a}_{dp}^H)\right] = \frac{P_n}{BT_{sub}}\left(\xi_{dp}\mathbf{I}_M\otimes(\mathbf{a}_{dp}\mathbf{a}_{dp}^H)\right)$$

où $\mathbf{a}_{dp} = \mathbf{a}(\vartheta_{dp})$. Par conséquent, le couplage des lobes secondaires aléatoires en distance du $c^{ième}$ signal de fouillis de forte intensité localisé à une case distance lointaine a une réponse $\boldsymbol{\chi}_{c_{sl}} \in C^{MN\times 1}$qui s'écrit de la manière suivante

$$\boldsymbol{\chi}_{c_{sl}} = \sum_{i=1}^{N_c} \alpha_i \left(\mathbf{r}_{c_{sl}} \odot \mathbf{b}(\varpi_i)\right) \otimes \mathbf{a}(\vartheta_i)$$

où $\mathbf{r}_{c_{sl}}$ de dimension $M \times 1$ représente les coefficients de la fonction de corrélation complexe sur tous les M sous-CIT pour la $c^{ième}$ signal de fouillis de forte intensité pour cette case distance. Les coefficients de $\mathbf{r}_{c_{sl}}$ de différents sous-CIT sont supposés aléatoires et décorrélés ; on suppose également que le fouillis est stationnaire sur un CIT. On peut donc faire l'approximation suivante

$$E\left[\mathbf{r}_{c_{sl}} \mathbf{r}_{c_{sl}}^H\right] = \frac{1}{BT_{sub}} \mathbf{I}_M.$$

De même en utilisant les propriétés de ces valeurs moyennes, on calcule la matrice de covariance $\mathbf{R}_{c_{sl}} \in C^{MN \times MN}$ de lobes secondaires aléatoires en distance pour le $c^{ième}$ fouillis de forte intensité de la manière suivante

$$\begin{aligned}
\mathbf{R}_{c_{sl}} &= E\left[\boldsymbol{\chi}_{c_{sl}} \boldsymbol{\chi}_{c_{sl}}^H\right] \\
&= E\left[\left(\sum_{i=1}^{N_c} \alpha_i \left(\mathbf{r}_{c_{sl}} \odot \mathbf{b}(\varpi_i)\right) \otimes \mathbf{a}(\vartheta_i)\right)\left(\sum_{i'=1}^{N_c} \alpha_{i'} \left(\mathbf{r}_{c'_{sl}} \odot \mathbf{b}(\varpi_{i'})\right) \otimes \mathbf{a}(\vartheta_{i'})\right)^H\right] \\
&= P_n E\left[\sum_{i=1}^{N_c} \xi_i \left(\mathbf{r}_{c_{sl}} \mathbf{r}_{c_{sl}}^H \odot \mathbf{b}_i \mathbf{b}_i^H\right) \otimes \left(\mathbf{a}_i \mathbf{a}_i^H\right)\right] = \frac{P_n}{BT_{sub}} \sum_{i=1}^{N_c} \xi_i \left(\mathbf{I}_M \odot \mathbf{b}_i \mathbf{b}_i^H\right) \otimes \left(\mathbf{a}_i \mathbf{a}_i^H\right)
\end{aligned}$$

où $\mathbf{b}_i = \mathbf{b}(\varpi_i)$ et $\mathbf{a}_i = \mathbf{a}(\vartheta_i)$.

II.3.4 Réponse totale pour une case distance et matrice de covariance

Les composantes du signal reçu total du radar passif aéroporté ont été décrites précédemment et nous pouvons l'exprimer pour la case distance sous test de la manière suivante

$$\boldsymbol{\chi} = \boldsymbol{\chi}_t + \boldsymbol{\chi}_u = \boldsymbol{\chi}_t + \boldsymbol{\chi}_c + \boldsymbol{\chi}_{dp_{sl}} + \sum_{c=1}^{N_{sc}} \boldsymbol{\chi}_{c_{sl}} + \boldsymbol{\chi}_n$$

où N_{sc} est le nombre de fouillis de forte intensité et $\boldsymbol{\chi}_n$ est un vecteur de bruit blanc complexe et Gaussien qui représente le bruit de réception. Pour simplifier les calculs, la puissance du bruit P_n est égale à 1 de manière à pouvoir référencer toutes les puissances des autres signaux par leur SNR par élément et par sous-CIT. $\boldsymbol{\chi}_u$ est un vecteur qui contient toutes les composantes indésirables (interférence et bruit). Il est facile de montrer que les composantes du signal $\boldsymbol{\chi}$ sont mutuellement décorrélées ; cela nous permet d'écrire la matrice de covariance des interférences plus bruit de la manière suivante

$$\mathbf{R}_u = E[\boldsymbol{\chi}_u \boldsymbol{\chi}_u^H] = \mathbf{R}_c + \mathbf{R}_{dp_{sl}} + \sum_{c=1}^{N_{sc}} \mathbf{R}_{l_{sl}} + \mathbf{R}_n$$

où $\mathbf{R}_c$, $\mathbf{R}_{dp_{sl}}$, $\mathbf{R}_{c_{sl}}$ et $\mathbf{R}_n$ sont respectivement les matrices de covariance du fouillis, du signal parvenu via lobes secondaires aléatoires en distance du trajet direct, des signaux parvenus via les lobes secondaires aléatoires du $c^{ième}$ fouillis, enfin du bruit.

II.4 Propriétés des lobes secondaires aléatoires en distance

Comme nous l'avons calculé précédemment, la réponse, couplée avec d'autres cases distance, des lobes secondaires en distance et aléatoires du signal direct s'écrit

$$\boldsymbol{\chi}_{dp_{sl}} = \alpha_{dp}\left(\mathbf{r}_{dp_{sl}} \odot \mathbf{1}\right) \otimes \mathbf{a}\left(\vartheta_{dp}\right)$$

et la matrice de covariance qui lui est associée

$$\mathbf{R}_{dp_{sl}} = \frac{P_n}{BT_{sub}}\left(\xi_{dp}\mathbf{I}_M \otimes \left(\mathbf{a}_{dp}\mathbf{a}_{dp}^H\right)\right).$$

Les lobes secondaires en distance et aléatoires du signal direct sont spatialement corrélés, élément par élément mais temporellement décorrélés, sous-CIT par sous-CIT. Dans ce cas, leur réponse dans le domaine spatial-Doppler est une ligne irrégulière le long de toutes les fréquences Doppler et pour la fréquence spatiale du signal direct ; sa puissance moyenne est inférieure de $1/(BT_{sub} \times M)$ à la valeur du pic du signal direct à la case distance d'origine. Le rang de la matrice de covariance $\mathbf{R}_{dp_{sl}}$ est égal à

$$\text{rank}\left(\mathbf{R}_{dp_{sl}}\right) = M.$$

La matrice de covariance de l'autocorrélation complexe $\mathbf{r}_{dp_{sl}}$ du signal direct est approximée par

$$E\left[\mathbf{r}_{dp_{sl}}\mathbf{r}_{dp_{sl}}^H\right] = \frac{1}{BT_{sub}}\mathbf{I}_M.$$

La réponse des lobes secondaires aléatoires du $c^{ième}$ fouillis de forte intensité et couplée sur plusieurs cases distance, s'écrit de la manière suivante

$$\boldsymbol{\chi}_{c_{sl}} = \sum_{i=1}^{N_c} \alpha_i\left(\mathbf{r}_{c_{sl}} \odot \mathbf{b}(\varpi_i)\right) \otimes \mathbf{a}(\vartheta_i)$$

et la matrice de covariance qui lui est associée

$$\mathbf{R}_{c_{sl}} = \frac{P_n}{BT_{sub}} \sum_{i=1}^{N_c} \xi_i(\mathbf{I}_M \odot \mathbf{b}_i\mathbf{b}_i^H) \otimes (\mathbf{a}_i\mathbf{a}_i^H).$$

III Traitement du signal pour le radar passif aéroporté

III.1 Présentation des méthodes de traitement pour la détection de cibles mobiles

Le milieu interférent vu par le radar passif aéroporté est toujours caractérisé par des niveaux élevés du signal direct et du fouillis comparés à ceux du bruit thermique. La chaine de traitements du signal du radar passif aéroporté est montrée sur la Figure III.1. Le récepteur de *N* canaux du radar passif aéroporté transforme le signal passif RF reçu à chaque élément en un signal IF adapté à l'échantillonnage complexe ; la digitalisation du signal et son stockage en échantillons en bande de base sont effectués par l'ADC. Pour pouvoir utiliser la totalité du système de réception à *N* canaux, une étape de calibration des canaux est indispensable pour compenser différents effets pratiques et non-idéaux comme les distorsions d'amplitude et de phase entre les éléments physiques d'un canal de réception ou entre les connections et câbles des différents canaux. On utilise généralement une matrice de correction qui est calculée dans le domaine fréquentiel et qui compense ces effets indésirables. On applique ensuite les traitements suivants, la suppression adaptative basée sur les moindres carrés et le traitement spatio-temporel adaptatif (STAP) en dimension réduite qui visent à supprimer les interférences. Le processus de suppression des interférences s'effectue ainsi en 2 temps. Premièrement, la suppression adaptative basée sur les moindres carrés appliquée avant le filtrage adapté permet de supprimer le signal direct et les signaux de fouillis de forte intensité provenant, via les lobes secondaires, de cases distance lointaines pour chaque élément de réception. Dans un second temps, le traitement STAP supprime le fouillis de la case distance sous test dans l'espace bidimensionnel espace-Doppler. Plus

précisément, afin de réduire la complexité des calculs (grande dimension) et le nombre de données secondaires nécessaires à l'estimation du filtre STAP, nous utilisons les méthodes de réduction de dimensions qui rendent possible l'application du STAP dans des conditions réalistes.

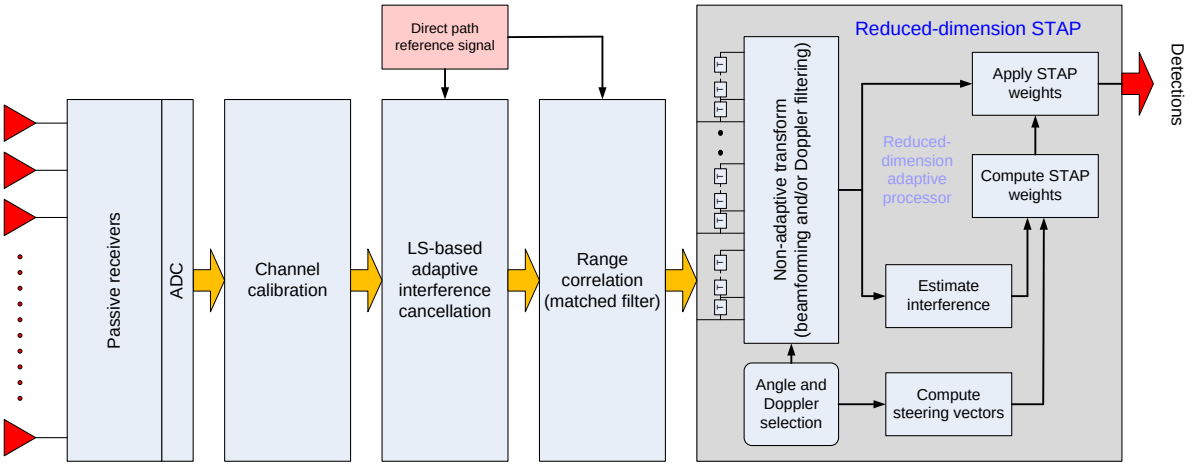

Fig. III.1: Chaine de traitements du signal du radar passif aéroporté

III.2 Suppression adaptative des interférences

La suppression adaptative des interférences peut être vue comme un filtrage FIR ayant comme entrée le signal direct de référence et le signal reçu avant filtrage adaptatif. En utilisant une implémentation basée sur les moindres carrés du filtre FIR adaptatif, le principe fondamental de cette méthode est de minimiser la puissance en sortie comme le montre la structure du filtre représentée dans la Figure III.2 [67]. La technique de suppression des interférences basée sur la minimisation de l'erreur en sortie au sens des moindres carrés, se base sur la différence optimale entre signal direct de référence affecté de différents poids et de ses versions décalées en Doppler, et du signal reçu ; les poids affectés au signal direct de référence sont optimaux au sens des moindres carrés. Le signal direct de référence et le signal reçu sont tous les deux composés du signal de la cible (si présente), des interférences (à supprimer) et du bruit ; ces signaux sont en entrée de filtre FIR adaptatif qui en sortie donne un signal reçu sans les composantes des interférences. La formulation mathématique de l'erreur en sortie peut s'écrire sous forme vectorielle de la manière suivante:

$$\mathbf{e} = \mathbf{x} - \mathbf{S}\mathbf{w}.$$

où $\mathbf{x}$ est le signal reçu, $\mathbf{S}$ est la matrice du signal direct de référence dont chaque colonne est une version unique et retardée du signal direct de référence et $\mathbf{w}$ est le vecteur des poids. Ainsi la minimisation de la puissance en sortie de filtre FIR adaptatif est équivalente à la suppression des composantes des interférences. La fonction de coût basée sur les moindres carrés qui minimise l'erreur quadratique s'écrit sous la forme

$$\min_{\mathbf{w}} \|\mathbf{e}\|^2 = \min_{\mathbf{w}} \|\mathbf{x} - \mathbf{S}\mathbf{w}\|^2.$$

L'erreur est nulle pour le vecteur optimal de poids suivant:

$$\mathbf{w} = (\mathbf{S}^H\mathbf{S})^{-1}\mathbf{S}^H\mathbf{x}.$$

Par conséquent, le signal reçu après l'application de l'algorithme de suppression adaptative des interférences s'écrit :

$$\mathbf{x}_{new} = \mathbf{x} - \mathbf{S}\mathbf{w}.$$

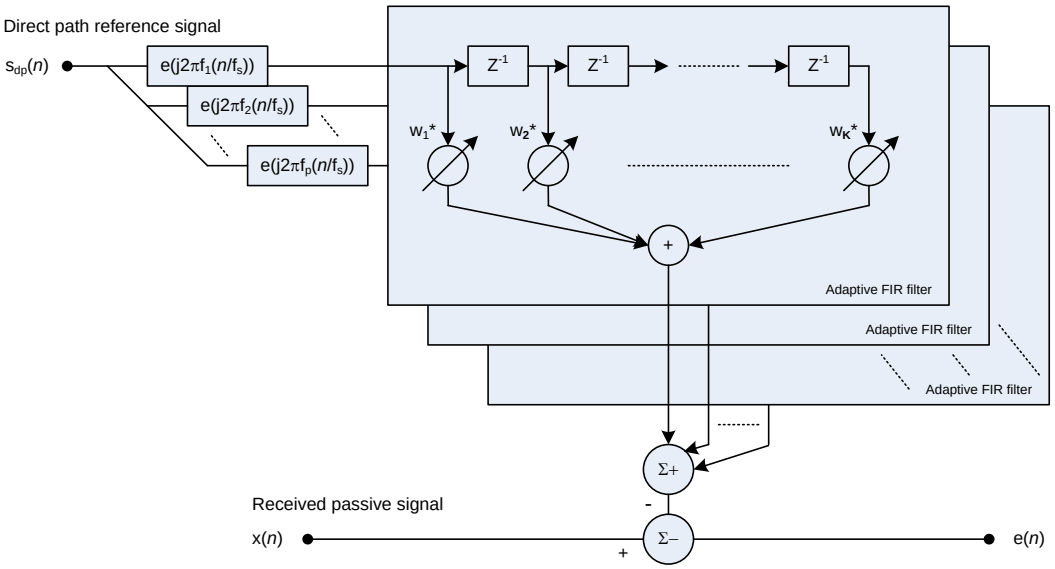

Fig. III.2: Structure of adaptive FIR filter.

III.3 Traitement spatio-temporel adaptatif en dimension réduite

Le fouillis vu par le radar passif aéroporté n'est généralement pas connue et ses propriétés doivent être estimées en utilisant des données secondaires présentes dans le cube de données CIT. La dimension MN du filtre STAP dépend directement de la longueur du réseau d'antenne et du CIT et peut varier de plusieurs centaines à des milliers. Malheureusement, le nombre de données secondaires nécessaires à une bonne estimation des propriétés du fouillis est proportionnel à la dimension du filtre STAP. De plus, les contraintes de puissance des émetteurs non coopératifs et la bande de fréquence étroite des signaux passifs limitent le nombre de cases distance. Enfin, le fouillis est souvent hétérogène et non stationnaire ce qui limite encore le nombre de données secondaires IID. Un nombre limité de données secondaires entrainent invariablement une dégradation dans la suppression du fouillis du traitement STAP. De plus le traitement STAP en pleine dimension représente une charge de calcul colossale. Pour toutes ces raisons, il n'est pas possible d'appliquer le STAP entièrement adaptatif à des situations réalistes. C'est pourquoi les traitements STAP avec réduction de dimensions sont des méthodes très attractives : elles permettent d'obtenir des bonnes performances de suppression du fouillis avec un nombre limité de données secondaires et aussi d'alléger la charge en calcul. L'approche sous-optimale des algorithmes STAP avec réduction de dimensions est basée sur des traitements spatiaux et temporels en cascade. Ces méthodes appliquent des transformations indépendantes des données comme prétraitements et réduisent ainsi les dégrées de liberté de l'adaptation. La plupart des méthodes de réduction de dimensions peuvent être classifiées en quatre catégories selon leur type de transformations non adaptatives [49, 75]. Une taxonomie de ces algorithmes STAP à réduction de dimensions est présentée sur la Figure III.3. Le schéma type de ces algorithmes STAP est de transformer les données initiales spatio-temporelles de dimensions $MN \times 1$ en des données de dimensions réduites $D \times 1$. Le vecteur du signal recu réduit $\tilde{\boldsymbol{\chi}}$ s'obtient par la matrice de transformation de dimensions $MN \times D$ de la manière suivante

$$\tilde{\boldsymbol{\chi}} = \mathbf{T}^H \boldsymbol{\chi}$$

où

$$\tilde{\boldsymbol{\chi}} = \alpha_t \tilde{\mathbf{v}}_t + \tilde{\boldsymbol{\chi}}_u.$$

$\tilde{\mathbf{v}}_t = \mathbf{T}^H \mathbf{v}_t$ étant le vecteur directionnel réduit de la cible et $\tilde{\boldsymbol{\chi}}_u$ la réponse spatio-temporelle réduite des interférences plus bruit. Le vecteur réduit de poids de dimension $D \times 1$ associé à ces transformations s'écrit de la manière suivante :

$$\tilde{\mathbf{w}} = \tilde{\mathbf{R}}_u^{-1} \tilde{\mathbf{g}}_t$$

où

$$\tilde{\mathbf{R}}_u = E[\tilde{\boldsymbol{\chi}}_u \tilde{\boldsymbol{\chi}}_u^H] = \mathbf{T}^H \mathbf{R}_u \mathbf{T}$$

est la matrice réduite de covariance de dimension $D \times D$ et $\tilde{\mathbf{g}}_t$ est le vecteur réduit de la réponse attendue qui s'obtient de la manière suivante :

$$\tilde{\mathbf{g}}_t = \mathbf{T}^H \mathbf{g}_t.$$

où $\mathbf{g}_t$ est le vecteur de la réponse de la cible de dimension non réduite. La sortie finale d'un tel filtre STAP s'obtient en appliquant le vecteur réduit de poids comme suit

$$z = \tilde{\mathbf{w}}^H \tilde{\boldsymbol{\chi}} = (\mathbf{T}\tilde{\mathbf{w}})^H \boldsymbol{\chi}.$$

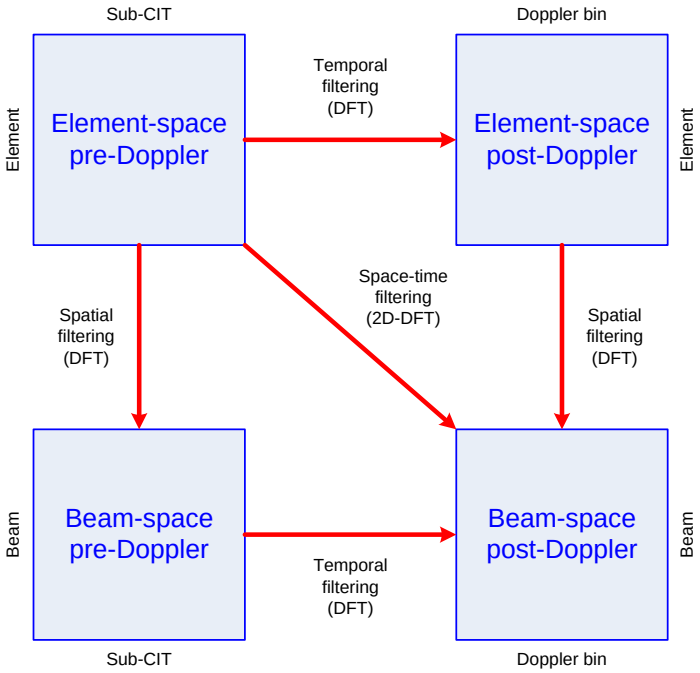

Fig. III.3: Taxonomie des algorithmes STAP à dimensions réduites.

Comme montré sur la Figure III.3, les algorithmes STAP à dimensions réduites sont classifiés selon le domaine dans lequel sont appliqués les poids adaptatifs. La stratégie « blanchiment puis filtrage » pour laquelle le filtrage STAP est appliqué avant le traitement Doppler est connue sous le nom de pre-Dopppler ; l'approche qui consiste à « filtrer puis blanchir » c'est-à-dire effectuer le filtrage STAP après traitement Doppler est nommée le post-Doppler. L'algorithme STAP espace-élément (element-space) consiste à combiner les signaux de tous les éléments pour lequel la réduction de dimension est effectuée par traitement adaptatif sur seulement quelques sous-CIT en même temps ou à combiner un faible nombre de sorties filtrées pour chaque élément. Le filtrage spatial peut aussi s'effectuer sur toutes les sorties des éléments pour chaque sous-CIT avant adaptation et les algorithmes qui forment les faisceaux (beamforming) avant adaptation sont appelés algorithmes STAP dans l'espace-faisceau (beam-space).

IV Simulations

IV.1 Configuration géométrique et des paramètres de simulation

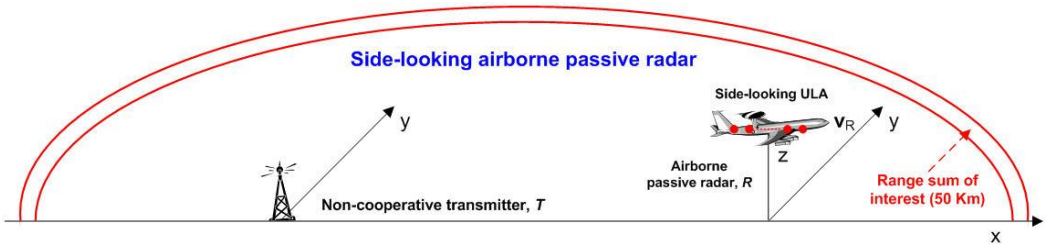

Fig. IV.1: Configuration géométrique en visée latérale.

Tab. IV.1: Paramètres de simulation.

Geometrical parameters	
Non cooperative transmitter height	200 m
Airborne passive radar altitude	1000 m
Airborne passive radar velocity	100 m/s
Ground baseline	20000 m
Normalized clutter reflectivity	–16 dB (rural land)
RMS surface slope	0.17 rad (rural land)
Passive signal parameters	
Random signal carrier frequency	600 MHz
Random signal bandwidth	8 MHz
Complex sampling bandwidth	10 MHz
Effective radiated power	8 KW
Transmit antenna pattern	Omnidirectional
Receive antenna element gain	5 dB
Receive antenna element pattern	Omnidirectional front-lobe (180° coverage) and insignificant back-lobe (unless otherwise stated)
Receiver noise figure	5 dB
Boltzmann's constant	1.38×10^{-23}
Receiver reference temperature	290 K
Total system losses	5 dB
Passive datacube parameters	
Number of elements	16
Sub-CIT repetition frequency	400 Hz ($\pm$200 Hz)
Sub-CIT repetition interval	2.5 ms
Number of sub-CITs	20
Normalized slope of clutter ridge (β)	1

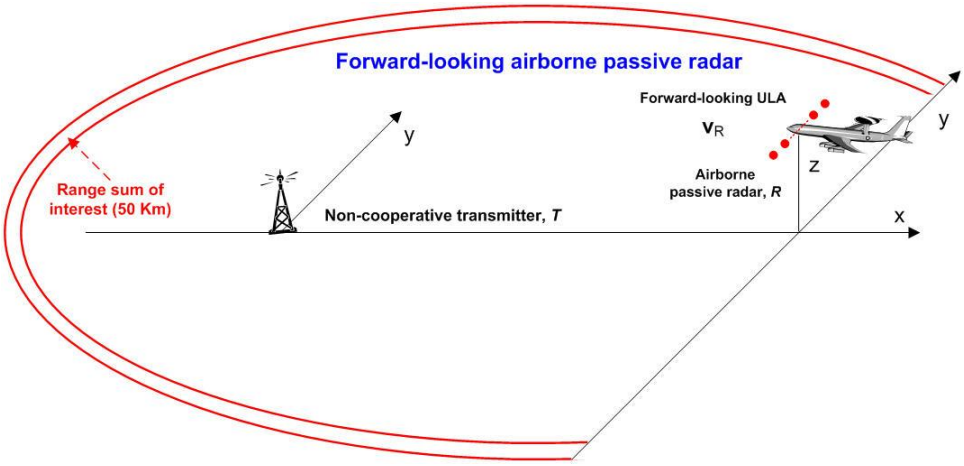

Fig. IV.2: Configuration géométrique en visée avant.

Pour évaluer les performances du radar passif aéroporté, nous considérons deux configurations géométriques, en visée latérale sur la Figure IV.1 et en visée avant sur la Figure IV.2, pour une couverture dans toutes les directions autour de la plateforme du radar passif. Dans la configuration en visée latérale, l'ULA est supposé être monté sur le fuselage latéral de la plateforme aéroporté ; la géométrie de la trajectoire de vol est telle que l'émetteur DVB-T et la plateforme aéroportée sont alignés suivant l'axe x et que la plateforme aéroporté s'éloigne dans la direction des x positifs. Dans la configuration en visée avant, l'ULA est supposé être monté sur le nez de la plateforme aéroportée avec le réseau d'antennes perpendiculaire au vecteur vitesse $\mathbf{v}_R$. Dans cette configuration, le radar passif vole vers l'émetteur dans la direction des x négatif pour modéliser un couplage fort entre le signal direct et le fouillis. La Terre est supposée plate et stationnaire. La trajectoire de vol est supposée parallèle à la surface terrestre. Les paramètres des configurations géométriques, du radar et du cube de données sont résumés dans le tableau IV.1. Le bilan de puissance pour la géométrie bistatique et les paramètres du signal passif du tableau IV.1 est calculé pour être applicable aux configurations en visée latérale et en visée avant.

IV.2 Spectre en puissance des interférences

En considérant le bilan de puissance et les paramètres géométriques des simulations, les composantes des interférences sont générées pour $K_e = 2MN = 640$ cases distance centrées autour de la distance bistatique de 50 Km (case distance sous test $l_d = 999$). Cette case distance est localisée à une distance de 15 Km de la plateforme aéroporté du radar selon la ligne de base. Ainsi pour la configuration en visée latérale, l'estimée SCM de la matrice de covariance des interférences $\widehat{\mathbf{R}}_u$ peut être calculée en moyennant sur $2MN$ données secondaires. Le spectre MVDR de toutes les composantes des interférences reçues par le radar passif aéroporté est représenté sur la Figure IV.3 ; ces composantes sont constituées du fouillis, des signaux issus des lobes secondaires aléatoires en distance du trajet direct et du fouillis de forte intensité ($N_{sc} = 298$) et du bruit. Nous voyons clairement la ligne diagonale et disjointe du fouillis ainsi que les effets de couplage des lobes secondaires du signal direct. Le niveau plancher du spectre est égal à la puissance du bruit thermique. Les lignes parallèles à l'axe des fréquences Doppler ($\vartheta = -0.5$) représentent le couplage des lobes secondaires du signal direct dans $\widehat{\mathbf{R}}_u$. Dans tous les cas, les lobes secondaires du signal direct sont localisés à la fréquence spatiale de l'émetteur non coopératif par rapport au réseau d'antenne. Le niveau plancher distribué sur toutes les fréquences spatiales correspond au couplage du fouillis de forte intensité. A des distances bistatiques courtes, ces lobes secondaires du fouillis de forte

intensité sont concentrés autour de la fréquence spatiale (direction) de l'émetteur puisque sa distance bistatique se trouve le long de la ligne de base. A mesure que la distance du fouillis de forte intensité augmente, l'étalement des fréquences spatiales est plus apparent à cause de l'augmentation de la distance bistatique constante. Ainsi le niveau plancher du spectre est plus élevée autour de la fréquence spatiale des lobes secondaires du signal direct.

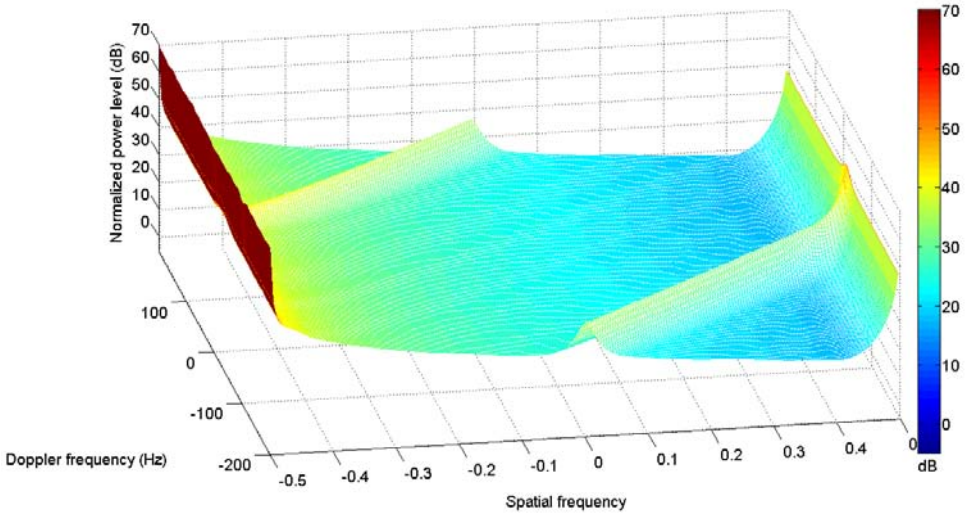

Fig. IV.3: Spectre MVDR pour la configuration en vise latérale (R_{sum} = 50 Km).

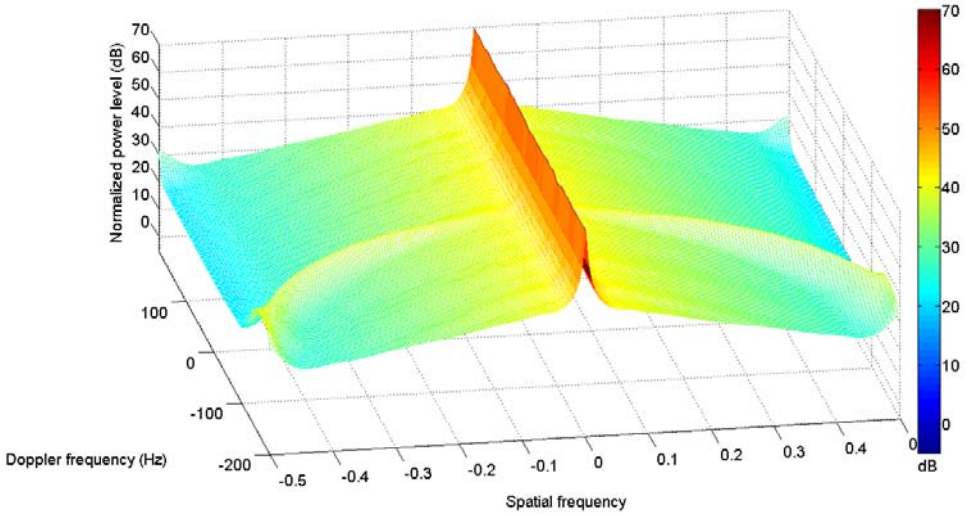

Fig. IV.4: Spectre MVDR pour la configuration en vise latérale (R_{sum} = 50 Km).

Pour la configuration en visée avant, de la même manière que précédemment, la matrice de covariance des interférences $\widehat{\mathbf{R}}_u$ est estimée en utilisant la SCM et en moyennant sur $2MN$ cases distance centrées autour de la distance bistatique à 50 Km (case distance sous test $l_d = 999$). A la distance bistatique d'intérêt, il a été montré que le fouillis contenu dans $\widehat{\mathbf{R}}_u$ est supposé indépendant en distance (stationnaire). Le spectre des interférences pour la configuration en visée avant est montré sur la Figure IV.4. Cette figure montre un scénario de fortes interférences avec un émetteur non coopératif situé sur le côté du réseau d'antenne. La ligne en demi-cercle dans les fréquences Doppler négatives correspond à la fréquence Doppler relative du fouillis stationnaire contenu dans $\widehat{\mathbf{R}}_u$ après filtrage adapté. La ligne le long de l'axe des fréquence Doppler ($\vartheta = 0$) représente le couplage des lobes secondaires

aléatoire en distance du signal direct contenu dans $\widehat{\mathbf{R}}_u$. Le spectre montre un seuil plus haut pour les fréquences spatiales associées aux lobes secondaires aléatoires en distance des $N_{sc} = 139$ fouillis de forte intensité pour lesquelles les couplages indésirables dominent le fouillis contenu dans $\widehat{\mathbf{R}}_u$. De même, les lobes secondaires du fouillis de forte intensité sont concentrés autour de la fréquence spatiale de l'émetteur non coopératif où son intensité augmente avec la distance bistatique. Ainsi le niveau plancher dû aux lobes secondaires du fouillis de forte intensité est plus élevé autour de la fréquence spatiale du signal direct.

IV.3 Résultats de la suppression adaptative des interférences et analyses

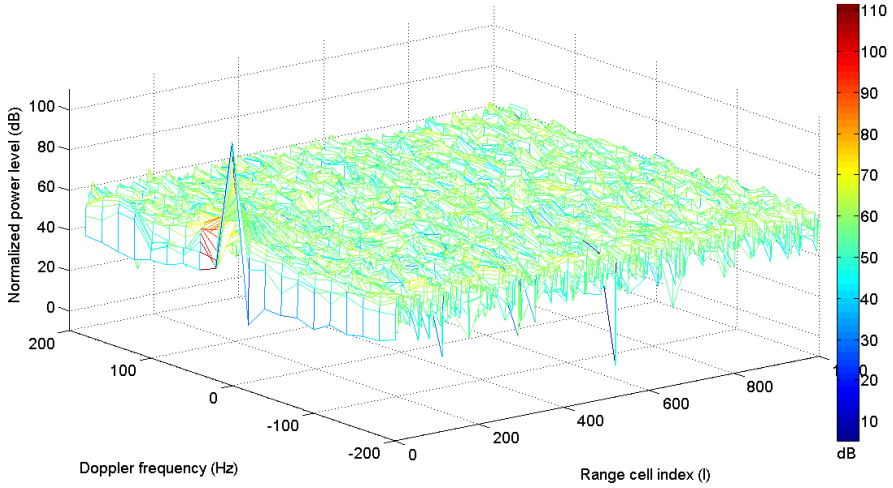

Fig. IV.5: Fonction d'ambiguïté pour un seul élément avant suppression adaptative.

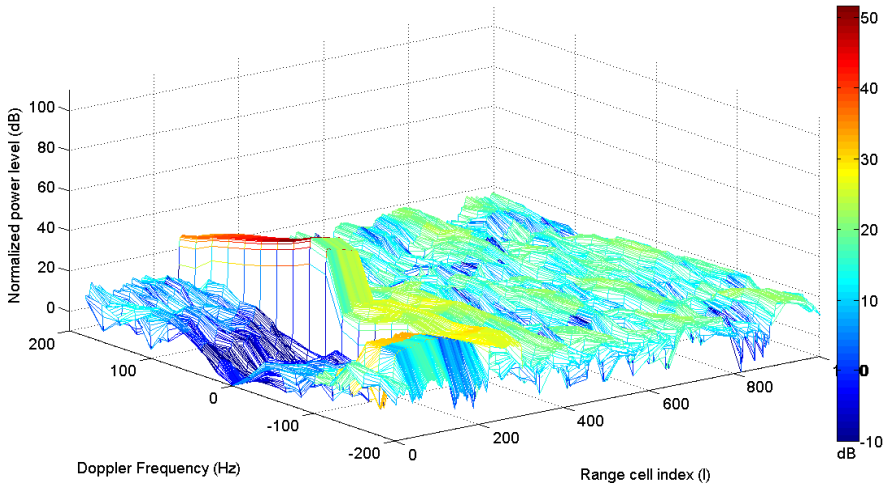

Fig. IV.6: Fonction d'ambiguïté pour un seul élément après suppression adaptative d'ordre 220.

On se place dans les configurations en visée latérale et en visée avant précédemment définies pour évaluer les performances de la suppression adaptive des interférences basée sur les moindres carrées. Comme la suppression des interférences est effectuée sur chaque élément, nous représentons les résultats par la fonction d'ambigüité croisée dans le domaine distance-Doppler. La Figure IV.5 montre cette fonction d'ambiguïté croisée pour le signal

reçu sur un unique élément dans la configuration à visée latérale sans suppression adaptative des interférences. Nous considérons seulement $N_{sc} = 298$ cellules de fouillis de forte intensité puisque il a été montré que la puissance des lobes secondaires du fouillis de forte intensité pour $N_{sc} > 298$ est inférieure à la puissance du bruit thermique de la case distance l_d en configuration en visée latérale. Comme nous l'avons vu, le signal le plus fort provient du signal direct d'un niveau par rapport au bruit de 111 dB (la puissance du signal direct par rapport au bruit par élément et par sous-CIT est égale à 98 dB + $10\log_{10} M$ dB). La majorité de la puissance du fouillis de forte intensité semble être masquée par la puissance des lobes secondaire aléatoire et en distance du signal direct dont la puissance d'environ 55 dB est inférieure de $10\log_{10}(1/(BT_{sub}M)) = 56$ dB comparée à la valeur du pic du signal direct. Dans le domaine spatial-Doppler, cette valeur de base de 55 dB (dans la fonction d'ambiguïté) qui est associé aux lobes secondaires du signal direct est localisée à une seule fréquence spatiale sur une ligne Doppler du même niveau. Néanmoins le niveau qui est associée aux lobes secondaires de fouillis de forte intensité occupe la totalité des fréquences spatiales ce qui dégrade fortement les performances de détection des cible mobiles. La Figure IV.6 montre les résultats de la fonction d'ambiguïté croisée avec suppression adaptative des interférences. Idéalement le filtre FIR adaptatif devrait fonctionner avec au moins un filtre d'ordre 298 sur toutes les 20 cases Doppler. Cependant nous nous limitons à un filtre d'ordre 220 pour des questions de coût et de charge de calcul ; de plus le filtre est appliqué sur 17 cases Doppler puisque le fouillis décalé en Doppler est relativement faible sur les 3 dernières cases. Nous montrons sur cette Figure IV.6 que le filtre FIR adaptatif supprime efficacement ces composantes des interférences dans les cases distance $l \leq 219$ et pour les 17 cases Doppler considérées. Des résidus du fouillis pour les cases distance $l \geq 219$ ne sont quant à eux pas totalement supprimer. La puissance de base est donc causée seulement par ces résidus de fouillis et est significativement inférieure à la puissance de base de la Figure IV.5.

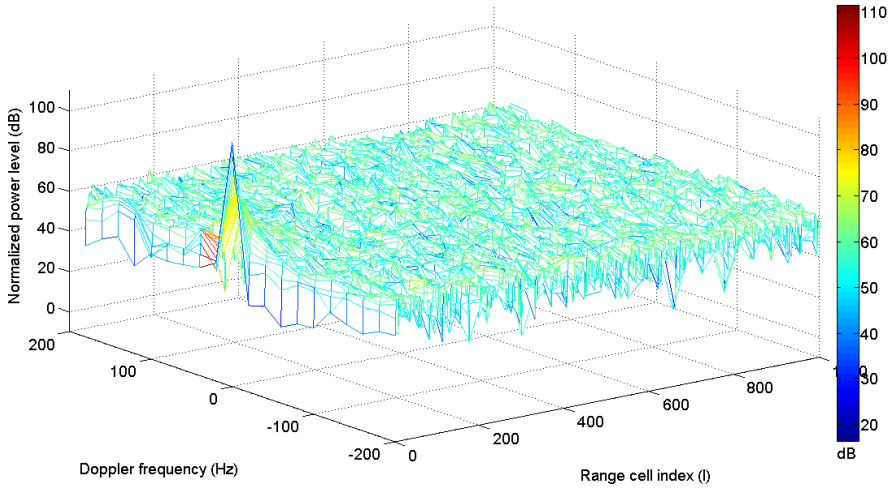

Fig. IV.7: Fonction d'ambiguïté pour un seul élément avant suppression adaptative.

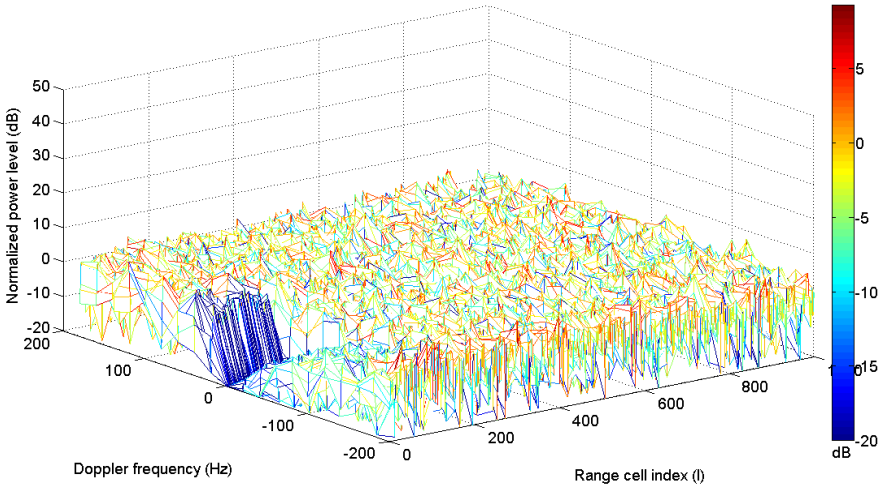

Fig. IV.8: Fonction d'ambiguïté pour un seul
élément après suppression adaptative d'ordre 150.

Nous considérons maintenant la configuration en visée avant en représentant la fonction d'ambiguïté croisée sans suppression adaptative des interférences sur la Figure IV.7. Comme précédemment, seulement $N_{sc} = 139$ cellules de fouillis de forte intensité sont prises en compte puisque le niveau des lobes secondaires de ce fouillis pour $N_{sc} > 139$ est inférieur au niveau plancher du bruit thermique dans la configuration en visée avant. La majorité du fouillis de forte intensité et de ses versions décalées en Doppler étalées sur les 20 cases Doppler et sur les cases distance avec un indice supérieur à $l = 138$ semble masquée par les lobes secondaire du signal direct. Ainsi la puissance seuil (causée par les lobes secondaires du signal direct) est approximativement inférieure de $10\log_{10}\left(1/(BT_{sub}M)\right)$ dB à la valeur pic du DNR. De même le niveau associé aux lobes secondaires du signal direct est localisé sur une ligne parallèle ($\vartheta_{dp} = 0$) le long de l'axe des fréquences Doppler ; le niveau des lobes secondaires du fouillis de forte intensité occupe toutes les fréquences spatiales ce qui dégrade fortement les performances de détection des cibles mobiles. La Figure IV.8 montre la fonction d'ambiguïté croisée avec l'utilisation d'un filtre FIR adaptatif d'ordre 150 sur toutes les cases Doppler pour supprimer les contributions du signal direct, du fouillis de forte intensité et de ses échos décalés en Doppler. Nous constatons que ces contributions sont efficacement supprimées et que le niveau plancher correspond bien au bruit thermique.

Sans prendre en compte le coût en charge de calcul de l'algorithme, la suppression adaptative des interférences basée sur les moindres carrée est capable de supprimer efficacement les interférences causées par le signal direct et le fouillis de forte intensité dans les deux configurations, visée latérale et avant. Le niveau des lobes secondaires de ces interférences dans la case distance sous test l_d est alors réduit également. Pour appliquer cette méthode, le nombre de poids (ordre du filtre FIR) doit être au minimum égal au nombre N_{sc} de fouillis de forte intensité pour toutes les cases Doppler qu'occupe ce fouillis. Le calcul du vecteur de poids nécessite l'inversion de la matrice $\mathbf{S}^H\mathbf{S}$. Ainsi, le principal inconvénient de cette méthode est la charge de calcul et la taille mémoire, ce qui peut rendre difficile sa mise en œuvre pour un fonctionnement en temps réel. Un autre inconvénient est la suppression des cibles aux distances proches, cibles qui sont supprimées en même temps que les interférences. Enfin, l'entrée du filtre FIR adaptatif nécessite la connaissance du signal direct de référence; dans des environnements réalistes, celui-ci peut être corrompu par différents signaux comme les propagations multiples. Par conséquent il est inévitable que les performances de suppression adaptative des interférences soient dégradées et que les

interférences ne soient pas totalement supprimées. Leurs lobes secondaires ne sont donc eux aussi pas totalement annulés à la case distance sous test l_d. Pour illustrer cette limitation de la suppression des interférences nous présentons les spectres MDVR de la case distance sous test sur les Figures IV.9 et IV.10 pour les configurations en visée latérale et en visée avant respectivement, en considérant une suppression de seulement 45 dB des lobes secondaires du signal direct et de 35 dB des lobes secondaires du fouillis de forte intensité. Malgré cette limitation, les interférences sont fortement réduites et leur puissance est généralement inférieure au bruit thermique.

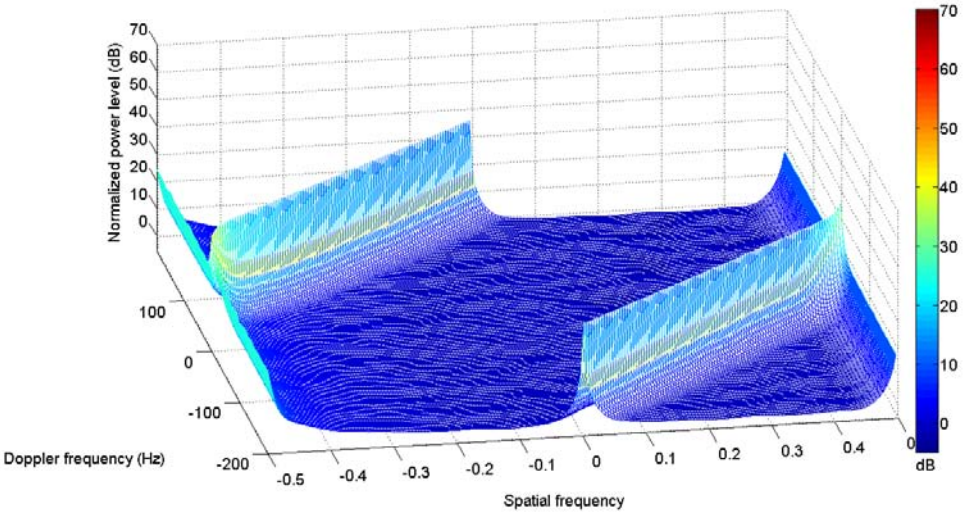

Fig. IV.9: Spectre MVDR pour la configuration en visée latérale (R_{sum} = 50 Km) après suppression adaptative des interférences.

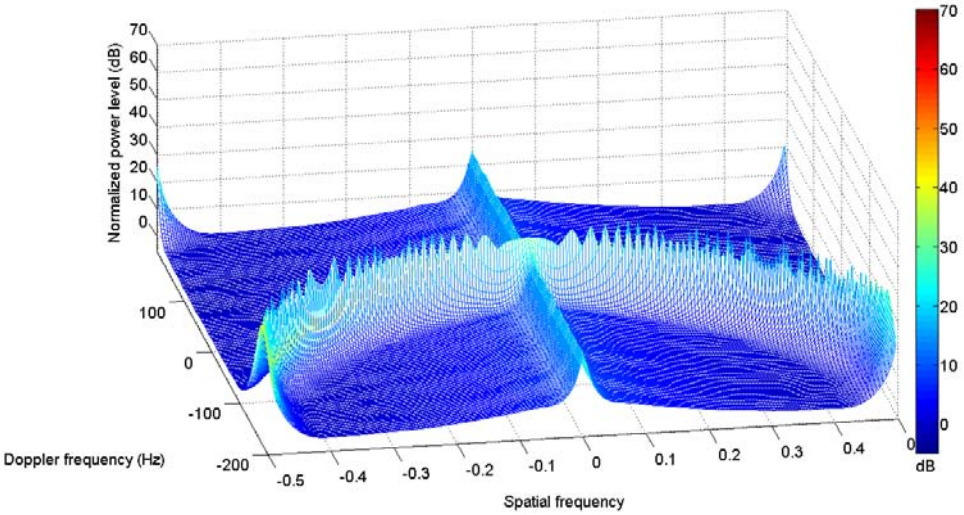

Fig. IV.10: Spectre MVDR pour la configuration en visée avant (R_{sum} = 50 Km) après suppression adaptative des interférences.

IV.5 Résultat du traitement spatio-temporel adaptatif en dimensions réduites

Pour les configurations en visée latérale et en visée avant, la suppression adaptative des interférences avec le filtrage adapté est capable d'annuler efficacement les interférences causées par le signal direct et le fouillis de forte intensité. Le reste des interférences contenu dans $\widehat{\mathbf{R}}_u$ est donc composé des résidus du signal direct et du fouillis de forte intensité et du fouillis stationnaire et localisé dans le domaine spatial-Doppler de la case distance sous-test. Les traitements que nous considérons dans cette section visent à supprimer ces interférences par l'utilisation d'algorithmes STAP en dimensions réduites avant l'étape de détection. Il est difficile de choisir une unique approche STAP en dimensions réduites qui serait la meilleure pour toutes les configurations possibles. Ces méthodes présentent des avantages et des inconvénients selon les configurations. Ainsi nous proposons d'appliquer le meilleur algorithme STAP en dimensions réduites selon la configuration.

Toutes les formations de faisceaux et filtrages Doppler sont effectuées avec un fenêtrage de Chebyshev de 30 dB. Nous considérons également que le nombre de données secondaires disponibles pour estimer la matrice de covariance $\widehat{\mathbf{R}}_u$ est égale au double du nombre de degrés de liberté du problème ; ces données secondaires sont situées sur des cases distance centrées autour de l_d. Nous présentons les résultats sous forme de pertes en SINR et du MDV à 12dB. Pour la configuration du radar passif aéroporté en visée latérale, les performances en termes de pertes en SINR et pour une distance bistatique de 50 Km ($l_d = 999$) des quatre algorithmes STAP en dimensions réduites considérés sont montrées sur les Figures IV.11 à IV.14. Les pertes en SINR pour le cas optimal sont également représentées pour une fréquence spatiale de 0. Les algorithmes STAP « element-space » dans les Figures IV.11 et IV.12 effectuent l'adaptation sur tous les éléments ; l'algorithme STAP « element-space » pre-Doppler réduit le domaine temporel en sous-CIT de taille $K = 2$ et l'algorithme STAP « element-space » post-Doppler réduit le domaine temporel en sous-CIT de taille $K = 2$. Les Figures IV.13 et IV.14 montrent les pertes en SINR des algorithmes « element-space » pré-Doppler avec $K_t = 2$ et $K_s = 3$ et post-Doppler avec $K_{tm} = 3$ et $K_{sm} = 3$. Les quatre algorithmes STAP en dimensions réduites donnent de bonnes performances relativement proches de celles de l'optimal. Les nœuds des filtres se forment sur les lignes disjointes et diagonales du fouillis. Les approches post-Doppler donnent un meilleur MDV et donc un meilleur UDSF. Les algorithmes STAP «beam-space » en dimensions réduites ont l'avantage de donner des performances identiques que les algorithmes « element-space » mais avec beaucoup moins de données secondaires.

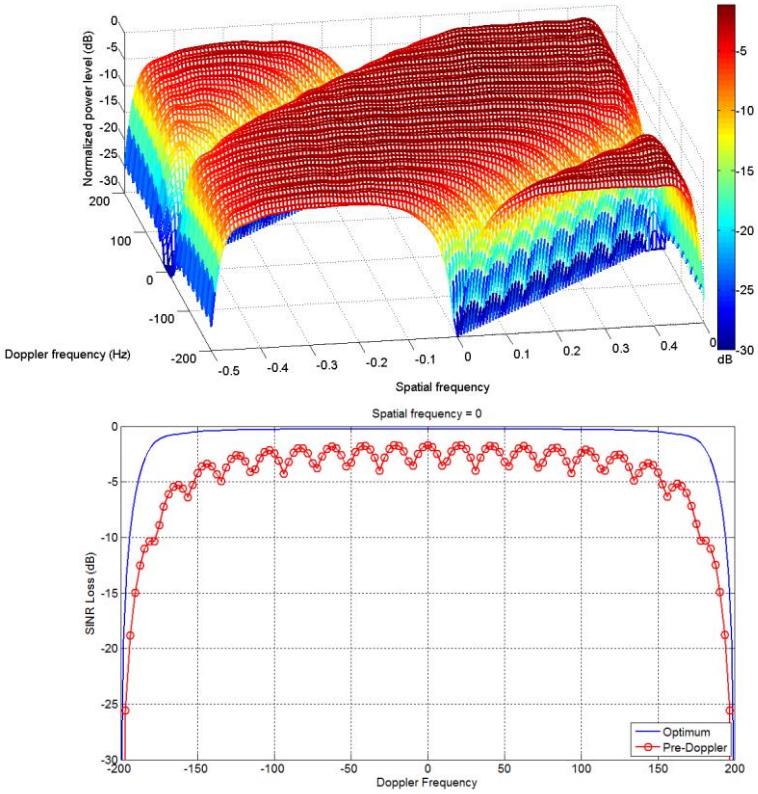

Fig. IV.11: Pertes en SINR et sa coupe à la fréquence spatiale nulle pour l'algorithme STAP pré-Doppler, $K = 2$.

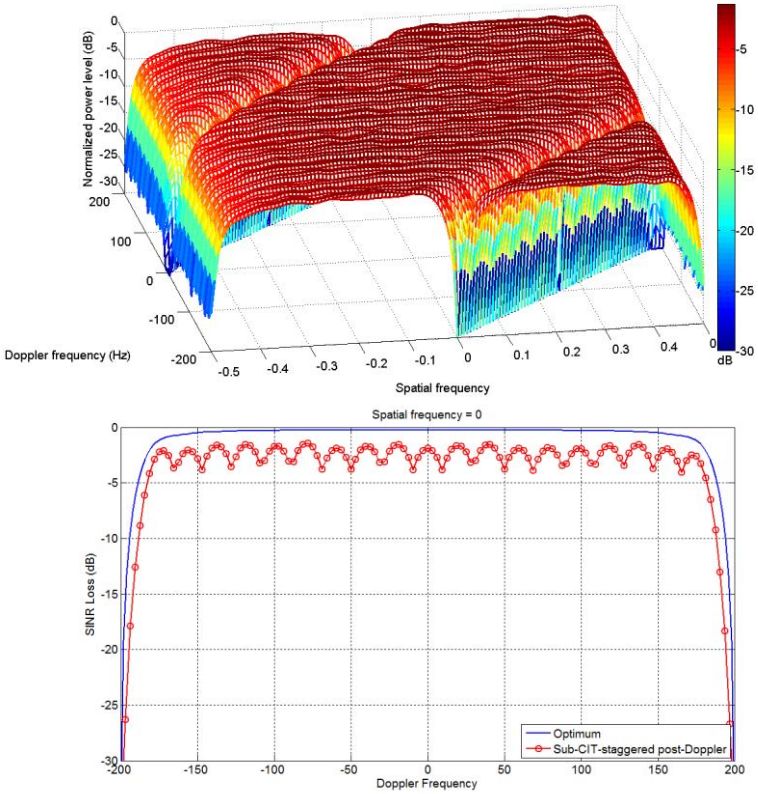

Fig. IV.12: Pertes en SINR et sa coupe à la fréquence spatiale nulle pour l'algorithme STAP « element-space » post-Doppler, $K = 2$.

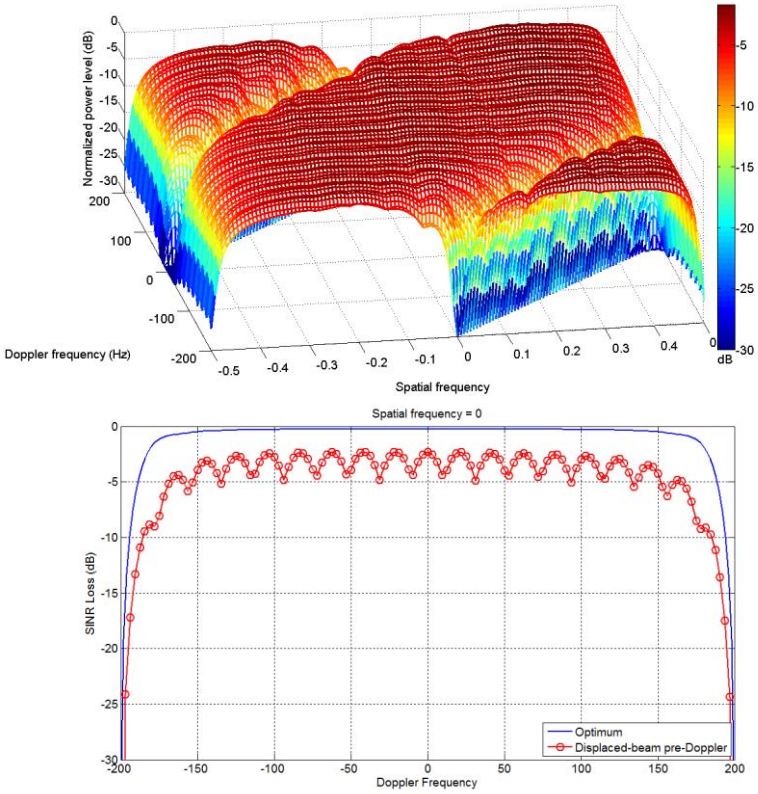

Fig. IV.13: Pertes en SINR et sa coupe à la fréquence spatiale nulle pour l'algorithme STAP « beam-space » pré-Doppler, $K_t = 2$ et $K_s = 3$.

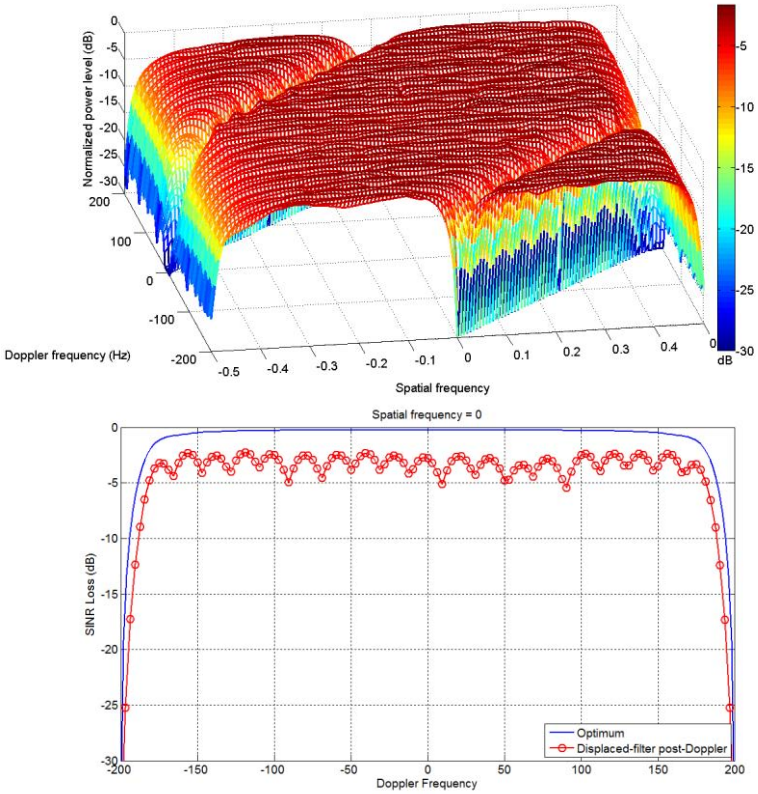

Fig. IV.14: Pertes en SINR et sa coupe à la fréquence spatiale nulle pour l'algorithme STAP « beam-space » post-Doppler, $K_{tm} = 3$ et $K_{sm} = 3$.

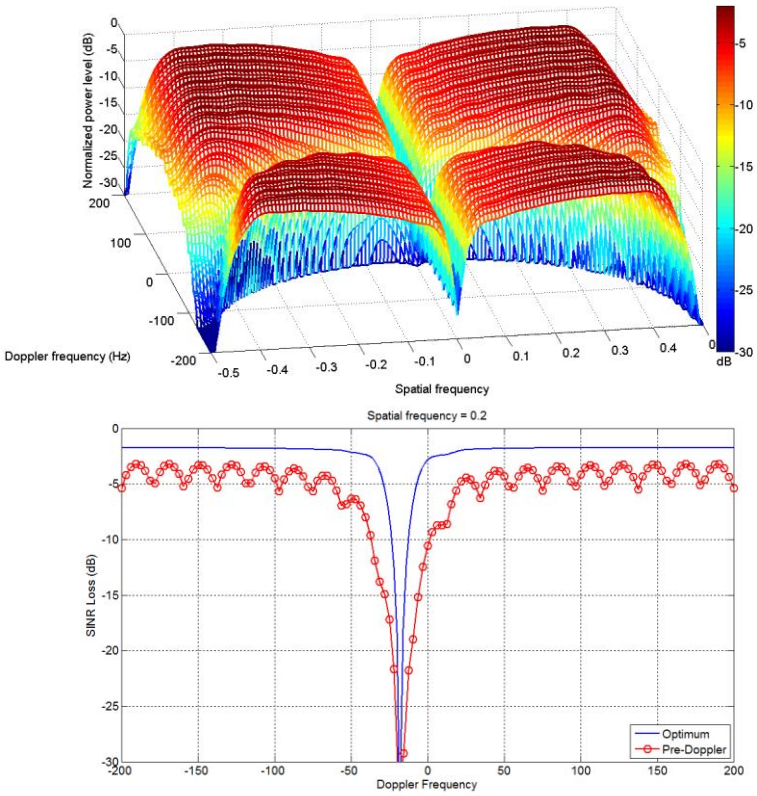

Fig. IV.15: Pertes en SINR et sa coupe à la fréquence spatiale 0.2 pour l'algorithme STAP « element-space » pré-Doppler, $K = 2$.

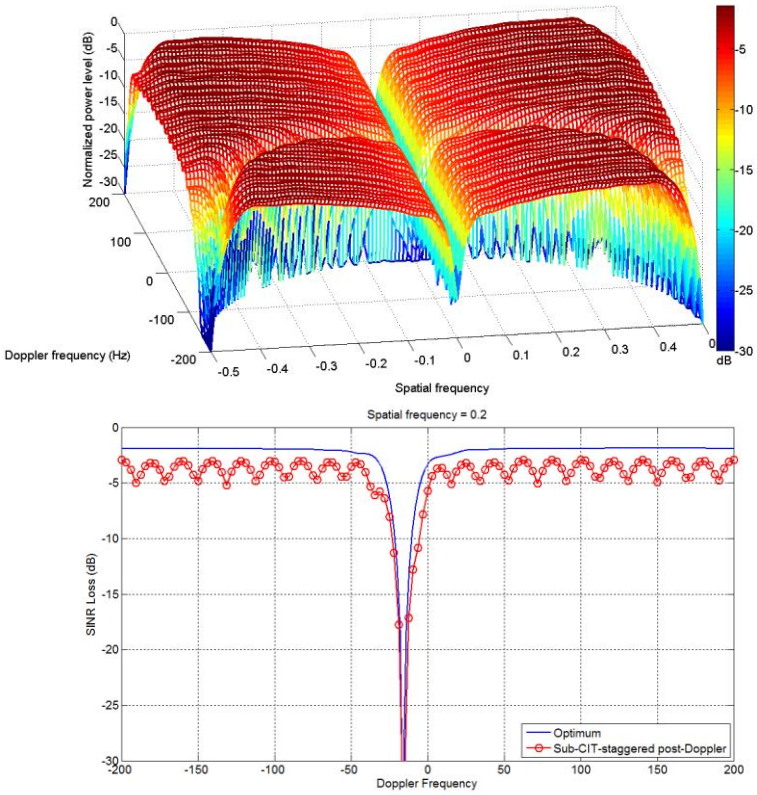

Fig. IV.16: Pertes en SINR et sa coupe à la fréquence spatiale 0.2 pour l'algorithme STAP « element-space » post-Doppler, $K = 2$.

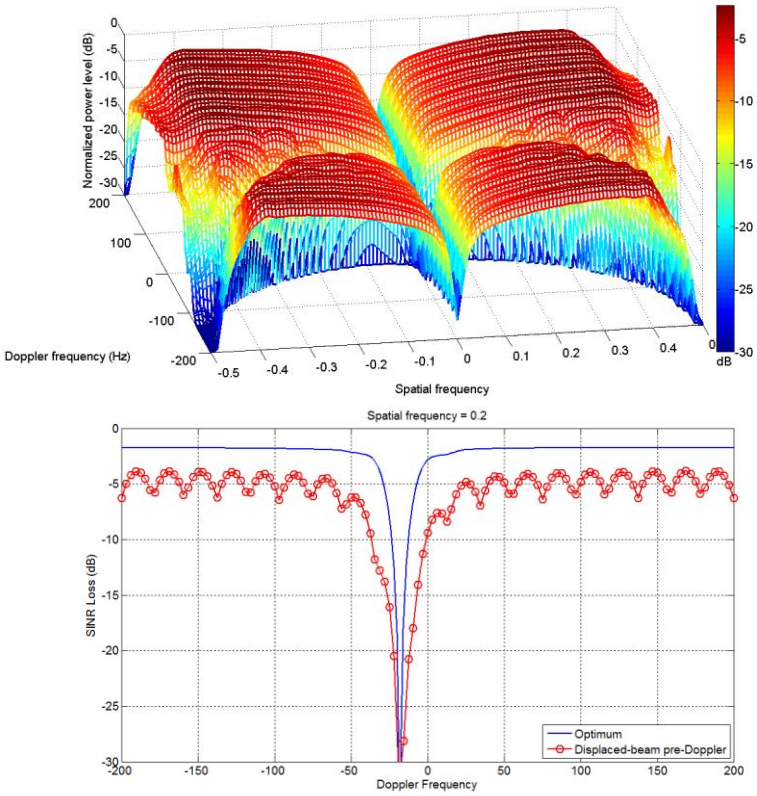

Fig. IV.17: Pertes en SINR et sa coupe à la fréquence spatiale 0.2 pour l'algorithme STAP « beam-space » pré-Doppler, $K_t = 2$ et $K_s = 4$.

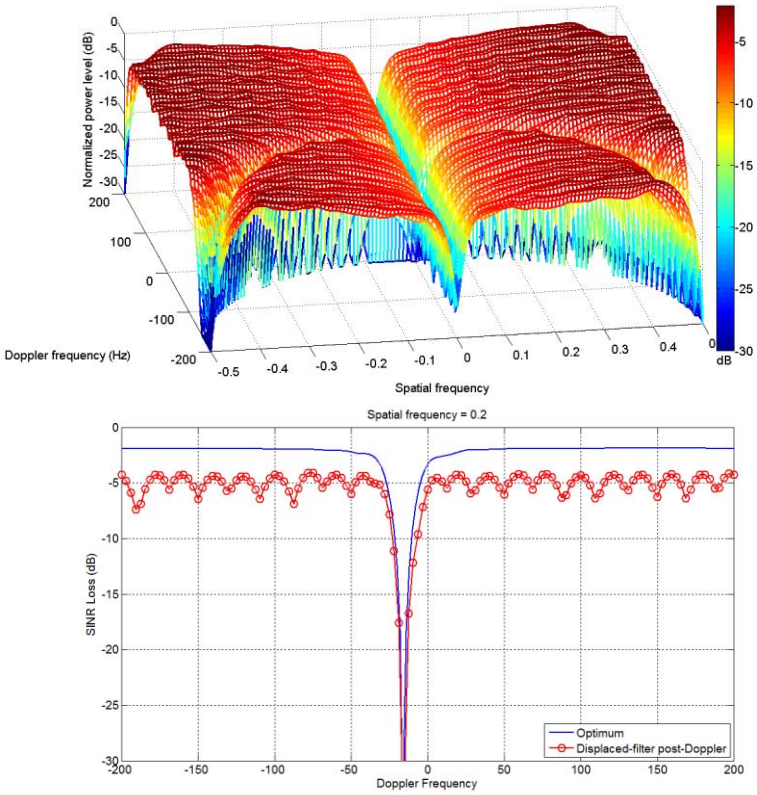

Fig. IV.18: Pertes en SINR et sa coupe à la fréquence spatiale 0.2 pour l'algorithme STAP « beam-space » post-Doppler, $K_{tm} = 4$ et $K_{sm} = 4$.

Nous présentons maintenant les performances des quatre algorithmes STAP pour la configuration en visée avant pour une case distance sous test 50 Km ($l_d = 999$) sur les Figures IV.15 to IV.18. Comme la configuration en visée avant induit de fortes interférences, la puissance des lobes secondaires du signal direct est supérieure à la puissance du bruit même après la suppression adaptative des interférences ; ces résidus de lobes secondaires se manifestent par une ligne à la fréquence spatiale nulle et parallèle à l'axe Doppler. De la même façon, les résidus de lobes secondaires du fouillis fort causent une augmentation du plancher de bruit concentrée autour de la fréquence spatiale nulle. Dans ce cas, nous présentons les pertes en SINR pour la fréquence spatiale égale à 0.2 pour évaluer les performances des algorithmes STAP. Les pertes en SINR pour le cas optimal sont inférieures de quelques dB à 0 à cause des résidus des lobes secondaires dans les régions sans fouillis. Nous représentons sur les pertes en SINR de l'algorithme STAP « element-space » pré-Doppler avec $K = 2$ sur la Figure IV.15 et celles de l'algorithme STAP « element-space » post-Doppler avec $K = 2$ sur la Figure IV.16. Le fouillis ayant une réponse en demi-cercle pour la configuration en visée avant, les pertes en SINR aux fréquences spatiales –0.5 et 0.5 sont très fortes. Les pertes en SINR des algorithmes STAP « beam-space » pré-Doppler avec $K_t = 2$ et $K_s = 4$ et post-Doppler avec for $K_{tm} = 4$ et $K_{sm} = 4$ sont respectivement présentées sur les Figures IV.17 et IV.18. A cause des résidus des lobes secondaires, nous devons considérer au moins 4 faisceaux pour effectuer l'adaptation et atteindre bonnes performances proches de celles de l'optimal. Les quatre approches STAP montrent de bonnes performances de suppression du fouillis en plaçant un nœud sur le demi-cercle qu'il occupe et également les résidus des lobes secondaires du signal direct en plaçant un nœud à la fréquence spatiale nulle ($\vartheta = 0$) pour toutes les fréquences Doppler. Enfin, comme pour la configuration en visée latérale les approches post-Doppler offrent de meilleurs MDV que les approches pré-Doppler. De plus les approches « beam-space » permettent de réduire le nombre de données secondaires avec les mêmes performances comparées aux approches « element-space ».

V Expérimentations avec un radar passif mobile au sol

V.1 Configuration et paramètres des essais expérimentaux

Les expérimentations du radar passif mobile et au sol sont menées de façon à reproduire au mieux le comportement d'un radar passif aéroporté. Les objectifs de ces expérimentations sont de collecter des données réelles, de valider la modélisation théorique des signaux passifs, d'évaluer les performances de traitements proposés dans un environnement réel. Pour cela, nous avons construit et mis en œuvre un banc d'essai expérimental d'un radar passif avec 4 canaux et un réseau d'antenne cornet à 4 éléments. Un générateur de signal permet de produire un signal au format DVB-T émis par une antenne séparée pour reproduire un signal non coopératif qui serait émis par un émetteur DVB-T. Le site de l'expérimentation est un terrain recouvert d'herbe qui constitue un fouillis de surface sur une fauchée de 600 m. La Figure V.1 montre la carte du site d'expérimentation avec le fouillis. Le radar passif au sol et la totalité du banc d'essai sont montés et opèrent à l'arrière d'un camion comme le monte la Figure V.1. L'émetteur et le réseau de réception dont les éléments sont espacés de $\lambda/2$ sont montés sur un stand élevé à une hauteur d'environ 3.5m par rapport au sol et sont séparés entre eux d'1m. Le stand est placé dans une direction parallèle au côté du camion dans une configuration monostatique en visée latérale. L'angle d'élévation de visée pour les antennes d'émission et de réception vaut approximativement quelques degrés pour pointer sur le centre de la largeur de la fauchée du fouillis. Les données complexes en bande de base sont enregistrées et traitées sur la plateforme qui se déplace à

une vitesse d'environ 7 m/s (vitesse du camion 25 Km/h). Le signal direct de référence est obtenu par une formation numérique de faisceaux dans la direction de l'antenne d'émission. Le cube de données passives pour un CIT de 0.2 s est constitué de signaux reçus par 4 canaux, 100 sous-CIT (chacun d'une durée de 2 ms) et de 20000 cases distance.

Fig. V.1: Carte des mesures du fouillis et photographie du banc de test du radar passif au sol monté sur un camion.

V.2 Traitement du signal et analyse

Pour montrer l'environnement interférent de nos expérimentations, nous représentons sur la Figure V.2 le spectre en puissance dans le domaine angle-Doppler d'un signal reçu provenant de la case distance $l = 5$ (75 m) qui contient majoritairement la réponse des lobes secondaires du signal direct. Comme prévu, la réponse de ces lobes secondaires est une ligne irrégulière à toutes les fréquences Doppler et à la fréquence spatiale normalisée du signal direct (ϑ_{dp} = –0.5). La valeur moyenne des lobes secondaires est environ égale à –62.5 dB ce qui est inférieur de $10\log_{10}(1/MBT_{sub}) = 62$dB du pic de la valeur du signal direct à la case distance de l'origine. Un niveau relativement haut à Doppler nul apparait : il est causé par une cohérence de la fonction de corrélation entre les sous-CIT pour des distances faibles ; cela montre que le signal DVB-T ne se comporte pas totalement comme du bruit. De plus, le spectre révèle la réponse du fouillis stationnaire comme une ligne diagonale dans le domaine angle-Doppler. Ces résultats sur données réelles valident la modélisation théorique et les simulations précédemment présentées.

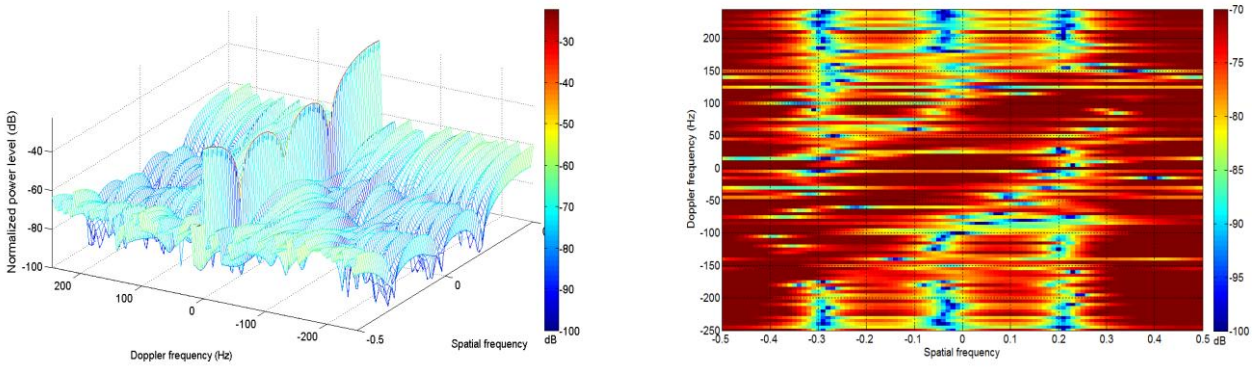

Fig. V.2: Spectre de puissance de la case distance $l = 5$.

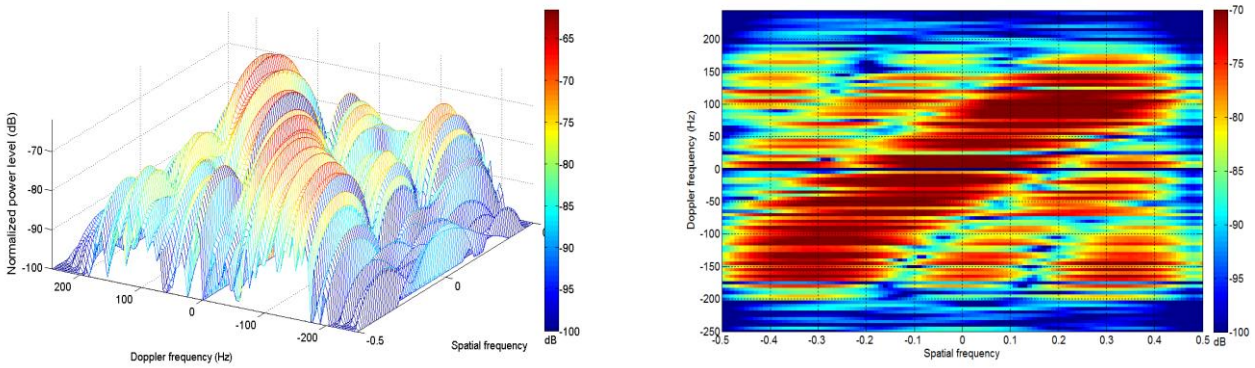

Fig. V.3: Spectre de puissance de la case distance $l = 5$
après suppression adaptative des interférences.

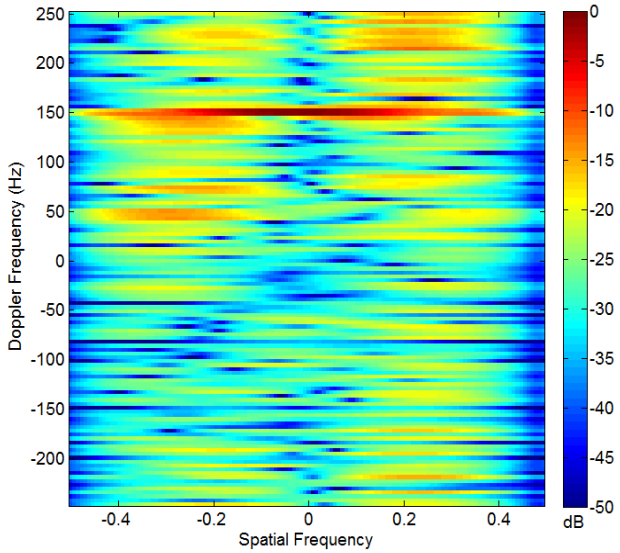

Fig. V.4: Réponse adaptée de l'algorithme STAP
« element-space » pré-Doppler, case Doppler 30 (151.5 Hz).

Le premier traitement appliqué aux données est la suppression adaptative des interférences qui vise à supprimer les lobes secondaires du signal direct et du fouillis de forte intensité de la case sous test, avant le filtrage adapté. Cette suppression annule la réponse du signal direct, du fouillis de forte intensité et de ses échos décalés en Doppler, les lobes secondaires de ces interférences étant elles-aussi supprimés. Les mesures montrent que seuls les lobes secondaires du signal direct ont une réponse plus grande que le bruit thermique pour des cases distance lointaines ; dans ce cas de figure, on utilise un filtre FIR adaptatif d'ordre 50 pour supprimer les lobes secondaires du signal direct et les effets de la cohérence de sa corrélation à distance faible (contributions à Doppler nul). Après l'application du filtre FIR adaptatif, nous obtenons sur la Figure V.3 le spectre en puissance dans le domaine angle-Doppler pour la case distance $l = 5$ (75 m). Nous constatons que les interférences dues aux lobes secondaires de signal direct et la cohérence de sa corrélation sont effectivement supprimés ; seule la contribution du fouillis stationnaire apparait sur une ligne diagonale du domaine angle-Doppler. Par comparaison avec la Figure V.2, la réponse du fouillis stationnaire est plus clairement visible ; ceci est vérifié pour les 48 premières cases distance. Pour les cases distance comprises entre $l = 49$ et 62, la réponse du fouillis est toujours visible mais de moindre intensité. Pour les cases distances lointaines $l \geq 63$, la réponse du

fouillis n'est plus visible et la puissance moyenne mesurée d'environ -102 dB ce qui correspond à nos attentes, c'est-à-dire au niveau de puissance du bruit thermique.

Après la suppression adaptative des interférences, nous appliquons un filtrage STAP en dimension réduite pour supprimer la réponse du fouillis stationnaire. Comme le nombre de cases distance et donc de données secondaires est limité, nous utilisons les algorithmes STAP « element-space » pré-Doppler et post-Doppler sur les 4 canaux de réseau de réception ; un fenêtrage de Chebyshev de 30 dB est appliqué pour les traitements Doppler et les données secondaires au nombre du double des degrés de liberté sont prises sur les cases distance centrées autour de $l = 20$. Nous représentons sur la in Figure V.4 la réponse adaptée donnée par l'algorithme STAP « element-space » pré-Doppler avec $K = 2$ pour la case Doppler 30 (151.5 Hz) et une fréquence spatiale nulle. La valeur maximum est atteinte pour la fréquence spatiale et Doppler de la cible potentielle. La résolution spatiale est faible car le nombre d'éléments est seulement de 4. Enfin on voit un nœud d'intensité faible sur la ligne occupée précédemment par le fouillis. Les pertes en SINR sont représentées sur la Figure V.5 pour l'algorithme STAP « element-space » pré-Doppler ; les pertes optimales y sont également représentées. Comme prévu, les deux courbes de pertes en SINR sont relativement semblables avec bien entendu une dégradation pour les pertes en SINR réelles. Les zones non occupées par le fouillis subissent une perte en SINR d'environ -5 dB. Les pertes deviennent significatives autour de la région de Doppler nul ce qui montre la capacité de l'algorithme STAP « element-space » pré-Doppler à supprimer le fouillis. Ces pertes sont plus élevées comparées au cas optimal et le nœud est aussi plus large ; cela s'explique par la nature réelle des données secondaires qui ne sont pas totalement IID. L'estimation de la matrice de covariance est donc une autre difficulté pour les environnements réels. Pour un MDV à 12 dB, les cibles doivent avoir une fréquence Doppler inférieure à -32 Hz ou supérieure à 29.5 Hz pour être détectées. Comparé au cas optimal avec un MDV de 1.11 m/s, le MDV réel avec l'algorithme STAP « element-space » pré-Doppler est en moyenne deux fois plus élevé et égale à 2.08 m/s. L'augmentation du nombre de sous-CIT à $K = 3$ dégrade significativement ce résultat avec un nœud du filtre plus large.

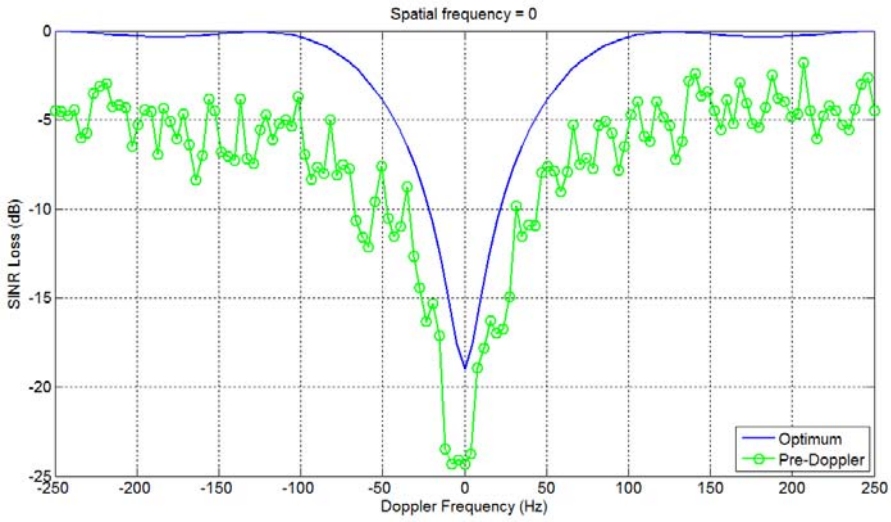

Fig. V.5: Pertes en SINR l'algorithme STAP « element-space » pré-Doppler, $K = 2$.

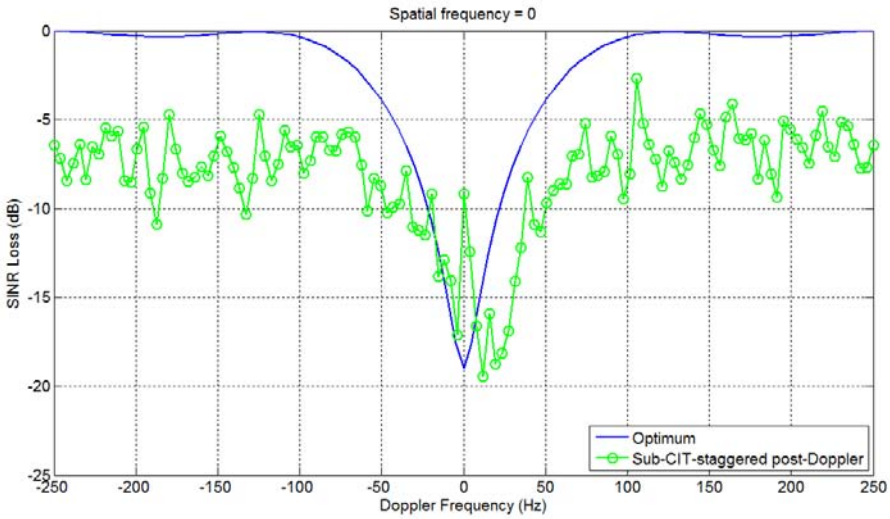

Fig. V.6 Pertes en SINR l'algorithme STAP « beam-space » post-Doppler, $K = 3$.

Les pertes en SINR de l'algorithme « element-space » post-Doppler sont montrées sur la Figure V.6 en fixant le nombre de sous-CIT à $K = 3$ (une taille $K = 2$ donne des résultats un peu moins bons). Nous représentons également les pertes en SINR pour le cas optimal comme référence. Les régions non occupées par le fouillis ont une perte en SINR d'environ -6.5 dB dans le cas réel ce qui est un peu moins bon que pour l'algorithme « element-space » pré-Doppler. Les pertes en SINR dans la région du nœud formé à Doppler nul sont moins élevées mais celles-ci ont tendance à varier pour les autres cases Doppler comparé à l'algorithme « element-space » pré-Doppler. En revanche on obtient un meilleur MDV mais cela nécessite un nombre plus important de données secondaires puisque la taille d'une sous-CIT est égale à $K = 3$. Pour un MDV à 12dB, les cibles avec une fréquence Doppler inférieure à -17 Hz et supérieures à 35.5 Hz sont détectées. Le MDV est en moyenne égale à 1.77 m/s ce qui est approximativement 1.5 fois supérieur au MDV optimal de 1.11 m/s. Par conséquent, pour nos expérimentations de radar passif mobil au sol, l'algorithme « element-space » post-Doppler donne des résultats légèrement meilleurs comparés à l'algorithme « element-space » pré-Doppler. Cela valide nos résultats de simulations pour lesquelles l'algorithme « element-space » post-Doppler donne un meilleur MDV et ainsi un meilleur UDSF.

IV Conclusions

Cette thèse est consacrée à l'étude du radar passif aéroporté ; plus précisément nous nous concentrons sur la mise en œuvre d'un tel radar dans un environnement réaliste où de nombreuses interférences rendent difficiles la détection de cible. Nos objectifs sont à la fois de proposer une modélisation valide et précise du signal et de proposer des solutions pour supprimer les interférences ; outre les formulations mathématiques associées au radar passif et aux méthodes associées, des simulations réalistes nous permettent d'illustrer et de vérifier nos résultats théoriques. Enfin, nous proposons de mettre en œuvre un radar passif mobile au sol dans un environnement réel pour valider notre étude

Le modèle théorique du signal reçu prend en compte les différentes contributions d'interférences. Pour la case distance sous test, ces interférences sont le fouillis, les lobes secondaires du signal direct, les lobes secondaires du fouillis de forte intensité et le bruit thermique. Les propriétés de chaque interférence ont été également présentées afin de définir complètement le modèle de signal passif. Ce modèle et des simulations nous permettent de

caractériser les effets de ces interférences sur le signal reçu pour la case sous test : le fouillis donne une réponse rectiligne et diagonale, les lobes secondaires du signal direct ont une réponse rectiligne à la fréquence spatiale de l'émetteur et pour toutes les fréquences Doppler et les lobes secondaires du fouillis fort sont localisés sur toutes les fréquences spatiales.

Pour supprimer ces interférences et rendre la détection de cibles possibles, nous avons présenté une chaine de traitements composée de deux principales étapes. La première est la suppression adaptative des interférences reposant sur une technique de moindres carrées et est équivalent à un filtre FIR dont les paramètres d'entrée sont le signal direct et le signal reçu. Ce filtre vise à supprimer les interférences dues au signal direct et au fouillis de forte intensité, plus précisément à leurs lobes secondaires. Les simulations montrent que cette méthode donne des résultats satisfaisants en parvenant à supprimer ou à réduire très fortement ces interférences. Un filtrage adapté en distance permet ensuite de former le cube de données CIT. La deuxième étape consiste à supprimer le fouillis présent dans la case sous test ainsi que les résidus provenant des lobes secondaires. Pour cela nous utilisons les algorithmes STAP à dimensions réduites ; la réduction de dimensions est primordiale car le nombre de données secondaires disponibles pour le radar passif est très limité. De plus la limitation des dimensions permet de réduire le coût de la charge de calcul. Les simulations pour les configurations en visée latérale et avant ont été effectuées en utilisant plusieurs algorithmes STAP à réductions de dimensions et en testant différentes tailles de réduction ; ces simulations ont montré que le fouillis et les résidus de lobes secondaires des autres interférences sont effectivement supprimés. Les algorithmes «element-space » (pré- ou post-Doppler) opèrent sur toute la dimension spatiale et permettent une bonne suppression des résidus de lobes secondaires du signal direct; les algorithmes « beam-space » opèrent sur un nombre réduit de faisceaux ce qui diminue le nombre de données secondaires nécessaires mais également les performances de suppression des lobes secondaires des autres interférences. Il est donc important de ne pas réduire trop fortement le nombre de faisceaux pour les algorithmes « beam-space » et d'utiliser directement les algorithmes «element-space » pour un réseau d'antenne avec peu d'éléments. Néanmoins nos simulations montrent que les algorithmes « beam-space » et «element-space » conduisent à des pertes en SINR comparables, mais avec moins de données secondaires pour l'approche « beam-space » ce qui est important dans le cas du radar passif aéroporté. Comparées aux méthodes pré-Doppler, les approches STAP post-Doppler ont montré de meilleurs MDV et de plus faibles pertes en SINR, proches du cas optimal.

Les expérimentions avec un radar passif mobile au sol ont été conduites de manière à reproduire au mieux les conditions de fonctionnement d'un radar passif aéroporté. Les résultats de ces données réelles nous ont permis de valider nos modèles de signal reçu, notamment en ce qui concerne les interférences. La case sous test présente toutes les contributions des interférences, fouillis et lobes secondaires du signal direct et du fouillis fort, avec les puissances attendues. Les traitements de suppression des interférences ont montré de bonnes performances. La suppression adaptative des interférences a permis de supprimer les lobes secondaires du signal direct et les traitements STAP ont annulé la réponse du fouillis présent dans la case distance sous test. Les approches pré-Doppler et post-Doppler donnent des résultats comparables. D'une manière générale, les résultats sur données réelles ont confirmé la validité de notre étude en termes de modélisation et de traitement et confirment l'intérêt du radar passif aéroporté pour la détection de cibles mobiles.

Chapter 1

Introduction

1.1 Passive radar

Traditional radar system transmits radio frequency signal into space and receives the returned echoes that bounce off the targets [1, 2]. This received signal is then use to detect and locate the targets in azimuth, elevation, range as well as its heading and radial velocity [3]. The critical drawback is that the radar's emission betrayed its own transmitter presence/location and in hostile environments this will greatly endanger the transmitting platform [4]. Passive radar is essentially a receiver-only radar system that usually dissociates the receiving antenna at different location from the transmitter [5]. It does not transmit signals; it only receives and thus operates independently without direct synchronization from the non-cooperative transmitter. The system receives electromagnetic radiation present in the environment, detecting distortions in the scattered waves to detect the targets as well as estimating target parameters. The time delay between transmission and reception of an EM wave can provide information of the range to the target, while Doppler shift in carrier frequency is related to target velocity. In addition, the power of the scattered wave, as compared to that of the transmitted wave, can provide an estimate of the effective EM capture area of the target [6].

During the last decade or more, there has been vast emerging interest in the possibilities of passive radar exploiting non-radar transmitters of opportunity as their sources of illumination for covert surveillance purposes and the potential advantages of these techniques are well known [7-9]. Particularly, the salient features are in its 'passive' operation and 'bistatic' configuration where the major benefits the passive radar offers are bulletized as follows. For passive operations,

- exploiting readily available broadcast or communication transmissions circumvent the needs to obtain frequency allocations in already highly congested spectral shared by numerous applications.
- CW-like broadcast and communication signals provide the passive radar with the apparent ability to handle targets at any range and with nearly any conceivable velocity without ambiguity. These signals also function around the clock (24/7) and most cover a substantial area.
- operating in the lower frequency bands has counter stealth capabilities since RCS reduction material used on stealth and low observable targets will be much less effective on passive radar operating in the lower frequency bands.
- it is virtually undetectable to surveillance receivers using conventional radio direction finding techniques, immune to deliberate directional jamming/interference and is usually resistance to anti-radiation missiles attack.
- the system is typically smaller, lighter in weight and more portable, less expensive, consumes much less power and requires less cooling effort than the active radar.

For bistatic configuration,

- the geometry allows for a covert means of moving target surveillance, provide warning of potential threats and expanding battlefield understanding.
- the bistatic operation provides improved detection of stealth targets through exploitation of potentially larger RCS since stealth technology calls for the aircraft to be shaped such that it deflects the EM energy impinging on the aircraft into directions other than the direction (monostatic) of illumination.

More recently, coupled with the abundance of high powered transmissions of opportunity and along with the cost-effective and efficient development of signal processing technology, there has been an upsurge of interest on passive radar research and development not only in the traditional radar dominated military communities but also in the commercial and academic communities. In the military domain, classified programs existed in several nations, but the first announcement of a commercial passive radar system was that by Lockheed-Martin Mission Systems in 1998 (first version and subsequent versions thereafter). Named the Silent Sentry system [10, 11], it exploits FM radio and analogue television transmitters as the non-cooperative transmitters. In 2007, a system named Home Alerter 100 that utilizes FM radio transmissions was developed by Thales and had been tested successfully in France and the rest of Europe [12]. In parallel, the unclassified passive radar research and development is ongoing at universities and research facilities around the world. The majority of this research has been focused on the signal and waveform from the transmitter of FM radio [13, 14], analogue television [15, 16], digital audio broadcast [17], digital video broadcast [18], cellular phone (GSM, UMTS) [19-21], WiMAX [22] and various broadcast, communication and navigation satellites [23-25]. A comprehensive description on each system characteristics, detection performance and capabilities can be found in [7].

Passive radar offers a wide range of potential applications that include ground surveillance [26, 27], maritime surveillance [22], air surveillance [13], atmospheric and ionospheric studies [28], oceanography (current mapping) [29], monitoring radioactive pollution [30], etc. Another interesting ground surveillance application of the passive radar is in the area of through-the-wall motion sensing [31, 32] for detecting the presence of living humans behind walls or other barriers in an urban environment where transmissions of opportunity are plentiful. This is of high interest to both the urban warfare and civilian law enforcement purposes. In addition, the feature of such an abundance of transmission of opportunity enables the fusing of a similar or hybrid (different) passive radar network into a multistatic passive radar system for a large area coverage.

1.2 Airborne passive radar

All the notable passive radars for military or civil/commercial moving target surveillance currently in service or in development are ground-based static systems and the operation of such systems with its associated signal processing schemes/techniques for MTI are well documented [8]. The application of the passive radar on an airborne platform is an interesting and novel concept and may provide a significant break-through in passive radar technology. The concept for the airborne passive radar is to have multiple passive receiving arrays (side-looking and forward-looking configurations) covering a 4π steradian angle around the airborne passive platform which make use of the ground-based stationary transmitter as the illuminator of opportunity as illustrated in Fig. 1.1. This challenging passive radar configuration would well find application for localized covert surveillance (up to tens of Km) on an airborne platform such as an unmanned aerial vehicle, helicopter, transport aircraft, etc.

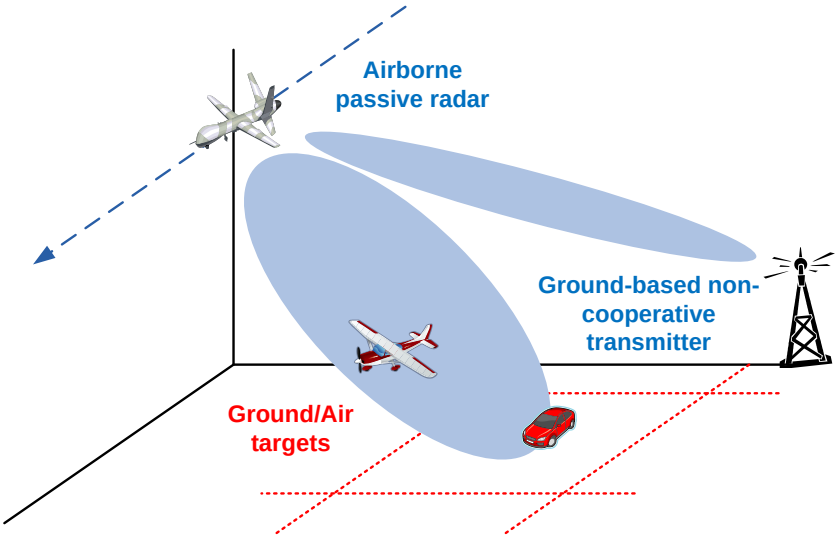

Fig. 1.1: Basic concept of airborne passive radar.

Research on the concept of the airborne passive radar and its performance/capabilities has not been extensively studied where comprehensive open literature concerning this topic is also limited. In [33], the feasibility of applying STAP to bistatic passive radar on a moving platform using DVB-T illuminators of opportunity was examined. The paper describes the generalization of STAP to noise-like signals where simulations showed that the PC and JDL methods are efficient in rejecting interferences for MTI. Subsequent papers [34, 35] by the same author present a new approach for passive target detections which combines Wiener filtering to achieve clutter rejection and the adaptation to noise-like signals of the amplitude and phase estimation method for improved MTI. Results of the bistatic passive detection of a real target for a 4-channel static passive radar system using DVB-T transmitter of opportunity highlighted the effectiveness of the signal processing algorithms. In [36], a two-channel (reference and surveillance channel) passive bistatic radar system was designed, constructed and installed on a light aircraft and the system flown with the intention of detecting low altitude commercial air targets. Subsequent processing has shown that the system has successfully detected inbound and outbound aircrafts from London's Heathrow and Gatwick airports as well as high altitude targets which establishes the viability of airborne passive bistatic radar system. The paper in [37] is the latest from a series of related papers [38-40] from Warsaw University of Technology, presenting the concept of the airborne passive radar and the preliminary results of two experiments carried out using a car and an aircraft mobile platform. In the car measurement campaign, a 6-channel receiver system for the passive radar was mounted inside the car with the associated antenna array installed onto the roof to collect the FM radio echo signal. An adaptive filter is used before cross-ambiguity function processing where a fast moving target outside the clutter Doppler bandwidth can be detected. The same system was then used for the airborne measurement campaign where the spread of the clutter is much more apparent but weaker in strength. In this case, STAP-like method of clutter cancellation would be needed for improved moving target detections which will be the follow-up work [37]. The airborne passive radar inherits all the advantages and benefits of the passive radar in the form of 'silent' and 'bistatic' mode of operation. The additional benefits for the airborne passive radar are such that target detections are made easier by the increase in visible range due to the elevated position of airborne platform. This increased in elevation also implies a reduction of the terrain masking effect and more favourable wave propagation conditions since there are less complex interactions with the ground. Moreover, a passive radar on an airborne platform will be also highly mobile and easy to deploy.

Given the numerous benefits the airborne passive radar can offers, however, it is not without any shortcomings. In fact, the airborne passive radar faces several issues pertaining to its performance and operational capability. First, the performance of the airborne passive radar, as in the static passive radar, is very much dependent on the geometrical configuration [5] and the non-cooperative signal properties and attributes [7, 41]. Knowing the location of the non-cooperative transmitter is important because a practical difficulty with the airborne passive radar is that of synchronization where this is accomplished by using the direct path signal as a reference. Bistatic operating configuration also has some disadvantages where its range/Doppler resolution and accuracy are generally not as good as those of a monostatic radar. Non-cooperative broadcast and communication transmitters have modulation that changes as a function of time and this causes the passive signal properties (correlation, bandwidth, etc) to vary considerably. The transmit power of the non-cooperative signals identifies the range performance of the passive radar. The direct path signal from the non-cooperative transmitter to the airborne passive radar is in general the largest signal received and can cause dynamic range problems with respect to moving target detections. However, this is in direct contradiction with the radar coverage issue as higher power means larger detection region. Thus, the influence of the non-cooperative signal properties (bandwidth, power, modulation, etc.) is a major issue on the capabilities and reliability of the airborne passive radar. Except for parameters associated with the airborne passive receiver, all other parameters are not within the control of the passive radar designer.

The basic principle of target detections in the passive radar is achieved by comparing the direct path signal (from the LOS non-cooperative transmitter) and echo signals off the moving targets. Thus, it is desired that the matched filter, which is a filter that optimally detects the transmitted signal in the presence of additive white Gaussian noise [42, 43], be used by the passive radar. The generalization of this cross-correlation coherent processing, which is the matched filter response to the joint time-delay and Doppler-shifted version of the passive signal (also known as cross-ambiguity function coherent processing [44]) it is matched to is given as

$$A(\tau, f) = \int_{-\infty}^{\infty} x(t) s_{dp}^{*}(t-\tau) e^{-j2\pi f t}\, dt \tag{1.1}$$

where $x(t)$ is the sum of all the signals received by the antenna element of the passive radar and $s_{dp}(t)$ is the direct path reference signal. τ is the time delay parameter and f is the Doppler frequency shift parameter to be searched for the values that cause $|A(\tau, f)|$ to peak. This concept may seems straightforward, however due to the CW, random and aperiodic nature of the passive signals, technical difficulties concerning direct path signal and strong clutter couplings complicate the MTI performance [45]. Given that the power of direct path and strong clutter is several tens of decibels stronger than the target power, the random range sidelobes couplings of these interfering signals into the detection range cell of interest will seriously influence target detection and estimation, making it a big challenge.

In the airborne passive radar utilizing a ground-based stationary transmitter, all of the Doppler is due only to the motion of the passive radar platform. Thus, the ground clutter received by the airborne passive radar is not only extended in both range and angle, it is also spread over a region in Doppler frequency where the Doppler shift of each individual clutter patch is proportional to the angle of arrival relative to the velocity vector [46-48]. A potential target may be obscured by not only the strong mainlobe clutter that originates from the same angle as the target, but also by sidelobe clutter that comes from different angles but has the same Doppler frequency. For the airborne passive radar with a side-looking array antenna, the two-dimension spectrum of the clutter energy is distributes along the diagonal line in the spatial-Doppler space as illustrated in Fig. 1.2 where it is modulated by the transmit beam

pattern. If a conventional one-dimensional filter (spatial or Doppler) is used to cancel the clutter via an inverse filter, a slow moving target will fall within the stopband of the filter and thus be also cancelled as shown. Thus, this spatial-Doppler dependent clutter can be effectively suppressed by two-dimensional filters, i.e. space-time filters. Space-time processing exploits the inter-relationships between the clutter angle of arrival and Doppler frequency where it exhibit a narrow ridge. A space-time filter therefore has a narrow notch to provide significant rejection of the two-dimensional clutter so that slow targets will fall into the passband. The advantages of STAP are that, firstly, it is able to improve slow moving target detection through better mainlobe clutter suppression. Secondly, STAP permits the detection of weak targets that might otherwise be obscured by sidelobe clutter. Thirdly, STAP provides detection in combined clutter and interference environment for the airborne passive radar due to the random range sidelobes of the direct path and of the strong clutter signals. As said, the two major issues concerning the random range sidelobes couplings of the direct path and of the strong clutter, as well as the spatial-Doppler dependent clutter ridge at the detection range cell need to be fully addressed and performance thoroughly analyzed for the airborne passive radar to be feasible and practical.

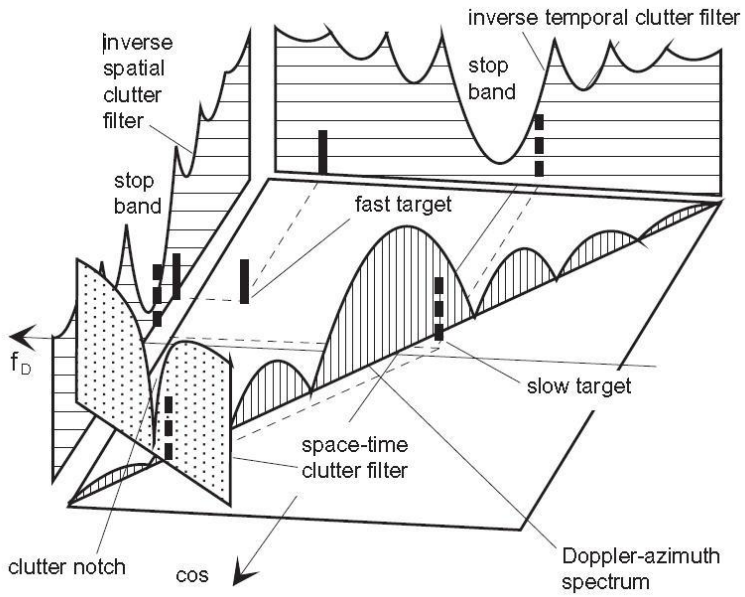

Fig. 1.2: The principle of space-time clutter filtering [46].

This research thesis titled “Signal Processing for Airborne Passive Radar” is devoted to the study of efficient signal processing schemes and techniques for interference suppression to improve moving target detections in the airborne passive radar. The initial research work is focused on identifying and analyzing the critical issues faced by the airborne passive radar on moving target detections, i.e. the signal environment for the airborne passive radar. Importantly to derived the models for the passive signals received by the airborne passive radar and the effects of these signals on the detection range cell of interest. Understanding these underlying problems, consequently, efficient and effective signal processing schemes/techniques applicable to the airborne passive radar will be developed and analyzed to address and mitigate these issues for improving moving target detection performance.

1.3 Original contributions

The original contributions for this research thesis are:

- Explanation of the passive coherent integration time datacube and the statistical analysis of the correlation function of the passive signal which formulates the datacube.
- Mathematical formulation of the space-time snapshot models for the passive signals as received by the airborne passive radar. Namely on the derivation of the space-time snapshots of the direct path, direct path random range sidelobes and random range sidelobes of the clutter and their corresponding covariance matrices.
- Analysis on the random range sidelobes properties of the direct path and of the clutter which includes their spatial-Doppler profile and rank of their covariance matrices.
- Simulations on the power profile which highlight the effects of the random range sidelobes couplings of the side-looking and forward-looking airborne passive radar under a realistic and practical environment and interference scenario.
- Application and performance analysis of the LS-based adaptive interference cancellation for direct path and strong clutter (Doppler-shifted clutter included) suppression in the side-looking and forward-looking airborne passive radar.
- Application and performance analysis of various reduced-dimension STAP for interference suppression in the side-looking and forward-looking airborne passive radar.
- For the purpose of the ground-based moving passive radar experimental trials, a low-cost experimental passive radar receiver test-bed has been designed, developed and implemented. The experiment trials that were conducted provide real measurement data to validate against the theoretical passive signal models that are derived and the simulations results. Applying the proposed signal processing schemes for the airborne passive radar on these data offers the most direct approach to validate and evaluate the suppression performance of these schemes to improve moving target detections.

1.4 Thesis outline

This Section describes the contents of each successive Chapter following this introduction Chapter.

Chapter 2 – Signal Modeling for Airborne Passive Radar

This Chapter first establishes the airborne passive radar bistatic geometry and the key parameters used to define the generalized space-time steering vector and derive the expressions for each of the received passive signal component. The statistical properties of the passive signal that play a significant role in the snapshots development for the signals received by the airborne passive radar are analyzed. In the initial signal modeling, the space-time snapshot expression for a discrete point scatterer is thoroughly described. This model is then particularized to the snapshot model of the target, direct path and clutter, as well as its corresponding random range sidelobes contributions. Subsequently, the spatial-Doppler characteristics and properties of the two-dimensional clutter profile and on the random range sidelobes of the direct path and of the strong clutter are also analyzed in detail.

Chapter 3 – Signal Processing for Airborne Passive Radar

Chapter 3 describes the signal processing schemes applicable for the airborne passive radar which can be segregated into a two step interference cancellation process. First, the direct path and strong clutter coupling components present in the received signal at each antenna element can be suppressed by the adaptive interference cancellation algorithm which is essentially an adaptive FIR filter. In mitigating these interfering signals, its corresponding random range sidelobes will also be suppressed by the same amount. Further cancellation on the undesirable residual random range sidelobes coupling (direct path random range sidelobes

that is localized in spatial frequency and the random range sidelobes of the strong clutter that has a limited spatial frequency span) and on the spatial-Doppler dependent clutter can be achieved using STAP. In particular, reduced-dimension STAP techniques provide solutions to this fundamental two-dimensional clutter suppression problem. This Chapter will analyze each of the four classes to be used for the airborne passive radar; namely the element-space pre-/post-Doppler and beam-space pre-/post-Doppler STAP techniques.

Chapter 4: Simulations on Airborne Passive Radar Signal Processing

This Chapter simulates the side-looking and forward-looking airborne passive radar in an interference scenario to envisage its operational capability and investigate its practical performance. As such, a typical bistatic airborne passive radar scenario utilizing a ground-based DVB-T transmitter is modeled where the random FM signal is used to represent the transmitted DVB-T waveform along with geometrical, signal and datacube parameters to model a realistic and practical environment and interference scenario. This Chapter presents the results, analyses and discussions for the complete simulations on the airborne passive radar signal processing. Namely on the performance of the adaptive interference cancellation and reduced-dimension STAP algorithms under this environment and interference simulation scenario.

Chapter 5: Experimental Trials on Ground-based Moving Passive Radar

Chapter 5 outlines the experimental details of the ground-based moving passive radar trials together with the signal processing results and analyses on moving target detections. The specifications of the 4-channel low-cost experimental passive radar test-bed having a 4-element horn antenna array together with the descriptions on the experimental trials are thoroughly explained. Signal processing schemes proposed for the airborne passive radar are then performed on the real measurement data. This enables the performance validation and evaluation of the signal processing schemes for interference suppression to improve moving target detections in the real world interference scenario where the trial results are comprehensively analyzed and discussed.

Chapter 6: Conclusion and Perspectives

This Chapter summarizes and gives concluding remarks on the research thesis. It also highlights some perspectives for further/future work along this research topic.

Chapter 2

Signal Modeling for Airborne Passive Radar

2.1 Introduction

The most important factor in evaluating the performance of the interference suppression schemes for the airborne passive radar is building an accurate data model. In this chapter, the spatial-temporal modeling of the passive signals received by the airborne passive radar is developed. The received passive signals will always contain a component due to the receiver noise and may contain components due to both desired targets and undesired interferences. For the airborne passive radar, undesired interference means either clutter, random range sidelobes coupling of the direct path and random range sidelobes coupling of the strong clutter signals or any combinations of these components. The research work first establishes the airborne passive radar bistatic geometry and the key parameters used to derive the expressions for each of the received passive signal component. In the initial signal modeling, the space-time snapshot expression for a discrete point scatterer is thoroughly described. This model is then particularized to the snapshot model of target, direct path and clutter, as well as their corresponding random range sidelobes contributions. Each component characterizes the returns received in an actual airborne passive radar. Upon derivation of the signal models, their spatial-Doppler properties and characteristics are analyzed. Consequently, these models for the airborne passive radar developed serves as the foundation for the analysis of the various signal processing and space-time processing approaches for interference suppression in Chapter 3.

2.2 Airborne passive radar geometry

The airborne passive radar considers a three dimensional bistatic geometry where the non-cooperative transmitter is ground-based (e.g. FM transmitter, DVB-T transmitter, DAB transmitter, etc.) with the passive radar on an airborne platform. This Section illustrates the bistatic geometry of the airborne passive radar and describes the parameters associated with the transmitter, scatterer and the passive radar.

2.2.1 Transmitter and passive radar bistatic geometry

Fig. 2.1 illustrates the non-cooperative transmitter T and the airborne passive radar R oriented in a bistatic geometrical configuration. The geometry indicates the passive radar at the origin of the x-y axis and at altitude H_R and transmitter at height H_T above the x-y ground plane. The baseline range is defined as R_{RT} with an azimuth and elevation angle between the passive radar and transmitter defined as ϕ_{RT} and θ_{RT} respectively. All angle variables ϕ and θ refer to the true azimuth and elevation and not the standard spherical coordinate system angles. The airborne passive radar moves horizontally (level flight parallel to the Earth) with a constant velocity vector $\mathbf{v}_R$ along the x-direction. A unit vector pointing in the direction of the passive radar to the transmitter is given by

$$\hat{\mathbf{k}}_{RT}(\phi_{RT},\theta_{RT}) = \cos\theta_{RT}\sin\phi_{RT}\,\hat{\mathbf{x}}_R + \cos\theta_{RT}\cos\phi_{RT}\,\hat{\mathbf{y}}_R + \sin\theta_{RT}\,\hat{\mathbf{z}}_R \quad (2.1)$$

where $\hat{\mathbf{x}}_R, \hat{\mathbf{y}}_R$ and $\hat{\mathbf{z}}_R$ are the unit vectors of the Cartesian coordinate system that is aligned with the passive radar.

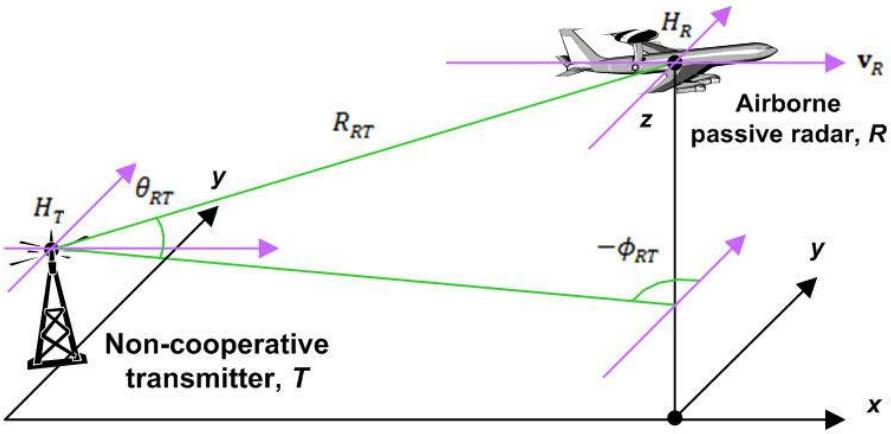

Fig. 2.1: Non-cooperative transmitter and airborne passive radar bistatic geometry.

The volume within which the airborne passive radar is able to detect targets (coverage) is determined by a combination of factors. Generally, there must be a propagation path from the transmitter to the target and from the target to the passive radar. In addition, to support the non-cooperative operations, there must also be a propagation path from the transmitter to the passive radar. For a smooth Earth, these LOS requirements are established by coverage circles centered at each site [5]. Targets in the area common to both circles have a LOS to both sites. For an $4/3$ Earth model, where the assume Earth radius is 4/3 that of the actual Earth radius, the radius of these coverage circles (slant range of target visibility to passive radar/transmitter) for the passive radar and transmitter in kilometres respectively is approximated by

$$\begin{aligned} r_R &= 130\left(\sqrt{H_t} + \sqrt{H_R}\right) \text{ and} \\ r_T &= 130\left(\sqrt{H_t} + \sqrt{H_T}\right) \end{aligned} \quad (2.2)$$

where H_t is the target altitude in kilometers. As with the ground-based static passive radar, the airborne passive radar needs to establish synchronization via a direct path link, thus adequate line-of-sight is also required between both sites. In this case, the baseline relationship is

$$R_{RT} \leq 130\left(\sqrt{H_R} + \sqrt{H_T}\right). \quad (2.3)$$

2.2.2 Scatterer bistatic geometry

Fig. 2.2 illustrates the scatterer bistatic geometry with respect to the non-cooperative transmitter and airborne passive radar. The scatterer s can be a moving target or a stationary ground clutter patch. The scatterer has distances R_{Ts} and R_{Rs} with respect to the transmitter and passive radar respectively. This gives a bistatic range sum $R_{sum} = R_{Ts} + R_{Rs}$. The triangle formed by the transmitter, passive radar and the scatterer is termed the bistatic angle β_s. The orientation of the scatterer is characterized by the azimuth and elevation angles denoted by ϕ_{Ts} and θ_{Ts} respectively with respect to the transmitter and azimuth and elevation angles denoted by ϕ_{Rs} and θ_{Rs} respectively with respect to the passive radar. Thus the unit vector pointing in the direction of the transmitter to the scatterer is given by

$$\hat{\mathbf{k}}_{Ts}(\phi_{Ts},\theta_{Ts}) = \cos\theta_{Ts}\sin\phi_{Ts}\,\hat{\mathbf{x}}_T + \cos\theta_{Ts}\cos\phi_{Ts}\,\hat{\mathbf{y}}_T + \sin\theta_{Ts}\,\hat{\mathbf{z}}_T \quad (2.4)$$

where $\hat{\mathbf{x}}_T, \hat{\mathbf{y}}_T$ and $\hat{\mathbf{z}}_T$ are the unit vectors of the Cartesian coordinate system that is aligned with the transmitter. Similarly the unit vector pointing from the passive radar to the scatterer is given by

$$\hat{\mathbf{k}}_{Rs}(\phi_{Rs},\theta_{Rs}) = \cos\theta_{Rs}\sin\phi_{Rs}\,\hat{\mathbf{x}}_R + \cos\theta_{Rs}\cos\phi_{Rs}\,\hat{\mathbf{y}}_R + \sin\theta_{Rs}\,\hat{\mathbf{z}}_R. \quad (2.5)$$

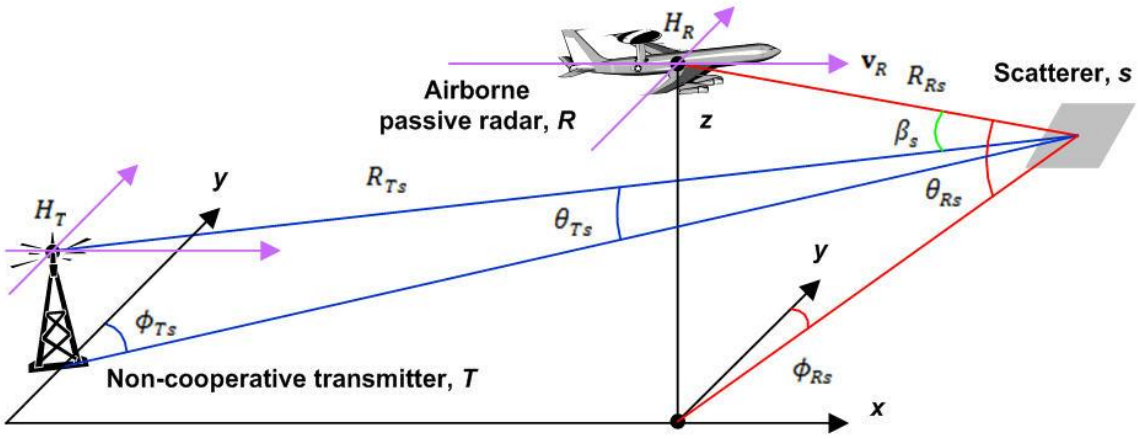

Fig. 2.2: Scatterer bistatic geometry.

2.3 Passive coherent integration time datacube

The airborne passive radar is a CW system residing on an airborne platform. The passive radar antenna array consists of N ULA, each having its own receiving channel. The elements in the ULA are considered to be identical. Pre-processing steps convert the RF passive signal collected at the antenna element of each receiving channel to complex baseband samples. The time interval over which the passive signal is collected is referred to as the CIT. For each element/channel, the CIT temporal dimension is segmented into M sub-CITs where M is the total number of sub-CITs. Each sub-CIT has duration T_{sub} and a sub-CIT repetition frequency of $f_{sub} = 1/T_{sub}$. For each sub-CIT, there are $L = T_{sub} \times f_{BW}$ range cells covering the range sum interval where L is the total number of range cells and f_{BW} being the complex sampling rate. Therefore, this multidimensional data set for MTI signal processing for the airborne passive radar is visualized as the $N \times M \times L$ cube of complex baseband samples [49]. $n = 0, \ldots, N-1$, $m = 0, \ldots, M-1$ and $l = 0, \ldots, L-1$ are the antenna element index, sub-CIT index and range cell index respectively. It is common to refer to the range dimension (l) as fast-time and the sub-CIT dimension (m) as slow-time. Along the range dimension, the range profile of the received passive signals is obtained by matched filter processing (range correlation). Thus, the range correlation (direct path and received signal) is carried out separately on a sub-CIT-by-sub-CIT basis where the result is a $1 \times L$ correlation function $\mathbf{r}$ for each sub-CIT. By lining up different $\mathbf{r}$ for different sub-CITs, a $M \times L$ correlation function matrix $\boldsymbol{\mathcal{R}}$ for each element can be formed, i.e. $\boldsymbol{\mathcal{R}} = [\mathbf{r}_0; \mathbf{r}_2; \cdots; \mathbf{r}_{M-1}]$. The mathematical formulation of this process will be explained thoroughly in the later Sections. Figure 2.3 illustrates a pictorial view of the passive CIT datacube [48]. Here, each row of the datacube corresponds to a spatial sample and each column to a slow-time sample while the L range samples extend in the third dimension. The $N \times M$ matrix, which is a slice of the datacube corresponding to the l^{th} range cell is

$$\mathbf{X}_l = \begin{bmatrix} x_{l(0,0)} & x_{l(0,1)} & \cdots & x_{l(0,M-1)} \\ x_{l(1,0)} & x_{l(1,1)} & & x_{l(1,M-1)} \\ \vdots & & \ddots & \vdots \\ x_{l(N-1,0)} & x_{l(N-1,1)} & \cdots & x_{l(N-1,M-1)} \end{bmatrix}. \tag{2.6}$$

Vectorizing by stacking each succeeding column one after the other yields the $MN \times 1$ vector $\boldsymbol{\chi}_l$, termed a space-time snapshot, for the l^{th} range cell.

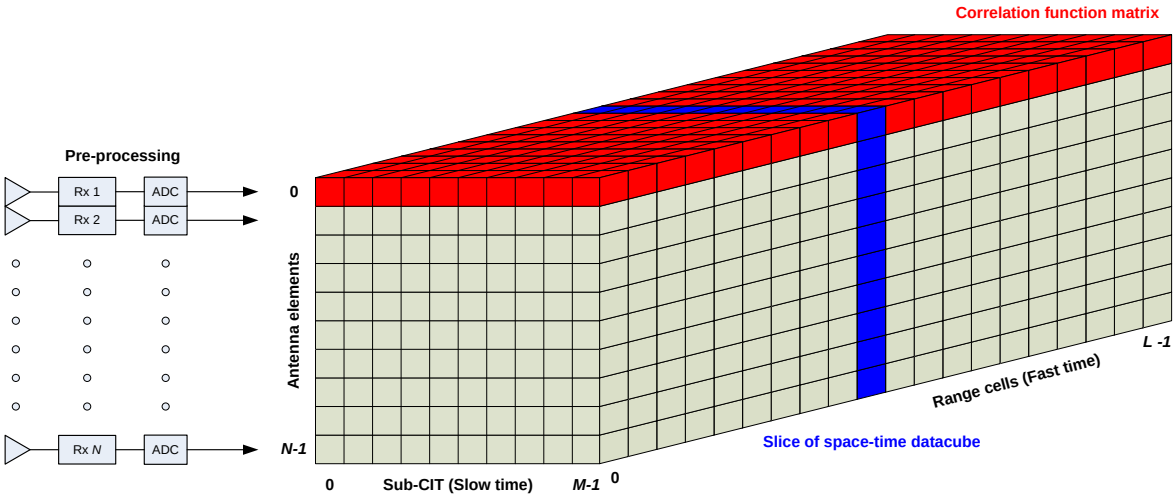

Fig. 2.3: Illustration of the passive CIT datacube.

2.4 Key measurement parameters

In general, the airborne passive radar is expected to determine three important measurement parameters for each scatterer of interest: the DOA, bistatic range sum and relative velocity with respect to the moving platform [8]. DOA relates to the spatial variation of phase delay across the antenna array and thus defines the spatial frequency. Doppler frequency results from the linear phase variation from sub-CIT to sub-CIT and bistatic range sum results from the total time delay from transmitter to the scatterer and to the passive radar. This section establishes the expressions for these three key parameters, as well as the definition of the airborne passive radar's resolution and maximum CIT. In addition, the airborne passive radar may also determine other measurement parameters such as amplitude (RCS) and polarization [50], but these will not be discussed.

2.4.1 Spatial frequency

In most cases, passive signals are narrowband since their modulation bandwidth B is such that $c/B \gg Nd$ where d is the interelement spacing. This condition insures that propagation delay across the N-element ULA is manifested as a simple phase shift. The spatial steering vector describes the varying phase among the elements resulting from a propagating plane wave emanating from the direction of the scatterer normal to $\hat{\mathbf{k}}_{Rs}(\phi_{Rs}, \theta_{Rs})$. For the relative time delay τ_n', representing the time it takes the passive signal to arrive at the n^{th} element with respect to the reference element of the ULA, the corresponding phase shift is $\gamma_n = -2\pi f_c \tau_n'$. Then $\tau_n' = -d_n/c$ where d_n is the distance the passive signal must travel after impinging on the reference element. For a side-looking ULA

as in Fig. 2.4, $d_n = nd\cos\theta_{Rs}\sin\phi_{Rs}$ where only the x-direction component is nonzero. The phase shift at the n^{th} antenna element follows as

$$\gamma_n = \frac{2\pi nd}{\lambda}\cos\theta_{Rs}\sin\phi_{Rs} \tag{2.7}$$

where λ is the wavelength of the passive signal. The spatial frequency is defined to be

$$\vartheta_s = \frac{d}{\lambda}\cos\theta_{Rs}\sin\phi_{Rs}. \tag{2.8}$$

Thus, the generalized spatial steering vector is then

$$\mathbf{a}(\phi,\theta) = [1 \quad \exp(j2\pi\vartheta) \quad \cdots \quad \exp(j2\pi(N-2)\vartheta) \quad \exp(j2\pi(N-1)\vartheta)]^T \tag{2.9}$$

where the subscript s has been dropped. The phase variation across the array for an arbitrary DOA is thus seen to nominally appear linear for a ULA. The spatial steering vector assumes a Vandermonde form because of the ULA geometry and of identical element patterns.

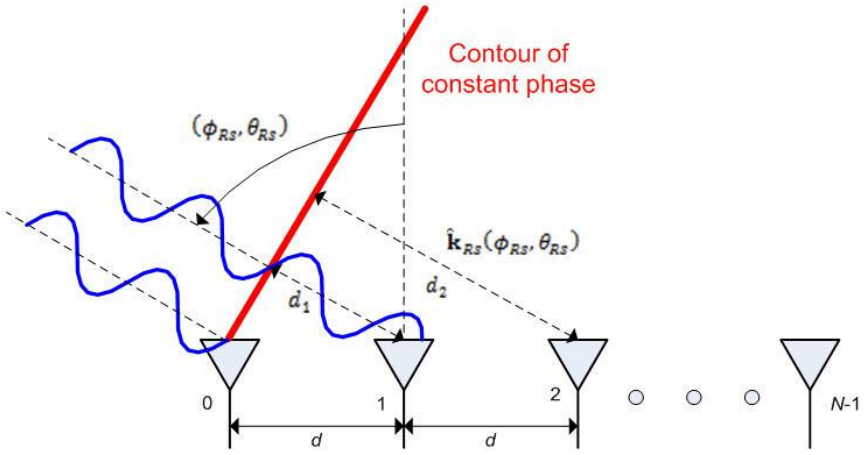

Fig. 2.4: Propagating passive signal impinging on the N-element ULA [8].

2.4.2 Doppler frequency

Beside DOA, another key parameter for separating moving scatterers from noise is Doppler frequency. Specifically, as with the spatial point scatterer, a Doppler-shifted point scatterer similarly produces a linear phase progression in time. Thus, Doppler processing involves testing for different linear phase slopes across this temporal aperture. Consider the unit vectors $\hat{\mathbf{k}}_{Ts}(\phi_{Ts},\theta_{Ts})$ and $\hat{\mathbf{k}}_{Rs}(\phi_{Rs},\theta_{Rs})$ pointing from the transmitter and passive radar to the stationary scatterer. The ground-based transmitter is stationary while the passive radar moves at a constant velocity v_R. Thus, the resulting Doppler frequency depends on only the passive radar motion which is the time rate of change of R_{Rs} (and normalized by λ) given by

$$f_s = \frac{v_R}{\lambda}\,\hat{\mathbf{k}}_{Rs}. \tag{2.10}$$

For the side-looking ULA, the resulting Doppler frequency corresponding to the stationary scatterer is

$$f_s = \frac{v_R}{\lambda}\cos\theta_{Rs}\sin\phi_{Rs} \tag{2.11}$$

and the corresponding normalized Doppler frequency is $\varpi_s = f_s T_{sub}$. In general, a temporal steering vector characterizes the time-varying linear phase variation between the first sub-CIT and each of the remaining $(M-1)$ sub-CITs. Thus, the generalized temporal steering vector is

$$\mathbf{b}(\varpi) = [1 \quad \exp(j2\pi\varpi) \quad \cdots \quad \exp(j2\pi(M-2)\varpi) \quad \exp(j2\pi(M-1)\varpi)]^T \tag{2.12}$$

where the subscript s has been dropped. It is in Vandermonde form also because of the uniform sub-CIT and that the passive radar velocity is constant.

2.4.3 Range sum and isorange

The bistatic range sum R_{sum} is the total distance travelled by the passive signal from the transmitter to the scatterer and to the passive radar's antenna reference point and is related to the round-trip time $\tau_{RT} = (R_{Ts} + R_{Rs})/c$. Scatterers located on a isorange surface have constant range sum (round-trip time), i.e. this surface is the locus of points which the sum of the distances to two fixed points is a constant. Hence, this is an ellipsoid of revolution with T and R as foci. Isorange surfaces are predominantly important concept in radar as the signal corresponding to one particular range is the resultant contribution of all scatterers located on the isorange surface associated with the range of interest. When the scatterers are located on a given plane, the intersection of this ellipsoid with this plane defines a isorange contour (or simply isorange) which is an ellipse. In particular, ground clutter is the return signal from distributed scatterers located on the x-y ground plane. Ground clutter patches contributing to the signal at the range of interest will be located along an isorange contour which is the intersection of the isorange surface with the ground surface. Obviously, moving scatterers travelling with a velocity vector tangential to the isorange will exhibit zero Doppler frequency.

2.4.4 Range resolution and Doppler resolution

The range and Doppler resolutions are important fundamental parameters in the design of the airborne passive radar since they preside the ability to separate between two or more targets by virtue of range and Doppler frequency (velocity). Generally, the nature of the passive signal and geometrical configuration determines these properties. The range resolution [5] of the passive radar is inversely related to the bandwidth of the passive signal B and decline with a larger target bistatic angle β_t given as

$$\Delta R = \frac{c}{2B\cos(\beta_t/2)} \tag{2.13}$$

which represents a minimum requirement for target separation in range. The Doppler resolution is determined by the CIT of the passive datacube and is conventionally taken to be

$$\Delta f = \frac{1}{CIT}. \tag{2.14}$$

Subsequently, the velocity resolution [5] can be derived as

$$\Delta V = \frac{\lambda}{2CIT\cos(\beta_t/2)}. \tag{2.15}$$

Range resolution is determined by the bandwidth of the passive signal while the frequency resolution is determined by the total duration for the coherent processing and both properties are independent of each other.

2.4.5 Maximum coherent integration time

CIT is an important parameter which sets the amount of signal processing gain due to coherent integration, leading to the desired effect of increasing the SNR. The two important constraints affecting the maximum CIT are that of target range cell migration and Doppler

cell migration [5]. Range cell migration occurs when the range resolution is smaller than the distance travelled by the target during integration, leading to an energy dispersal in the range correlation as it moves through multiple range cells. For no range cell migration (and the assumption of no range migration compensation), the maximum distance the target travels over the CIT is limited by the range resolution. Thus, the condition for the maximum CIT without inducing target range cell migration is transformed into the inequality

$$CIT < \frac{\Delta R}{v_{t(max)}} \tag{2.16}$$

where $v_{t(max)}$ is the maximum relative velocity between the target and the passive radar. The inequality $<$ in Equation (2.16) (and in Equations (2.17) and (2.18) thereafter) states that the CIT should be considerably smaller than the right-sided term. Doppler migration occurs when the target accelerates through several Doppler cells during integration, leading to an energy dispersal in Doppler correlation. For no Doppler cell migration, the requirement of $\Delta f > \left(a_{t(max)} CIT\right)/\lambda$ must be satisfied where $a_{t(max)}$ is the maximum bistatic target acceleration. This leads to the inequality for maximum CIT without inducing target Doppler frequency cell migration as

$$CIT < \sqrt{\frac{\lambda}{a_{t(max)}}}. \tag{2.17}$$

Summarizing, the maximum CIT must satisfy

$$CIT < min\left(\frac{\Delta R}{v_{t(max)}}, \sqrt{\frac{\lambda}{a_{t(max)}}}\right). \tag{2.18}$$

2.5 Passive signal models

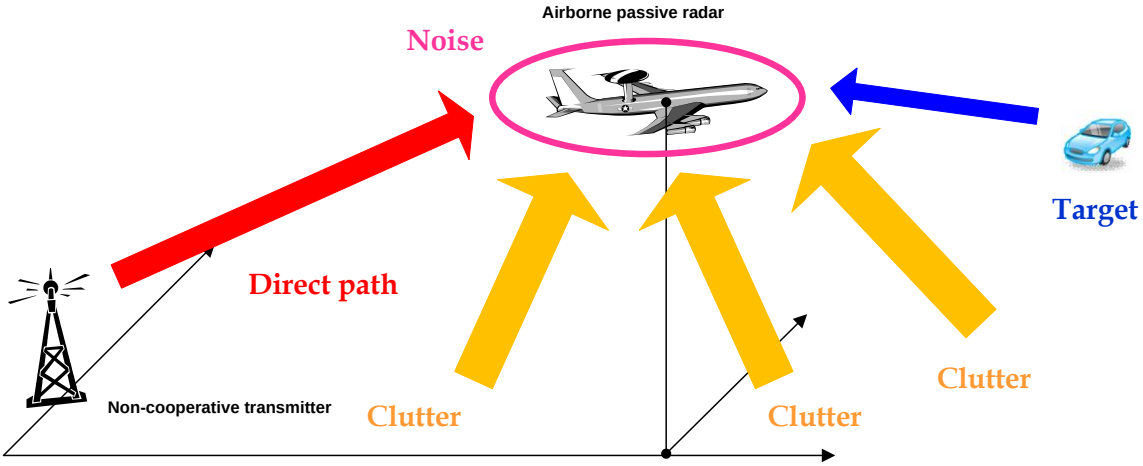

Fig 2.5: Typical airborne passive radar interference scenario.

For the airborne passive radar, the detection of moving targets is the primary objective. For fast moving target outside the clutter Doppler bandwidth, conventional Doppler processing is adequate. Thus, the detection of slow and small target is the main challenge. During target detection, the airborne passive radar encounters the effects of strong interfering signals returns alongside a weak return from the moving target against the thermal noise environment. This severe interfering environment is usually characterized by the high levels

of direct path and ground clutter. Ground clutter (or simply clutter) is the result of propagation effects in the environment due to reflection and scattering from the local terrain and from fixed objects such as buildings, foliage, etc [45]. As a result and due to the properties of the passive signal (which will be apparent later), the random range sidelobes of the direct path signal and that of the strong clutter signals will exhibit significant coupling into further range cells of interest [51]. Together with the spatial-Doppler dependent clutter at the detection range cell, these undesirable effects will strongly exacerbate the background interference. Fig. 2.5 depicts a graphical illustration on the interference scenario of the airborne passive radar. Therefore, the goal will be to provide significant suppression of these interferences to improve detection performance of targets lying in the interferences Doppler bandwidth.

As the first step, the most important factor in evaluating the performance of the interference suppression methods is building an accurate signal model. The detailed examination begins with a mathematical transmit signal model. Passive signal received from a single element is characterized with associated losses due to range attenuation, variation due to target RCS, Doppler frequency changes resulting from the relative scatterer's velocity, and so on. Thereafter, a framework is generated to encapsulate the returns from all elements in the array and all sub-CITs acting upon a single scatterer. The full airborne passive radar target and interference environment is built around the model derived from this scatterer; namely the target, clutter, direct path and their corresponding random range sidelobes models are introduced along with thermal noise. Each component characterizes the passive signal received by the airborne passive radar. Prior to that, some statistical analyses of the generalized passive signal are given where the results will have paramount importance to the detection performance of the airborne passive radar.

2.5.1 Statistical analysis of passive signal

The electromagnetic spectrum is abundant in transmissions from sources such as television and radio stations, satellite links and other communications and broadcast systems. A characteristic which distinguishes the majority of these transmissions is that they are CW, random and aperiodic signals. They are generated from random information such as speech, music, video and message, and modulated (analog or digital) in some manner to a known frequency and bandwidth. Some passive signals may contain a small amount of periodicity where these deterministic repetitive components for signalling, controlling or any other purposes introduce ambiguities outside zero range and Doppler frequency. As a result, a number of supplementary and unwanted deterministic peaks can be expected in the AF of such a passive signal [41]. A target response will therefore produce several ambiguities outside its position, but these are deterministic in range and Doppler and it has been shown how to cope with [18] and thus will not pose issue in the framework of the passive signal snapshot development.

In general, passive signal can be considered as self-uncorrelated when delayed in time and shifted in frequency, a property which is usually enhanced with modulation. The result is that this transmission of opportunity is similar to the band-limited continuous-time random signal (white noise, etc.). This type of signal approximates a thumbtack form of the AF and it exhibits promising radar waveform properties [42]. Thus, the airborne passive radar CIT datacube has a key advantage of being unambiguous in range and Doppler frequency. The sub-CIT duration can be arbitrary chosen depending on the maximum detection range and in turn also sets the limit of the unambiguous Doppler frequency space which is a compromise. For the statistical analysis, an approximate model for the sampled version (discrete time) of

the CW passive signal from the non-cooperative transmitter is modelled as a complex random process $s(n)$ with zero mean and variance σ^2. That is

$$\begin{gathered} E[s(n)] = 0, \\ E[|s(n)|^2] = \sigma^2 \text{ and} \\ E[s(n)s^*(n+\tau)] = 0 \text{ for } \tau \neq 0 \end{gathered} \tag{2.19}$$

where τ is the discrete time delay. The auto-correlation function of the complex random process is given by

$$r(\tau) = \frac{1}{\mathcal{N}} \sum_{n=1}^{\mathcal{N}} s(n)s^*(n+\tau) \tag{2.20}$$

where $\mathcal{N} = BT$ is the number of samples in the passive signal. It can be further shown that

$$E[|r(\tau)|^2] = \begin{cases} \left(1 + \frac{1}{BT}\right)\sigma^4, \text{for } \tau = 0 \\ \frac{1}{BT}\sigma^4, \text{otherwise} \end{cases} \tag{2.21}$$

where T is the time duration of the random signal. The calculations used to derive these results can be found in Appendix A. Equation (2.21) reveals the shape of the auto-correlation function of a random signal. Normalizing Equation (2.21) provides a spike of unit height at $\tau = 0$, i.e. $|r(0)|^2 = 1$, surround by a pedestal of value

$$E[|r(\tau)|^2] = \frac{\frac{1}{BT}\sigma^4}{\left(1 + \frac{1}{BT}\right)\sigma^4} = \frac{1}{1+BT} \approx \frac{1}{BT}, \text{for } BT \gg 1 \text{ and } \tau \neq 0. \tag{2.22}$$

These expected value of the random signal matches well with the simulations as will be apparent. For this purpose, a random signal that is frequency modulated is generated to replicate the broadcast transmissions, namely that from the DBV-T transmitter, where the energy of the random information is spread over the signal bandwidth of 8 MHz. Fig. 2.6 depicts the $M \times L$ auto-correlation function $\boldsymbol{\mathcal{R}}$ of the random signal having B = 8 MHz, T_{sub} = 2.5 ms, M = 20 and f_{BW} = 10 MHz for a single element (CIT = 0.05 s). In this case, $\boldsymbol{\mathcal{R}} = [\mathbf{r}_0; \mathbf{r}_1; \cdots; \mathbf{r}_{M-1}]$ where $\mathbf{r}_m$ is the $1 \times L$ correlation function vector of the m^{th} sub-CIT. It will be convenient at this point of time to define a column vector $\mathbf{r}_l$ representing the correlation function coefficients across all the M sub-CITs at a particular range cell where $\mathbf{r}_0$ is the $M \times 1$ correlation function coefficients (column vector) at the origin range cell, i.e. $\boldsymbol{\mathcal{R}} = [\mathbf{r}_0, \mathbf{r}_1, \cdots, \mathbf{r}_{L-1}]$. The representation of $\mathbf{r}_m$ and $\mathbf{r}_l$ have been indicated in Fig. 2.6 for a clearer insight. The auto-correlation function for each sub-CIT (sub-CIT duration T_{sub} and bandwidth B) shows a spike at the origin ($l = 0$) with a pedestal whose average values lies around –43 dB, which is exactly the calculated value. The pedestal, which is the temporal sidelobes of the correlation function of the passive signals, is commonly known as the random range sidelobes. It is clearly evident that the auto-correlation function exhibit significant level of random range sidelobes (for $l \neq 0$) which is incoherent across sub-CIT-to-sub-CIT. The properties of the auto-correlation function matrix $\boldsymbol{\mathcal{R}}$ can be summarize as,

$$E[|\boldsymbol{\mathcal{R}}(m,l)|^2] = \begin{cases} 1, \text{for } l = 0 \text{ and for all } m \\ \frac{1}{BT_{sub}}, \text{otherwise} \end{cases} . \tag{2.23}$$

For each sub-CIT, the auto-correlation function of the random signal can be considered as a single peak at the origin and having a pedestal which is on average $1/(BT_{sub})$ lower than its peak value [42]. Correspondingly, Fig. 2.7 illustrates the $M \times L$ auto-correlation function $\boldsymbol{\mathcal{R}}$

of a LFMCW signal having the same bandwidth, complex sampling rate, PRI of 2.5 ms and M = 20. As expected, the auto-correlation of a LFMCW signal takes the shape of the sinc function. It can be seen that the major difference stems in the range sidelobes where it is coherent across pulse-to-pulse and at a sigificant lower level for the LFMCW signal as compared to the random signal. The vast difference in range sidelobes level between these two signals is clearly evident. Thus, for the airborne passive radar, it is quite apparent that the random range sidelobes of the passive (random) signal will exhibit undesirable coupling effects into further range cells of interest, as opposed to the active airborne Doppler radar utilizing coherent pulsed or continuous wave signal (i.e. LFMCW signal).

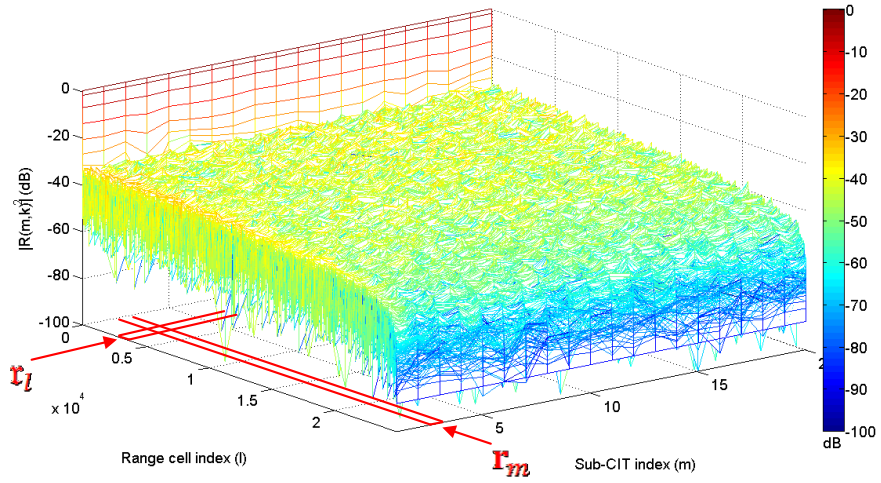

Fig. 2.6: Auto-correlation function of random signal.

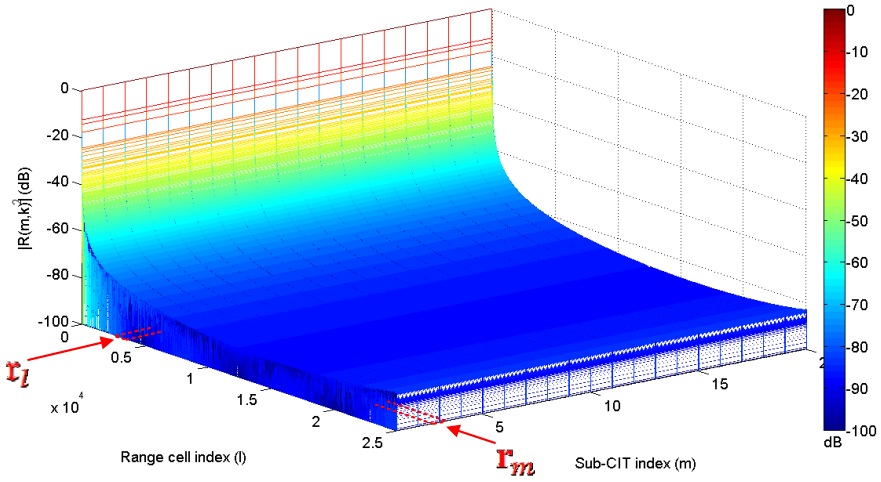

Fig. 2.7: Auto-correlation function of LFMCW signal.

2.5.2 Direct path reference signal

The stationary ground-based non-cooperative transmitter transmits a CW passive signal from its antenna that is modelled mathematically as

$$s_{tx}(t) = a_{tx}u(t)e^{j2\pi f_c t} \tag{2.24}$$

where $u(t)$ denotes the complex modulating function of the passive signal and a_{tx} is the transmit passive signal amplitude. Here, the time duration of $s_{tx}(t)$ equals the CIT.

Consequently, the passive signal received by the airborne passive radar is the transmitted passive signal with a time delay τ_{dp} due to the baseline distance and a Doppler shift f_{dp} due to the relative velocity between the stationary transmitter and the radar given as

$$s_{dp}(t) = a_{dp}u\big(t - \tau_{dp}\big)e^{j2\pi(f_c+f_{dp})(t-\tau_{dp})} \tag{2.25}$$

where a_{dp} is the direct path amplitude. According to the assembly of the datacube, $s_{dp}(t)$ is reformatted where the passive signal CIT duration is segmented into *M* sub-CITs to form the temporal dimension. Mathematically, the received baseband direct path reference signal can be written as

$$s_{dp}(t) = \alpha_{dp}\sum_{m=0}^{M-1} u_m\big(t - \tau_{dp} - mT_{sub}\big)e^{j2\pi f_{dp}t} \tag{2.26}$$

where the direct path amplitude and constant phase terms are grouped into a single complex amplitude α_{dp}. $u_m(t)$ is the complex modulating function of the m^{th} sub-CIT of duration T_{sub} and the finite summation of *M* terms represents the CIT. Thus, the m^{th} sub-CIT within $s_{dp}(t)$ can be written as

$$s_{m,dp}(t) = \alpha_{dp}u_m\big(t - \tau_{dp}\big)e^{j2\pi f_{dp}t}. \tag{2.27}$$

This expression for the direct path reference signal for a single sub-CIT will be the mathematical model used for matched filter processing on a sub-CIT-by-sub-CIT basis in the subsequent Section. The direct path reference signal (free of target and clutter signals) will be assumed to be available to the processor either by beamforming or collected with an auxiliary antenna.

The sub-CIT signal is of duration T_{sub} and upon normalization, has unit energy given by

$$\int_0^{T_{sub}} |u_m(t)|^2 dt = 1. \tag{2.28}$$

Hence, the energy in the transmitted signal is

$$E_{tx} = \int_0^{MT_{sub}} |s_{tx}(t)|^2 dt = ME_{sub} = Ma_{tx}^2 \tag{2.29}$$

where E_{sub} is the energy transmitted in a single sub-CIT of duration T_{sub}.

2.5.3 Scatterer model

The development of the snapshot models for the received passive signal begin by first considering a single discrete moving point (or stationary) scatterer. Assuming a scatterer at a particular range cell where its return signal received at each element is the transmitted passive signal with a time delay $\tau_{n,s}$ from the transmitter to scatterer to the n^{th} element and a Doppler shift f_s (assumed to be equal for all elements) due to the relative velocity between the scatterer and the passive radar given as

$$s_{n,s}(t) = a_s u\big(t - \tau_{n,s}\big)e^{j2\pi(f_c+f_s)(t-\tau_{n,s})} \tag{2.30}$$

where a_s represents the scatterer amplitude attenuated by the effects of atmosphere and RCS. For localized surveillance, $\tau_{n,s}$ can be consider to be small as compared to T_{sub}, i.e. $T_{sub} \gg \tau_{n,s}$. f_s can be assumed to be always smaller than the sub-CIT repetition frequency (unambiguous) since the sub-CIT duration can be arbitrary chosen. Scatterer delay to the n^{th} element $\tau_{n,s}$ consists of τ_s and $\tau'_{n,s}$ where according to the bistatic geometry, the delay equal to the round-trip time to the scatterer is $\tau_s = (R_{Ts} + R_{Rs})/c$ and

$\tau'_{n,s} = -n(d/c)\cos\theta_{Rs}\sin\phi_{Rs}$ is the relative delay measured from the reference element to the n^{th} element. Given that the passive signal is narrowband, i.e. $u\left(t-\tau_s-\tau'_{n,s}\right) \approx u(t-\tau_s)$, thus

$$\begin{aligned} s_{n,s}(t) &= a_s u(t-\tau_s) e^{j2\pi(f_c+f_s)(t-\tau_s-\tau'_{n,s})} \\ &= \alpha_s u(t-\tau_s) e^{j2\pi(f_c+f_s)t} e^{-j2\pi f_c \tau'_{n,s}} \end{aligned} \tag{2.31}$$

where several constant phase terms have been combined into the single complex amplitude α_s. Given the scatterer phase delay to the n^{th} element expressed in terms of the spatial frequency as $-2\pi f_c \tau'_{n,s} = n2\pi\vartheta_s$, therefore

$$s_{n,s}(t) = \alpha_s u(t-\tau_s) e^{j2\pi(f_c+f_s)t} e^{j2\pi n\vartheta_s}. \tag{2.32}$$

After down conversion, the n^{th} element signal is

$$s_{n,s}(t) = \alpha_s u(t-\tau_s) e^{j2\pi f_s t} e^{j2\pi n\vartheta_s}. \tag{2.33}$$

Similarly as in the direct path reference signal, $s_{n,s}(t)$ is segmented into *M* sub-CITs to form the temporal dimension for subsequent match filter processing. Now, the baseband scatterer signal can be rewritten as,

$$s_{n,s}(t) = \alpha_s \sum_{m=0}^{M-1} u_m(t-\tau_s-mT_{sub})\, e^{j2\pi f_s t} e^{j2\pi n\vartheta_s} \tag{2.34}$$

where $u_m(t)$ is the complex modulating function of the m^{th} sub-CIT.

This resulting baseband signal is passed through a matched filter (range correlation) where the output is simply the convolution of the filter impulse response (direct path reference signal) with the scatterer signal that is carried out separately on a sub-CIT-by-sub-CIT basis over the CIT duration,

$$x_{n,s}(t) = \int_{-\infty}^{\infty} s_{n,s}(\tau) h_m(t-\tau) d\tau \tag{2.35}$$

where $s_{n,s}(t)$ represents the received signal at the n^{th} antenna element and $h(t)$ is the matched filter impulse response for each sub-CIT given by $h_m(t) = s^*_{m,dp}(-t)$. It must be noted that the matched filter processing for each sub-CIT (to be carried out for the CIT duration) has a different sub-CIT impulse response where the subscript m in $h_m(t)$ mathematically signify this explanation. This differs from the active airborne pulsed Doppler radar where the matched filter processing is carried out for a single transmit reference pulse within the pulse train of *M* pulses and that the impulse response is consistent [52]. Hence, the matched filter output for the n^{th} element is

$$\begin{aligned} x_{n,s}(t) = \int_{-\infty}^{\infty} \alpha_s \sum_{m=0}^{M-1} u_m(\tau-\tau_s-mT_{sub}) e^{j2\pi f_s\tau} e^{j2\pi n\vartheta_s} \alpha^*_{dp} \\ u^*_m\left(t-\tau-\tau_{dp}\right) e^{-j2\pi f_{dp}\tau} d\tau \end{aligned} \tag{2.36}$$

$$= \alpha_s e^{j2\pi n\vartheta_s} \int_{-\infty}^{\infty} \sum_{m-0}^{M-1} u_m(\tau-\tau_s-mT_{sub})\, u^*_m\left(t-\tau-\tau_{dp}\right) e^{j2\pi\left(f_s-f_{dp}\right)\tau} d\tau$$

where α^*_{dp} has been absorbed into α_s. Following, the relative time delay and relative Doppler shift of the scatterer are introduced and given as $\tau_i = \tau_s - \tau_{dp}$ and $f_i = f_s - f_{dp}$ respectively and for standardization, all the subscript s will be changed to i. Thus,

$$x_{n,i}(t) = \alpha_i e^{j2\pi n\vartheta_i} \sum_{m=0}^{M-1} \int_{-\infty}^{\infty} u_m(\tau - \tau_i - mT_{sub}) u_m^*(t-\tau) e^{j2\pi f_i \tau} d\tau. \tag{2.37}$$

To simplify further, let $\beta = \tau - \tau_i - mT_{sub}$ which implicitly redefines τ in the integral as $\tau = \beta + \tau_i + mT_{sub}$ with $d\beta/d\tau = 1$. Rearranging Equation (2.37)

$$x_{n,i}(t) = \alpha_i e^{jn2\pi\vartheta_i} \sum_{m-0}^{M-1} e^{j2\pi m f_i T_{sub}} \int_{-\infty}^{\infty} u_m(\beta) u_m^*(\beta + \tau_i + mT_{sub} - t) e^{j2\pi f_i \beta} d\beta \tag{2.38}$$

where $e^{j2\pi f_i \tau_i}$ has been absorbed into α_i. Furthermore, assume that for the airborne passive radar, the passive signal time-bandwidth product and the expected range of scatterer Doppler frequencies are such that the signal is insensitive to the scatterer Doppler shift (this assumption may not be valid for high velocity platform, i.e. spaceborne platforms). Mathematically, this is equivalent to the expression

$$\begin{aligned} &\int_{-\infty}^{\infty} u_m(\beta) u_m^*(\beta + \tau_i + mT_{sub} - t) e^{j2\pi f_i \beta} d\beta \\ &\approx \int_{-\infty}^{\infty} u_m(\beta) u_m^*(\beta + \tau_i + mT_{sub} - t) d\beta. \end{aligned} \tag{2.39}$$

Therefore

$$x_{n,i}(t) = \alpha_i e^{jn2\pi\vartheta_i} \sum_{m-0}^{M-1} e^{j2\pi m f_i T_{sub}} \int_{0}^{T_{sub}} u_m(\beta) u_m^*(\beta + \tau_i + mT_{sub} - t) d\beta. \tag{2.40}$$

It can be noted that the exponential term after the summation represents normalized Doppler frequency $f_i T_{sub} = \varpi_i$. In addition, the integral term is the correlation function for the m^{th} sub-CIT within the train of M sub-CITs [1]. Thus,

$$x_{n,i}(t) = \alpha_i e^{jn2\pi\vartheta_i} \sum_{m-0}^{M-1} e^{j2\pi m\varpi_i} r_m(t - \tau_i - mT_{sub}) \tag{2.41}$$

where

$$r_m(t - \tau_i) = \int_{0}^{T_{sub}} u_m(\beta) u_m^*(\beta - t + \tau_i) d\beta \tag{2.42}$$

and from Section 2.5.1

$$E[|r_m(t-\tau_i)|^2] = \begin{cases} 1, \text{for } t = \tau_i \text{ and for all } m \\ \dfrac{1}{BT_{sub}}, \text{otherwise} \end{cases}. \tag{2.43}$$

Equation (2.43) considers that $T_{sub} \gg \tau_i$ where range correlation loss is negligible. Therefore, the discretized form of the matched filter output of the scatterer samples from the n^{th} element, m^{th} sub-CIT and l^{th} range cell is,

$$x_{nml,i} = \alpha_i e^{jn2\pi\vartheta_i} e^{j2\pi m\varpi_i} r_{ml}. \tag{2.44}$$

r_{ml} is the correlation function coefficients (direct path reference and scatterer signal) from the m^{th} sub-CIT and l^{th} range cell, i.e. r_{ml} is a complex sample in $\boldsymbol{\mathcal{R}}(m,l)$. Therefore, this expression represents the passive signal response after transmission, reflection from the scatterer, down converted and matched filtered at each element of the array, for each sub-CIT within the CIT and each range cell within the sub-CIT. Some simplifications can be made to further reduce the expression into a more manageable form suitable for linear algebra

operations. With this in mind, further derivation of the scatterer response can be classified into two detection scenarios. The first considers the scatterer range cell and the second situation looks at the range cell containing the random range sidelobes of the scatterer.

First, interest is focused on the range cell (time delay τ_i) where the scatterer is present. Taking into account the correlation function normalization where $r_m(\tau_i) = 1$ for $\tau = \tau_i$ and for all m as in Equation (2.43), the scatterer samples at this range cell for the n^{th} element and from the m^{th} sub-CIT is

$$x_{nm,i} = \alpha_i e^{jn2\pi\vartheta_i} e^{j2\pi m\varpi_i}. \tag{2.45}$$

It can be seen that one exponential term depends on the spatial index n and the other depends on the temporal index m. Thus, the spatial snapshot for the m^{th} sub-CIT can be written as

$$\mathbf{x}_m = \left[x_{0,m}; x_{1,m}; \ldots; x_{N-1,m}\right] = \alpha_i e^{j2\pi m\varpi_i}\mathbf{a}(\vartheta_i) \tag{2.46}$$

where the $N \times 1$ spatial steering vector $\mathbf{a}(\vartheta_i)$ is defined to be

$$\mathbf{a}(\phi_{Ri}, \theta_{Ri}) = \left[1; e^{j\frac{2\pi d}{\lambda}\cos\theta_{Ri}\sin\phi_{Ri}}; \ldots; e^{j\frac{2\pi d}{\lambda}(N-1)\cos\theta_{Ri}\sin\phi_{Ri}}\right] \tag{2.47}$$

or

$$\mathbf{a}(\vartheta_i) = \left[1; e^{j2\pi\vartheta_i}; \cdots; e^{j2\pi(N-1)\vartheta_i}\right]. \tag{2.48}$$

Hence, the scatterer data is assembled in the form of a space-time snapshot

$$\boldsymbol{\chi}_i = \alpha_i\left[\mathbf{a}(\vartheta_i); e^{j2\pi\varpi_i}\mathbf{a}(\vartheta_i); \cdots; e^{j2\pi(M-1)\varpi_i}\mathbf{a}(\vartheta_i)\right] = \alpha_i\mathbf{b}(\varpi_i)\otimes\mathbf{a}(\vartheta_i) \tag{2.49}$$

where the $M \times 1$ temporal steering vector $\mathbf{b}(\varpi_t)$ is defined to be,

$$\mathbf{b}(\varpi_i) = \left[1; e^{j2\pi\varpi_i}; \cdots; e^{j2\pi(M-1)\varpi_i}\right]. \tag{2.50}$$

The relationship between the spatial and temporal steering vectors forming the components of the scatterer sample matrix is characterized by the Kronecker product.

Next, consider the range cell (time delay $\tau \neq \tau_i$ or range cell $l \neq l_i$) which contain the random range sidelobes of the scatterer response. The scatterer samples at this range cell for the n^{th} element and from the m^{th} sub-CIT is

$$x_{nm,i} = \alpha_i e^{jn2\pi\vartheta_i} e^{j2\pi m\varpi_i} r_m \tag{2.51}$$

where r_m is the correlation function coefficients for the m^{th} sub-CIT at this particular range cell. Using the steering vectors as defined in the preceding paragraph and $\mathbf{r}_l$ as given in Section 2.5.1, the scatterer random range sidelobes space-time snapshot is simply

$$\boldsymbol{\chi}_i = \alpha_i\left(\mathbf{r}_{sl}\odot\mathbf{b}(\varpi_i)\otimes\mathbf{a}(\vartheta_i)\right), \text{for } l \neq l_i \tag{2.52}$$

and $\mathbf{r}_{sl}$ is the $M \times 1$ correlation function coefficients (random range sidelobes) for the scatterer across all the M sub-CITs at this particular range cell. The subscript sl is used to represents the range cell that contain the random range sidelobes of the scatterer. It has been shown from Equation (2.43) that the expected value of $\mathbf{r}_{sl}$, i.e. $E[|\mathbf{r}_{sl}|^2]$ averaged across l range cells for large l and $l \neq l_i$ is on average $1/(BT_{sub})$ lower than its corresponding peak value at range cell l_i. The generic scatterer and its associated random range sidelobes snapshots form the basic and serves as the foundation for subsequent development of the target and interference models.

2.5.4 Target model

A target is defined as a moving point scatterer that is to be detected. Consider the target range cell where a single target is present. Thus, the target snapshot $\boldsymbol{\chi}_t \in C^{MN\times 1}$ at this range cell is simply

$$\boldsymbol{\chi}_t = \alpha_t\big(\mathbf{b}(\varpi_t)\otimes\mathbf{a}(\vartheta_t)\big) \tag{2.53}$$

where α_t, ϖ_t and ϑ_t are the complex amplitude, normalized Doppler frequency and spatial frequency of the target respectively. $\vartheta_t = (d/\lambda)\cos\theta_{Rt}\sin\phi_{Rt}$ and $\varpi_t = (v_t/\lambda)\cos\theta_{Rt}\sin\phi_{Rt}\,T_{sub}$ where ϕ_{Rt} and θ_{Rt} are the azimuth and elevation angles between the target and the passive radar. The $MN \times 1$ target steering vector is

$$\mathbf{v}(\vartheta_t, \varpi_t) = \mathbf{b}(\varpi_t)\otimes\mathbf{a}(\vartheta_t) = \mathbf{v}_t \tag{2.54}$$

and thus

$$\boldsymbol{\chi}_t = \alpha_t\mathbf{v}_t. \tag{2.55}$$

The target complex amplitude α_t can be expressed as the target power as $P_t = \alpha_t^2$ where it can be obtain directly from the radar Equation. The single sub-CIT target SNR for a single element at the receiver output is given by

$$\xi_t = \frac{P_t}{P_n} = \frac{P_T G_T(\phi_{Tt},\theta_{Tt}) G_R(\phi_{Rt},\theta_{Rt})\lambda^2\sigma_t(\phi_{Tt},\theta_{Tt},\phi_{Rt},\theta_{Rt})}{(4\pi)^3 {R_{Tt}}^2 {R_{Rt}}^2 F k_B T_0 B_n L_{tot}} \tag{2.56}$$

where P_n is the thermal noise power per element per sub-CIT. P_T is the transmit power, $G_T(\phi_{Tt},\theta_{Tt})$ and $G_R(\theta_{Rt},\phi_{Rt})$ are the gains of the transmitter antenna and passive radar antenna in the direction of the target respectively, $\sigma_t(\phi_{Tt},\theta_{Tt},\phi_{Rt},\theta_{Rt})$ is the target bistatic RCS, R_{Tt} are R_{Rt} are the distance from the transmitter to the target and the distance from the target to the passive radar respectively, F is the receiver noise figure, k_B is the Boltzmann's constant, T_0 is the reference temperature (290 Kelvins), B_n is the effective receiver bandwidth and L_{tot} is the total system losses. Rearranging Equation (2.56), the target signal power is expressed as

$$P_t = \alpha_t^2 = P_n\xi_t \tag{2.57}$$

where the target amplitude is then given by

$$\alpha_t = \sqrt{P_n\xi_t}. \tag{2.58}$$

α_t is typically very small and thus even for large targets, its SNR is considerably lower as compared to that of the DNR and CNR. If otherwise, there is no need for adaptive processing to suppress the undesirable interferences. For this reason the target random range sidelobes that couple into further range cells of interest are usually insignificant and can be ignored.

2.5.5 Noise model

The ultimate limitation on detection performance is additive white thermal noise (that is the only noise source assumed) generated by the passive airborne radar receiver. Given that each antenna element has its own receiving channel, therefore noise is present at all times and it is statistically uncorrelated across each element. For noise sample y_{nm} on the n^{th} element and m^{th} sub-CIT, the expected value is

$$E\big[y_{n1,m}x^*_{n2,m}\big] = P_n\delta_{n1-n2} \tag{2.59}$$

where

$$\delta_m = \begin{cases}1, m = 0\\ 0, m \neq 0\end{cases} \tag{2.60}$$

is the Kronecker delta function and P_n is the receiver noise power per element per sub-CIT. The noise is assumed to be mutually uncorrelated temporally as well which is valid for a sub-CIT repetition frequency much less than the waveform bandwidth, given that the bandwidth is also much less than the carrier frequency of the passive signal, i.e. $f_{sub} \ll B \ll f_c$. Thus, the expected value is

$$E\left[y_{n,m1}y_{n,m2}^{*}\right] = P_n\delta_{m1-m2}. \tag{2.61}$$

Given these correlation properties of Equations (2.59) and (2.61) lead to the noise component of the space-time covariance matrix $\mathbf{R}_n \in C^{MN\times MN}$, formed by the noise snapshot $\boldsymbol{\chi}_n \in C^{MN\times 1}$, being the scaled identity matrix

$$\mathbf{R}_n = E[\boldsymbol{\chi}_n\boldsymbol{\chi}_n^H] = P_n\mathbf{I}_M\otimes\mathbf{I}_N = P_n\mathbf{I}_{MN} \tag{2.62}$$

where $\mathbf{I}_{MN}$ is a square identity matrix of dimension $MN \times MN$. $\boldsymbol{\chi}_n$ can be represented by a $MN \times 1$ vector of complex white Gaussian noise samples. It is usually convenient to define a normalization of $P_n = 1$ so that all signal levels can be referenced by their SNR per element and per sub-CIT. However, this quantity can also be calculated from the noise spectral density and the receiver bandwidth as $Fk_BT_0B_n$.

2.5.6 Clutter model

Passive radar clutter is generically defined as the returns from any scatterers deemed to be not of tactical significance. For the airborne passive radar, the Earth's surface is the major source of clutter and is the only type of clutter to be considered. The return from an individual clutter patch is identical in form to that of the scatterer. However, several key differences beyond form play an important role in the model derivation. First, the clutter is distributed in both angle and range and is spread in Doppler frequency. Secondly, assuming the Earth's surface is stationary, the only induced Doppler shift is due to the passive radar platform velocity relative to the clutter patch. Under these observations, bistatic ground clutter is analyzed using constant isorange (range cell) around the transmitter and passive radar. Further segmentation of the range cell results in N_c independent clutter patches that is evenly distributed in azimuth where each patch is within the range resolution cell and has a constant velocity with respect to the passive radar platform within the CIT. Assuming no LOS coverage constraint, the clutter snapshot $\boldsymbol{\chi}_c \in C^{MN\times 1}$ at a particular range cell (unambiguous) is given by

$$\boldsymbol{\chi}_c = \sum_{i=1}^{N_c}\alpha_i\mathbf{b}(\varpi_i)\otimes\mathbf{a}(\vartheta_i) = \sum_{i=1}^{N_c}\alpha_i\mathbf{v}(\vartheta_i,\varpi_i) \tag{2.63}$$

where $\mathbf{v}_i = \mathbf{v}(\vartheta_i,\varpi_i)$ is the clutter steering vector for the i^{th} patch. α_i, ϖ_i and ϑ_i are the complex random amplitude, normalized Doppler and spatial frequency of the i^{th} clutter patch respectively. As mentioned, $\vartheta_i = (d/\lambda)\sin\phi_{Ri}\cos\theta_{Ri}$ and $\varpi_i = (v_R/\lambda)\sin\phi_{Ri}\cos\theta_{Ri}\,T_{sub}$ where ϕ_{Ri} and θ_{Ri} are the azimuth and elevation angles between the clutter patch and the passive radar.

The complex random clutter amplitudes α_i of the clutter patches are assumed to be statistically uncorrelated whose mean power is given by $E[|\alpha_i|^2] = P_i$. The contribution from the i^{th} clutter patch has a CNR per element per sub-CIT given by

$$\xi_i = \frac{P_i}{P_n} = \frac{P_TG_T(\phi_{Ti},\theta_{Ti})G_R(\phi_{Ri},\theta_{Ri})\sigma_b^0(\phi_{Ti},\theta_{Ti},\phi_{Ri},\theta_{Ri})A_c\lambda^2}{(4\pi)^3R_{Ti}^2R_{Ri}^2Fk_BT_0B_nL_{tot}} \tag{2.64}$$

where R_{Ti} are R_{Ri} are the distance from the transmitter to the i^{th} clutter patch and the distance from the i^{th} clutter patch to the passive radar respectively. $G_T(\phi_{Ti},\theta_{Ti})$ and $G_R(\theta_{Ri},\phi_{Ri})$ are the gain of the transmitter antenna and passive radar antenna in the direction of the i^{th} clutter patch respectively and $\sigma_b^0(\phi_{Ti},\theta_{Ti},\phi_{Ri},\theta_{Ri})$ is the clutter cross section (bistatic scattering coefficient) per unit area of clutter cell area A_c. From Equation (2.64), the i^{th} clutter signal power is expressed as

$$P_i = E[|\alpha_i|^2] = P_n \xi_i \tag{2.65}$$

where the i^{th} clutter amplitude is then given by

$$\alpha_i = \sqrt{P_n \xi_i}. \tag{2.66}$$

Due to clutter variability, returns from different clutter patches are assumed uncorrelated as shown by

$$E\left[\alpha_i \alpha_{i'}^*\right] = P_n \xi_i \delta_{i-i'}. \tag{2.67}$$

Using the expected value properties of Equation (2.65) and (2.67), the clutter covariance matrix $\mathbf{R}_c \in C^{MN \times MN}$ can be expressed as

$$\begin{aligned} \mathbf{R}_c = E[\boldsymbol{\chi}_c \boldsymbol{\chi}_c^H] &= E\left[\left(\sum_{i=1}^{N_c} \alpha_i \mathbf{b}(\varpi_i) \otimes \mathbf{a}(\vartheta_i)\right)\left(\sum_{i'=1}^{N_c} \alpha_{i'} \mathbf{b}(\varpi_{i'}) \otimes \mathbf{a}(\vartheta_{i'})\right)^H\right] \\ &= P_n \sum_{i=1}^{N_c} \xi_i (\mathbf{b}_i \mathbf{b}_i^H) \otimes (\mathbf{a}_i \mathbf{a}_i^H) = P_n \sum_{i=1}^{N_c} \xi_i \mathbf{v}_i \mathbf{v}_i^H \end{aligned} \tag{2.68}$$

where $\mathbf{b}_i = \mathbf{b}(\varpi_i)$, $\mathbf{a}_i = \mathbf{a}(\vartheta_i)$ and $\mathbf{v}_i = \mathbf{v}(\vartheta_i, \varpi_i)$. Obviously, the clutter snapshot/covariance developed only applies for range cells corresponding to ranges greater than the bistatic range sum where lesser ranges will not include ground clutter.

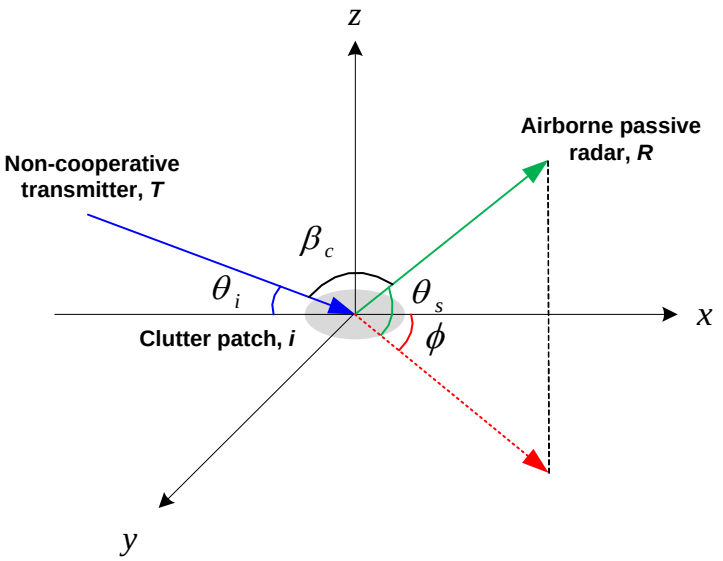

Fig. 2.8: Coordinate system for bistatic clutter measurements.

σ_b^0 is the clutter cross section scattering coefficient or bistatic scattering coefficient per unit area of the illuminated surface occupying a clutter cell area A_C and it varies as a function of the surface composition, frequency and geometry. σ_b^0 is related to the bistatic RCS of the ground clutter σ_i by $\sigma_i = \sigma_b^0 A_C$. Fig. 2.8 shows the clutter-centered coordinate system used more conveniently (as compared to $\phi_{Ti}, \theta_{Ti}, \phi_{Ri}, \theta_{Ri}$) for describing the dependencies of σ_b^0 on grazing angle θ_i (incident angle in x-z plane), scattering angle θ_s (plane containing z axis) and on the out-of-plane angle ϕ (in x-y plane). In general, two measurement sets are of interest: in-plane where $\phi = 180°$ and out-of-plane where $\phi < 180°$ [5]. According to the different value of θ_i and θ_s, the in-plane ground clutter data can be divided into three regions: low grazing angle region where $\theta_i \leq 3°$ or $\theta_s \leq 3°$; specular ridge region where $140° \leq \theta_i +$

$\theta_s \leq 220°$; and the remaining cases make up the bistatic scatter region. In the bistatic scattering region, the per unit cross section is the geometric mean of the sines of the incident and scattering angles modelled by $(\sigma_b^0)_b = \gamma\sqrt{\sin\theta_i \sin\theta_s}$ where γ is a normalized reflectivity parameter. For the low grazing angle region, the per unit area cross section is the arithmetic mean of the incident and scattering angles and is modelled as $(\sigma_b^0)_l = \gamma \sin[(\theta_i + \theta_s)/2]$. In the specular ridge region, the per unit area cross section is given by a variation of the theory of forward scattering from rough surfaces, $(\sigma_b^0)_s = exp[-(\beta_c/\sigma_s)^2]$ where σ_s is the root mean square surface slope and β_c is the angle between the vertical and bistatic bisector of θ_i and θ_s, i.e. $\beta_c = |90° - (\theta_i + \theta_s)/2|$.

2.5.7 Random range sidelobes models

Other than the target (if present), clutter and noise that are present at the detection range cell of interest, the random range sidelobes coupling effects of the direct path and of the strong clutter signals into this range cell can be significant as well. The direct path snapshot $\boldsymbol{\chi}_{dp} \in C^{MN\times 1}$ at the origin range cell $(l = 0)$ is given as

$$\boldsymbol{\chi}_{dp} = \alpha_{dp}\mathbf{b}(\varpi_{dp} = 0)\otimes\mathbf{a}(\vartheta_{dp}) = \alpha_{dp}\mathbf{1}\otimes\mathbf{a}(\vartheta_{dp}) \tag{2.69}$$

where α_{dp} and ϑ_{dp} are the complex amplitude and spatial frequency of the direct path respectively and $\vartheta_{dp} = (d/\lambda)\cos\theta_{TR}\sin\phi_{TR}$. For the direct path snapshot, the Doppler frequency is neutralized (given by the temporal steering column vector of $\mathbf{1} = \text{ones}(M, 1)$**)** as it has inherent zero Doppler frequency since the direct path reference signal used for matched filter processing has the same Doppler frequency due to the passive radar platform motion. Correspondingly, the random range sidelobes coupling of the direct path signal into further range cells has the snapshot $\boldsymbol{\chi}_{dp_{sl}} \in C^{MN\times 1}$ expression given by

$$\boldsymbol{\chi}_{dp_{sl}} = \alpha_{dp}(\mathbf{r}_{dp_{sl}}\odot\mathbf{1})\otimes\mathbf{a}(\vartheta_{dp}) \tag{2.70}$$

where $\mathbf{r}_{dp_{sl}}$ represents the $M \times 1$ complex auto-correlation function coefficients (random range sidelobes) across all the M sub-CITs at this particular range cell. The direct path amplitude α_{dp} can be expressed as the direct path power as $P_{dp} = \alpha_{dp}^2$ where the DNR per element per sub-CIT is given as

$$\xi_{dp} = \frac{P_{dp}}{P_n} = \frac{P_T G_T(\phi_{RT}, \theta_{RT}) G_R(\phi_{RT}, \theta_{RT})\lambda^2}{(4\pi)^2 R_{RT}^2 F k_B T_0 B_n L_{tot}} \tag{2.71}$$

where $G_T(\phi_{RT}, \theta_{RT})$ and $G_R(\theta_{RT}, \phi_{RT})$ are the gain of the transmitter antenna and passive radar antenna in the direction of the passive radar and transmitter respectively. Rearranging Equation (2.71), the direct path signal power is expressed as

$$P_{dp} = \alpha_{dp}^2 = P_n\xi_{dp} \tag{2.72}$$

where the direct path amplitude is then given by

$$\alpha_{dp} = \sqrt{P_n\xi_{dp}}. \tag{2.73}$$

The coefficients of $\mathbf{r}_{dp_{sl}}$ from different sub-CITs are considered random and uncorrelated, and further assume for simplicity that the direct path signal is stationary over the CIT. Thus, it can be approximated that

$$E[\mathbf{r}_{dp_{sl}}\mathbf{r}_{dp_{sl}}^H] = \frac{1}{BT_{sub}}\mathbf{I}_M. \tag{2.74}$$

Using the expected value properties of Equation (2.72) and (2.74), the direct path random range sidelobes covariance matrix $\mathbf{R}_{dp_{sl}} \in C^{MN\times MN}$ can be expressed as

$$\begin{aligned}\mathbf{R}_{dp_{sl}} &= E\left[\boldsymbol{\chi}_{dp_{sl}}\boldsymbol{\chi}_{dp_{sl}}^{H}\right] \\ &= E\left[\left(\alpha_{dp}\left(\mathbf{r}_{dp_{sl}}\odot\mathbf{1}\right)\otimes\mathbf{a}\left(\vartheta_{dp}\right)\right)\left(\alpha_{dp}\left(\mathbf{r}_{dp_{sl}}\odot\mathbf{1}\right)\otimes\mathbf{a}\left(\vartheta_{dp}\right)\right)^{H}\right] \\ &= P_n E\left[\xi_{dp}\left(\mathbf{r}_{dp_{sl}}\mathbf{r}_{dp_{sl}}^{H}\right)\otimes\left(\mathbf{a}_{dp}\mathbf{a}_{dp}^{H}\right)\right] = \frac{P_n}{BT_{sub}}\left(\xi_{dp}\mathbf{I}_M\otimes\left(\mathbf{a}_{dp}\mathbf{a}_{dp}^{H}\right)\right)\end{aligned} \tag{2.75}$$

where $\mathbf{a}_{dp} = \mathbf{a}\left(\vartheta_{dp}\right)$. Correspondingly, the random range sidelobes coupling of the c^{th} strong clutter signal into further range cell has the snapshot $\boldsymbol{\chi}_{c_{sl}} \in C^{MN\times 1}$ expression given by

$$\boldsymbol{\chi}_{c_{sl}} = \sum_{i=1}^{N_c}\alpha_i\left(\mathbf{r}_{c_{sl}}\odot\mathbf{b}(\varpi_i)\right)\otimes\mathbf{a}(\vartheta_i) \tag{2.76}$$

where $\mathbf{r}_{c_{sl}}$ represents the $M\times 1$ complex correlation function coefficients (random range sidelobes) across all the M sub-CITs for the c^{th} strong clutter at this particular range cell. The emphasis of strong on clutter explicitly states the fact that the random range sidelobes coupling of this clutter is higher than thermal noise at the further range cells of interest. As per Equation (2.74), the coefficients of $\mathbf{r}_{c_{sl}}$ from different sub-CITs are considered random and uncorrelated, and further assume for simplicity that the clutter signal is stationary over the CIT. Thus, it can be approximate that

$$E\left[\mathbf{r}_{c_{sl}}\mathbf{r}_{c_{sl}}^{H}\right] = \frac{1}{BT_{sub}}\mathbf{I}_M. \tag{2.77}$$

Using the expected value properties of Equation (2.65), (2.67) and (2.77), the random range sidelobes covariance matrix $\mathbf{R}_{c_{sl}} \in C^{MN\times MN}$ for the c^{th} strong clutter is derived as

$$\begin{aligned}\mathbf{R}_{c_{sl}} &= E\left[\boldsymbol{\chi}_{c_{sl}}\boldsymbol{\chi}_{c_{sl}}^{H}\right] \\ &= E\left[\left(\sum_{i=1}^{N_c}\alpha_i\left(\mathbf{r}_{c_{sl}}\odot\mathbf{b}(\varpi_i)\right)\otimes\mathbf{a}(\vartheta_i)\right)\left(\sum_{i'=1}^{N_c}\alpha_{i'}\left(\mathbf{r}_{c'_{sl}}\odot\mathbf{b}(\varpi_{i'})\right)\otimes\mathbf{a}(\vartheta_{i'})\right)^{H}\right] \\ &= P_n E\left[\sum_{i=1}^{N_c}\xi_i\left(\mathbf{r}_{c_{sl}}\mathbf{r}_{c_{sl}}^{H}\odot\mathbf{b}_i\mathbf{b}_i^{H}\right)\otimes\left(\mathbf{a}_i\mathbf{a}_i^{H}\right)\right] = \frac{P_n}{BT_{sub}}\sum_{i=1}^{N_c}\xi_i\left(\mathbf{I}_M\odot\mathbf{b}_i\mathbf{b}_i^{H}\right)\otimes\left(\mathbf{a}_i\mathbf{a}_i^{H}\right)\end{aligned} \tag{2.78}$$

where $\mathbf{b}_i = \mathbf{b}(\varpi_i)$ and $\mathbf{a}_i = \mathbf{a}(\vartheta_i)$. For N_{sc} strong clutter where their random range sidelobes coupling into further range cell can be considered as significant, Equation (2.76) can be further expressed as a more complete form as

$$\sum_{c=1}^{N_{sc}}\boldsymbol{\chi}_{c_{sl}} = \sum_{c=1}^{N_{sc}}\sum_{i=1}^{N_c}\alpha_{c,i}\left(\mathbf{r}_{c_{sl}}\odot\mathbf{b}(\varpi_{c,i})\right)\otimes\mathbf{a}\left(\vartheta_{c,i}\right). \tag{2.79}$$

Correspondingly, Equation (2.78) can also be further expressed as

$$\sum_{c=1}^{N_{sc}}\mathbf{R}_{c_{sl}} = \sum_{c=1}^{N_{sc}}E\left[\boldsymbol{\chi}_{c_{sl}}\boldsymbol{\chi}_{c_{sl}}^{H}\right] = \frac{P_n}{BT_{sub}}\sum_{c=1}^{N_{sc}}\sum_{i=1}^{N_c}\xi_{c,i}\left(\mathbf{I}_M\odot\mathbf{b}_{c,i}\mathbf{b}_{c,i}^{H}\right)\otimes\left(\mathbf{a}_{c,i}\mathbf{a}_{c,i}^{H}\right) \tag{2.80}$$

In summary, Equation (2.70) and (2.79) are the random range sidelobes snapshots and Equation (2.75) and (2.80) are the random range sidelobes covariance matrices of the direct path and of the strong clutter, respectively, that couples into the further range cells of interest.

2.5.8 Consolidated snapshot and covariance matrix

The snapshot of each component that contributes to the total signal received by the airborne passive radar has been described independently. In a typical target present scenario, the composite snapshot is composed of the target return, clutter returns, random range sidelobes contributions of the direct path and of the strong clutter and thermal noise. As such, the space-time snapshot for the airborne passive radar at the detection range cell of interest is thus

$$\boldsymbol{\chi} = \boldsymbol{\chi}_t + \boldsymbol{\chi}_u = \boldsymbol{\chi}_t + \boldsymbol{\chi}_c + \boldsymbol{\chi}_{dp_{sl}} + \sum_{c=1}^{N_{sc}} \boldsymbol{\chi}_{c_{sl}} + \boldsymbol{\chi}_n \tag{2.81}$$

where $\boldsymbol{\chi}_u$ consists of all the undesired components (interference plus noise) and $\boldsymbol{\chi}$ is commonly known as the H_1 hypothesis (target present). $\boldsymbol{\chi}_t$ is 0 if no target is present and in this case, $\boldsymbol{\chi} = \boldsymbol{\chi}_u$ will be known as the null hypothesis H_0. For Equation (2.81), it is easy to prove that the components in $\boldsymbol{\chi}_u$ are all statistically independent [49]. This results in the interference plus noise covariance matrix for H_0 given by

$$\mathbf{R}_u = E[\boldsymbol{\chi}_u \boldsymbol{\chi}_u^H] = \mathbf{R}_c + \mathbf{R}_{dp_{sl}} + \sum_{c=1}^{N_{sc}} \mathbf{R}_{c_{sl}} + \mathbf{R}_n \tag{2.82}$$

where $\mathbf{R}_c$, $\mathbf{R}_{dp_{sl}}$, $\mathbf{R}_{c_{sl}}$ and $\mathbf{R}_n$ are the clutter, direct path random range sidelobes, c^{th} strong clutter random range sidelobes and noise covariance matrix respectively.

2.5.9 Power spectrum and eigenspectrum

Based on the covariance matrix for the airborne passive radar, the angle-Doppler power spectrum can be generated which gives the spectral representation of the covariance matrix. The covariance matrix represents the data which are to be analyzed in terms of a variable steering vector $\mathbf{v}(\vartheta, \varpi)$. Thus, steering over the whole range of spatial and Doppler values is equivalent to cascading a set of beams with a Doppler filter bank. Fourier and minimum variance are two estimators widely used for space-time power spectrum estimation [53]. Consider a generalized covariance matrix $\mathbf{R}$, the power of the signal-match estimator for this covariance matrix is given by

$$\mathbf{P}_{sm}(\vartheta, \varpi) = \frac{|\mathbf{v}^H \boldsymbol{\chi}|^2}{\mathbf{v}^H \mathbf{v}} = \frac{\mathbf{v}^H \mathbf{R} \mathbf{v}}{MN} \tag{2.83}$$

where $\mathbf{v}$ seeks for signal components in $\mathbf{R}$. $\mathbf{P}_{sm}$ attempts to becomes a maximum wherever the steering vector coincides with the signal vector in $\mathbf{R}$. This is two-dimension (angle-Doppler) power of the signal snapshot and can be implemented by the two-dimension Fourier transform of the signal at the particular range cell and thus is also known as the Fourier power spectrum. The Fourier power estimator exhibits spatial and Doppler spurious response, producing sidelobes patterns that are not representative of the covariance matrix components [46]. A high resolution technique that provides high resolution spectral power estimation is the MVDR estimator. The MVDR estimator is defined as

$$\mathbf{P}_{mv}(\vartheta, \varpi) = \frac{\mathbf{v}^H \mathbf{v}}{\mathbf{v}^H \mathbf{R}^{-1} \mathbf{v}}. \tag{2.84}$$

It is well-known that $\mathbf{P}_{mv}$ provides better spectral resolution than $\mathbf{P}_{sm}$. The main advantage of the MVDR estimator is that it is very close to the components contained in the covariance matrix as there is no spurious sidelobes. However, it is computationally intensive as it requires inversion of the $MN \times MN$ matrix.

Another kind of spectral representation of the covariance matrix is the rank-ordered eignevalues known as the eigenspectrum [54] which reveals in particular the number of DOF of the signal and interferences portion of the observed covariance matrix which cannot be obtained from the power spectrum. The generalized covariance matrix **R** can be decomposed into eigenvectors and eigenvalues as follows,

$$\mathbf{R} = \mathbf{E}\boldsymbol{\Lambda}\mathbf{E}^{H} \tag{2.85}$$

where $\boldsymbol{\Lambda} = \mathrm{diag}(\lambda_1, \ldots, \lambda_{MN})$ is a diagonal matrix of eigenvalues λ_i and **E** is the unitary matrix of eigenvectors. Since **R** is positive definite, the eigenvalues are positive. The eigenvector represents a mode of the interference (spatial and Doppler) while the eigenvalue represents the corresponding power. It provides insight into the INR and the number of interference eigenvalues reveals the rank of the interference scenario which is the minimum number required for the interference filter.

2.6 Properties of clutter

In this Section, the basic characteristics and properties of the clutter for the airborne passive radar are analyzed. These include the spatial-Doppler characteristics of the clutter and the rank of clutter covariance matrix. The efficiency of the clutter suppression depends significantly on these properties. Certainly, these properties of the clutter also affect the properties of its corresponding random range sidelobes. Also discussed are the imperfection of the clutter profile due to velocity misalignment of the ULA.

2.6.1 Clutter ridge and aliasing

For the airborne passive radar, the spatial frequency for a single stationary clutter patch as defined in Section 2.5.6 is

$$\vartheta_i = \frac{d}{\lambda}\cos\theta_{Ri}\sin\phi_{Ri}. \tag{2.86}$$

The resulting Doppler frequency corresponding to this patch depends on only the passive radar platform motion since the ground-based non-cooperative transmitter is stationary. Thus, for a side-looking ULA with no velocity misalignment, the Doppler frequency is

$$f_i = \frac{v_R}{\lambda}\cos\theta_{Ri}\sin\phi_{Ri} \tag{2.87}$$

and the normalized Doppler frequency in terms of spatial frequency is

$$\varpi_i = f_i T_{sub} = \frac{v_R}{\lambda}\cos\theta_{Ri}\sin\phi_{Ri}\,T_{sub} = \frac{v_R T_{sub}}{d}\vartheta_i. \tag{2.88}$$

Immediate inspection reveals that this function is linear with respect to the spatial frequency. The slope of the clutter line [55] is therefore

$$\beta = \frac{v_R T_{sub}}{d}. \tag{2.89}$$

Thus, the slope β is simply the number of inter-element spacings traversed by the passive radar platform during one sub-CIT repetition interval. For half-wavelength inter-element spacing, $\beta = (2v_R T_{sub})/\lambda$ is equivalently the number of times the clutter Doppler spectrum aliases into the unambiguous Doppler space. Equation (2.88) defines the locus in an angle-Doppler space where clutter is present and this locus is referred to as clutter ridge.

The clutter ridge span in Doppler space depends on the platform velocity, the passive carrier wavelength and the sub-CIT repetition interval. Fig. 2.9 illustrates examples of the clutter ridge plotted for different velocities ($\beta = 0, 0.5, 1$ and 2) with T_{sub} fixed. For

simplicity, the y-axis is taken to be the true clutter normalized Doppler frequency. To ease in the understanding of the clutter properties, it is not necessary to take into consider the relative Doppler frequency between the direct path reference and clutter signal due to matched filter processing. In addition, the clutter range to passive radar altitude ratio is considered to be large, i.e. $\cos\theta_{Ri} \approx 1$. Unless otherwise stated, these two assumptions for the clutter will be used in all the simulations of this Section. $\beta = 0$ signifies a stationary passive radar scenario where the clutter at all spatial frequencies exhibit zero Doppler frequency. If $\beta \leq 1$, the clutter is said to be unambiguous in Doppler which means that there may be a clutter free region in Doppler and only at most one angle for the clutter will exhibit the same Doppler frequency as the target as illustrated in Fig. 2.9(b) and 2.9(c). As the value of β increases (for $\beta > 1$), the clutter becomes Doppler ambiguous and the clutter ridge folds over within the Doppler space. In this case, there may be multiple angles at which the sidelobe clutter has the same Doppler frequency as a target as in Fig. 2.9(d). This aliasing of the clutter ridge requires more DOF to suppress as the more Doppler ambiguous it gets. In addition, the value of β is not restricted to integer value and for non-integer value it will have implications on the corresponding eigenspectrum as will be shown next.

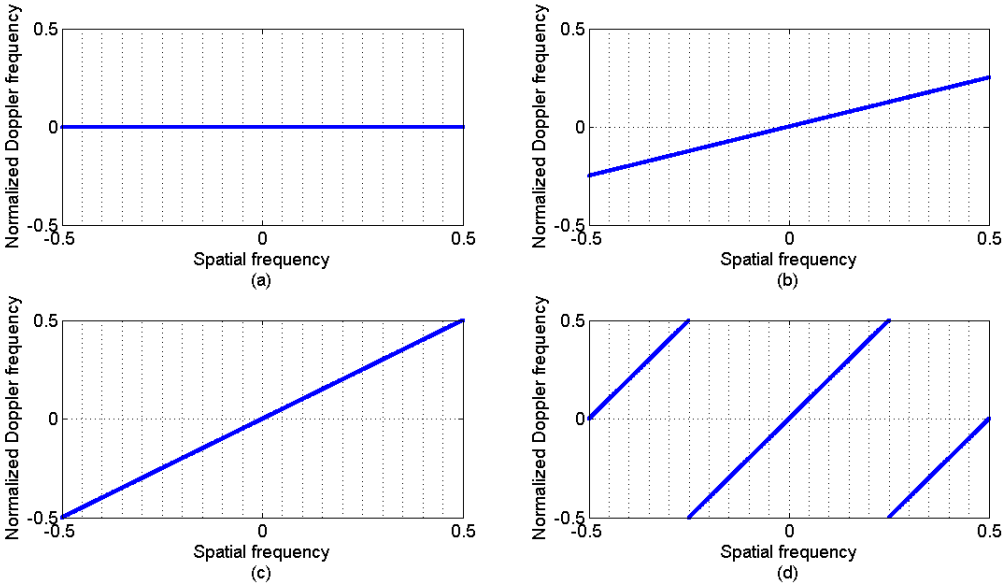

Fig. 2.9: Clutter ridge for (a) $\beta = 0$, (b) $\beta = 0.5$, (c) $\beta = 1$ and (d) $\beta = 2$ (Doppler ambiguous).

2.6.2 Rank of clutter covariance matrix

The rank of clutter (interference) covariance matrix is an indicator of both the complexity of the clutter (interference) scenario and the number of DOF required to successfully mitigate it. The special structure embodied in the clutter ridge suggests that the clutter covariance matrix is of low rank. Brennan and Staudaher developed the theorem (Brennan's Rule) regarding the clutter rank [56] which is approximately

$$\text{rank}(\mathbf{R}_c) \approx \lfloor N + (M-1)\beta \rceil \tag{2.90}$$

where the bracket $\lfloor \quad \rceil$ indicate rounding to the nearest integer as β is not necessarily an integer and β is given in Equation (2.89). When β is an integer, Equation (2.90) can be replaced by an equality. Brennan's Rule assumes a sidelooking monostatic airborne radar scenario where it is also applicable for the airborne passive radar utilizing a stationary ground-based non-cooperative transmitter. Examination of this result can provide insight into

why it holds quite closely in most situations. Each individual clutter patch contributes a space-time steering vector $\mathbf{v}(\vartheta_i, \beta\vartheta_i)$ to a particular space-time snapshot at a constant range cell. The phase of the clutter for the n^{th} element and m^{th} sub-CIT can be written as

$$\gamma_{nm} = 2\pi(n + m\beta)\vartheta_i = \frac{2\pi}{\lambda}[(n + m\beta)d]\cos\theta_{Ri}\sin\phi_{Ri}. \tag{2.91}$$

The clutter Doppler essentially causes the spatial snapshot due to the m^{th} sub-CIT to appear as it is received by an array whose position has moved by $m\beta d$. Thus, the effective position of the n^{th} element and m^{th} sub-CIT is

$$d_{nm} = (n + m\beta)d. \tag{2.92}$$

Observations of clutter are, in effect, repeated by different elements on different sub-CIT as the passive radar moves during the CIT. Given the total snapshot dimension of MN, the number of independent clutter observations will be less since only independent observations contribute to the clutter rank of the clutter covariance matrix. For the case where $\beta = 1$, there are exactly $N + M - 1$ distinct observations in the value of rank($\mathbf{R}_c$) as indicated by Brennan's Rule. As evident from Equation (2.90), the clutter rank increases linearly with β or equivalently with the amount of Doppler ambiguity.

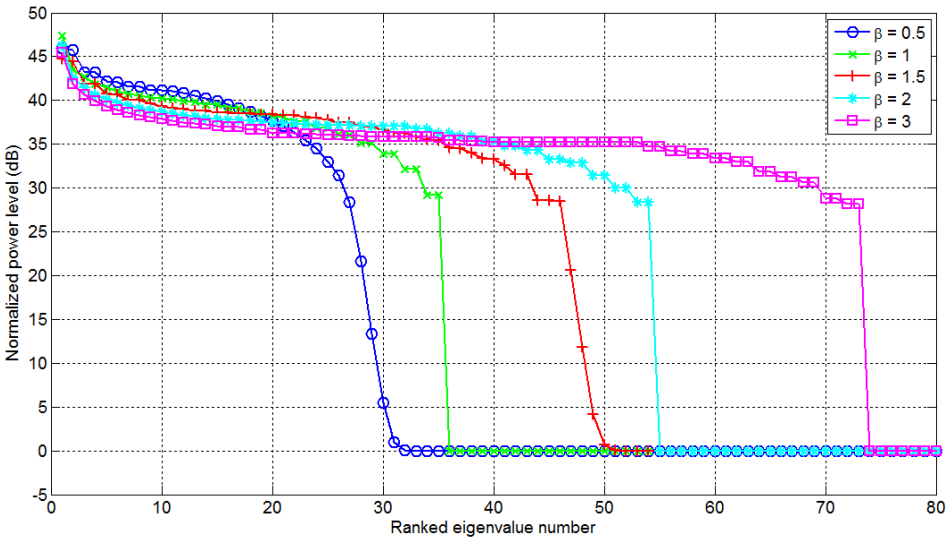

Fig. 2.10: Clutter eigenspectrum with different platform velocities for $N = 16$ and $M = 20$.

Fig. 2.10 shows the eigenspectrum plots of the clutter covariance matrices for $\beta = 0.5, 1, 1.5, 2$ and 3 where $N = 16$ and $M = 20$ for a side-looking ULA with CNR of 30 dB. This example (specified by the given values of N, M, CNR, β and side-looking configuration) will be used in the subsequent simulations for properties analyses in the remaining of this Chapter. According to Brennan's rule, there will be 26 non-zero eigenvalues for $\beta = 0.5$, 35 for $\beta = 1$, 45 for $\beta = 1.5$, 54 for $\beta = 2$ and 73 for $\beta = 3$. When β is an integer, the eigenspectrum exhibits a sharp cutoff as the covariance matrix is singular and Brennan's rule correctly predicts its rank. However, when β is not an integer, the eigenspectrum exhibits a gradual decrease as opposed to the sharp cutoff [55]. In this case, Brennan's rule no longer provides the exact rank. Nevertheless, it does indicate the point of initial descent and in fact, Brennan's rule prediction is slightly lower than the true rank for non-integer β. Brennan's rule is extremely useful in predicting the eigenvalues of the clutter covariance matrix seen by the airborne passive radar. However, in practical scenarios, there are several other phenomena that tend to increase the rank of clutter covariance matrix significantly beyond

that is predicted by Brennan's rule. Among these are the intrinsic clutter motion and the misalignment of the velocity vector and the array axis which will be investigated next.

2.6.3 Array orientation – velocity misalignment

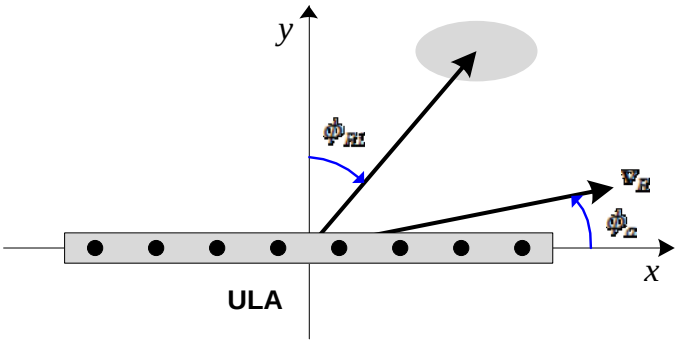

Fig. 2.11: Array geometry with velocity misalignment angle ϕ_a.

The relationship between the spatial and Doppler characteristics of clutter as seen by the airborne passive radar depends on the array axis relative to the platform velocity vector $\mathbf{v}_R$ [57]. The analysis so far assumed that $\mathbf{v}_R$ was perfectly aligned with the array axis. For the airborne passive radar, the interest is for medium range MTI around the solid spherical volume of the passive radar platform. In this case, as mentioned, six sets of ULA in side-looking and forward-looking configurations are proposed for all-round coverage. With a side-mounted ULA, in practice, the direction of the motion may be slightly offset from the array axis due to aircraft crab caused by implementation and structural constraint where the passive radar platform is placed. For surveillance in the forward region, the ULA is typically mounted in the aircraft nose. In this case the array axis is approximately normal to the velocity vector.

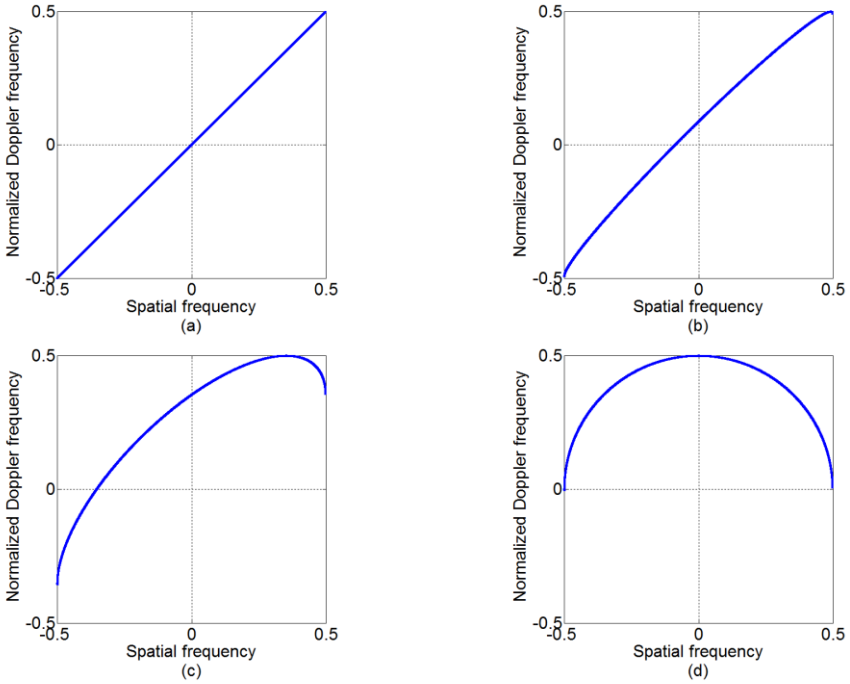

Fig. 2.12: Clutter ridge for (a) $\phi_a = 0°$, (b) $\phi_a = 10°$, (c) $\phi_a = 45°$ and (d) $\phi_a = 90°$.

Expressions for clutter Doppler and spatial frequency had been given and in general, two angles are required to specify the direction for each. Fig. 2.11 depicts the array geometry with velocity misalignment angle [49] where for the ULA, both the velocity vector and array axis lie in the horizontal plane parallel to the Earth's surface but differ in direction by an angle ϕ_a known as the misalignment angle. The impact of velocity misalignment on the spatial-Doppler relationship of the i^{th} clutter is the introduction of ϕ_a into the Doppler frequency as

$$f_i = \frac{v_R}{\lambda} \cos\theta_{Ri} \sin(\phi_{Ri} + \phi_a) \tag{2.93}$$

and normalized Doppler frequency as

$$\varpi_i = \beta\eta \cos\theta_{Ri} \sin(\phi_{Ri} + \phi_a) \tag{2.94}$$

where $\beta = (v_R T_{sub})/d$ and $\eta = d/\lambda$. Velocity misalignment produces a clutter ridge that instead of being a line in the variables of $\cos\theta_{Ri} \sin\phi_{Ri}$ and Doppler frequency is an ellipse. Manipulation of Equation (2.94) leads to the standard elliptical form

$$\beta^2\vartheta_i^2 - 2\beta \cos\phi_a \,\vartheta_i\varpi_i + \varpi_i^2 = \beta^2\eta^2(\cos\theta_{Rs} \sin\phi_a)^2 \tag{2.95}$$

where $\vartheta_i = \eta \cos\theta_{Ri} \sin\phi_{Ri}$. Equation (2.95) yields a rotated ellipse in the normalized spatial-Doppler coordinates where the clutter ellipse are rotated from the ϑ_i and ϖ_i axes by an angle ψ_a determined by

$$\cot 2\psi_a = \frac{1-\beta^2}{2\beta \cos\phi_a} \tag{2.96}$$

where the rotation angle is measured clockwise from the positive ϖ_i-axis. For a side-looking array with no misalignment angle, $\phi_a = 0°$. Then Equation (2.95) is reduces to

$$\beta^2\vartheta_i^2 - 2\beta\vartheta_i\varpi_i + \varpi_i^2 = 0 \tag{2.97}$$

and therefore

$$\beta\vartheta_i = \varpi_i. \tag{2.98}$$

This is a straight line in the $\vartheta_i - \varpi_i$ plane with the slope defined by β. In the case of a forward-looking array, i.e. $\phi_a = 90°$, Equation (2.95) becomes

$$\beta^2\vartheta_i^2 + \varpi_i^2 = \beta^2\eta^2(\cos\theta_{Ri})^2 \tag{2.99}$$

and

$$(\cos\theta_{Ri} \sin\phi_{Ri})^2 + (\cos\theta_{Ri} \sin(\phi_{Ri} + \phi_a))^2 = (\cos\theta_{Ri})^2 \tag{2.100}$$

which is a set of concentric circles with radii $\cos\theta_{Ri}$. Larger circles are therefore associated with a larger range sum.

Fig. 2.12 shows clutter ridges with velocity misalignment for different values of ϕ_a for the frontlobe of the ULA (backlobe ignored) where $\beta = 1$. No velocity misalignment results in the linear plot (Fig. 2.12(a)) where it can be considered to be a degenerate ellipse and as misalignment is introduced, an ellipse results. Intermediate misalignment angles result in elliptical clutter trajectories of various eccentricities while larger curves result from greater passive radar to clutter distances. As mentioned, for $\phi_a = 90°$ (forward-looking array), the clutter ridge is a semicircle. Fig. 2.13 depicts the clutter eigenspectrum for different values of misalignment angle. The power distribution of the highest eigenvalue is changed slightly as the Doppler distribution of clutter power is altered by the misalignment. As ϕ_a increases, the tails of the eigenspectrum extend outwards as the rank of the covariance matrix increases. Brennan's rule relies on a linear relationship between the spatial and Doppler frequency and is no longer applicable when $\phi_a \neq 0$ [49] as the linearity is no longer present. When misalignment angle is present, the rank will be higher than that predicted by Brennan's rule.

These results suggest that more DOF will be required for effective clutter suppression when misalignment is present.

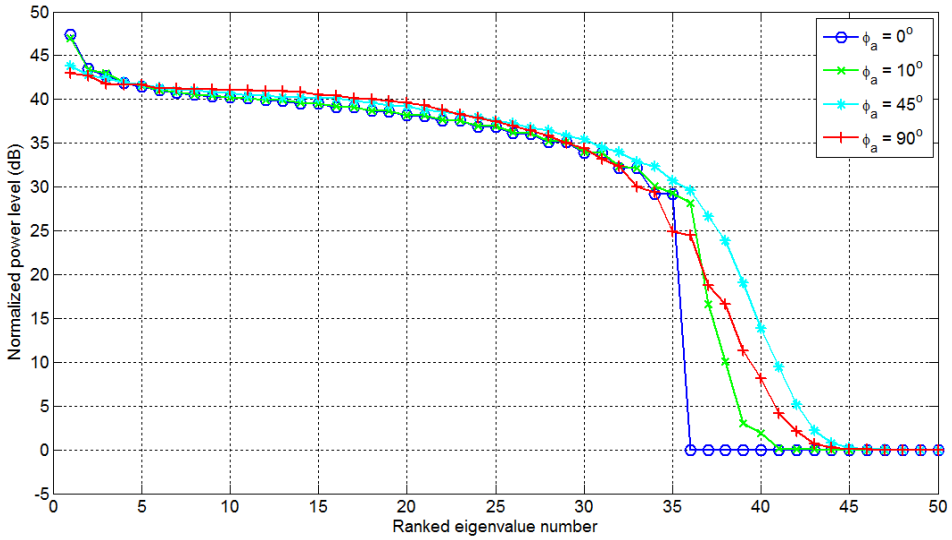

Fig. 2.13: Clutter eigenspectrum for different values of misalignment angle for $N = 16$ and $M = 20$.

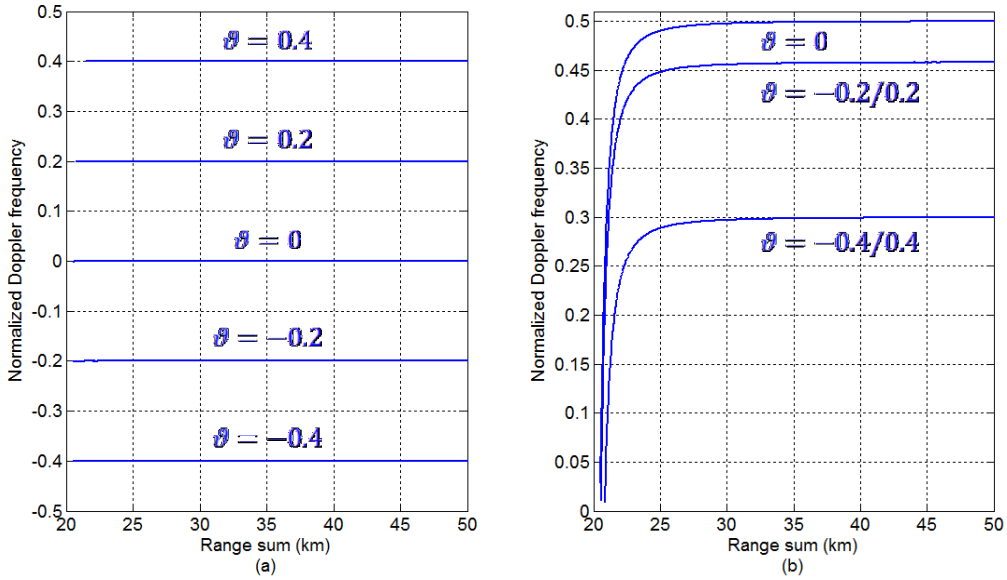

Fig. 2.14: Clutter normalized Doppler frequency against range sum for (a) side-looking ULA and (b) forward-looking ULA.

On the range dependency of the clutter Doppler frequency, Fig. 2.14 depicts the plot of the clutter normalized Doppler frequency against the range sum (for various spatial frequencies) for a (a) side-looking and (b) forward-looking ULA of the airborne passive radar. The simulation geometry is such that the non-cooperative transmitter and passive radar (right side of transmitter) are aligned on the x-plane at altitude 200 m and 1000 m respectively, with a ground baseline of 20 km where the passive radar flies away from the transmitter along the x-axis. For a side-looking array where $\phi_a = 0°$, the normalized Doppler frequency is $\varpi_i = \beta\vartheta_i$ which means that the Doppler frequency does not depend on the range (range

independent) as in Fig. 2.14(a). This is an expected results since the cone angle $\cos\theta_{Ri}\sin\phi_{Ri}$ coincide with the iso-Doppler surface on the clutter plane (ground). For a forward-looking array where $\phi_a = 90°$, the normalized Doppler frequency is

$$\varpi_i = \pm\sqrt{\beta^2\eta^2(\cos\theta_{Ri})^2 - \beta^2\vartheta_i^2}. \tag{2.101}$$

A numerical evaluation of Equation (2.101) leads to curves for the forward-looking array as illustrated in Fig. 2.14(b). For the forward-looking array, the Doppler frequency of clutter echoes exhibit only positive Doppler frequencies and they are symmetrical about the array broadside. As prominently seen, at short range sum, the clutter Doppler frequency is dependent on the range sum where the major range dependence is in the area $R_{sum} \leq 30$ km [58] which is approximately 5 km away from the passive radar along the extended baseline. In this case, these (short range sum) clutter are said to be non-stationary. Subsequently, for $R_{sum} > 30$ km, the clutter Doppler frequency are considered to be range independent and thus are stationary.

For non-stationary bistatic clutter, there exists some degree of variation for the clutter angle-Doppler behaviour over the range sum dimension as illustrated in Fig. 2.14(b). Thus, non-stationarity degrades the quality of the secondary data set, thereby diminishing the moving target detection performance of the STAP through covariance matrix estimation errors (more of this will be explained in the next Chapter). STAP implementation must accommodate clutter non-stationarity to achieve increasing level of performance approaching the optimal condition. Techniques for ameliorating the non-stationary nature of bistatic clutter generally fall into one of three categories [8]: localized training, time-varying weights and data warping. As a summary, reduced-dimension [49, 55] and reduced-rank [46, 55] STAP are localized processing strategy which results in fewer adaptive DOFs and hence a requirement for substantially reduced training data. It attempts to select training data in the vicinity of detection range cell to minimize the degree of non-stationarity over the reduced training regions. Time-varying weights [59, 60] allow the weight vector to vary linearly over the range sum dimension to approximately track the changing cutter angle-Doppler response. The basic ideal involves taking the Taylor series expansion of the weight vector and retaining constant and linear terms. Essentially, a doubling of the processor's DOFs occurs where these DOFs vary over range sum. Lastly, deterministic data warping methods include Doppler warping [57], higher order Doppler warping [61] and angle-Doppler compensation [62]. These techniques apply a range-varying modulation which seek to align the space-time clutter data to a reference, thereby partially homogenizing the training set. Deterministic weightings require *a priori* knowledge of the airborne platform operating parameters where the nondeterministic adaptive data warping methods [61, 62] use the measured data to estimate certain unknown parameters of the compensation approach.

2.7 Properties of noise and direct path random range sidelobes

As a matter of fact, the noise space-time covariance matrix is of full rank, i.e.

$$\text{rank}(\mathbf{R}_n) = MN. \tag{2.102}$$

As in Equation (2.70) and (2.75), the direct path random range sidelobes snapshot that is coupled into further range cell of interest is

$$\boldsymbol{\chi}_{dp_{sl}} = \alpha_{dp}\left(\mathbf{r}_{dp_{sl}} \odot \mathbf{1}\right) \otimes \mathbf{a}\left(\vartheta_{dp}\right) \tag{2.103}$$

and the corresponding covariance matrix is derived as

$$\mathbf{R}_{dp_{sl}} = \frac{P_n}{BT_{sub}}\left(\xi_{dp}\mathbf{I}_M \otimes \left(\mathbf{a}_{dp}\mathbf{a}_{dp}^H\right)\right). \tag{2.104}$$

For the direct path random range sidelobes, it is spatially correlated from element to element but temporally uncorrelated from sub-CIT-to-sub-CIT. In this case, the direct path random sidelobes snapshot will appear as an irregular ridge spread across all Doppler frequencies having the spatial frequency as the direct path signal. Thus, the direct path random sidelobes looks like thermal noise temporally but like a point scatterer in the spatial domain. Likewise, the spectral representation of the direct path random range sidelobes covariance matrix will be a ridge in a single spatial frequency but spread across all Doppler frequencies where the average value of the ridge is $1/(BT_{sub} \times M)$ lower than the peak value of the direct path signal at the origin range cell. The direct path random range sidelobes space-time covariance matrix has a rank

$$\text{rank}\left(\mathbf{R}_{dp_{sl}}\right) = M. \tag{2.105}$$

The low rank nature of this direct path random range sidelobes covariance matrix that is an undesirable effect for the airborne passive radar will be helpful in the design of efficient adaptive processing architectures.

The covariance matrix of the complex auto-correlation coefficient $\mathbf{r}_{dp_{sl}}$ (random range sidelobes) of the direct path can be approximated as

$$E\left[\mathbf{r}_{dp_{sl}}\mathbf{r}_{dp_{sl}}^{H}\right] = \frac{1}{BT_{sub}}\mathbf{I}_{M}. \tag{2.106}$$

This can be illustrated numerically where Fig. 2.15(a) shows the random range sidelobes time-only (single element) covariance matrix of the direct path that is generated from the auto-correlation function of the random signal as in Fig. 2.6. The result matches that of the theoretical Equation (2.106) of $(1/BT_{sub})\mathbf{I}_M$ as in Fig. 2.15(b).

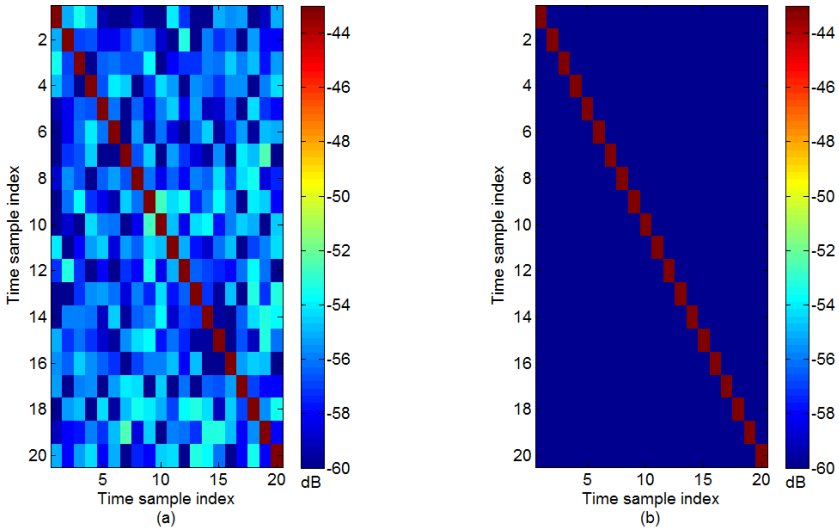

Figure 2.15: (a) Numerical and (b) theoretical random range sidelobes time-only covariance matrix for $M = 20$.

2.8 Properties of strong clutter random range sidelobes

As in Equation (2.76) and (2.78), the random range sidelobes snapshot of the c^{th} strong clutter that is coupled into further range cell of interest is

$$\boldsymbol{\chi}_{c_{sl}} = \sum_{i=1}^{N_c} \alpha_i\left(\mathbf{r}_{c_{sl}} \odot \mathbf{b}(\varpi_i)\right) \otimes \mathbf{a}(\vartheta_i) \tag{2.107}$$

and the corresponding covariance matrix is derived as

$$\mathbf{R}_{c_{sl}} = \frac{P_n}{BT_{sub}} \sum_{i=1}^{N_c} \xi_i (\mathbf{I}_M \odot \mathbf{b}_i \mathbf{b}_i^H) \otimes (\mathbf{a}_i \mathbf{a}_i^H). \tag{2.108}$$

Comparing Equation (2.108) to that of the clutter covariance matrix $\mathbf{R}_c$ of Equation (2.68), one similar and two distinct properties can be noted. First, the random range sidelobes exhibit the same span of spatial frequencies to its corresponding strong clutter. The two differences are that, firstly, at a specific spatial frequency due to the i^{th} clutter path, the Doppler frequency of its corresponding random range sidelobes will not be unique. Instead, it is spread across all Doppler frequencies given that these random sidelobes are incoherent from sub-CIT-to-sub-CIT (temporally uncorrelated). Secondly, at a given spatial frequency, the average value of the random range sidelobes is approximately $1/(BT_{sub}M)$ lower than the peak value of the corresponding strong clutter at the same spatial frequency. If the strong clutter exhibits the full span of spatial frequencies, then its corresponding random range sidelobes space-time covariance matrix will be of full rank. The analysis of the covariance matrix of the complex cross-correlation coefficient $\mathbf{r}_{c_{sl}}$ (random range sidelobes) for the c^{th} strong clutter follows exactly that of $\mathbf{r}_{dp_{sl}}$ in the preceding Section.

2.9 Summary

The generic bistatic geometry of the airborne passive radar utilizing a stationary ground-based non-cooperative transmitter has been introduced, together with the passive CIT datacube model and key measurement parameters to define the generalized space-time steering vector. The statistical analysis of the passive signal is necessary in the snapshots development for the signal received by the airborne passive radar which is a major contribution. The vital property is in the correlation function of the passive signal which exhibits a single peak at the origin surrounded by pedestal of energy which is on average lower than the peak by the reciprocal of its time-bandwidth product. Next, the space-time snapshot models for each of the passive signal received by the airborne passive radar are derived and presented. In a typical target present scenario, other than the target component, a snapshot at the detection range cell of interest will also contains undesired components which include clutter returns, random range sidelobes contributions of the direct path and of the strong clutter, and the background thermal noise. Mathematically, the space-time snapshot for the airborne passive radar at the detection range cell of interest is

$$\boldsymbol{\chi} = \boldsymbol{\chi}_t + \boldsymbol{\chi}_u = \boldsymbol{\chi}_t + \boldsymbol{\chi}_c + \boldsymbol{\chi}_{dp_{sl}} + \sum_{c=1}^{N_{sc}} \boldsymbol{\chi}_{c_{sl}} + \boldsymbol{\chi}_n. \tag{2.109}$$

Different from conventional pulsed Doppler radar, $\boldsymbol{\chi}_u$ has additional snapshot terms that correspond to the direct path random range sidelobes and the random range sidelobes of N_{sc} number of strong clutter. Subsequently, based on the snapshot models, the expressions for their corresponding covariance matrices are derived. The spatial-Doppler characteristics and properties of the two-dimensional clutter profile and on the random range sidelobes of the direct path and of the strong clutter are also analyzed where the efficiency of the interference suppression depends significantly on these properties. The characteristics and properties of the models developed in this Chapter will serve as the input to the interference cancellation technique and various adaptive space-time processing algorithms in the subsequent Chapter.

Chapter 3

Signal Processing for Airborne Passive Radar

3.1 Introduction

For the airborne passive radar, during moving target detection, it encounters the effects of strong interfering signal returns against weak returns from the targets where this severe interfering environment is usually characterized by the high levels of direct path and clutter against the thermal noise background. As a result and due to the properties of the passive signal, the random range sidelobes of the direct path and of the strong clutter will exhibit significant coupling effects into further range cells. In addition, for the clutter received by the airborne passive radar, the motion-induced spread of its Doppler spectrum may mask the weak and slow moving targets. Understanding these underlying challenges, signal processing schemes applicable to the airborne passive radar can be studied to improve moving target detections performance. The signal processing schemes for the airborne passive radar can be segregated into a two step interference cancellation process. First, the direct path and strong clutter coupling components present in the received signal at each antenna element can be suppressed by the adaptive interference cancellation algorithm prior to matched filter processing. In mitigating these interfering signals, its corresponding random range sidelobes will also be suppressed by the same amount. Further cancellation on the undesirable residual random range sidelobes couplings (direct path random range sidelobes that is localized in spatial frequency and the random range sidelobes of the strong clutter that has a limited spatial frequency span) and on the spatial-Doppler dependent clutter can be achieved using STAP. In particular, due to reasons of computational complexity (large dimensionality) and sample support required for weights training in a practical scenario, reduced-dimension STAP techniques provide solutions to this fundamental two-dimensional clutter suppression problem. Thus, the capabilities and performance of these signal processing schemes for the airborne passive radar using non-cooperative transmitter for improved air and ground moving target detections will be analyzed and addressed in this Chapter.

3.2 Adaptive interference cancellation

The airborne passive radar target and its severe interference environment as depicted in Fig. 2.5 is usually characterized by the high levels of direct path and clutter against the thermal noise background. Given that the power of direct path and strong clutter is several tens of decibels stronger than the target power, the random range sidelobes coupling effects of these interfering signals into further range cells will seriously influence target detection and estimation. Without cancellation, these sidelobes coupling that is above thermal noise can make target detection virtually impossible [45]. The space-time snapshot for each contributing component to the received passive signal had been developed. The composite snapshot $\boldsymbol{\chi}$ at the detection range cell of interest l_d is composed of the target return $\boldsymbol{\chi}_t$, clutter returns $\boldsymbol{\chi}_c$, direct path random range sidelobes $\boldsymbol{\chi}_{dp_{sl}}$, strong clutter random range sidelobes $\boldsymbol{\chi}_{c_{sl}}$ and thermal noise $\boldsymbol{\chi}_n$ where mathematically

$$\boldsymbol{\chi} = \boldsymbol{\chi}_t + \boldsymbol{\chi}_c + \boldsymbol{\chi}_{dp_{sl}} + \sum_{c=1}^{N_{sc}} \boldsymbol{\chi}_{c_{sl}} + \boldsymbol{\chi}_n. \tag{3.1}$$

Equation (3.1) gives the resultant snapshot for the target, interferences and noise response upon matched filter processing on the space-time received passive signal for the airborne passive radar. Obviously, interferences that strongly inhibit target detections that need to be suppressed are that of clutter $\boldsymbol{\chi}_c$, direct path random range sidelobes $\boldsymbol{\chi}_{dp_{sl}}$ and strong clutter random range sidelobes $\boldsymbol{\chi}_{c_{sl}}$. The spatial-Doppler dependent stationary clutter $\boldsymbol{\chi}_c$ (at l_d) can be effectively suppressed by STAP. STAP can also be used to suppress the random range sidelobes coupling of the direct path and of those strong clutter that has a limited spatial frequency span. However, more DOFs will be needed and this definitely degrades the mainlobe clutter cancellation STAP performance. In addition, targets that fall within these spatial frequencies span of the random range sidelobes will also be suppressed as well. Moreover, for random range sidelobes covariance matrix of the strong clutter that is of full rank, moving target detection will be sidelobes limited and therefore STAP will not improve detection performance. Fortunately, the issue concerning the random range sidelobes couplings of the direct path and of the strong clutter can be separately dealt with prior to STAP. In this case, the direct path and strong clutter present in the received signal at each element can be suppressed by the adaptive interference cancellation algorithm prior to matched filter processing. In mitigating these interfering signals, their corresponding random range sidelobes that manifest into further range cells will also be suppressed by the same amount, diminishing these undesirable coupling effects on the target. The snapshots definition for the direct path and N_{sc} number of strong clutter random range sidelobes are reproduced here as

$$\begin{gathered} \boldsymbol{\chi}_{dp_{sl}} = \alpha_{dp}\left(\mathbf{r}_{dp_{sl}} \odot \mathbf{1}\right) \otimes \mathbf{a}\left(\vartheta_{dp}\right) \text{ and} \\ \sum_{c=1}^{N_{sc}} \boldsymbol{\chi}_{c_{sl}} = \sum_{c=1}^{N_{sc}} \sum_{i=1}^{N_c} \alpha_{c,i}\left(\mathbf{r}_{c_{sl}} \odot \mathbf{b}(\varpi_{c,i})\right) \otimes \mathbf{a}\left(\vartheta_{c,i}\right). \end{gathered} \tag{3.2}$$

The objective is thus to suppress, as much as possible, the level of $\boldsymbol{\chi}_{dp_{sl}}(\alpha_{dp})$ and $\boldsymbol{\chi}_{c_{sl}}(\alpha_{c,i})$ with the paramount result in having these signals to be below that of $\boldsymbol{\chi}_n$ at the detection range cells.

The basic concept behind the adaptive interference cancellation is such that the received passive signal after filtering can be modelled as the output of an FIR system where the input is the direct path reference signal and received signal before adaptive filtering. Then, the motivation will be to minimize the power of the output of the adaptive filter. For adaptive interference cancellation based on the FIR model, the algorithms are mainly classified into two categories. The first being the LS approach which minimizes a deterministic sum of squared errors [65, 66]. The other is the stochastic-gradient method that employs a gradient descent optimization procedure [67]. Algorithms that fall into these adaptive techniques category are the LMS, NLMS and RLS transversal filters where the performance comparison of these algorithms for disturbance cancellation in passive radar can be found in [68]. The adaptive interference cancellation used for the airborne passive radar for interference suppression will be focused on the LS approach.

3.2.1 Least squares approach for adaptive finite impulse response filtering

An effective adaptive FIR filter for adaptive interference cancellation for the airborne passive radar can be obtained by resorting to the LS approach where the fundamental

principle is to minimize the power at the output of the adaptive filter [65]. The aim is not only to suppress the direct path and zero-Doppler strong clutter, but also to cancel away Doppler-shifted strong clutter signals. For that, the algorithm estimates the strength of the direct path, significant clutter and significant Doppler-shifted clutter couplings in the received signal and then coherently subtracting these interfering signals from the received signal at each element prior to matched filter processing. Based on the LS error criterion, the cancellation technique subtracts optimally weighted direct path reference signal, as well as its delayed and Doppler-shifted versions from the received signal where the weights are optimal in the LS sense.

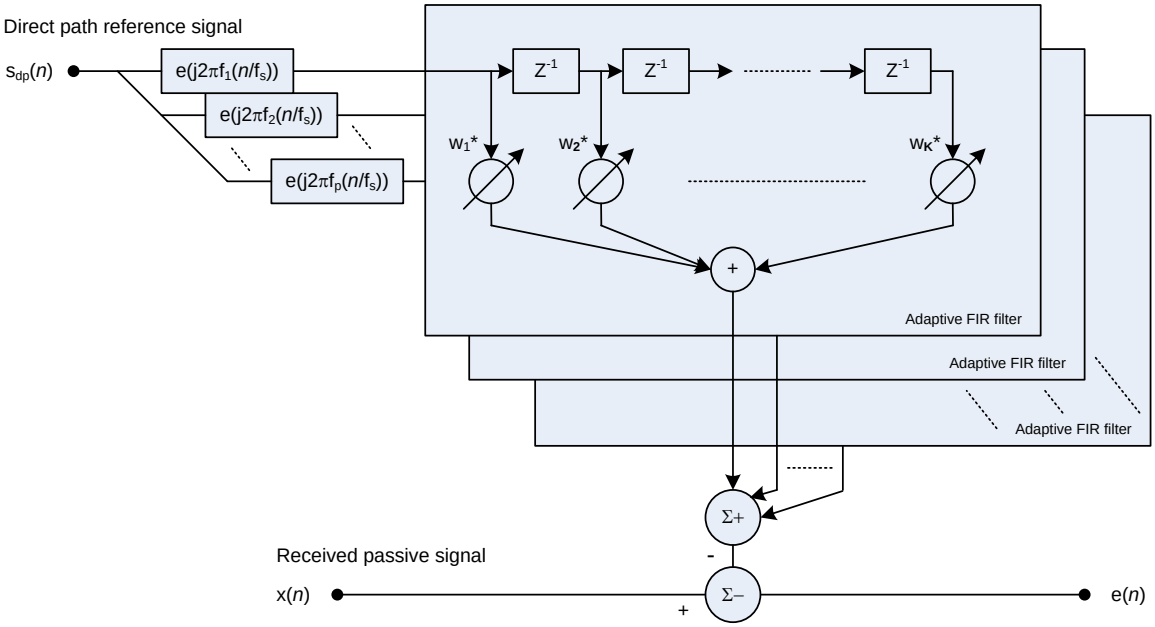

Fig. 3.1: Structure of adaptive FIR filter.

For the LS-based adaptive interference cancellation algorithm, the adaptive filter structure is shown in Fig. 3.1 [67]. Both the direct path reference signal and the received passive signal consisting of target (if present), undesired interference (to be suppressed) and noise are the inputs of the adaptive FIR filter. Consequently, the output will be the received signal free of interference components. For mathematical modelling of the algorithm, the complex sample of the direct path reference signal is given by

$$\mathbf{s}_{dp} = (s_{dp}(1) \quad s_{dp}(2) \quad \cdots \quad s_{dp}(\mathcal{N}))^T \tag{3.3}$$

and the complex sample of the received signal is

$$\mathbf{x} = (x(1) \quad x(2) \quad \cdots \quad x(\mathcal{N}))^T \tag{3.4}$$

where $\mathcal{N}$ is the number of samples in the received signal at each element of CIT duration. From Equation (3.3), the direct path reference signal is redefined as a $\mathcal{N} \times Q$ direct path reference signal matrix where each column is a unique delayed copy of the direct path reference signal as

$$\mathbf{S}_{dp} = \begin{bmatrix} s_{dp}(1) & s_{dp}(0) & \dots & s_{dp}(-Q+2) \\ s_{dp}(2) & s_{dp}(1) & \cdots & s_{dp}(-Q+3) \\ \vdots & \vdots & \ddots & \vdots \\ s_{dp}(\mathcal{N}) & s_{dp}(\mathcal{N}-1) & \cdots & s_{dp}(\mathcal{N}-Q+1) \end{bmatrix} \tag{3.5}$$

where Q is the number of cancellation weights (order) for the adaptive FIR filter. For the airborne passive radar, this number Q corresponds to the order that is larger than the strong clutter index where the random range sidelobes will be above thermal noise at the range cells

of interest. Equation (3.5) is then reformulated into a larger matrix to include the Doppler-shifted version of $\mathbf{S}_{dp}$ as

$$\mathbf{S} = \left[e^{j2\pi f_1(n/f_s)}\mathbf{S}_{dp} \quad e^{j2\pi f_2(n/f_s)}\mathbf{S}_{dp} \quad e^{j2\pi f_3(n/f_s)}\mathbf{S}_{dp} \quad \cdots \quad e^{j2\pi f_P(n/f_s)}\mathbf{S}_{dp}\right] \tag{3.6}$$

where $n = 1, \ldots, \mathcal{N}$ is the time index, $p = 1, \ldots, P$ is the Doppler frequency index and f_p is the Doppler frequency corresponding to the p^{th} Doppler cell where the Doppler-shifted strong clutter in this Doppler cell is to be suppressed. $\mathbf{S} \in C^{\mathcal{N}\times QP}$ and therefore, the corresponding $QP \times 1$ weighting vector is

$$\mathbf{w} = (w(1) \quad w(2) \quad \cdots \quad w(QP))^T. \tag{3.7}$$

The output error can then be written in vector form as

$$\mathbf{e} = \mathbf{x} - \mathbf{S}\mathbf{w}. \tag{3.8}$$

Hence, the aim is to minimize the power at the output of the adaptive FIR filter which equates to cancelling the interference components. The cost function to minimize the error sum of squares based on the LS error criterion is

$$\min_{\mathbf{w}} \|\mathbf{e}\|^2 = \min_{\mathbf{w}} \|\mathbf{x} - \mathbf{S}\mathbf{w}\|^2. \tag{3.9}$$

Equating the derivative of the cost function to zero, the optimized solution of the weighting vector is

$$\mathbf{w} = (\mathbf{S}^H\mathbf{S})^{-1}\mathbf{S}^H\mathbf{x}. \tag{3.10}$$

Equation (3.10) gives the weighting coefficients that minimize the sum of the squares of the residual (error) between the received signal and the direct path reference signal and together with its delayed and Doppler-shifted versions. Subsequently, the received signal after the application of the adaptive interference cancellation algorithm is

$$\mathbf{x}_{new} = \mathbf{x} - \mathbf{S}\mathbf{w}. \tag{3.11}$$

It should be noted that, depending on the clutter profile and its random range sidelobes couplings, the order (Q) of the adaptive FIR filter for each Doppler cell need not be consistent.

Tab. 3.1: Parameters for ambiguity function coherent processing simulations.

Passive signal parameters	
Random signal carrier frequency	600 MHz
Random signal bandwidth	8 MHz
CIT	0.05 s
Time-bandwidth product	56 dB
DNR (for CIT duration)	100 dB
Total CNR ratio from zero to the 40^{th} range cell (for CIT duration)	([70: –0.5:50]) dB
Target SNR	20 dB
Target Doppler frequency	60 Hz (Normalized Doppler frequency of 0.15)
Target range	Range cell index of 180 ($l = 180$)

To envisage the performance for the LS-based adaptive interference cancellation algorithm, simulations on an assumed interference scenario are carried out. The direct path reference signal is assumed to exhibit zero Doppler frequency. The received signals (at each element and for the CIT duration) consist of the direct path and clutter, as well as the Doppler-shifted clutter signals. Since the cancellation is performed on each element, the results will be depicted as the ambiguity function coherent processing plot (Doppler-range plot) as in Equation (1.1). The parameters used for the signals and the ambiguity function

coherent processing are tabulated as in Tab. 3.1. For reason of simplicity and ease of performance analysis, clutter are simulated up to the 41 range cells ($l = 0$ to 40). In addition, the total power for the Doppler-shifted clutter is assume to be spread in a descending profile centered around the zero Doppler cell and outwards to the next five positive and five negative Doppler cells (total across eleven Doppler cells including the zero Doppler cell).

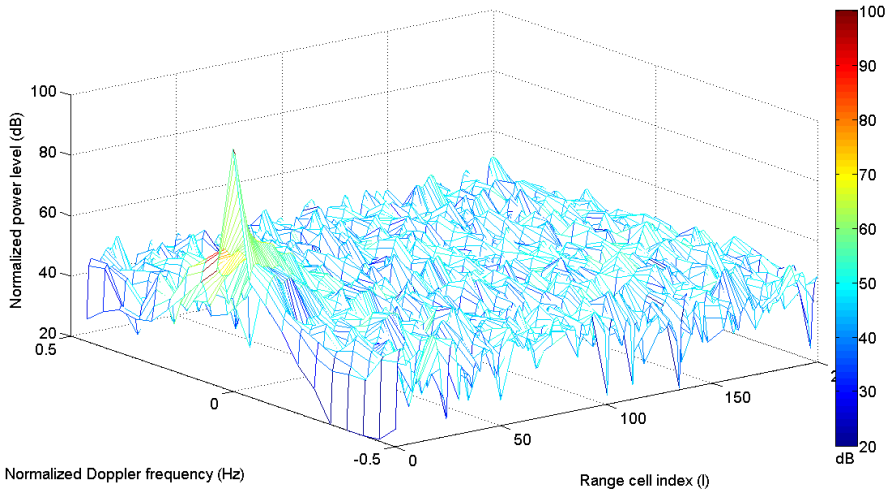

(a)

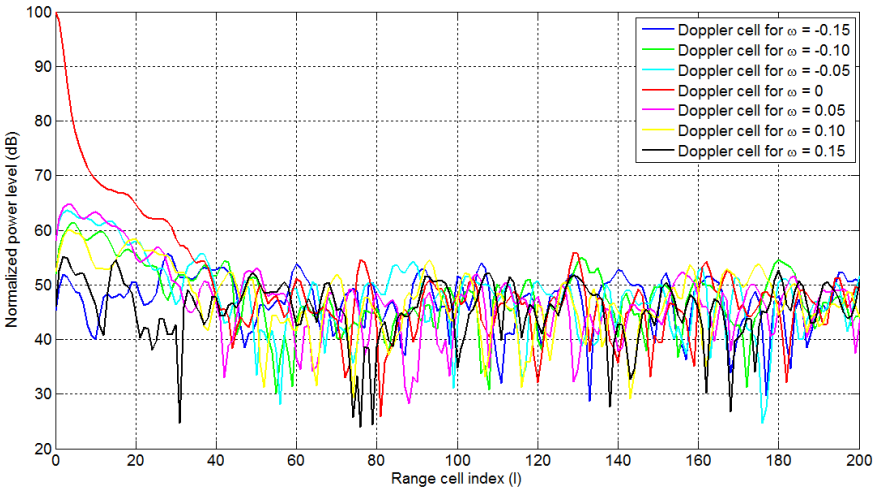

(b)

Fig. 3.2: (a) Ambiguity function plot and corresponding
(b) Doppler cell cuts without adaptive interference cancellation.

Fig. 3.2 depicts the ambiguity function plot and Doppler cell cuts without the adaptive interference cancellation. The ambiguity function plot (and all subsequent plots) has been normalized to the thermal noise level of 0 dB. As seen, the strongest signal is that of the direct path with a DNR of 100 dB. Surrounding the direct path are the Doppler-shifted clutter spread across eleven Doppler cells and in range cells up to $l = 40$. Evidently, the pedestal (random range sidelobes of the direct path) of 43.8 dB is approximately $10\log_{10}\left(1/(CIT \cdot B)\right)$ dB lower than the peak value. This high level of pedestal totally overwhelmed the target SNR of 20 dB. Next the adaptive interference cancellation algorithm is used to suppress only the zero-Doppler components where the adaptive FIR filter order of 50 is used. Fig. 3.3 shows the resulting ambiguity function plot and Doppler cell cuts. A deep null (spanning

from the origin range cell to the 49th range cell) along the zero Doppler cell that is prominently seen demonstrated that the zero Doppler components (direct path and zero Doppler clutter) had been effectively suppressed. The resulting pedestal is now due to the random range sidelobes of the remaining Doppler-shifted clutter and comparing with Fig. 3.2, this pedestal is much lower in level. However, the random range sidelobes of the strong Doppler-shifted clutter are still above that of the target, rendering it undetectable. Fig. 3.4 depicts the ambiguity function plot and Doppler cells cuts where the 50th-order adaptive FIR filter is used to totally suppress all of the direct path, clutter and Doppler-shifted clutter signals. Deep nulls can be prominently seen over the range and Doppler cells that the adaptive filtering algorithm operates on which demonstrate that all these interfering signals had been effectively suppressed. The resulting pedestal is due to that of thermal noise. The target located at the 180th range cell with a normalized Doppler frequency of 0.15 can be detected at 20 dB above the noise pedestal which is exactly its simulated parameters.

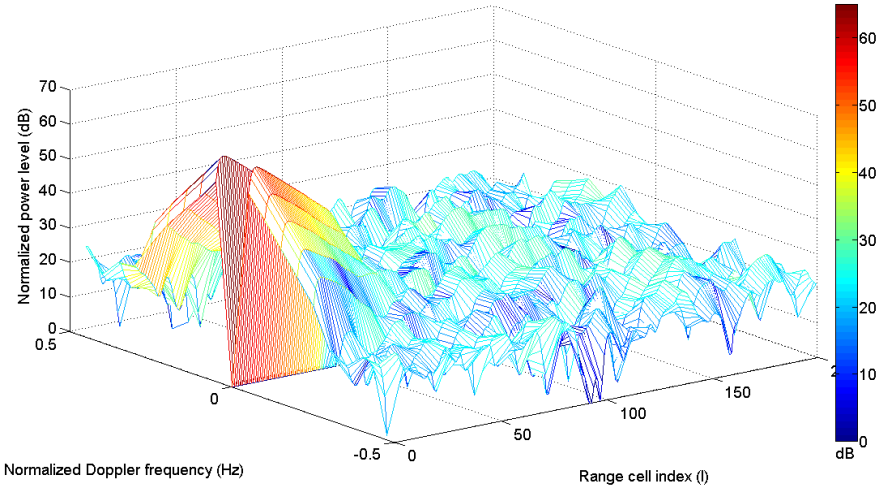

(a)

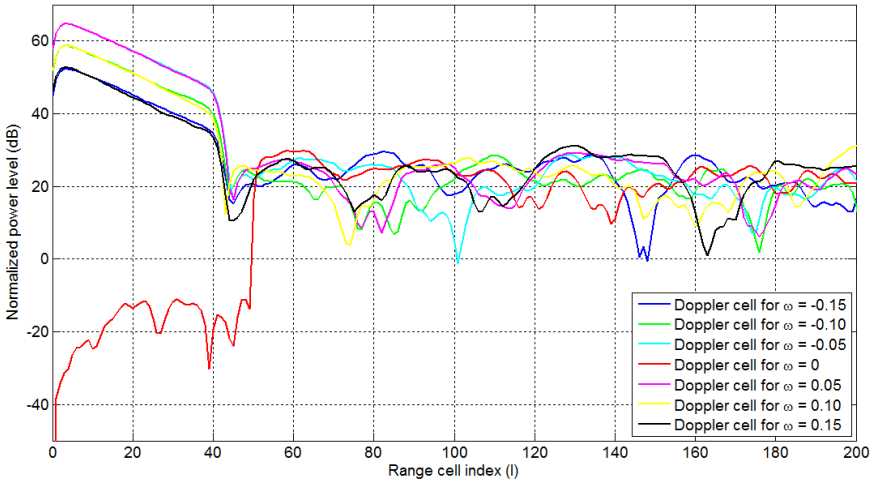

(b)

Fig. 3.3: (a) Ambiguity function plot and corresponding (b) Doppler cell cuts after direct path and zero-Doppler clutter adaptive interference cancellation.

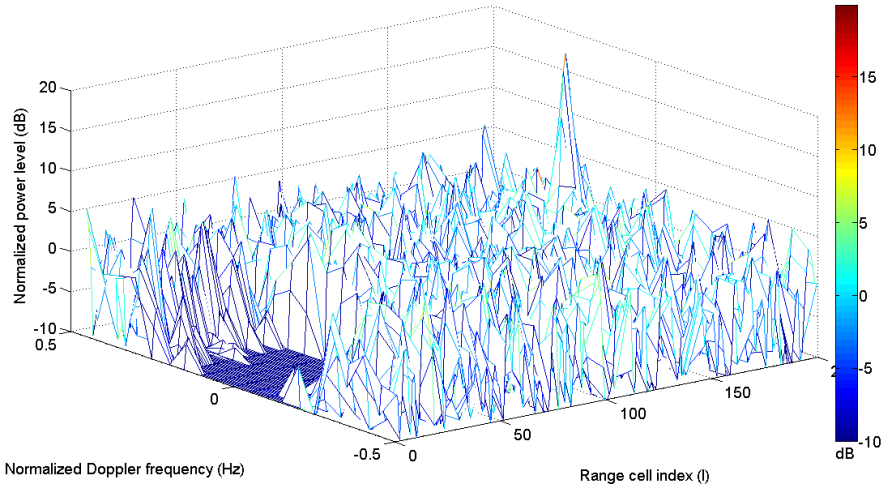

(a)

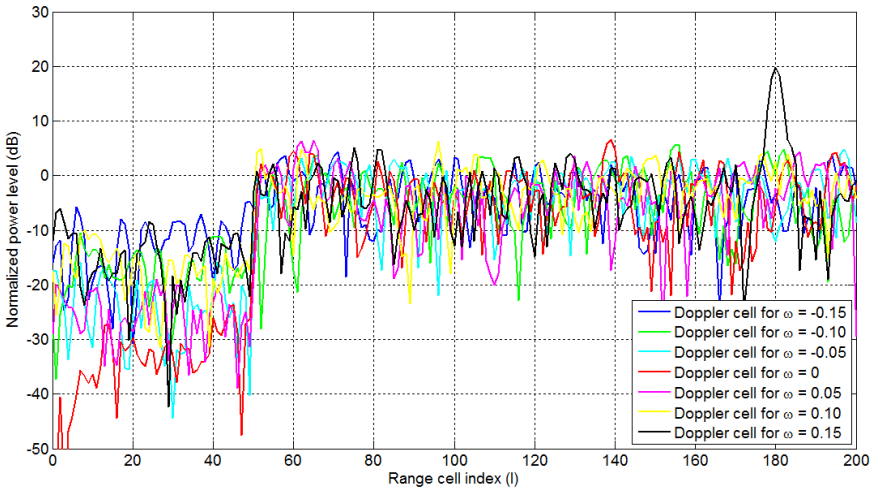

(b)

Fig. 3.4: (a) Ambiguity function plot and corresponding (b) Doppler cell cuts after direct path, clutter and Doppler-shifted clutter adaptive interference cancellation.

The LS-based adaptive interference cancellation algorithm ensure the minimization of the output power of the adaptive FIR filter which effectively cancels the strong interfering signals comprising the direct path, strong clutter and Doppler-shifted strong clutter in the received signal of each antenna element. This lowers the corresponding random range sidelobes of these interfering signals that manifest into further range cells by the same amount. However, the adaptive interference cancellation is not without any drawbacks. Firstly, the operation of the adaptive FIR filter is computational intensive since the weight vector requires the evaluation and inversion of the matrix $\mathbf{S}^H\mathbf{S}$ where its dimension can be extremely large. Secondly, short range targets that fall within the range and Doppler cells where the adaptive FIR filtering operates will be suppressed by the algorithm as well. Nevertheless, the approach effectively suppresses the direct path and strong clutter coupling components (Doppler-shifted clutter included) present in the received signal which lower their corresponding random range sidelobes couplings into further detection range cells of interest.

3.3 Space-time adaptive processing

The need for joint space and time processing in MTI for the airborne passive radar arises from the inherent two-dimensional nature of clutter [55] where the motion-induced spread of the clutter Doppler spectrum may mask the weak and slow moving targets. The motivation is to suppress this clutter and the residual interferences (random range sidelobes) effectively. STAP is able to achieve this by combining spatial and temporal samples (in slow-time) from the passive CIT datacube to enhance target signals and suppress the interference. The output signal of the STAP is given to a detector to determine the presence or absence of a target at a specific range cell. This space-time processor is essentially a linear filter that combines all the data from the range cell of interest to produce a scalar output where the process can be represented by an MN-dimensional weight vector. Thus, the output z can be defined as

$$z = \mathbf{w}^H \boldsymbol{\chi} \tag{3.13}$$

where $\mathbf{w}$ is the weight vector and Section 2.5 provides the space-time snapshot model $\boldsymbol{\chi}$ for the airborne passive radar. Ideally, the space-time processor provides coherent gain on target while forming spatial and Doppler response nulls to suppress clutter and random range sidelobes couplings. As the interference scenario is not known in advance, the weight vector must be determined in a data-adaptive way from the received signals. A single weight vector is optimized for a specific angle and Doppler and multiple weight vectors that form a filter bank are computed to cover all potential target angles and Doppler frequencies of interest.

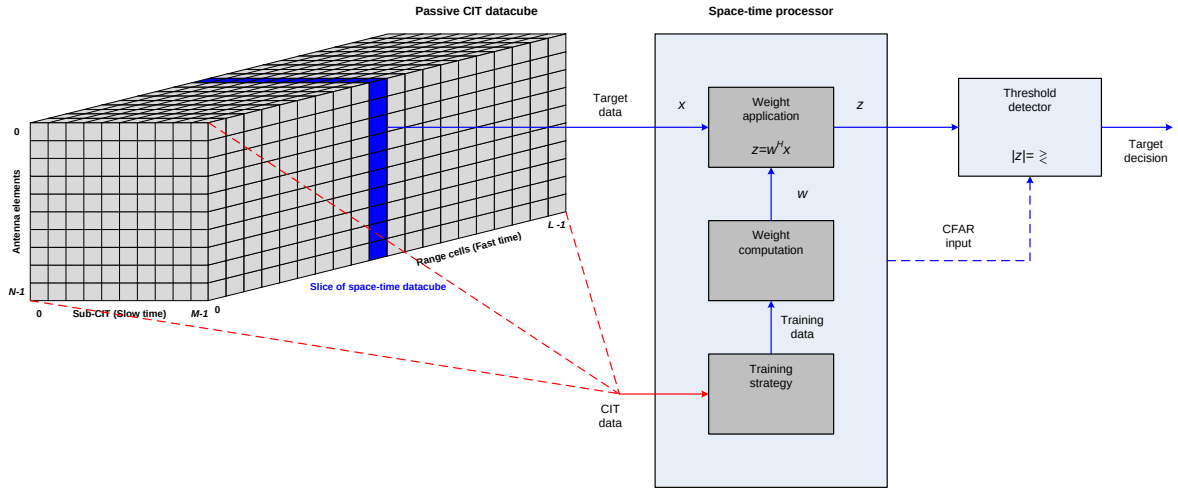

Fig. 3.5: General structure of a space-time adaptive processor with target detector [49].

The general structure of the space-time processor architecture is given in Fig. 3.5. In summary, first, the training strategy is applied where the training (secondary) data from range cells surrounding the range of interest is used to obtain the best estimate the interference. Following that, the adaptive weight vector (based on the secondary data) is computed which is solving a linear system of equations. Finally, the process of weight application refers to the computing of the scalar output or test statistic. This output scalar is compared to a threshold to determine target presence at each spatial-Doppler cell. The space-time processor that computes and applies a separate adaptive weight (size MN) to every element and every sub-CIT is said to be fully adaptive. Fully adaptive space-time processing for airborne radar was first proposed by Brennan [56] and is a natural extension of adaptive antenna processing [69, 70] to a two-dimensional space-time problem. From Equation (2.55) and (2.81), the snapshot at the detection range cell of interest where a target is present is given by

$$\boldsymbol{\chi} = \alpha_t \mathbf{v}_t + \boldsymbol{\chi}_u. \tag{3.14}$$

It is well known that the optimum space-time filter is given within a scale factor [71] by

$$\mathbf{w} = \mathbf{R}_u^{-1}\mathbf{v}_t \tag{3.15}$$

where $\mathbf{R}_u = E[\boldsymbol{\chi}_u \boldsymbol{\chi}_u^H]$ is the interference-plus-noise covariance matrix. The weight vector is optimum given that it maximizes SINR, maximizes probability of detection for a given false alarm probability and with the proper choice of scale factor minimizes output power subject to a unity gain constraint in the target direction [49]. Due to the high spatial and Doppler sidelobes of the optimum processor, it may be desirable to consider a suboptimum weight vector of the fully adaptive STAP given by

$$\mathbf{w} = \mathbf{R}_u^{-1}\mathbf{g}_t \tag{3.16}$$

where $\mathbf{g}_t$ is formed by tapering the target steering vector. Thus, the vector

$$\mathbf{g}_t = \mathbf{t} \odot \mathbf{v}_t \tag{3.17}$$

will produce a low-sidelobe adapted pattern where

$$\mathbf{t} = \mathbf{t}_b \otimes \mathbf{t}_a. \tag{3.18}$$

In Equation (3.18), $\mathbf{t}_a$ is an $N \times 1$ vector containing the desired low-sidelobe spatial response and $\mathbf{t}_b$ is an $M \times 1$ vector of the desired low-sidelobe Doppler response.

The weight vector as in Equation (3.15) assumed knowledge of the covariance matrix $\mathbf{R}_u$. In practice, $\mathbf{R}_u$ must be estimated from the finite data available where SMI algorithms [72] are considered using K_e snapshots to form the SCM estimation of $\mathbf{R}_u$ as

$$\widehat{\mathbf{R}}_u = \frac{1}{K_e}\sum_{l=1}^{K_e} \boldsymbol{\chi}_l \boldsymbol{\chi}_l^H. \tag{3.19}$$

The secondary snapshots $\boldsymbol{\chi}_l$ cover a range interval surrounding but not including the range cell of interest as well as guard cells on either side. Correspondingly, the SMI weight vector is thus

$$\mathbf{w} = \widehat{\mathbf{R}}_u^{-1}\mathbf{g}_t. \tag{3.20}$$

Given the covariance matrix estimation, the SMI weight vector is suboptimum and an additional performance loss will be incurred. This loss depends on the number of training data and it has been shown that if the data used in the estimation are IID (secondary data has same probability distribution and are mutually independent) and the number of data is twofold the dimension of $\boldsymbol{\chi}_u$, i.e. $K_e \geq 2MN$, the resulted SINR loss will be within 3dB [73] of the known covariance result.

3.3.1 Space-time adaptive processing performance metrics

There are various standard metrics [49, 55] employed to assess the performance of the STAP algorithms. The first is the adapted pattern (spatial-Doppler response) which is essentially the two-dimensional Fourier transform of the weight vector defined by

$$P_{\mathbf{w}}(\vartheta, \varpi) = |\mathbf{w}^H \mathbf{v}(\vartheta, \varpi)|^2. \tag{3.21}$$

Ideally, the adapted pattern has nulls in the directions and Doppler frequencies of interference sources while gain is maximized at the spatial and Doppler frequency of the presumed target. Output SINR is a common metrics for STAP performance. It is the ratio of the desired target power over the undesired interference-plus-noise power given by

$$\text{SINR} = \frac{P_n \xi_t |\mathbf{w}^H \mathbf{v}_t|^2}{\mathbf{w}^H \mathbf{R}_u \mathbf{w}}. \tag{3.22}$$

Substitution of the optimum weight vector into Equation (3.22) leads to the optimum SINR

$$\mathrm{SINR}_o = P_n \xi_t \mathbf{v}_t^H \mathbf{R}_u^{-1} \mathbf{v}_t. \tag{3.23}$$

Similarly, tapered fully adaptive produces a suboptimum SINR given by

$$\mathrm{SINR}_c = \frac{P_n \xi_t |\mathbf{g}_t^H \mathbf{R}_u^{-1} \mathbf{v}_t|^2}{\mathbf{g}_t^H \mathbf{R}_u^{-1} \mathbf{g}_t}. \tag{3.24}$$

One of the most important metric is the SINR loss which is the output SINR referenced to the optimum output SNR, denoted SNR_o, defined by

$$\mathrm{L}_{\mathrm{SINR}} = \frac{\mathrm{SINR}}{\mathrm{SNR}_o} = \frac{\mathrm{SINR}}{MN\xi_t}. \tag{3.25}$$

Thus, $\mathrm{L}_{\mathrm{SINR}}$ represents a comparison between the optimum matched filter with noise only. A useful figure of merit can be used to describe the velocity coverage provided by a STAP algorithm. The MDV is defined as the velocity closest to that of the mainlobe clutter at which acceptable SINR loss is achieved. Setting $f_L(x)$ and $f_U(x)$ to be the Doppler frequencies below and above the mainlobe clutter Doppler at which the acceptable SINR loss is achieved define the MDV as

$$f_{min}(x) = \frac{1}{2}\big(f_U(x) - f_L(x)\big) \tag{3.26}$$

which is equal to one-half of the width of the mainlobe clutter notch. The MDV is then

$$\mathrm{MDV}(x) = \frac{\lambda}{2} f_{min}. \tag{3.27}$$

A target whose velocity differs from the mainlobe clutter velocity by less than the MDV will fall into the clutter notch and cannot be detected within acceptable SINR loss threshold.

3.4 Reduced-dimension space-time adaptive processing

While STAP is optimal (subject to the assumed statistical distributions of secondary data), its implementation over the airborne passive radar faces several critical issues [74]. Firstly, it requires a significant amount of secondary data to support where the number of $K_e \geq 2MN$ IID secondary data is required to confine the SINR loss to within 3 dB. For the airborne passive radar, the interference scenario is typically unknown a priori and must be estimated from the secondary data within the passive CIT datacube. The adaptive weight size MN is likely to range from several hundreds to several thousands, depending on the antenna array length and the CIT. As this dimension of the adaptive weight vector becomes larger, so does the amount of data required for a good estimate of the interference environment. On the other hand, due to the power budget of the non-cooperative transmitter and the narrowband passive signal bandwidth, the number of range cells collected may be limited. Adding to the practical scenario that clutter is often heterogeneous and non-stationary, this limits the amount of secondary data which can be assumed IID and thus will not be a good representative of the interference at the target range cell. Short of sufficient IID data support leads to a degradation of the performance of STAP. STAP requires the inverse of the covariance matrix for construction of the optimal weights where the number of operational counts for matrix inversion is in an order of the cube of the dimension of the matrix. The sheer computational load required for fully adaptive STAP, in the time necessary for real-time operations, is simply beyond the capabilities of current digital processor technology. All these factors make fully adaptive STAP impractical. By reducing the adaptive weights dimensionality, the performance and statistical convergence with a limited amount of data can be dramatically improved and also the computational load eased. As a result, reduced

dimensionality sub-optimal approaches, known as reduced-dimension STAP algorithms, have been proposed in which spatial and temporal processing operations are cascaded. Reduced-dimension STAP methods apply data independent transformations to pre-filter the data and reduce the number of adaptive DOFs. Most of the reduced-dimension algorithms can be classified into four main categories by the type of non-adaptive transformation applied by the algorithms [49, 75]. Taxonomy of reduced-dimension STAP is shown in Fig. 3.6. The generic architecture of the reduced-dimension STAP is to the transform the original $MN \times 1$ space-time snapshot into a new and smaller $D \times 1$ vector $\tilde{\boldsymbol{\chi}}$ by means of a $MN \times D$ transformation matrix $\mathbf{T}$ as

$$\tilde{\boldsymbol{\chi}} = \mathbf{T}^H \boldsymbol{\chi}. \tag{3.28}$$

From Equation (3.14), the transformed data is decomposed as

$$\tilde{\boldsymbol{\chi}} = \alpha_t \tilde{\mathbf{v}}_t + \tilde{\boldsymbol{\chi}}_u \tag{3.29}$$

where $\tilde{\mathbf{v}}_t = \mathbf{T}^H \mathbf{v}_t$ is the transformed target steering vector and $\tilde{\boldsymbol{\chi}}_u = \mathbf{T}^H \boldsymbol{\chi}_u$ is the transformed interference-plus-noise space-time snapshot. Thus, the corresponding reduced-dimension $D \times 1$ weight vector is

$$\tilde{\mathbf{w}} = \tilde{\mathbf{R}}_u^{-1} \tilde{\mathbf{g}}_t \tag{3.30}$$

where

$$\tilde{\mathbf{R}}_u = E[\tilde{\boldsymbol{\chi}}_u \tilde{\boldsymbol{\chi}}_u^H] = \mathbf{T}^H \mathbf{R}_u \mathbf{T} \tag{3.31}$$

is the $D \times D$ covariance matrix of the transformed data and $\tilde{\mathbf{g}}_t$ is a $D \times 1$ desired response. Given a desired response $\mathbf{g}_t$ for a fully adaptive processor, the partially adaptive processor utilizes the desired response

$$\tilde{\mathbf{g}}_t = \mathbf{T}^H \mathbf{g}_t. \tag{3.32}$$

Applying the reduced-dimension weights vector yields the final output

$$z = \tilde{\mathbf{w}}^H \tilde{\boldsymbol{\chi}} = (\mathbf{T}\tilde{\mathbf{w}})^H \boldsymbol{\chi}. \tag{3.33}$$

As seen in Fig. 3.6, the reduced-dimension STAP algorithms are classified by the domain in which the adaptive weighting occurs. The ‘whitened then filter’ approach where STAP is performed before Doppler filtering is known as the pre-Doppler processing where STAP after Doppler processing refers to the ‘filter then adapt’ process of post-Doppler processing. Element-space STAP adaptively combine signals from all the elements where dimensionality reduction is achieved through adaptive processing only a few sub-CITs at a time or by adaptively combining a small number of filtered outputs on each element. Spatial filtering may also be performed on the element outputs of each sub-CIT prior to adaptation and algorithms that perform beamforming prior to adaptive processing are referred to as beam-space STAP algorithms. The remaining of this Section will analyze each of these four classes to be used for the airborne passive radar which closely parallel the work in [49]. Conditions for which the reduced-dimension STAP, with known covariance, provides performance equal to fully adaptive STAP are derived. In general, reduced-dimension processing is unavoidably associated with some SINR loss (as will be apparent later). However, it may actually provide better performance with limited secondary data support owing to a much less estimation loss.

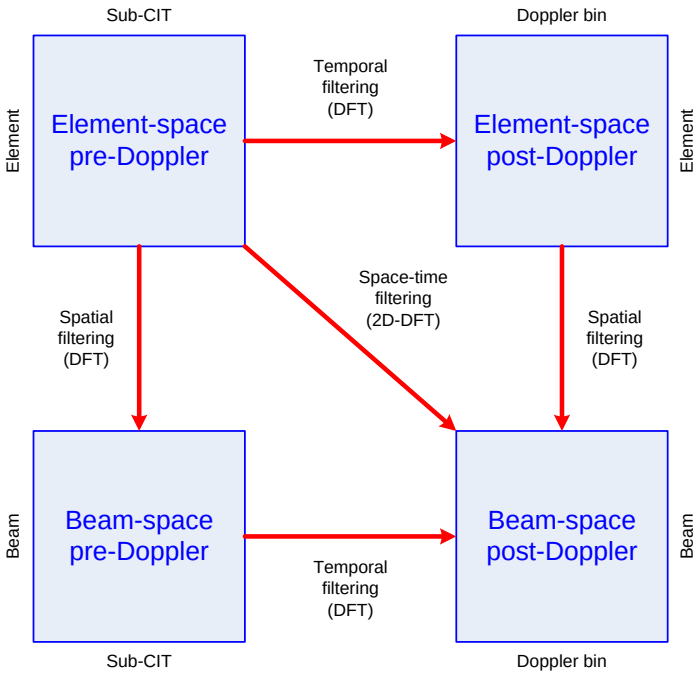

Fig 3.6: Taxonomy of reduced-dimension STAP algorithms.

3.4.1 Element-space pre-Doppler space-time adaptive processing

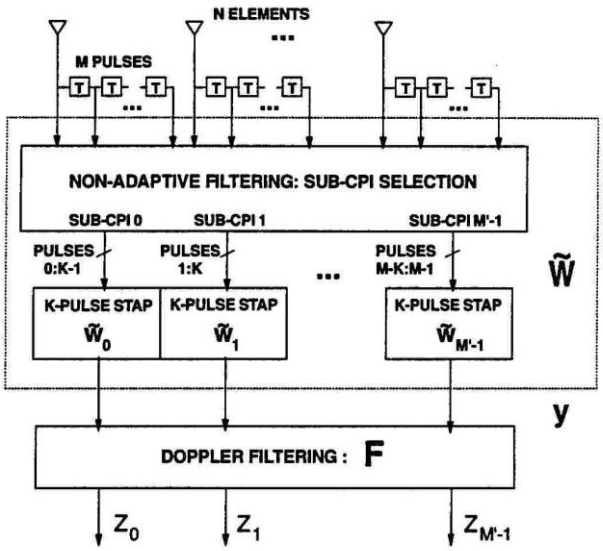

Fig. 3.7: Block diagram for element-space pre-Doppler full CIT STAP [49].

Element-space pre-Doppler STAP is a reduced dimensionality processing scheme which maintains full spatial adaptivity but adapts over only a few sub-CITs at a time rather than over all sub-CITs within the CIT [49]. Adaptive processing is then followed by a fixed (non-adaptive) Doppler filter bank that provides coherent integration over the full CIT and the means for velocity estimation. Fig. 3.7 shows the block diagram for element-space pre-Doppler full CIT processing. In the processing, the set of M sub-CITs (within the CIT) is divided into overlapping subset-CIT of K sub-CITs. Thus, there are $M' = M - K + 1$ subset-CITs with the 0^{th} subset-CIT consisting of sub-CIT $0, \cdots, K-1$ and the m'^{th} subset-CIT consisting of sub-CITs $m', \cdots, m' + K - 1$ where $m' = 0, \ldots, M' - 1$ is the subset-CIT index. Adaptive processing is then performed separately for each set of subset-CIT over all N

elements. A $KN \times 1$ space-time weight vector is computed and applied to each subset-CIT. Finally, the M' output sub-CITs are subsequently passed through a standard Doppler filter bank to obtain the final output.

Mathematically, the m'^{th} subset-CIT consisting of pulses $m', \cdots, m' + K - 1$ may be written as

$$\tilde{\boldsymbol{\chi}}_{m'} = (\mathbf{J}_{m'} \otimes \mathbf{I}_N)^H \boldsymbol{\chi} \tag{3.34}$$

where

$$\mathbf{J}_{m'} = \begin{bmatrix} \mathbf{0}_{m' \times K} \\ \mathbf{I}_K \\ \mathbf{0}_{(M-K-m') \times K} \end{bmatrix} \tag{3.35}$$

is an $M \times K$ selection matrix that chooses the m'^{th} subset-CIT from the CIT. The m'^{th} subset-CIT weight vector is given by

$$\widetilde{\mathbf{w}}_{m'} = \widetilde{\mathbf{R}}_{um'}^{-1} \tilde{\mathbf{g}}_t \tag{3.36}$$

where $\widetilde{\mathbf{R}}_{um'}^{-1}$ is the $KN \times KN$ interference covariance matrix of the m'^{th} subset-CIT and $\mathbf{g}_t$ is the $KN \times 1$ desired response which does not change from one subset-CIT to the next. It is clear that the interference covariance matrix size has been reduced by a factor of M/K relative to fully adaptive STAP. The subset-CIT weight vectors can be decomposed into their spatial beamformer components for each sub-CIT where

$$\widetilde{\mathbf{w}}_{m'} = \left[\widetilde{w}_{m',0}; \widetilde{w}_{m',1}; \cdots; \widetilde{w}_{m',K-1}\right] \tag{3.37}$$

so that $\widetilde{\mathbf{w}}_{m',k}$ represents the spatial weight vector for the k^{th} pulse of m'^{th} subset-CIT. The output signal from the m'^{th} subset-CIT is then

$$y_{m'} = \widetilde{\mathbf{w}}_{m'}^H \tilde{\boldsymbol{\chi}}_{m'} = \sum_{k=0}^{K-1} \widetilde{\mathbf{w}}_{m',k}^H \mathbf{x}_{m',k}, m' = 0,1, \cdots, M' - 1. \tag{3.38}$$

The outputs from all subset-CITs are then assembled into an $M' \times 1$ vector as

$$\mathbf{y} = [y_0; y_1; \cdots; y_{M'-1}] = \widetilde{\mathbf{W}}^H \boldsymbol{\chi} \tag{3.39}$$

where $\widetilde{\mathbf{W}}$ is an $MN \times M'$ matrix containing the weights from all subset-CITs and is given by

$$\widetilde{\mathbf{W}} = \begin{bmatrix} \widetilde{\mathbf{w}}_{0,0} & \mathbf{0} & \cdots & \mathbf{0} \\ \widetilde{\mathbf{w}}_{0,1} & \vdots & \cdots & \mathbf{0} \\ \vdots & \widetilde{\mathbf{w}}_{1,0} & \ddots & \vdots \\ \widetilde{\mathbf{w}}_{0,K-1} & \widetilde{\mathbf{w}}_{1,1} & \ddots & \mathbf{0} \\ 0 & \vdots & \ddots & \widetilde{\mathbf{w}}_{M-K,0} \\ \vdots & \widetilde{\mathbf{w}}_{1,K-1} & \ddots & \widetilde{\mathbf{w}}_{M-K,1} \\ \mathbf{0} & \vdots & \cdots & \vdots \\ \mathbf{0} & \mathbf{0} & \cdots & \widetilde{\mathbf{w}}_{M-K,K-1} \end{bmatrix}. \tag{3.40}$$

The subset-CIT output signals are processed by a length M' Doppler filter bank. Let $\mathbf{U} = [\mathbf{u}_0; \mathbf{u}_1; \cdots; \mathbf{u}_{M'-1}]$ be an $M' \times M'$ DFT matrix. Thus, The Doppler filter bank is represented by the matrix

$$\mathbf{F} = [\mathbf{f}_0; \mathbf{f}_1; \cdots; \mathbf{f}_{M'-1}] = \text{diag}(\mathbf{t}_d)\mathbf{U}^* \tag{3.41}$$

where $\mathbf{t}_d$ is a $M' \times 1$ taper for the Doppler filters and the m^{th} Doppler filter is given by $\mathbf{f}_m = \mathbf{t}_d \odot \mathbf{u}_m^*$. The normalized Doppler frequency spacing between two adjacent filters is $1/M'$ and the center frequencies of Doppler filter bank are $[0,1/M', 2/M', \cdots, (M'-1)/M']$. Then, the Doppler filter bank output is

$$\mathbf{z} = [z_0; z; \cdots; z_{M'-1}] = \mathbf{F}^H \mathbf{y} \tag{3.42}$$

where the signal $z_m = \mathbf{f}_m^H \mathbf{y}$ is the final output for the m^{th} Doppler bin. The output signal can also be expressed in terms of the full dimension snapshot as

$$z_m = \mathbf{f}_m^H \widetilde{\mathbf{W}}^H \boldsymbol{\chi} = \mathbf{w}_m^H \boldsymbol{\chi} \tag{3.43}$$

where

$$\mathbf{w}_m = \widetilde{\mathbf{W}} \mathbf{f}_m \tag{3.44}$$

is the m^{th} Doppler bin composite weight vector that represents all of the processing steps (adaptive and fixed) involved in producing the final output. The algorithm performance can be computed in the usual way as defined in Section 3.3.1.

The element-space pre-Doppler STAP provides weight updates every sub-CIT. This is desirable where the environment changes from sub-CIT-to-sub-CIT. The clutter component of the subset-CIT covariance matrix has rank

$$\text{rank}\left(\widetilde{\mathbf{R}}_c\right) = [N + (K-1)\beta]. \tag{3.45}$$

Although the interference within the subset-CIT is still less than full rank, its rank becomes a larger fraction of the snapshot dimension as K gets smaller. Full spatial adaptivity for the element-space pre-Doppler STAP provides sufficient degrees of freedom to cancel the residual random range sidelobes of the direct path and of the strong clutter and clutter simultaneously.

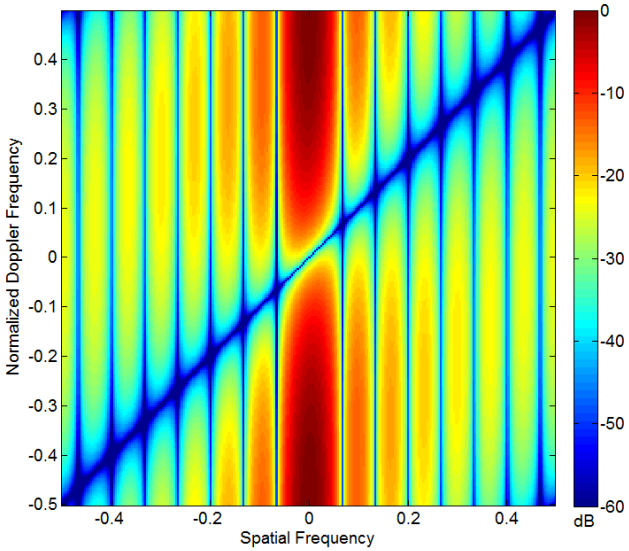

Fig.3.8: Element-space pre-Doppler STAP subset-CIT adapted pattern, $K = 2$.

To illustrate the performance of element-space pre-Doppler STAP, consider the clutter-only scenario as in Section 2.6 where $N = 16$ and $M = 20$ for a side-looking ULA with a CNR of 30 dB and $\beta = 1$. This example will be used in all subsequent simulations for algorithm analyses in the remaining of this Chapter. For simplicity, the y-axis is taken to be the true clutter normalized Doppler frequency. No spatial and Doppler tapers are assumed. Let $K = 2$ so that for each subset-CIT, a $2N = 32$-dimensional weight vector is computed. Fig. 3.8 shows the adapted pattern from a single subset-CIT where it is assumed that the target spatial frequency is at 0. As anticipated, the pattern exhibits a deep null along the clutter ridge. The composite adapted pattern for Doppler bin 6 ($\varpi = 0.316$) is plotted in Fig. 3.9 where the response has its maximum focused at both the spatial frequency and normalized Doppler frequency of a potential target. As expected, deep null is formed along the clutter ridge. The SINR loss of element-space pre-Doppler STAP for both $K = 2$ and

$K = 3$ cases are shown in Fig. 3.10 where the fully adaptive STAP is also included for reference. The performance of element-space pre-Doppler STAP is quite close to that of the optimum fully adaptive algorithm but the additional straddle loss is obvious. It is because when implementing the Doppler filtering over the full CIT, a fixed Doppler filter bank is applied to cover the whole Doppler space and for targets whose Doppler frequency is not at the center frequency of one of the Doppler filters, an additional straddling loss will occurred. As seen, $K = 3$ pre-Doppler exhibits a wider notch at the mainlobe clutter Doppler because of the wider notch implied by the 3-sub-CIT binomial steering vector.

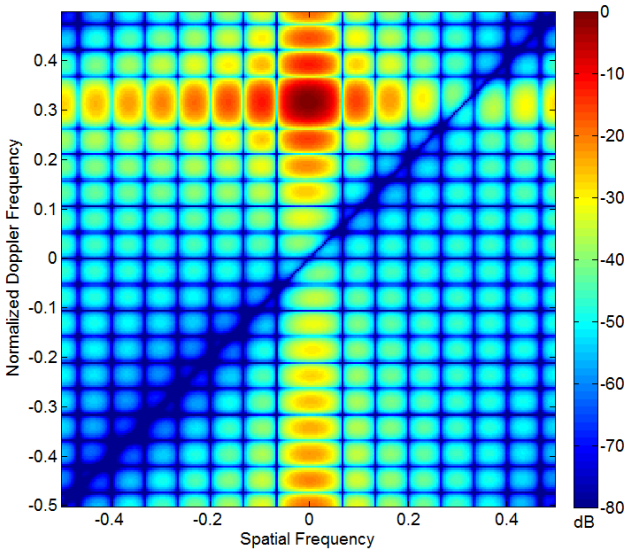

Fig.3.9: Composite adapted pattern for element-space pre-Doppler STAP, Doppler bin 6.

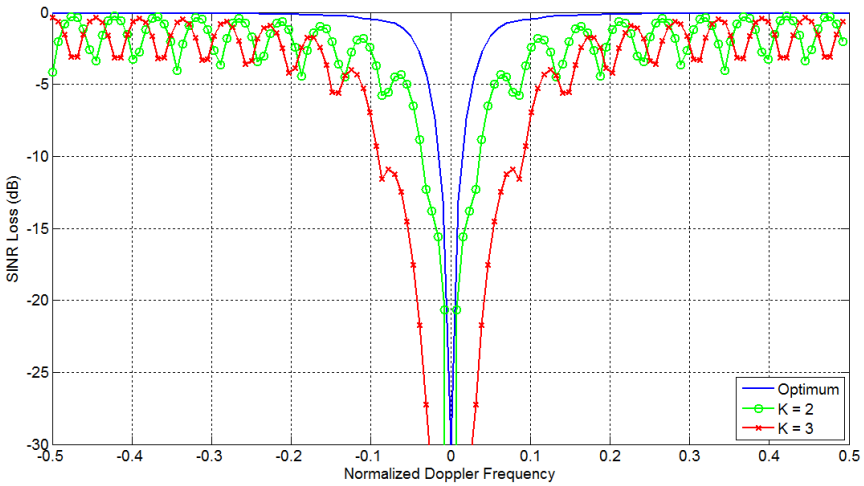

Fig. 3.10: SINR loss for element-space pre-Doppler STAP.

3.4.2 Element-space post-Doppler space-time adaptive processing

Whereas element-space pre-Doppler STAP adaptively processing a few sub-CITs at a time, element-space post-Doppler reduce the dimensionality of the problem by implementing Doppler filtering of the data from each element without adaptation prior to adaptive weight processing. A Doppler filter, with its potentially for very low Doppler sidelobes, can localize

the clutter in angle and thereby reduce the required number of adaptive DOF. The simplest element-space post-Doppler algorithm (post-Doppler adaptive beamforming or factored post-Doppler STAP) uses a single filter bank per element and the spatial and temporal processing are performed as separate and distinct operations [49]. It is assumed that Doppler filtering suppresses mainlobe clutter nonadaptively and localizes the competing sidelobe clutter in angle. Within each Doppler filter, adaptive processing places spatial nulls both at the angles of interfering signals and at the angles where the sidelobe clutter Doppler falls within the Doppler passband. If performance is acceptable, this is an excellent approach because a significant reduction in dimensionality has been achieved where it only requires solving M separate N-dimensional adaptive problems. However, the factored post-Doppler STAP can perform rather poorly due to the small aperture size and Doppler resolution of the airborne passive radar. The algorithm must rely on Doppler filtering to reject clutter within the mainbeam and constrain sidelobe clutter to a small spatial region. A short CIT results in decreased Doppler resolution and this is compounded by the need for reduced Doppler sidelobes [46]. Thus, factored post-Doppler will not be considered in this Section.

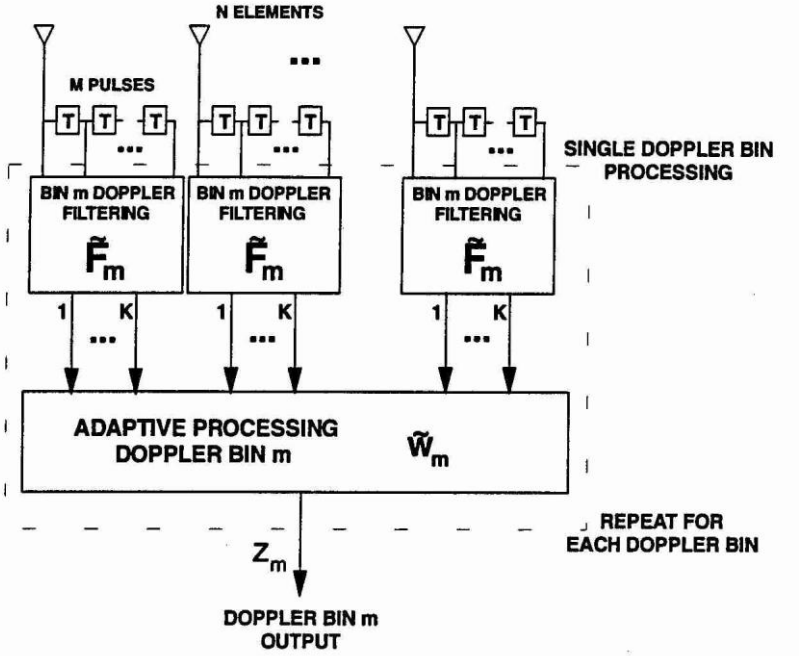

Fig. 3.11: Block diagram for multiwindow post-Doppler STAP [49].

The multi-window post-Doppler STAP [76] alleviates this problem by considering the adaptive combination of multiple Doppler filters from each element. Each filter may be thought of as a different windowing of the M sub-CITs of data. A block diagram of the processing for a single target Doppler bin is depicted in Fig. 3.11. Given a single Doppler bin, each element has an identical bank of K filters and for $K = 1$, this case is simply the factored post-Doppler STAP. K is typically small and therefore the adaptive problem dimension is reduced by a factor of M/K. The filtered KN signals are adaptively weighted to produce the output for this Doppler bin where the process is repeated for each bin. As in Fig. 3.11, the mathematical analysis of multiwindow post-Doppler STAP first define $\tilde{\mathbf{F}}_m$ as an $M \times K$ matrix with K columns representing sets of M filters applied to each element. The m^{th} bin space-time snapshot (dimension $KN \times 1$) is given by

$$\tilde{\boldsymbol{\chi}}_m = \left(\tilde{\mathbf{F}}_m \otimes \mathbf{I}_N\right)^H \boldsymbol{\chi} \tag{3.46}$$

And the adaptive weight vector for the m^{th} bin is given by

$$\tilde{\mathbf{w}}_m = \tilde{\mathbf{R}}_{um}^{-1}\tilde{\mathbf{g}}_t \tag{3.47}$$

where

$$\tilde{\mathbf{R}}_{um} = E[\tilde{\boldsymbol{\chi}}_{um}\tilde{\boldsymbol{\chi}}_{um}^H] \tag{3.48}$$

is the $KN \times KN$ interference-plus-noise covariance matrix. The desired response $\tilde{\mathbf{g}}_t$ is chosen according to

$$\tilde{\mathbf{g}}_t = \left(\tilde{\mathbf{F}}_m \otimes \mathbf{I}_N\right)^H \mathbf{g}_t. \tag{3.49}$$

Finally, the output of the m^{th} Doppler bin is

$$z_m = \tilde{\mathbf{w}}_m^H \tilde{\boldsymbol{\chi}} = \mathbf{w}_m^H \boldsymbol{\chi} \tag{3.50}$$

where the composite weight vector for the m^{th} Doppler bin is

$$\mathbf{w}_m = \left(\tilde{\mathbf{F}}_m \otimes \mathbf{I}_N\right)\tilde{\mathbf{w}}_m. \tag{3.51}$$

Once the adaptive weights are computed, the algorithm performance can be computed in the usual way.

Two criteria must be met in designing the Doppler filter $\tilde{\mathbf{F}}_m$ [49]. First, it must pass the band of Doppler frequencies of the targets centered at ϖ_m. Secondly, $\tilde{\mathbf{F}}_m$ is chosen to minimize the number of DOF required for clutter cancellation. The clutter covariance has a rank that is a function of $\tilde{\mathbf{F}}_m$ and thus $\tilde{\mathbf{F}}_m$ will be designed such that the clutter rank after filtering is minimum. If the assumptions of Brennan's rule are met (assumption of no velocity misalignment and zero ICM) and a $K \times K$ nonsingular matrix Q and a length $M' = M - K + 1$ vector $\mathbf{f} = [f_0; f_1; \cdots; f_{M'-1}]$ exist such that

$$\tilde{\mathbf{F}}_m\mathbf{Q} = \begin{bmatrix} f_0 & & \mathbf{0} \\ f_1 & \ddots & \vdots \\ \vdots & & f_0 \\ f_{M'-1} & & f_1 \\ \vdots & \ddots & \vdots \\ \mathbf{0} & & f_{M'-1} \end{bmatrix} = \text{Toeplitz}\left(\left[\mathbf{f}; \mathbf{0}_{(K-1)\times 1}\right], \left[\mathbf{f}_0; \mathbf{0}_{1\times(K-1)}\right]\right). \tag{3.52}$$

Then rank of the clutter component is minimum and equal to

$$\text{rank}\left(\tilde{\mathbf{R}}_{cm}\right) = [N + (K-1)\beta]. \tag{3.53}$$

This theorem will be referred to as the post-Doppler version of Brennan's rule.

Two implementations of the Doppler filter matrix $\tilde{\mathbf{F}}_m$ have been considered. The first case corresponds to $\mathbf{Q} = \mathbf{I}_k$ where each element has a bank of M'-sub-CIT Doppler filters that produces K output sub-CITs for each Doppler bin. For each Doppler bin, an adaptive processor combines the K sub-CITs from each element to produce the output signal for that bin [77]. This viewpoint of staggered subset-CITs leads to the name sub-CIT-staggered post-Doppler. Sub-CIT-staggered post-Doppler satisfies conditions with either uniformly weighted or tapered Doppler filters. Suppose $\mathbf{U} = [\mathbf{u}_0; \mathbf{u}_1; \cdots; \mathbf{u}_{M-1}]$ is an $M' \times M$ matrix formed from the first M' rows of the $M \times M$ DFT matrix and let $\mathbf{t}_f$ being an $M' \times 1$ Doppler filter taper. The resulting Doppler filter bank for sub-CIT-staggered, where the normalized Doppler frequency spacing between two adjacent filters is $1/M$, is given by

$$\mathbf{F} = [\mathbf{f}_0; \mathbf{f}_1; \cdots; \mathbf{f}_{M-1}] = \text{diag}\left(\mathbf{t}_f\right)\mathbf{U}^* \tag{3.54}$$

where

$$\mathbf{f}_m = \mathbf{t}_f \odot \mathbf{u}_m \tag{3.55}$$

is the m^{th} Doppler filter impulse response. The Doppler filter matrix $\tilde{\mathbf{F}}_m$ for sub-CIT-staggered post-Doppler is then

$$\tilde{\mathbf{F}}_m = \text{Toeplitz}\left(\left[\mathbf{f}_m; \mathbf{0}_{(K-1)\times 1}\right], \left[\mathbf{f}_{m0}; \mathbf{0}_{1\times(K-1)}\right]\right). \quad (3.56)$$

The second case utilizes a single Doppler filter of length M for each element. The m^{th} Doppler bin output is formed by adaptively combining the spatial samples from a cluster of K adjacent Doppler bin centered at the m^{th} bin center frequency. This approach is called adjacent-bin post-Doppler and also termed as extended factored STAP [78]. In specifying the form of $\tilde{\mathbf{F}}_m$ for adjacent-bin post-Doppler STAP, let $\mathbf{U}$ be the $M \times M$ DFT matrix and let $\mathbf{t}_f$ be an $M \times 1$ Doppler filter taper. Thus, the Doppler filter bank is equal to

$$\mathbf{F} = \text{diag}(\mathbf{t}_f)\mathbf{U}^*. \quad (3.57)$$

When K is odd, i.e., $K = 2P + 1$, the m^{th} Doppler bin output adaptively combines signals from Doppler bins $m - P, \cdots, m + P$. Therefore

$$\tilde{\mathbf{F}}_m = [\mathbf{f}_{m-P}, \cdots, \mathbf{f}_m, \cdots, \mathbf{f}_{m+P}] \quad (3.58)$$

The adjacent filters are defined to wrap around the Doppler space edges. When K is even, the output bin frequencies are positioned between the filter center frequencies for symmetry about the output bin frequencies.

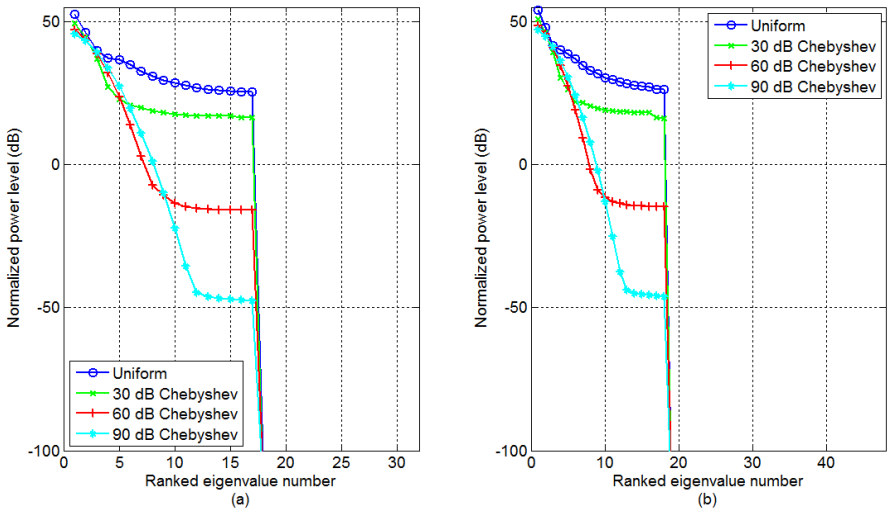

Fig. 3.12: Clutter eigenspectra of sub-CIT-staggered post-Doppler STAP for (a) $K = 2$ and (b) $K = 3$, Doppler bin 6.

Fig 3.12 depicts the clutter covariance eigenspectra (without noise component) for the same clutter-only scenario in the preceding Section (side-looking ULA where $N = 16$, $M = 20$, CNR = 30 dB and $\beta = 1$) for sub-CIT-staggered post-Doppler STAP with (a) $K = 2$ and (b) $K = 3$ respectively. The plots correspond to the clutter covariance eigenspectra for Doppler bin 6 where different Doppler filter tapers are used. The clutter rank of sub-CIT-staggered post-Doppler is 17 and 18 for $K = 2$ and $K = 3$ respectively as predicted. The shape of the eigenspectrum depends on the filter shape and the clutter power spectrum density in Doppler (angle). For both plots, in general, the level of the smaller eigenvalues falls as the Doppler sidelobe level is reduced. Fig 3.13 depicts the corresponding clutter covariance eigenspectra for adjacent-bin post-Doppler STAP with (a) $K = 2$ and (b) $K = 3$ respectively. It can be prominently seen that the clutter eigenspectra exhibit a sharp drop only when a uniform taper is used where the rank is also 17 and 18 for $K = 2$ and $K = 3$ respectively. With tapered Doppler filters, adjacent-bin post-Doppler no longer satisfies the Brennan's rule theorem and the clutter rank is much larger. Still, as the Doppler sidelobe level is reduced, the number of significant eigenvalues (with respect to thermal noise)

is also reduced. With $K = 2$, comparing Fig. 3.12(a) and 3.13(a), it can be expected that the sub-CIT-staggered post-Doppler will provide better performance for moderate Doppler tapers. With $K = 3$, the system DOF is enough to handle the clutter rank induced by the moderate Doppler taper in adjacent-bin post-Doppler approach as evident in Fig. 3.13(b).

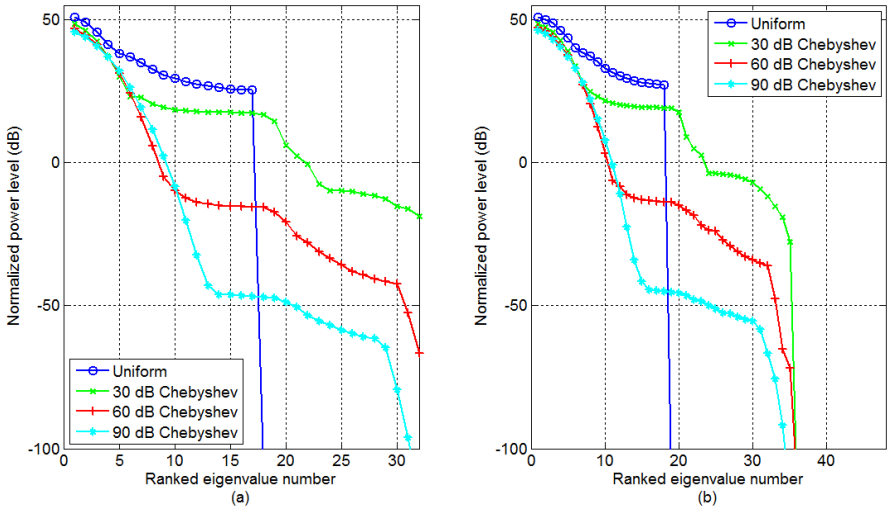

Fig. 3.13: Clutter eigenspectra of adjacent-bin post-Doppler STAP for (a) $K = 2$ and (b) $K = 3$, Doppler bin 6.

The adapted pattern for the sub-CIT-staggered post-Doppler and adjacent-bin post-Doppler for both having uniform taper and $K = 2$ are plotted in Figs. 3.14 and 3.15 respectively. The target steering vector is at 0 spatial frequency and normalized Doppler frequency of 0.3 (Doppler bin 6). As seen, both Figs have maximum response focused at the spatial frequency and normalized Doppler frequency of a potential target where the deep null is formed along the clutter ridge. For adjacent-bin post-Doppler (Fig. 3.15), the Doppler bin output frequency is midway between Doppler bin 6 and Doppler bin 7, i.e., normalized Doppler frequency of 0.325, as in Equation (3.58). This frequency mismatch can be avoided when K is odd. Next, the SINR loss performance for element-space post-Doppler STAP using different Doppler filters for the same clutter-only scenario in the preceding Section is depicted. Figs. 3.16 and 3.17 show the sub-CIT-staggered post-Doppler STAP for $K = 2$ and $K = 3$ respectively, while Figs. 3.18 and 3.19 show the adjacent-bin post-Doppler STAP for $K = 2$ and $K = 3$ respectively. It is shown that the performance of sub-CIT-staggered post-Doppler for $K = 2$ and $K = 3$ is quite close to the optimum case where only a few dBs of straddling loss is apparent. Generally, the sub-CIT-staggered post-Doppler outperforms adjacent-bin post-Doppler given the same number of DOF and Doppler sidelobes. For the adjacent-bin post-Doppler with $K = 2$, the SINR loss is also similar to the optimum performance when uniform taper is applied. However, with a 30 dB taper, the increased clutter rank manifests itself as a performance loss over the lower frequencies Doppler space and this result will be more severe for a stronger interference scenario (larger CNR). With heavier Doppler tapering, the SINR loss can be reduced and the difference between the two post-Doppler approaches is lessened. For adjacent-bin post-Doppler with $K = 3$, the increase in DOF can easily handle the increased clutter rank in adjacent-bin post-Doppler caused by moderate Doppler taper. In this case, the algorithm for the same Doppler taper has better SINR loss performance and tends to the optimum values.

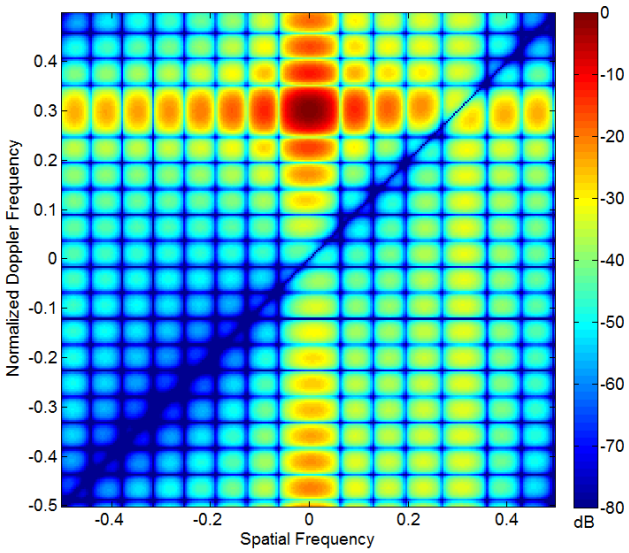

Fig. 3.14: Adapted pattern for sub-CIT-staggered post-Doppler STAP, Doppler bin 6 and $K = 2$.

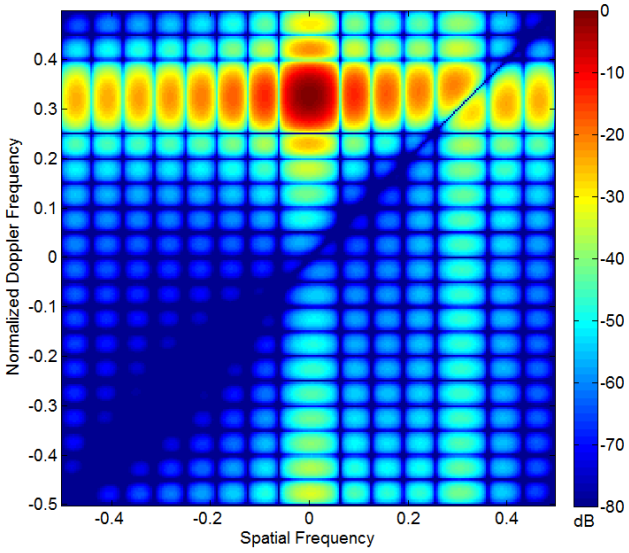

Fig. 3.15: Adapted pattern for adjacent-bin post-Doppler STAP, Doppler bin 6 and $K = 2$.

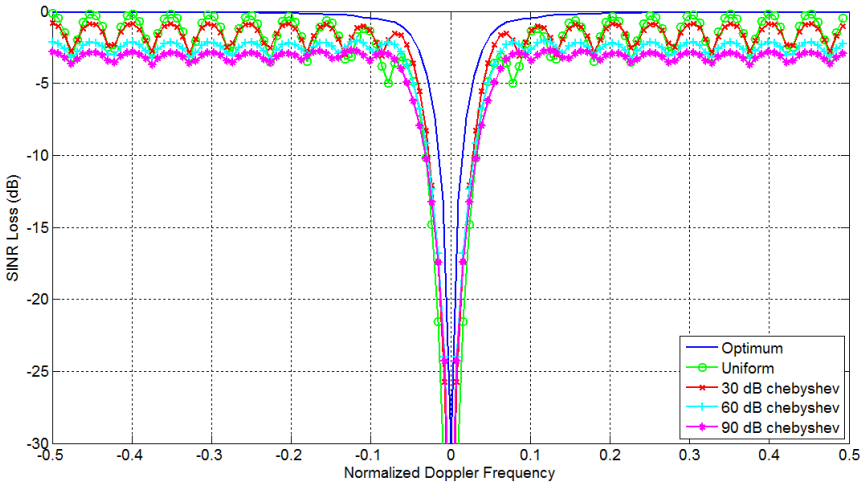

Fig. 3.16: Sub-CIT-staggered post-Doppler STAP, $K = 2$.

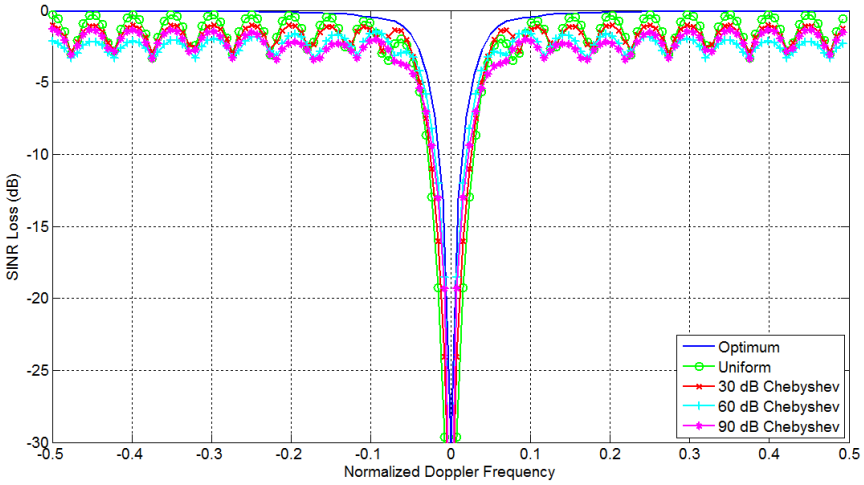

Fig. 3.17: Sub-CIT-staggered post-Doppler STAP, $K = 3$.

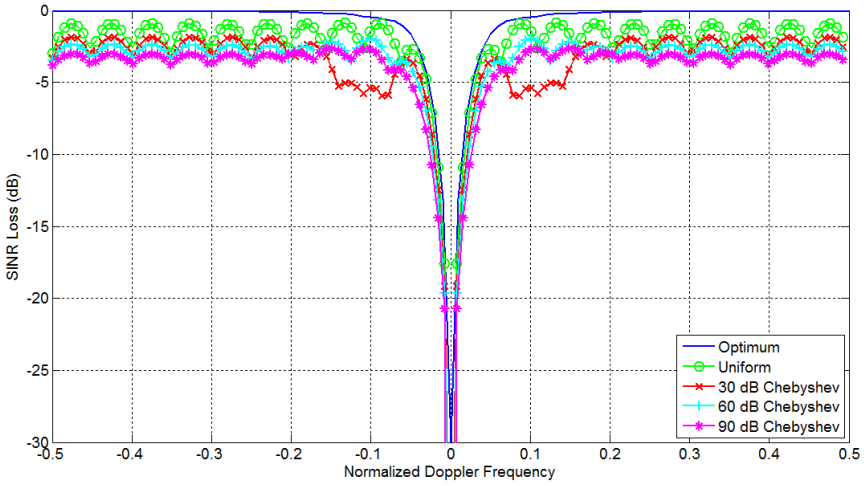

Fig. 3.18: Adjacent-bin post-Doppler, $K = 2$.

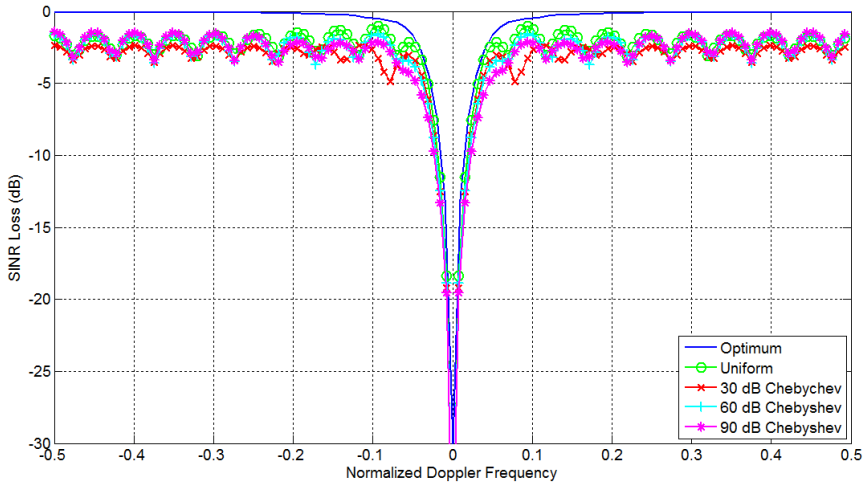

Fig. 3.19: Adjacent-bin post-Doppler, $K = 3$.

3.4.3 Beam-space pre-Doppler space-time adaptive processing

Element-space techniques become impractical for large ULA in which case beam-space approaches provide additional dimensionality reduction [49]. The block diagram of beam-space pre-Doppler STAP algorithm is illustrated in Fig. 3.20 where the signals from each sub-CIT are beamformed and then a subset-CIT of sub-CITs from a selected set of beams are used for adaptation. In this case, the problem dimensionality is reduced in two ways. First the data from the element-sub-CIT domain is transformed to the beam-sub-CIT domain with an $N \times K_s$ beamformer matrix $\tilde{\mathbf{G}}$ to produce a small number of K_s beam outputs. Adaptive processing then combine a small subset of K_t sub-CIT from the K_s beam outputs one at a time. Thus, the adaptive problem dimensionality is $K = K_s K_t$ and typically $K_s \ll N$ and $K_t \ll M$ so that a significant reduction in problem size is achieved. A separate adaptive problem is solved for each subset-CIT and the outputs from all subset-CITs are then coherently processed with an $M' = M - K_t + 1$-sub-CIT Doppler filter bank.

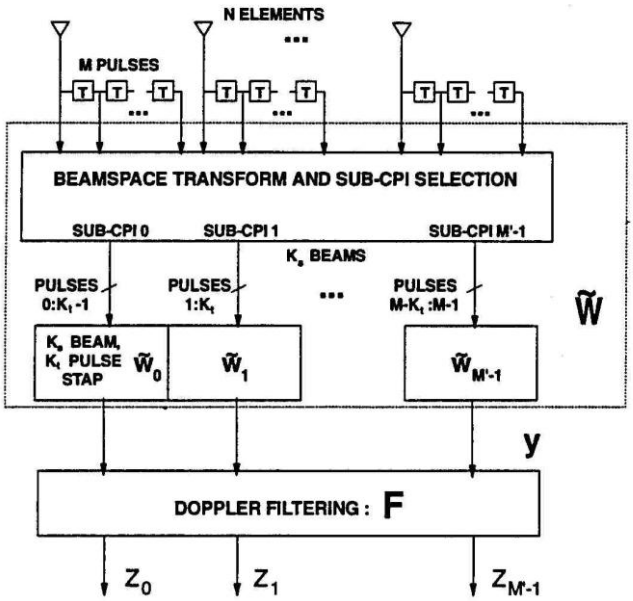

Fig. 3.20: Block diagram for beam-space pre-Doppler full CIT STAP [49].

The analysis proceeds in similar fashion to element-space pre-Doppler where first, let the m'^{th} subset-CIT snapshot consisting of sub-CITs $m', \ldots, m' + K_t - 1$ be

$$\tilde{\boldsymbol{\chi}}_{m'} = \left(\mathbf{J}_{m'} \otimes \tilde{\mathbf{G}}\right)^H \boldsymbol{\chi} \tag{3.59}$$

where $\mathbf{J}_{m'}$ is the $M \times K_t$ selection matrix that chooses the sub-CITs $m', \ldots, m' + K_t - 1$ from the CIT as in Equation (3.35). The m'^{th} subset-CIT weight vector is

$$\tilde{\mathbf{w}}_{m'} = \tilde{\mathbf{R}}_{um'}^{-1} \tilde{\mathbf{u}}_t \tag{3.60}$$

where $\tilde{\mathbf{R}}_{um'}$ is the $K_t K_s \times K_t K_s$ interference-plus-noise covariance matrix of the m'^{th} subset-CIT and $\tilde{\mathbf{u}}_t$ is a $K_t K_s \times 1$ desired response. The desired response for beam-space pre-Doppler is chosen such that

$$\tilde{\mathbf{u}}_t = \left(\mathbf{I}_{K_t} \otimes \tilde{\mathbf{G}}\right)^H \tilde{\mathbf{g}}_t = \left(\tilde{\mathbf{t}}_b \odot \tilde{\mathbf{b}}(\varpi_b)\right) \otimes \tilde{\mathbf{G}}^H (\mathbf{t}_a \odot \mathbf{a}_t) \tag{3.61}$$

where $\tilde{\mathbf{g}}_t$ is the desired subset-CIT response for element-space pre-Doppler, $\tilde{\mathbf{t}}_b$ is the $K_t \times 1$ binomal taper and $\mathbf{t}_a$ represent the $N \times 1$ spatial taper. Upon obtaining the weight vector $\tilde{\mathbf{w}}_{m'}$, it can be applied to produce the subset-CIT output

$$y_{m'} = \tilde{\mathbf{w}}_{m'}^H \tilde{\boldsymbol{\chi}}_{m'}. \tag{3.62}$$

It is useful to think of the subset-CIT weight vector in terms of its constituent spatial components. Let $\tilde{\mathbf{w}}_{m',k}$ be the $K_s \times 1$ spatial weight vector for the k^{th} sub-CIT of the m'^{th} subset-CIT. The subset-CIT weight vector can be rearranged to form a $K_s \times K_t$ weight matrix

$$\tilde{\mathbf{w}}_{m'} = \left[\tilde{\mathbf{w}}_{m',0}; \tilde{\mathbf{w}}_{m',1}; \cdots; \tilde{\mathbf{w}}_{m',K_t}\right] \tag{3.63}$$

so that

$$\tilde{\mathbf{w}}_{m'} = \mathrm{vec}\left(\tilde{\mathbf{W}}_{m'}\right). \tag{3.64}$$

The m'^{th} subset-CIT output can then be written as

$$y_{m'} = \left[\left(\mathbf{J}_{m'} \otimes \tilde{\mathbf{G}}\right) \tilde{\mathbf{w}}_{m'}\right]^H \boldsymbol{\chi} = \left[\left(\mathbf{I}_M \otimes \tilde{\mathbf{G}}\right) \mathrm{vec}\left(\tilde{\mathbf{W}}_{m'} \mathbf{J}_{m'}^H\right)\right]^H \boldsymbol{\chi}. \tag{3.65}$$

Assemble the outputs from all subset-CITs into an $M' \times 1$ vector as

$$y = [\mathbf{y}_0; \mathbf{y}_1; \cdots; \mathbf{y}_{M'-1}] = \left[\left(\mathbf{I}_M \otimes \tilde{\mathbf{G}}\right) \tilde{\mathbf{W}}\right]^H \boldsymbol{\chi} \tag{3.66}$$

where,

$$\begin{aligned} \tilde{\mathbf{W}} &= \left[\mathrm{vec}\left(\tilde{\mathbf{W}}_0 \mathbf{J}_0^T\right), \mathrm{vec}\left(\tilde{\mathbf{W}}_1 \mathbf{J}_1^T\right), \cdots, \mathrm{vec}\left(\tilde{\mathbf{W}}_{M'-1} \mathbf{J}_{M'-1}^T\right)\right] \\ &= \begin{bmatrix} \tilde{\mathbf{w}}_{0,0} & \mathbf{0} & \cdots & \mathbf{0} \\ \tilde{\mathbf{w}}_{0,1} & \vdots & \cdots & \mathbf{0} \\ \vdots & \tilde{\mathbf{w}}_{1,0} & \ddots & \vdots \\ \tilde{\mathbf{w}}_{0,K_t-1} & \tilde{\mathbf{w}}_{1,1} & \ddots & \mathbf{0} \\ \mathbf{0} & \vdots & \ddots & \tilde{\mathbf{w}}_{M-K_t,0} \\ \vdots & \tilde{\mathbf{w}}_{1,K_t-1} & \ddots & \tilde{\mathbf{w}}_{M-K_t,1} \\ \mathbf{0} & \vdots & \cdots & \vdots \\ \mathbf{0} & \mathbf{0} & \cdots & \tilde{\mathbf{w}}_{M-K_t,K_t-1} \end{bmatrix} \end{aligned} \tag{3.67}$$

is an $MK_s \times M'$ matrix containing the weights from all subset-CITs. Finally, the subset-CIT output signals are processed by a length M' Doppler filter bank denoted by $\mathbf{F} = [\mathbf{f}_0; \mathbf{f}_1; \cdots; \mathbf{f}_{M'-1}]$ where the final output of the m^{th} Doppler filter is given by

$$z_m = \mathbf{f}_m^H \mathbf{y} = \mathbf{w}_m^H \boldsymbol{\chi} \tag{3.68}$$

and the beam-space pre-Doppler composite weight vector is given

$$\mathbf{w}_m = \left(\mathbf{I}_M \otimes \tilde{\mathbf{G}}\right) \tilde{\mathbf{W}} \mathbf{f}_m \tag{3.69}$$

The algorithm performance can then be computed in the usual way.

The clutter covariance rank for beam-space pre-Doppler depends on $\widetilde{\mathbf{G}}$ and is achieved if the assumptions of Brennan's rule are satisfied and if there exists a $K_s \times K_s$ nonsingular matrix $\mathbf{Q}$ and a length $N' = N - K_s + 1$ vector $\mathbf{g} = [g_0; g_1; \cdots; g_{N'-1}]$ such that

$$\widetilde{\mathbf{G}}\mathbf{Q} = \begin{bmatrix} g_0 & & 0 \\ g_1 & \ddots & \vdots \\ \vdots & & \mathbf{g}_0 \\ g_{N'-1} & & \mathbf{g}_1 \\ \vdots & \ddots & \vdots \\ \mathbf{0} & & \mathbf{g}_{N'-1} \end{bmatrix} = \text{Toeplitz}\left(\left[\mathbf{g}; \mathbf{0}_{(K_s-1)\times 1}\right], \left[g_0; \mathbf{0}_{1\times(K_s-1)}\right]\right). \tag{3.70}$$

Then the rank of clutter covariance matrix is minimum and equal to

$$\text{rank}\left(\widetilde{\mathbf{R}}_c\right) = K_s + (K_t - 1)\beta. \tag{3.71}$$

The conditions for which minimum clutter rank is achieved are equivalent to the conditions for which DPCA clutter cancellation is possible where Equation (3.70) with $\mathbf{Q} = \mathbf{I}_{K_s}$ is precisely that required by DPCA. The beamformer matrix $\mathbf{Q} = \mathbf{I}_{K_s}$ form of beam-space pre-Doppler will be referred to as displaced-beam pre-Doppler STAP. In practice, constructing a set of beamformers to satisfy $\widetilde{\mathbf{G}}\mathbf{Q}$ is much more difficult than constructing a set of Doppler filters since the spatial errors due to antenna element mismatches are typically relatively high (20 – 50 dB) [49]. Moreover, the need to suppress direct path random range sidelobes (and probably limited random range sidelobes of the strong clutter) coupling spatially may result in adaptive beamformers that deviate from that required for minimum clutter rank. Another beam-space post-Doppler approach, called adjacent-beam pre-Doppler STAP, utilizes a set of adjacent beams where each uses the full aperture. In adjacent-beam pre-Doppler STAP, $\mathbf{G}$ is an $N \times N$ matrix beamformer whose columns are beamformers steered to different angles and $\mathbf{J}$ is an $N \times K_s$ selection matrix that selects the columns of $\mathbf{G}$ corresponding to a cluster of adjacent beams centered at the transmit direction. Thus, the clutter cancellation beamformer matrix for the adjacent-beam pre-Doppler is

$$\widetilde{\mathbf{G}} = \mathbf{G}\mathbf{J}. \tag{3.72}$$

With no tapering, adjacent-beam pre-Doppler satisfies $\widetilde{\mathbf{G}}\mathbf{Q}$ with $\mathbf{Q} \neq \mathbf{I}_{K_s}$ and when tapering on receive is employed, the adjacent-beam approach may not satisfy the minimum rank assumptions.

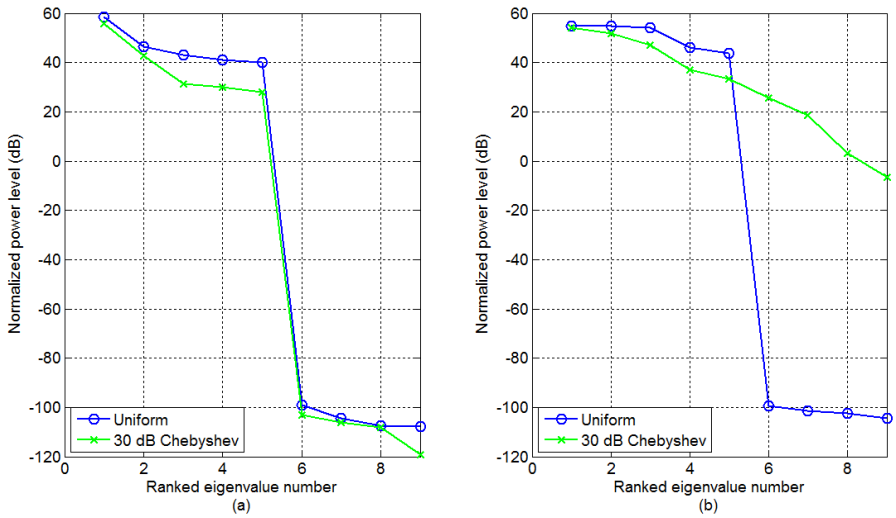

Fig. 3.21: Clutter eigenspectra for (a) displaced-beam pre-Doppler and (b) adjacent-beam pre-Doppler STAP, Doppler bin 6, $K_t = 3$ and $K_s = 3$.

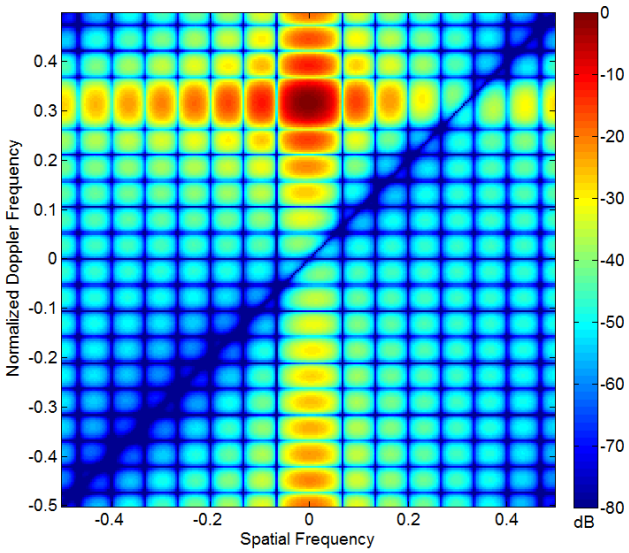

Fig. 3.22: Adapted pattern for displaced-beam pre-Doppler STAP, Doppler bin 6, $K_t = 2$ and $K_s = 2$.

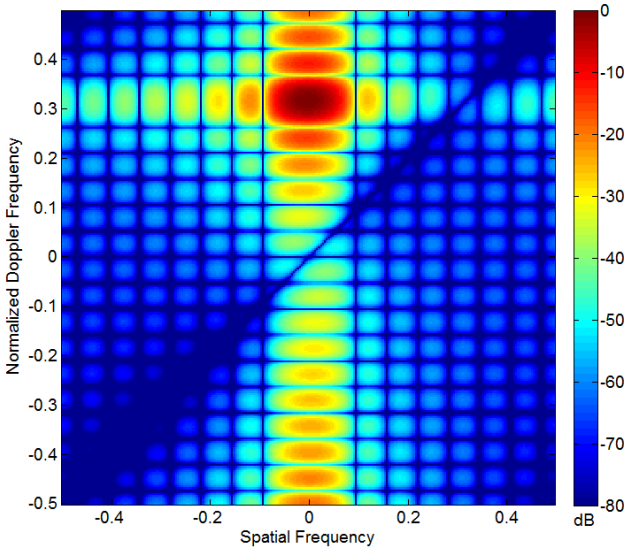

Fig. 3.23: Adapted pattern for adjacent-beam pre-Doppler STAP, Doppler bin 6, $K_t = 2$ and $K_s = 2$.

Fig. 3.21 depicts the clutter covariance eigenspectra (without noise component) for the same clutter-only scenario in the preceding Section (side-looking ULA where $N = 16$, $M = 20$, CNR = 30 dB and $\beta = 1$) for (a) displaced-beam pre-Doppler STAP and (b) adjacent-beam pre-Doppler STAP respectively. In each plot, the results for uniform taper and with a 30 dB Chebyshev taper for Doppler bin 6 with $K_t = 3$ and $K_s = 3$ are shown. For the displaced-beam pre-Doppler, in both cases, the clutter rank is 5 as predicted. However, for the adjacent-beam pre-Doppler, the clutter eigenspectrum exhibits a sharp drop only when a uniform taper is used. With tapered beamformers, it no longer satisfies the Brenan's rule theorem and the clutter rank is larger (full rank). The adapted pattern for the displaced-beam pre-Doppler and adjacent-beam pre-Doppler with $K_t = 2$ and $K_s = 2$ and for uniform taper are plotted in Figs. 3.22 and 3.23 respectively. The target steering vector is at 0 spatial

frequency and normalized Doppler frequency of 0.316 (Doppler bin 6). In adjacent-beam pre-Doppler, for $K_s = 2$, the two adjacent beams formed are spaced at the spatial frequency of $\pm 1/(2N)$ on either side of the target's spatial frequency so that the output spatial frequency remains the same steering angle (spatial frequency). Again, in both techniques, a deep null along the diagonal is successfully formed to suppress the clutter. Closer examination conclude that the mainlobe adapted pattern for the adjacent-beam pre-Doppler exhibit a wider spatial pattern as compared to that of displaced-beam pre-Doppler approach where the implication is on the practical spatial resolution beamwidth when adapting the adjacent-beam pre-Doppler STAP.

The SINR loss performance for beam-space pre-Doppler STAP is illustrated using the same clutter-only scenario. For displaced-beam pre-Doppler, with $K_t = 2$, the number of beams is varied and Fig 3.24 and 3.25 depict the performance for the case where no tapering and a 30 dB Chebyshev taper is used respectively. For the displaced-beam pre-Doppler method, performance is excellent for as few as two beams since the number of adaptive DOF must be greater than the clutter rank and the equivalent condition

$$K_s \geq \beta + \frac{1}{K_t - 1} \tag{3.73}$$

is satisfied. Using more beam outputs does little to improve the performance as shown in Fig. 3.24. With a tapered beamformer, similar results are obtained since the number of DOF is always larger than the clutter rank. The SINR loss performance for the previous corresponding plots but using the adjacent-beam pre-Doppler STAP algorithm are depicted in Fig. 3.26 and 3.27 respectively. With no taper, the clutter rank is as given in Equation (3.71) and two beams are sufficient for effective clutter cancellation. With a taper, the clutter rank is increased and for a small amount of beams, the performance suffers at Doppler frequencies close to the mainlobe clutter. The algorithm needs at least three beams to achieve acceptable performance and even then, the performance is a few dBs inferior to that of the displaced-beam pre-Doppler with the same number of beams.

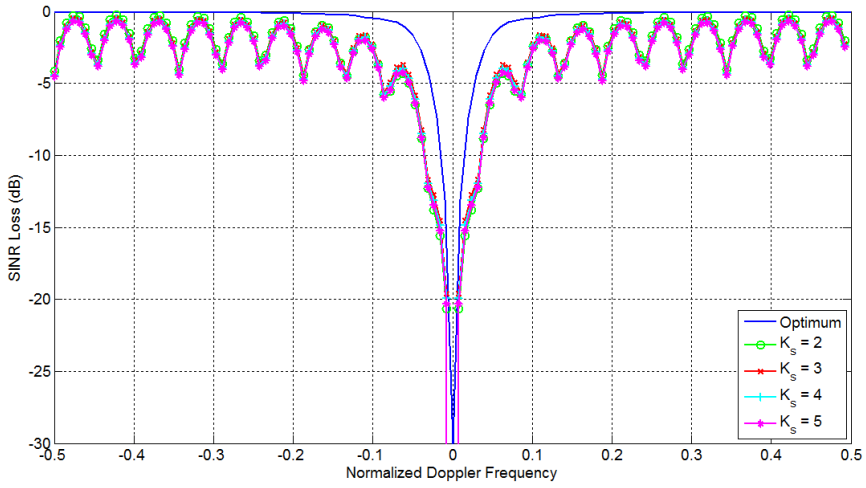

Fig. 3.24: SINR loss performance for untapered displaced-beam pre-Doppler STAP, $K_t = 2$.

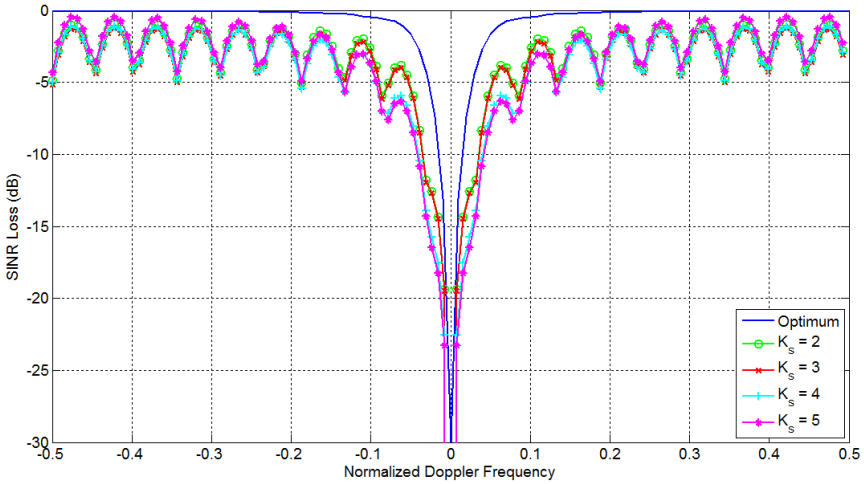

Fig. 3.25: SINR loss performance for displaced-beam pre-Doppler STAP with a 30 dB Chebyshev taper, $K_t = 2$.

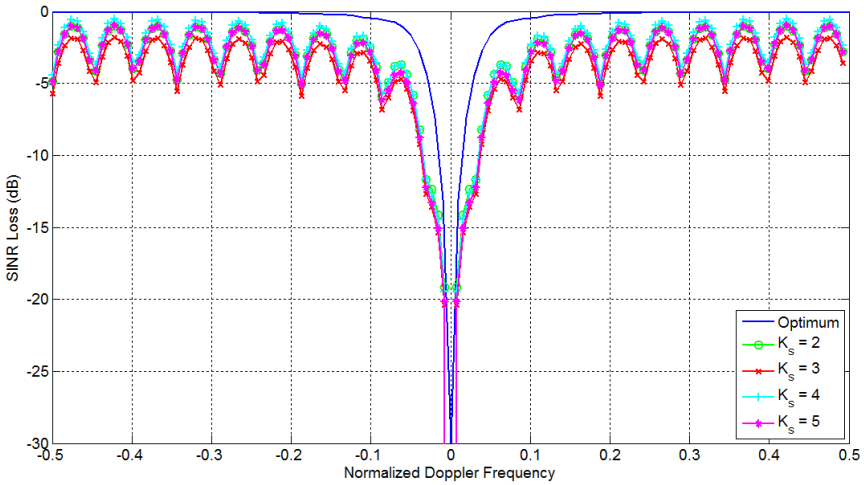

Fig. 3.26: SINR loss performance for untapered adjacent-beam pre-Doppler STAP, $K_t = 2$.

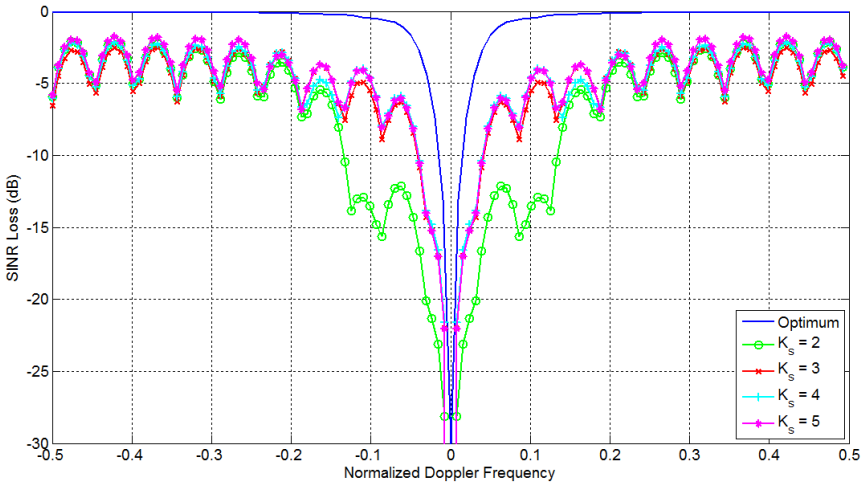

Fig. 3.27: SINR loss performance for adjacent-beam pre-Doppler STAP with a 30 dB Chebyshev taper, $K_t = 2$.

3.4.4 Beam-space post-Doppler space-time adaptive processing

The beam-space post-Doppler technique performs both fixed beamforming and Doppler filtering on the data prior to adaptation. This transforms each element-sub-CIT cell into a beam-Doppler cell where the bank of space-time filters are formed by cascading spatial beamformers on each sub-CIT with Doppler filters on each beam over all sub-CITs. This class is therefore called beam-space post-Doppler STAP as in Fig. 3.28. The filtered signals are then adaptively combined to produce the Doppler bin output. This process is then repeated for each Doppler bin. Combined beamforming and Doppler filtering is intended to localize the interference both spatially and spectrally prior to adaptation so that fewer outputs need to be combined adaptively. The adaptation will then be done on a subset of the resultant beam-Doppler filter outputs where significant reductions in the number of adaptive DOF are possible.

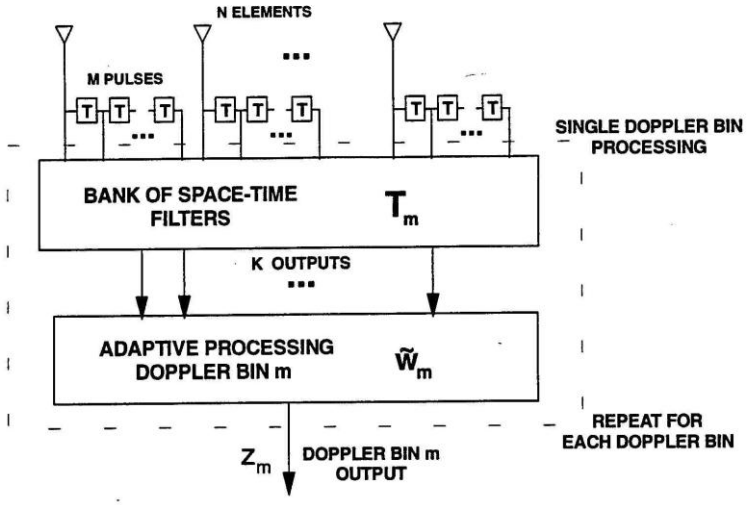

Fig. 3.28: Block diagram of single bin processing for beam-space post-Doppler STAP [49].

Beam-space post-Doppler STAP requires solving a separate adaptive problem in each target Doppler bin. The analysis of beam-space post-Doppler STAP is on $\mathbf{T}_m$ which is a $MN \times K$ preprocessor for the m^{th} Doppler bin adaptation where K is the size of the reduced-dimension snapshot. There are two types of preprocessors that are considered. The first is a separable $MN \times K$ preprocessor of the form

$$\mathbf{T}_m = \tilde{\mathbf{F}}_m \otimes \tilde{\mathbf{G}} \tag{3.74}$$

where $\tilde{\mathbf{F}}_m$ is an $M \times K_t$ matrix of Doppler filters, $\tilde{\mathbf{G}}$ is an $N \times K_s$ matrix of beamformers and $K = K_s K_t$. This type of preprocessor is said to be separable because it may be implemented by cascading multiple beamformers on each sub-CIT with multiple Doppler filters on each beam (or vice versa). Here, assume that both $\tilde{\mathbf{F}}_m$ and $\tilde{\mathbf{G}}$ are of full column rank. The transformed snapshot for the m^{th} Doppler bin is given by

$$\tilde{\boldsymbol{\chi}}_m = \left(\tilde{\mathbf{F}}_m \otimes \tilde{\mathbf{G}}\right)^H \boldsymbol{\chi}. \tag{3.75}$$

The m^{th} Doppler bin adaptive weight vector is

$$\tilde{\mathbf{w}}_m = \tilde{\mathbf{R}}_{um}^{-1} \tilde{\mathbf{u}}_t \tag{3.76}$$

where $\tilde{\mathbf{R}}_{um}$ is the $K_s K_t \times K_s K_t$ interference-plus-noise covariance matrix of the m^{th} Doppler bin and $\tilde{\mathbf{u}}_t$ is a $K_s K_t \times 1$ desired response. The desired response is chosen according as

$$\tilde{\mathbf{u}}_t = \left(\tilde{\mathbf{F}}_m \otimes \tilde{\mathbf{G}}\right)^H \mathbf{g}_t. \tag{3.77}$$

Thus, the final output signal of the m^{th} Doppler bin is given by

$$z_m = \tilde{\mathbf{w}}_m^H \tilde{\boldsymbol{\chi}}_m = \mathbf{w}_m^H \boldsymbol{\chi} \tag{3.78}$$

where the beam-space post-Doppler composite weight vector is

$$\mathbf{w}_m = \left(\tilde{\mathbf{F}}_m \otimes \tilde{\mathbf{G}}\right) \tilde{\mathbf{w}}_m. \tag{3.79}$$

The algorithm performance can then be computed in the usual way.

For K_s and K_t, the rank of clutter covariance depends upon both $\tilde{\mathbf{F}}_m$ and $\tilde{\mathbf{G}}$. A beam-space post-Doppler version of Brennan's rule provides conditions that results in minimum clutter rank such that the assumptions of Brennan's rule and the conditions for $\tilde{\mathbf{G}}$ and $\tilde{\mathbf{F}}_m$ are satisfied. First, there exists a $K_s \times K_s$ nonsingular matrix $\mathbf{Q}_s$ and a length $N' = N - K_s + 1$ vector $\mathbf{g} = [g_0; g_1; \cdots; g_{N'-1}]$ such that

$$\tilde{\mathbf{G}}\mathbf{Q}_s = \begin{bmatrix} g_0 & & \mathbf{0} \\ g_1 & \ddots & \vdots \\ \vdots & & g_0 \\ g_{N'-1} & & g_1 \\ \vdots & \ddots & \vdots \\ \mathbf{0} & & g_{N'-1} \end{bmatrix} = \text{Toeplitz}\left(\left[\mathbf{g}; \mathbf{0}_{(K_s-1)\times 1}\right], \left[g_0; \mathbf{0}_{1\times(K_s-1)}\right]\right) \tag{3.80}$$

and there exists a $K_t \times K_t$ nonsingular matrix $\mathbf{Q}_t$ and a length $M' = M - K_t + 1$ vector $\mathbf{f} = [f_0; f_1; \cdots; f_{M'-1}]$ such that

$$\tilde{\mathbf{F}}_m\mathbf{Q}_t = \begin{bmatrix} f_0 & & \mathbf{0} \\ f_1 & \ddots & \vdots \\ \vdots & & f_0 \\ f_{M'-1} & & f_1 \\ \vdots & \ddots & \vdots \\ \mathbf{0} & & f_{M'-1} \end{bmatrix} = \text{Toeplitz}\left(\left[\mathbf{f}; \mathbf{0}_{(K_t-1)\times 1}\right], \left[f_0; \mathbf{0}_{1\times(K_t-1)}\right]\right). \tag{3.81}$$

Then the rank of clutter covariance matrix is minimum and equal to

$$\text{rank}\left(\tilde{\mathbf{R}}_{cm}\right) = K_s + (K_t - 1)\beta. \tag{3.82}$$

In practice, the numerical rank of the clutter covariance matrix may be even less than the theoretical value as parts of the clutter ridge may be suppressed to well below thermal noise by the combined angle and Doppler sidelobes of the preprocessor. To differentiate between beam-space post-Doppler approaches, the special case $\mathbf{Q}_s = \mathbf{I}_{K_s}$ and $\mathbf{Q}_t = \mathbf{I}_{K_t}$ will be referred to as displaced-filter beam-space post-Doppler.

The second type of preprocessor is formed by choosing a subset of the outputs of a separable processor [79, 80]

$$\mathbf{T}_m = (\mathbf{F} \otimes \mathbf{G})\mathbf{J}_m \tag{3.83}$$

where $\mathbf{F}$ is $M \times M$, $\mathbf{G}$ is $N \times N$ and $\mathbf{J}_m$ is an $MN \times K$ selection matrix that picks a subset of angle-Doppler filters. The block diagram for the preprocessor in Equation (3.83) is shown in Fig. 3.29. In this algorithm, the input snapshot is passed through a two-dimensional DFT that may be represented as

$$\mathbf{T} = \mathbf{F} \otimes \mathbf{G} \tag{3.84}$$

where

$$\mathbf{F} = \text{diag}\left(\mathbf{t}_f\right)\mathbf{U}_m^*, \; \mathbf{G} = \text{diag}\left(\mathbf{t}_g\right)\mathbf{U}_N^*. \tag{3.85}$$

$\mathbf{U}_M$ and $\mathbf{U}_N$ are $M \times M$ and $N \times N$ DFT matrices respectively and $\mathbf{t}_f$ and $\mathbf{t}_g$ are tapers in Doppler and angle respectively. Thus, the output for the m^{th} Doppler bin target filter is formed by adaptively combining the signals from a subset of K_m filters denoted by the

$MN \times K_m$ selection matrix $\mathbf{J}_m$ where the chosen subset must contain the target filter. The snapshot for the m^{th} Doppler bin adaptation is given by

$$\tilde{\boldsymbol{\chi}} = \left((\mathbf{F}\otimes\mathbf{G})\mathbf{J}_m\right)^H \boldsymbol{\chi} = \mathbf{J}_m^T(\mathbf{F}\otimes\mathbf{G})^H\boldsymbol{\chi}. \tag{3.86}$$

The issue now is the choice of $\mathbf{J}_m$ for each Doppler bin, i.e. filter selection. One selection strategy is to choose a rectangular block of filters that is centered on and includes the target filter known as adjacent-filter beam-space post-Doppler STAP where $K_m = K_{sm}K_{tm}$, K_{sm} is the number of angle beams and K_{tm} is the number of Doppler filters in the m^{th} block. The adjacent-filter selection matrix is separable,

$$\mathbf{J}_m = \mathbf{J}_{tm}\otimes\mathbf{J}_{sm} \tag{3.87}$$

where $\mathbf{J}_{tm}$ and $\mathbf{J}_{sm}$ are the appropriate $M \times K_t$ and $N \times K_s$ selection matrices. It leads to the separable preprocessor

$$\mathbf{T}_m = \tilde{\mathbf{F}}_m\otimes\tilde{\mathbf{G}} \tag{3.88}$$

where

$$\tilde{\mathbf{F}}_m = \mathbf{F}\mathbf{J}_{tm} \text{ and } \tilde{\mathbf{G}} = \mathbf{G}\mathbf{J}_{sm}. \tag{3.89}$$

It can be shown that the preprocessor for the adjacent-filter beam-space post-Doppler STAP satisfies the beam-space post-Doppler version of Brennan's rule when the two-dimensional DFT is not tapered.

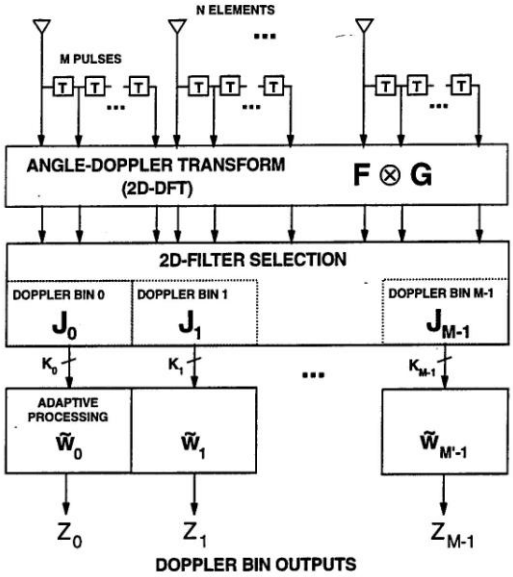

Fig. 3.29: Block diagram for beam-space post-Doppler STAP utilizing a single 2D-FFT [49].

To illustrate the performance of the beam-space post-Doppler STAP, consider again the same clutter-only scenario as in the preceding Section (side-looking ULA where $N = 16$, $M = 20$, CNR = 30 dB and $\beta = 1$). Fig. 3.30 depicts the clutter covariance eigenspectra for (a) displaced-filter post-Doppler STAP and (b) adjacent-filter post-Doppler STAP respectively. In each plot, the results for uniform taper and with a 30 dB Chebyshev taper in both angle and Doppler for Doppler bin 6 with $K_t = 3$ and $K_s = 3$ are shown. Based on beam-space post-Doppler version of Brenan's rule, the clutter rank is 5. For the displaced-filter pre-Doppler, in both cases, the clutter rank is as predicted. However, for the adjacent-filter pre-Doppler, the clutter eigenspectrum exhibits a sharp drop only when a uniform taper is used and with tapered beamformers and Doppler filters, Brenan's rule theorem is no longer satisfied and the clutter rank is larger. The adapted pattern for the displaced-filter post-

Doppler and adjacent-filter post-Doppler STAP with $K_t = 2$ and $K_s = 2$ and for uniform taper are plotted in Figs. 3.31 and 3.32 respectively. As before, the target steering vector is at 0 spatial frequency and normalized Doppler frequency of 0.3 (Doppler bin 6). In adjacent-filter post-Doppler, for $K_s = 2$, the two adjacent beams formed are spaced at the spatial frequency of $\pm 1/(2N)$ on either side of the target's spatial frequency so that the output spatial frequency remains the same steering angle (spatial frequency). However, the Doppler bin output frequency is midway between Doppler bin 6 and Doppler bin 7, i.e., normalized Doppler frequency of 0.325. Again, in both techniques, a deep null along the diagonal is successfully formed to suppress the clutter. Closer examination revealed the significant wider mainlobe adapted pattern in both spatial and Doppler domain for the adjacent-filter post-Doppler as compared to that of displaced-filter post-Doppler approach. This is a practical concern on the spatial resolution beamwidth and Doppler resolution for the adjacent-beam pre-Doppler STAP approach.

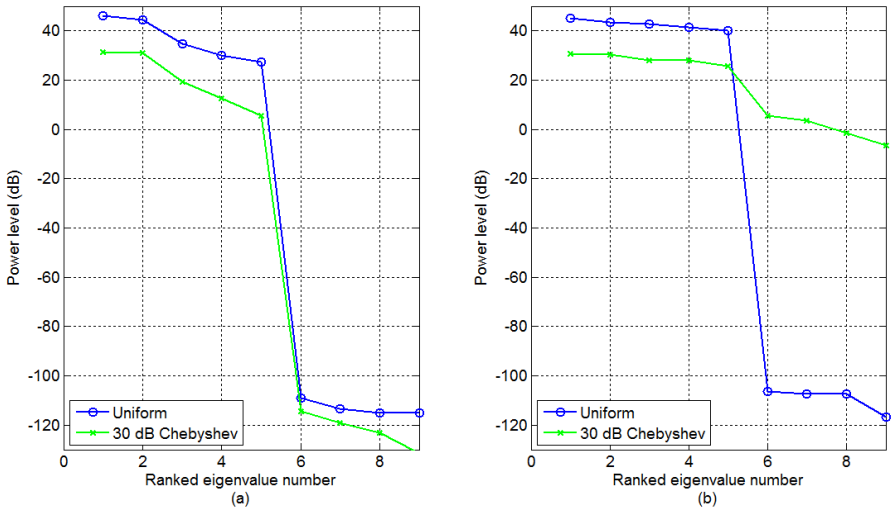

Fig. 3.30: Clutter eigenspectra for (a) displaced-filter post-Doppler and (b) adjacent-filter post-Doppler STAP, $K_t = 3$ and $K_s = 3$.

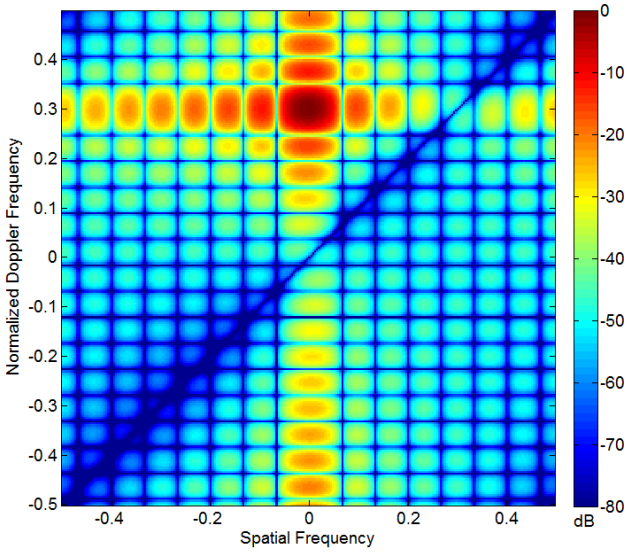

Fig. 3.31: Adapted pattern for displaced-filter post-Doppler STAP, Doppler bin 6, $K_t = 2$ and $K_s = 2$.

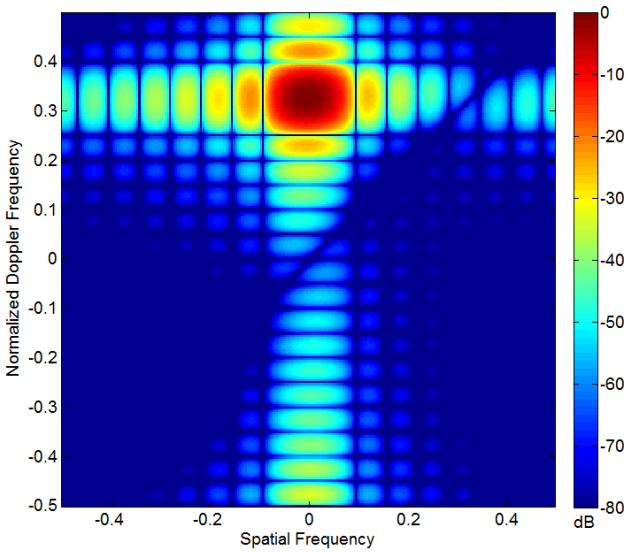

Fig. 3.32: Adapted pattern for adjacent-filter post-Doppler STAP, Doppler bin 6, $K_t = 2$ and $K_s = 2$.

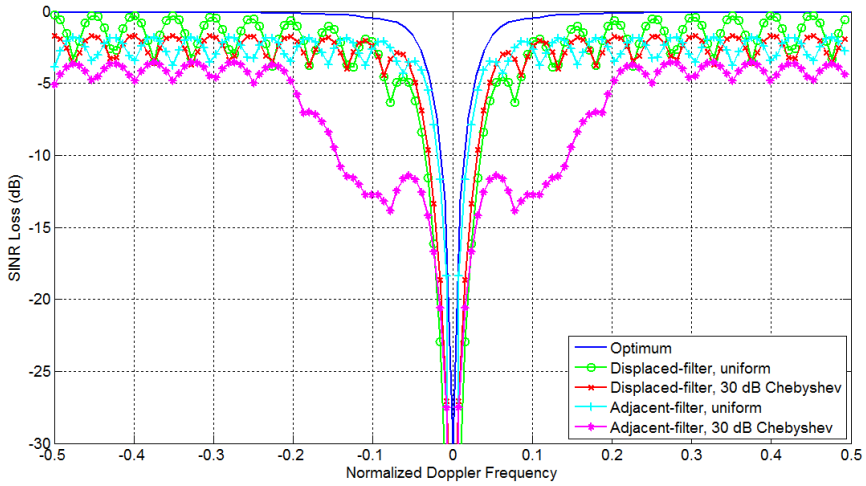

Fig. 3.33: SINR loss performance for beam-space post-Doppler STAP, $K_{tm} = 2$ and $K_{sm} = 2$.

The SINR loss performance for beam-space post-Doppler STAP is illustrated next for both approaches with uniform taper and a 30 dB Chebyshev taper in both angle and Doppler. Fig. 3.33 depicts SINR loss plots for the case $K = 4$ DOF with $K_{tm} = 2$ and $K_{sm} = 2$. With uniform taper, both displaced-filter and adjacent-filter post-Doppler provide near optimum performance with 4 DOF. For tapered filters, displaced-filter approach suffers only a small taper loss over the whole Doppler space since Brennan's rule is satisfied. On the other hand, the adjacent-filter post-Doppler approach suffers a significant loss in performance at Doppler frequencies close to mainlobe clutter. This loss can be alleviated with heavier taper applied since tapering suppresses much of the clutter nonadaptively. However, its performance is still inferior to that of displaced-filter post-Doppler approach. Figs. 3.34 and 3.35 show similar plot to Fig. 3,33 where the DOF dimensionality is increase to 9 with $K_{tm} = 3$ and $K_{sm} = 3$ and 16 with $K_{tm} = 4$ and $K_{sm} = 4$ respectively. As seen, the performance of adjacent-filter post-Doppler improved. In general, as the number of selected filters increases, the relative

difference between displaced-filter and adjacent-filter approaches lessens as there are sufficient DOFs to suppress the clutter.

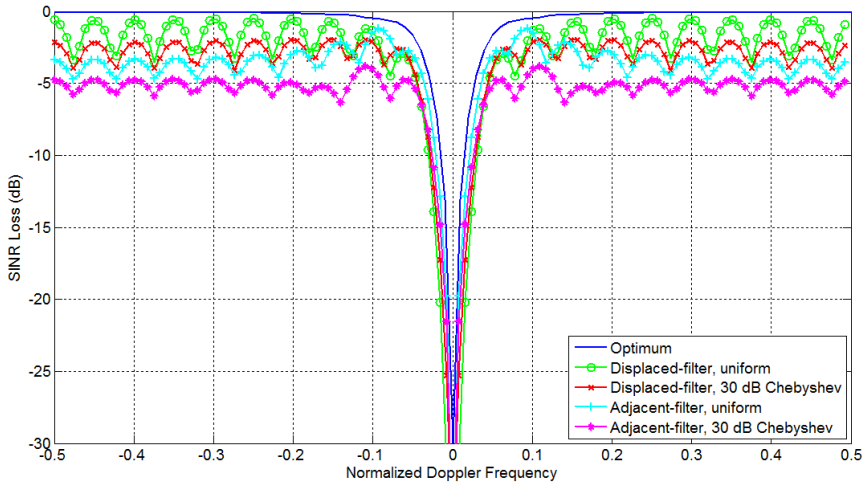

Fig. 3.34: SINR loss performance for beam-space post-Doppler STAP, $K_{tm} = 3$ and $K_{sm} = 3$.

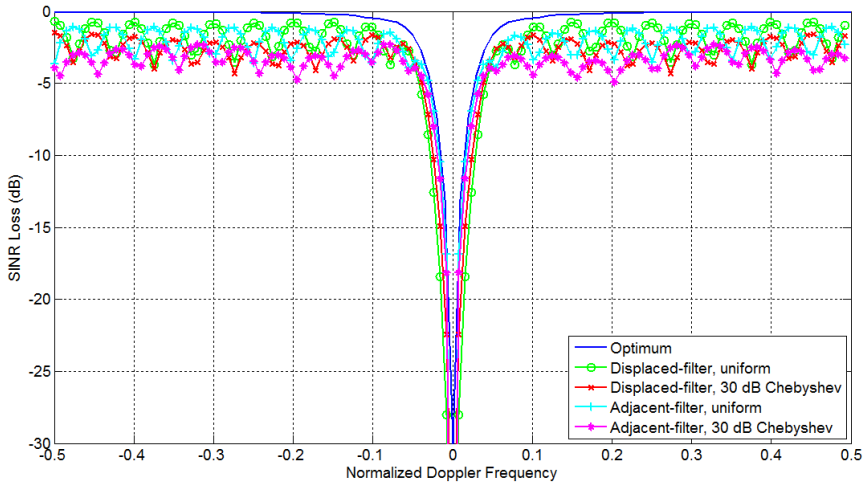

Fig. 3.35: SINR loss performance for beam-space post-Doppler STAP, $K_{tm} = 4$ and $K_{sm} = 4$.

3.5 Summary

Different from conventional pulsed Doppler radar, the random range sidelobes couplings of the direct path and of the strong clutter are important considerations on moving target detections performance for the airborne passive radar. In addition, for the clutter received by the airborne passive platform, the motion-induced spread of its Doppler spectrum may mask the weak and slow moving targets which further complicate the problem. Thus, the signal processing schemes for the airborne passive radar calls for the effective suppression of these interference to improve moving target detections performance. The basic concept for interference suppression for the airborne passive radar can be segregated into a two step cancellation process. First, the direct path and strong clutter present in the received signal at each antenna element, whose random range sidelobes inhibit target detections at the further range cell of interest, can be suppressed by the adaptive cancellation algorithm prior to matched filter processing. The adaptive interference cancellation technique based on the LS

approach is able to suppress the direct path, strong clutter and Doppler-shifted strong clutter signals received at each antenna element. Simulations on a generalized direct path and clutter (Doppler-shifted clutter included) scenario demonstrated that the algorithm is effective in cancelling these interfering signals. Subsequently, in mitigating these undesirable interference, its corresponding random range sidelobes that manifest into further range cells will also be suppressed by the same amount. However, the drawbacks of the adaptive interference cancellation algorithm are in its exhaustive computational load and the cancellation of targets that fall within the range and Doppler cells where the algorithm operates. Further cancellation on the undesirable residual random range sidelobes couplings (residual direct path random range sidelobes and residual random range sidelobes of the strong clutter that span a limited spatial frequency) and more importantly on the spatial-Doppler dependent clutter can be achieved using STAP. In particular, due to reasons of computational complexity (large dimensionality) and sample support required for weights training in a practical airborne passive radar scenario limited by the power budget and passive signal bandwidth, reduced-dimension STAP techniques provide solutions to this fundamental two-dimensional clutter suppression problem. For reduced-dimension STAP algorithms, they are classified by the type of non-adaptive transformation on the datacube. The four main types are the element-space pre-/post-Doppler and beam-space pre-/post-Doppler algorithms. In-depth theoretical analysis and discussions of these algorithms in each domain provides conditions for pre-processor design and insight into the relationships between different architectures. Simulations done on a typical clutter-only scenario where $N = 16$ and $M = 20$ for a side-looking ULA with a CNR of 30 dB and $\beta = 1$ facilitate the exhaustive understanding of the characteristics, merits and drawbacks for each algorithm. These properties had been comprehensively outlined and discussed in their respectively Section.

In summary, the theoretical analyses and simulations addressing the signal processing for the airborne passive radar that have been outlined in this Chapter paved the way for the modeling of a typical bistatic airborne passive radar utilizing a ground-based DVB-T transmitter. This is to envisage the operational capability and investigate the practical performance of the airborne passive radar which is the subject of the next Chapter.

Chapter 4

Simulations on Airborne Passive Radar Signal Processing

4.1 Introduction

Chapter 2 had been devoted to the development of the data models for the desired and interfering passive signals received by the airborne passive radar. In particular, the spatial-Doppler properties of clutter and the random range sidelobes of the direct path and of the strong clutter are thoroughly analyzed. Chapter 3 addresses the associated signal processing schemes and techniques applicable to the airborne passive radar for moving target detections. First, the direct path and strong clutter coupling components present in the received passive signal at each antenna element can be suppressed by the adaptive interference cancellation algorithm prior to matched filter processing. This reduces the magnitude of the random range sidelobes couplings of these interfering signals into further range cells. This is followed by the application of the joint space and time processing since the clutter returns received by the airborne passive radar have a motion induced Doppler spread which in turn is the function of the spatial frequency. Reduced-dimension STAPs enable the effective suppression of the clutter ridge as well as the residual random range sidelobes couplings (direct path random range sidelobes and random range sidelobes of the strong clutter that have a limited spatial frequency span) to improve weak and slow moving target detections.

The preceding Chapters complete the theoretical studies and analyses for the airborne passive radar and its associated signal processing schemes for MTI. In order to envisage the operational capability and investigate the practical performance of the airborne passive radar, a typical bistatic airborne passive radar scenario utilizing a ground-based DVB-T transmitter is modelled. The random signal is used as an approximate model for the transmitted DVB-T waveform along with the geometrical, passive signal and passive datacube parameters to model a realistic and practical environment and interference scenario. This Chapter presents the results, analyses and discussions for the complete simulations on the airborne passive radar signal processing.

4.2 Simulation geometry and parameters

To envisage and evaluate the practical performance of the airborne passive radar, two geometrical scenarios will be adopted to model the side-looking and forward-looking configurations as shown in Figs. 4.1 and 4.2 respectively. These two configurations allow the airborne passive radar to have an all-round coverage around the airborne passive platform for covert surveillance. In the simulations, the passive radar resides on an airborne platform with the ULA consisting of 16 identical elements. In the side-looking configuration as in Fig. 4.1, the ULA is assumed to be mounted on the fuselage (side) of the airborne platform where the simulation flight geometry is such that the DVB-T transmitter and the airborne passive radar are aligned on the x-axis with the passive radar flying away from the transmitter in the

positive x-direction. In Fig. 4.2, the ULA is assumed to be mounted on the nose of the airborne platform (array axis normal to the velocity vector $\mathbf{v}_R$) to represent the forward-looking configuration and having the simulation geometry as in Fig. 4.1. However in this scenario, the passive radar flies towards the transmitter in the negative x-direction to model a severe direct path and strong clutter couplings interference scenario. These two geometrical scenarios will be referred to explicitly as the side-looking and forward-looking configurations. The simulation model for the airborne passive radar incorporates a flat and stationary Earth assumption and that the level flight path is parallel to the Earth's surface. The complete geometrical, passive signal and passive datacube simulation parameters are tabulated in Tab. 4.1. For a constant velocity target (no Doppler range cell migration) and based on the signal bandwidth of 8 MHz, the maximum CIT without inducing target range cell migration is calculated to be 187.5 ms. For the passive CIT datacube, 20 sub-CITs each with a sub-CIT duration of 2.5 ms are used where the CIT is 50 ms. Thus, this value is less than the maximum permitted CIT to ensure that no target range cell migration occurs. For simplicity and convenient, the slope of the clutter line β equating to 1 is chosen.

Fig. 4.1: Side-looking airborne passive radar geometry.

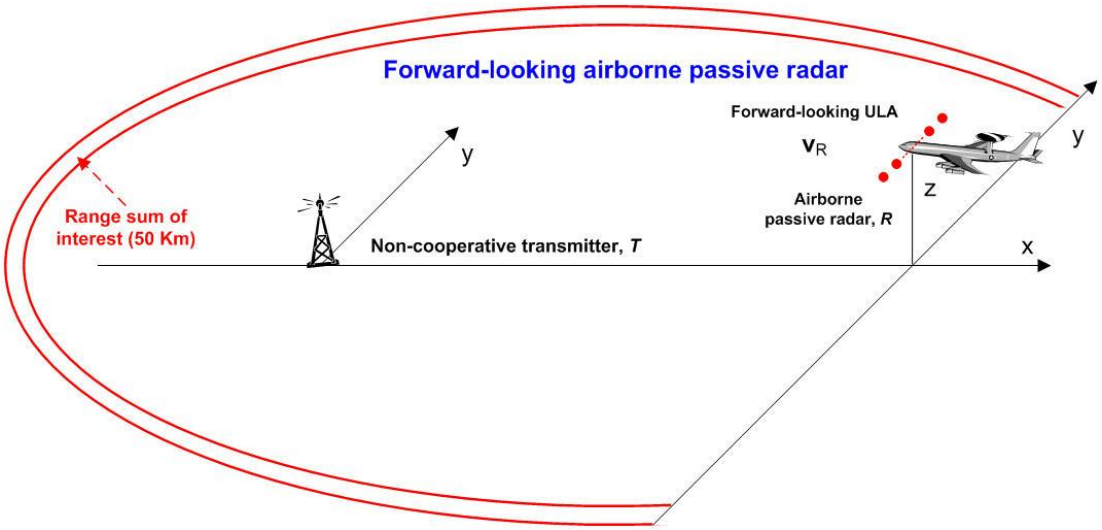

Fig. 4.2: Forward-looking airborne passive radar geometry.

Tab. 4.1: Parameters for the airborne passive radar simulations.

Geometrical parameters	
Non-cooperative transmitter height	200 m
Airborne passive radar altitude	1000 m
Airborne passive radar velocity	100 m/s
Ground baseline	20000 m
Normalized clutter reflectivity	–16 dB (rural land)
RMS surface slope	0.17 rad (rural land)
Clutter patch size	2 m × 2 m
Passive signal parameters	
Random signal carrier frequency	600 MHz
Random signal bandwidth	8 MHz
Complex sampling bandwidth	10 MHz
Effective radiated power	8 KW
Transmit antenna pattern	Omnidirectional (in azimuth)
Receive antenna element gain	5 dB
Receive antenna element pattern	Omnidirectional front-lobe (180° coverage in azimuth) and insignificant back-lobe (unless otherwise stated)
Receiver noise figure	5 dB
Boltzmann's constant	1.38×10^{-23}
Receiver reference temperature	290 K
Total system losses	5 dB
Passive datacube parameters	
Number of elements	16
Sub-CIT repetition frequency	400 Hz ($\pm$200 Hz)
Sub-CIT repetition interval	2.5 ms
Number of sub-CITs	20
Normalized slope of clutter ridge (β)	1

4.3 Power budget, power spectra and eigenspectra results and analyses

The power budget accordingly to the bistatic geometrical and passive signal parameters in Tab. 4.1 is calculated which is applicable for both side-looking and forward-looking airborne passive radar configurations. These simulations compute the power of the signals received by each element of the ULA in a typical and realistic interference scenario. Fig. 4.3 depicts the clutter bistatic scattering coefficient σ_b^0 (clutter cross section per unit area) accordingly to the airborne passive radar bistatic geometry. In-plane bistatic scattering region is located close to the transmitter and passive radar site along (or slightly off) the x-axis and having higher values of $(\sigma_b^0)_b$ which is close to the given normalized reflectivity of –16 dB [5]. Lower level of $(\sigma_b^0)_l$ can be expected for all other in-plane calculations which fall into the low grazing angle region. Given the low transmitter height and passive radar altitude against a relatively long baseline, no specular ridge region exists for the simulation geometry. For out-of-plane bistatic clutter, σ_b^0 usually approaches a minimum as out-of-plane angle ϕ

approaches $90°$ as clearly shown. In addition, out-of-plane σ_b^0 values are not significantly different (within 5 dB) from in-plane σ_b^0 values for $\phi \leq 10°$ and $\phi \geq 140°$, i.e. angles close to in-plane conditions. Consequently, using the values of σ_b^0 and together with the parameters in Tab. 4.1, the absolute clutter power distribution can be computed as illustrated in Fig. 4.4. Examining Fig. 4.4, the power profile can be segregated into three distinct operating regions for the airborne passive radar. The first two are the airborne passive radar and the non-cooperative transmitter centered region which are the small ovals around the passive radar and transmitter respectively, and thirdly, the passive radar-transmitter centered region (also called the cosite region) which is any of the ovals (bigger) surrounding both passive radar and transmitter., i.e. for longer range surveillance. The interest for the airborne passive radar is of course on the region centered around the airborne passive platform and cosite region for localized covert ground and air moving target surveillance. The results of the clutter power distribution, together with the direct path and noise power will be used for the exact formulation of the interference snapshots for the airborne passive radar.

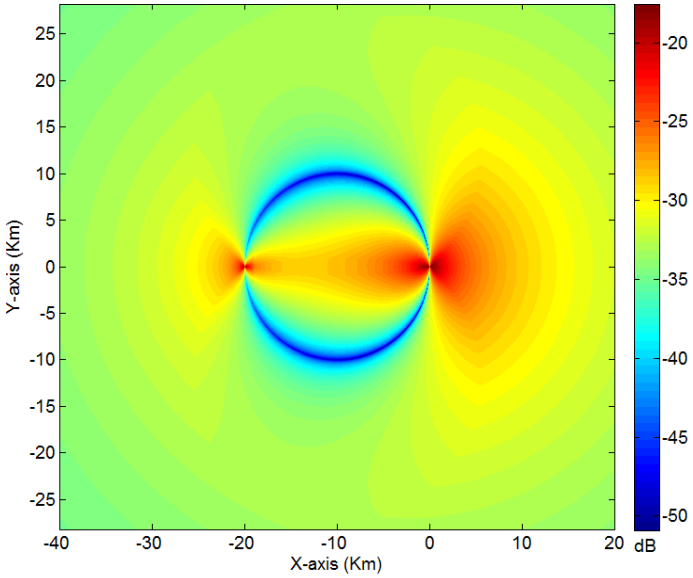

Fig. 4.3: Clutter bistatic scattering coefficient for the airborne passive radar scenario.

Fig. 4.5 depicts the DNR and CNR per element per sub-CIT plotted against range sum for both side-looking and forward-looking configurations. For both configurations, the DNR at the origin range cell ($l = 0$) is consistent and calculated to be 97.96 dB. In the side-looking configuration, the CNR (that is summed according to the range resolution cell) for the next five clutter range cells away from the origin are 58.75 dB, 60.27 dB, 60.81 dB, 60.76 dB and 60.21 dB respectively. For the forward-looking configuration, they are 61.7597 dB, 63.28 dB, 63.82 dB, 63.77 dB and 63.22 dB respectively. The DNR is approximately 34 dB stronger than the strongest CNR for the forward-looking configuration. The CNR for the forward-looking configuration shows an approximately 3 dB increase compared to the side-looking configuration for range sum ≤ 21 Km ($l \leq 33$). For short range clutter, the isorange sum contours are located within the ground baseline and therefore the clutter cell area is doubled in the forward-looking configuration. Thus, the forward-looking configuration exhibits stronger clutter returns (3 dB) than the side-looking configuration. As computed, for further range sum ($l > 34$), the side-looking configuration has a slightly bigger CNR (within 2 dB) up to the range sum of approximately 44 Km. Thereafter, both array orientations have similar

CNR values since the range sum ellipse becomes more and more circular with respect to the passive radar and transmitter. The CNR at the range sum of 50 Km ($l = 999$) is calculated to be 26.60 dB and 26.74 dB for the side-looking and forward-looking configuration respectively.

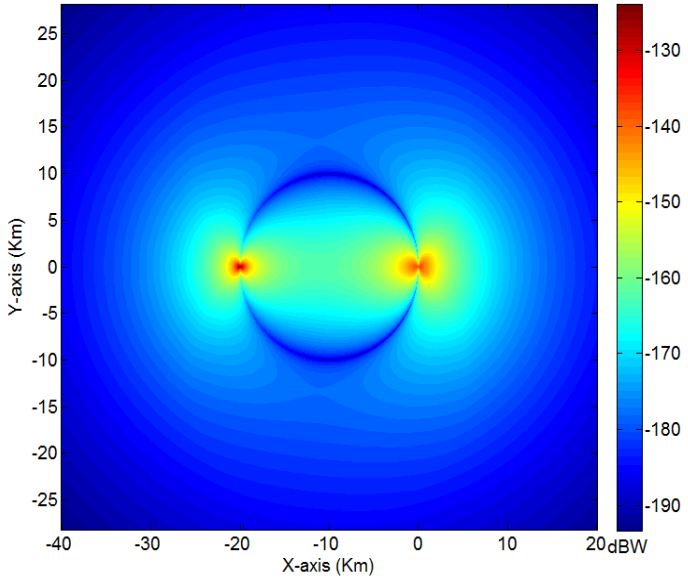

Fig. 4.4: Clutter power distribution for the airborne passive radar scenario.

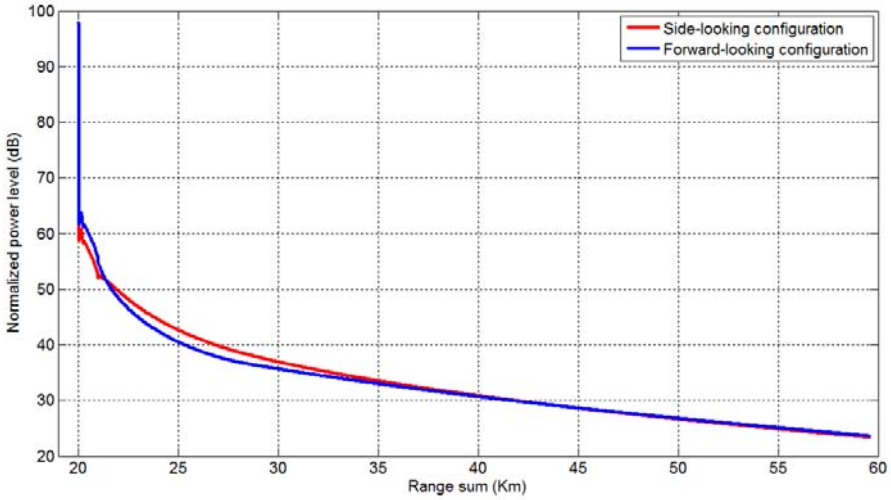

Fig. 4.5: DNR and CNR per element per sub-CIT against range sum.

4.3.1 Side-looking configuration

Based on the results/parameters in the preceding Section, the spatial-Doppler power spectrum for each of the undesired component that contribute to the inference scenario for the airborne passive radar will be depicted in the subsequent Figs. For the side-looking configuration, the absolute spatial and Doppler frequency of the direct path reference signal is –0.5 and –200 Hz respectively. Fig. 4.6 depicts the power spectrum for the direct path snapshot and its corresponding random range sidelobes along incremental range cells. The origin range cell ($l = 0$) represents the direct path signal as received by the airborne passive

radar. In the geometry, the direct path enters the airborne passive radar at the array endfire (ϑ_{dp} = –0.5). The Doppler frequency of the direct path is neutralized (0 Hz) since the direct path reference signal used for matched filter processing has the same Doppler frequency due to the passive radar platform motion. Likewise, the Doppler frequency of the clutter in the simulations represents the relative Doppler frequency after matched filter processing. The DNR per element per sub-CIT is approximately 98 dB, thus giving a peak value of 123 dB (98 dB + $10\log_{10}(MN)$ dB) at the origin range cell as shown. Next, focus is on further range cells ($l > 0$) where these power profiles correspond to the random range sidelobes of the direct path. The random range sidelobes snapshots of the direct path component appear as an irregular ridge spread across all Doppler frequencies having the same normalized spatial frequency as the direct path. Since the sidelobes of the direct path is temporally uncorrelated from sub-CIT-to-sub-CIT, it looks like thermal noise temporally but like a point scatterer in the spatial domain. The average value of the random range sidelobes is approximately 68 dB which is about $10\log_{10}(1/MBT_{sub})$ dB lower than the peak value of the direct path at the origin range cell.

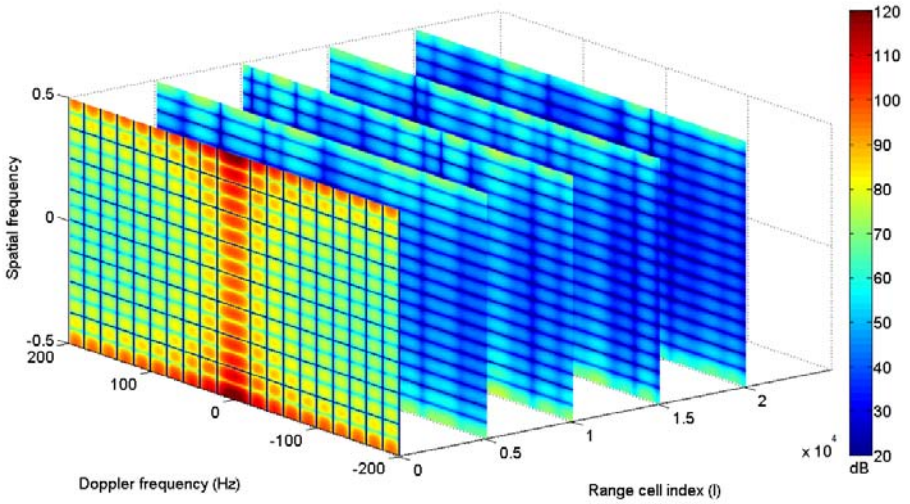

Fig. 4.6: Power spectrum of the direct path and its sidelobes snapshots along different range cells.

Fig. 4.7 depicts the power spectrum for the strong clutter snapshot at range cell $l = 19$ (range sum of 20.6 Km) and its corresponding random range sidelobes. The short ridge on the positive Doppler frequencies that originate from the zero Doppler corresponds to the short range sum clutter. For the simulation configuration, the isorange sum contours from this range cell lies within the ground baseline of the bistatic geometry. Thus, the spatial and Doppler frequencies of the clutter ridge span from –0.5 to –0.235 and 0 Hz to 106 Hz respectively. The power profiles at further range cells ($l > 19$) shows the corresponding random range sidelobes of this strong clutter. In addition to the spread in Doppler, the random range sidelobes are also spread in spatial frequencies (as opposed to a discrete direction for the direct path random range sidelobes) which correspond to the spatial frequency span of the contributing clutter. As seen, the sidelobes coupling of this strong clutter are significantly weaker than that of the direct path random range sidelobes but still above that of the thermal noise (at 0 dB). At a given spatial frequency, the average value of the random range sidelobes is still approximately $10\log_{10}(1/MBT_{sub})$ dB lower than the peak value of the corresponding clutter at the same spatial frequency. Next, Fig. 4.8 depicts the power spectrum for the clutter snapshot at range cell $l = 999$ (range sum of 50 Km) and

its corresponding random range sidelobes. The disjointed diagonal clutter ridge span across all the normalized spatial and Doppler frequencies and so is its corresponding random range sidelobes. Given the weaker power level for this further range sum clutter, its corresponding random range sidelobes is calculated to be below that of the thermal noise as shown. In essence, the random range sidelobes of the clutter spanned the spatial frequencies according to its contributing clutter as opposed to a discrete direction for the direct path random range sidelobes.

Fig. 4.9 depicts the power spectrum for the noise snapshots. Obviously, the expected value across all the snapshots will have a mean value of 0 dB.

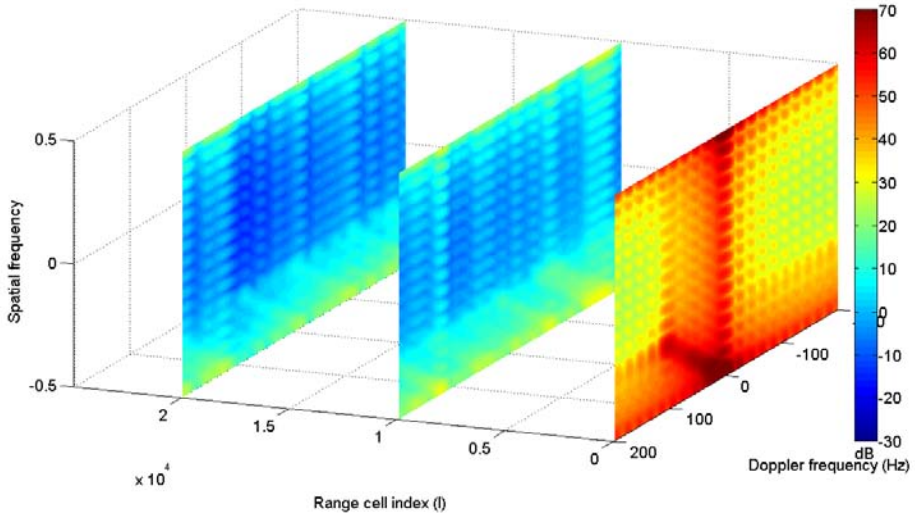

Fig. 4.7: Power spectrum of the strong clutter at range cell $l = 19$ and its sidelobes snapshots along different range cells.

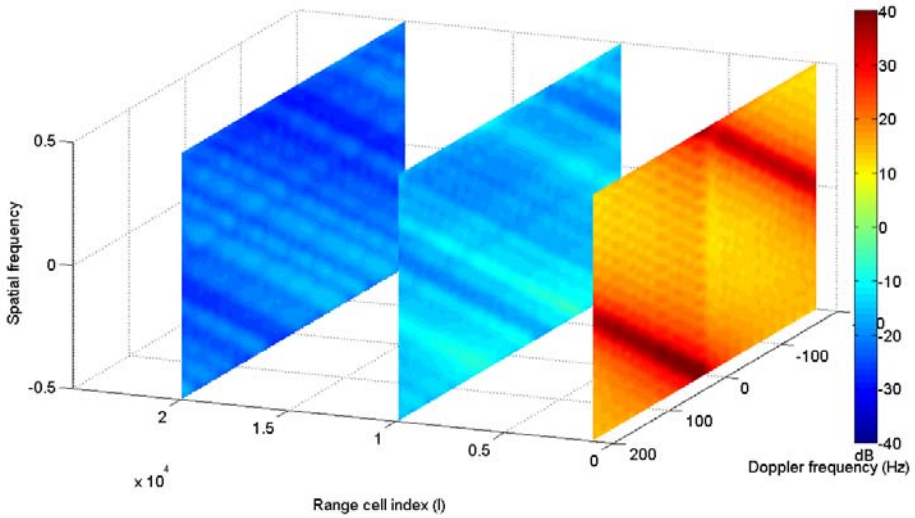

Fig. 4.8: Power spectrum of the clutter at range cell $l = 999$ and its sidelobes snapshots along different range cells.

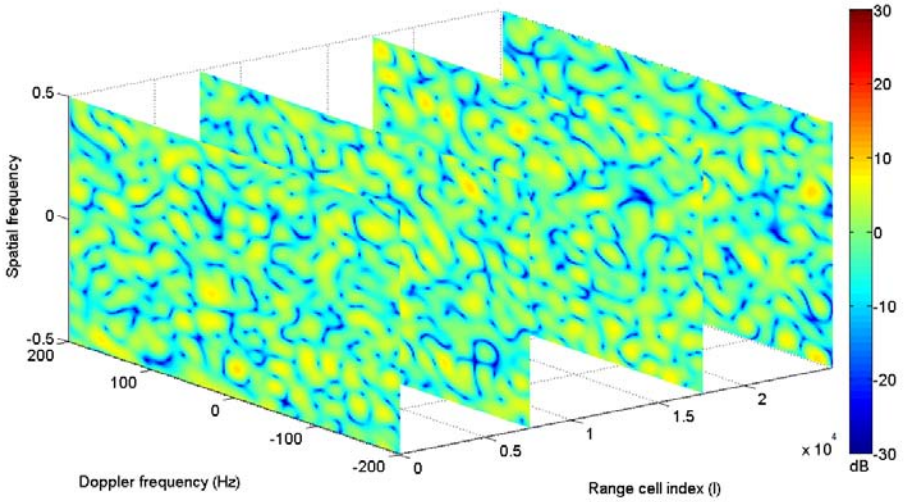

Fig. 4.9: Power spectrum of noise snapshots along different range cells.

The snapshots estimates for each contributing components to the interference scenario is generated for $K_e = 2MN = 640$ range cells centered at the range sum of 50 Km (detection range cell $l_d = 999$). This range sum of 50 Km has a distance of 15 Km away from the airborne passive radar along the extended baseline. Thus, the SCM estimate $\widehat{\mathbf{R}}_u$ of the interference scenario for the side-looking airborne passive radar can be computed by averaging over the $2MN$ snapshots. Fig. 4.10 depicts the MVDR spectrum of the side-looking configuration for the case where only the clutter, direct path random range sidelobes and noise are present. The disjointed diagonal clutter ridge as well as the direct path random range sidelobes coupling into $\widehat{\mathbf{R}}_u$ can be prominently seen. The pedestal of the spectrum is that of thermal noise. The parallel ridge along the Doppler frequency axis ($\vartheta = -0.5$) represents the direct path random range sidelobes coupling into $\widehat{\mathbf{R}}_u$. In any case, the direct path sidelobes will always be localized to the spatial frequency of the non-cooperative transmitter with respect to the antenna array. Next, Fig. 4.11 depicts the MVDR spectrum of the interference scenario for the composite interfering signals as received by the airborne passive radar which includes the random range sidelobes coupling effects of $N_{sc} = 298$ strong clutter. It is calculated that the sidelobes couplings of these strong clutter will be higher than thermal noise at l_d. The spectrum shows a much higher pedestal on all spatial frequencies attributed by the $N_{sc} = 298$ strong clutter random range sidelobes couplings into $\widehat{\mathbf{R}}_u$. At short range sum, these sidelobes of the strong clutter are concentrated around the spatial frequency (direction) of the transmitter since its range sum lies within the ground baseline of the bistatic geometry (its spatial frequency span is limited). As the index of the strong clutter increases, the spatial frequencies spreading will be more apparent due to the increasing isorange sum which covers a larger spatial frequency span. Thus, the pedestal of Fig. 4.11 (due to the random range sidelobes of the $N_{sc} = 298$ strong clutter) is more elevated around the spatial frequency of the direct path random range sidelobes. Further conclusion on the clutter random range sidelobes properties could be drawn. For increasing range sum, the Doppler bandwidth of the clutter increases where it also exhibits a larger span of spatial frequencies (Figs. 4.7 and 4.8). In analogous, the level of random range sidelobes coupling of the strong clutter into $\widehat{\mathbf{R}}_u$ will be lower since it occupies a larger span of spatial frequencies. Furthermore, as the range sum increases, its CNR will also be weaker (Fig. 4.5).

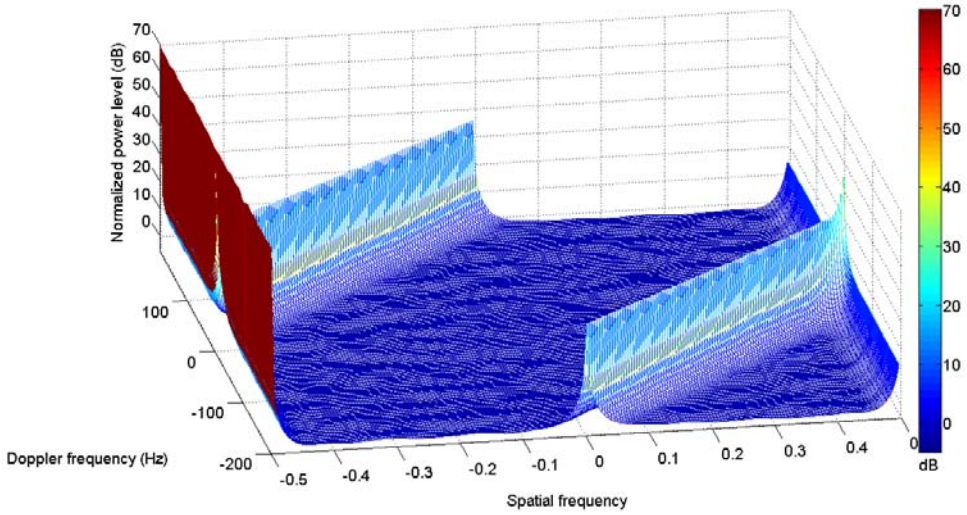

Fig. 4.10: MVDR spectrum for side-looking airborne passive radar (centered at R_{sum} = 50 Km) using the random signal (clutter, direct path random range sidelobes and noise components only).

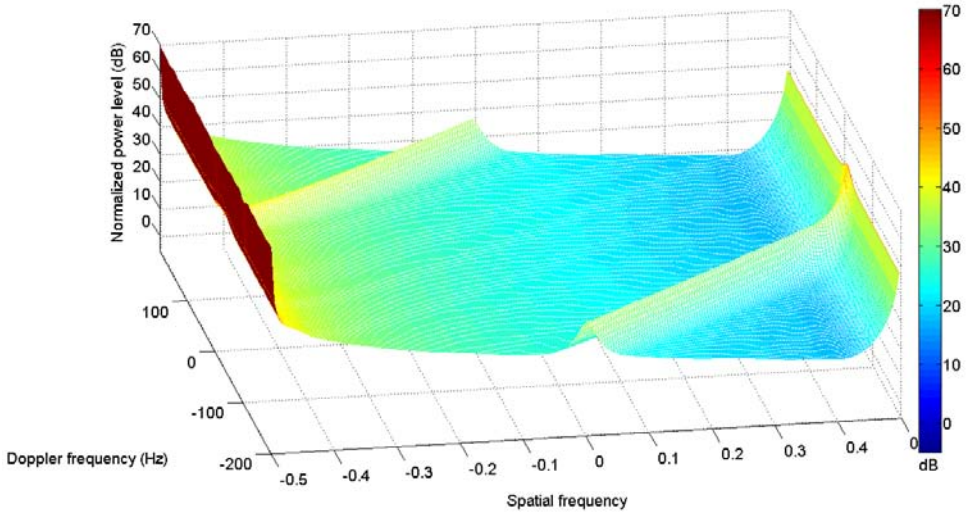

Fig. 4.11: MVDR spectrum for side-looking airborne passive radar (centered at R_{sum} = 50 Km) using the random signal for the interferences scenario in Fig. 4.1.

Fig. 4.12 depicts the MVDR spectrum for the same interference scenario as in Fig. 4.11 but simulated using the LFMCW signal. Here, other than the clutter ridge that is present, a single peak (unique Doppler frequency of 0 Hz) due to the sidelobes of the direct path is evident given that the LFMCW signal is coherent from pulse-to-pulse. The direct path range sidelobes level (52.6 dB) of the LFMCW signal is less significant (compared to the random signal) since its range sidelobes is considerably lower around range cell l_d. For the range sidelobes of the strong clutter, due to the coherency of the LFMCW signals, these sidelobes are spatially and temporally correlated whose spatial-Doppler profile lies exactly on the clutter ridge diagonal of $\widehat{\mathbf{R}}_u$. These sidelobes of the strong LFMCW clutter are much lower in level in comparison to the clutter in $\widehat{\mathbf{R}}_u$ and therefore are embedded within. Thus, the coherent range sidelobes of the direct path and strong clutter of the LFMCW signal do not increase the overall rank of the interference covariance matrix.

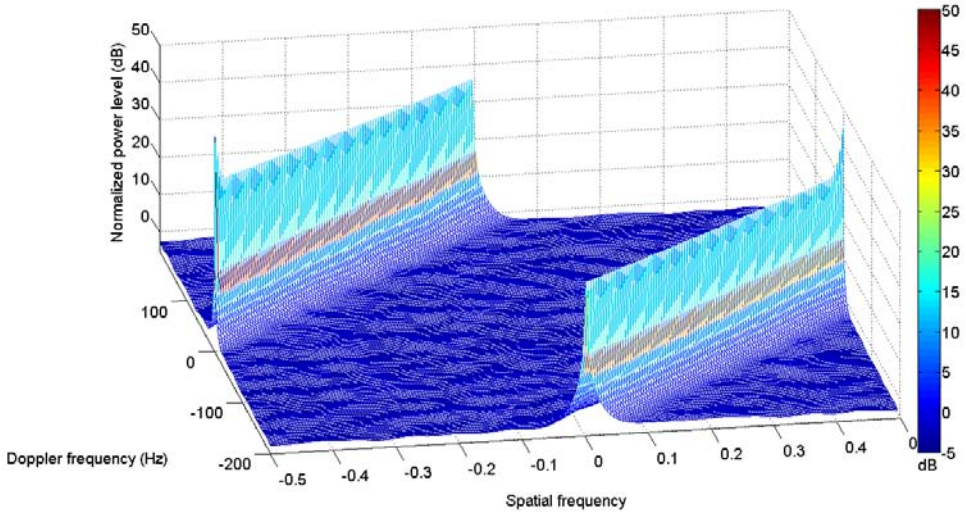

Fig. 4.12: MVDR spectrum for side-looking airborne passive radar (centered at R_{sum} = 50 Km) using the LFMCW signal for the interference scenario in Fig. 4.1.

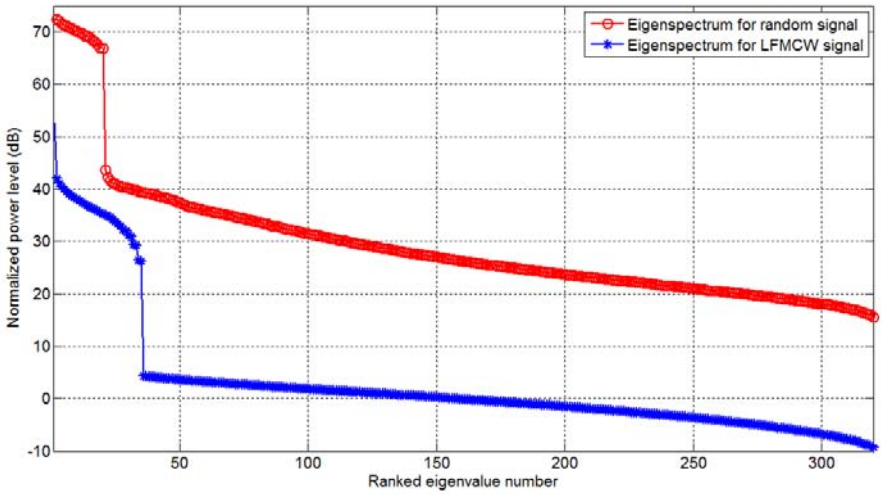

Fig 4.13: Eigenspectrum for side-looking airborne passive radar (centered at R_{sum} = 50 Km) using the random and LFMCW signal.

Fig. 4.13 depicts the interference eigenspectrum for the side-looking configuration for both the random and LFMCW signals yielding the MVDR spectra of Figs. 4.11 and 4.12 respectively. The rank of the clutter only covariance matrix is approximately $\lfloor N + (M-1)\beta \rfloor \approx 35$. In the case of the LFMCW signal, the rank of the significant eigenvalues is the same as that of the clutter only scenario since the direct path and strong clutter range sidelobes couplings are superimposed on the clutter and thus do not add to the overall rank. However, the eigenvalue of the direct path coherent sidelobes is higher than the clutter, thus a single spike on the eigenspectrum as shown. For the case utilizing the random signal, the number of eigenvalues above the noise floor increases dramatically with the random range sidelobes couplings of the direct path and of the strong clutter $\widehat{\mathbf{R}}_u$. The first M eigenvalues correspond to that of the direct path sidelobes which is the strongest in $\widehat{\mathbf{R}}_u$, making MTI close to the spatial frequency a big challenge. The clutter and strongest clutter random range sidelobes exhibit similar power level and thus their corresponding eigenvalues cannot be prominently separated in the eigenspectrum. The strong clutter sidelobes cause a severe

increase of nonzero eigenvalues as evident by the roll-off of the eigenspectrum well above the noise floor. Although its level is at least 30 dB lower than that of the direct path random range sidelobes, these sidelobes couplings of the strong clutter spanned over all the spatial frequencies which means its covariance matrix is of full rank.

4.3.2 Forward-looking configuration

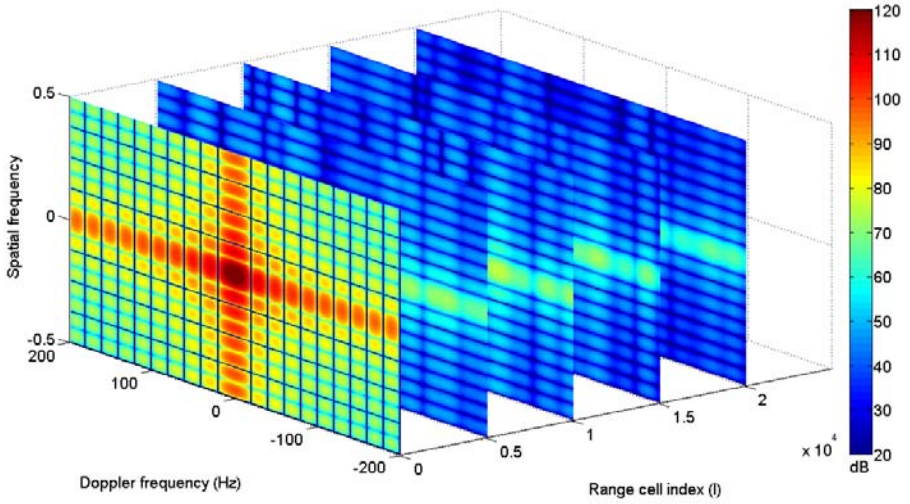

Fig. 4.14: Power spectrum of the direct path and its sidelobes snapshots along different range cells.

For the forward-looking configuration, the absolute spatial and Doppler frequency of the direct path reference signal is 0 and 200 Hz respectively. Fig. 4.14 depicts the power spectrum for the direct path snapshot and its corresponding random range sidelobes snapshots along incremental range cells. In the geometry, the direct path enters the airborne passive radar at the array broadside ($\vartheta_{dp} = 0$) while the Doppler frequency is neutralized (0 Hz) since it represents the relative Doppler frequency after matched filter processing and likewise for the Doppler frequency (after matched filtering) of the clutter. The analyses for the direct path and its corresponding random range sidelobes for the forward-looking configuration follow exactly that for the side-looking configuration where as shown, the average value of the sidelobes is approximately $10\log_{10}(1/MBT_{sub})$ dB lower than the peak value of the direct path at the origin range cell. Figs. 4.15 and 4.16 depicts the power spectrum for the strong clutter snapshot at range cell $l = 9$ (range sum of 20.3 Km) and $l = 19$ (range sum of 20.6 Km) and their corresponding random range sidelobes respectively. For the forward-looking configuration, the Doppler frequency of clutter exhibit only negative Doppler frequencies and it is symmetrical about the array axis normal (velocity vector). Comparing Figs. 4.15 and 4.16, the spatial-Doppler clutter profile variation for short range clutter is evident as explained in Section 2.6.3 for the forward-looking configuration. The spatial and Doppler frequency span of the short range clutter is dependent on the range sum according to the geometry. Short range clutter exhibits a circular spatial-Doppler profile and the circle become larger with increasing range sum, i.e. thus the clutter spatial-Doppler frequency dependency on the range sum. For range sum larger than the ground baseline, the circle begins to open up and finally degenerate into a semicircle when $R_{sum} \gg R_{RT}$. The spatial-Doppler profile variation stabilizes at further range where for this forward-looking geometry, the range dependent problem of the clutter no longer persists for $R_{sum} > 30$ km ($l > 332$) as seen in Fig. 2.14(b). For these non-stationary (range dependent) short range clutter, its

corresponding random range sidelobes will not be implicated since they will be spread in Doppler in any case. The random range sidelobes of the strong clutter will manifest as a severe interference coupling into further range cells as apparent in the MVDR spectrum. Next, Fig. 4.17 depicts the power spectrum for the clutter snapshot at range sum $l = 999$ (range sum of 50 Km) and its corresponding random range sidelobes snapshots. The clutter exhibit a semicircle spatial-Doppler profile which spanned across all normalized spatial and negative Doppler frequencies. Its corresponding random range sidelobes is simulated to be below that of the thermal noise as shown. Clutter range cells for $l > 332$ are range independent and thus clutter snapshots around this range sum of $l = 999$ are considered to be stationary.

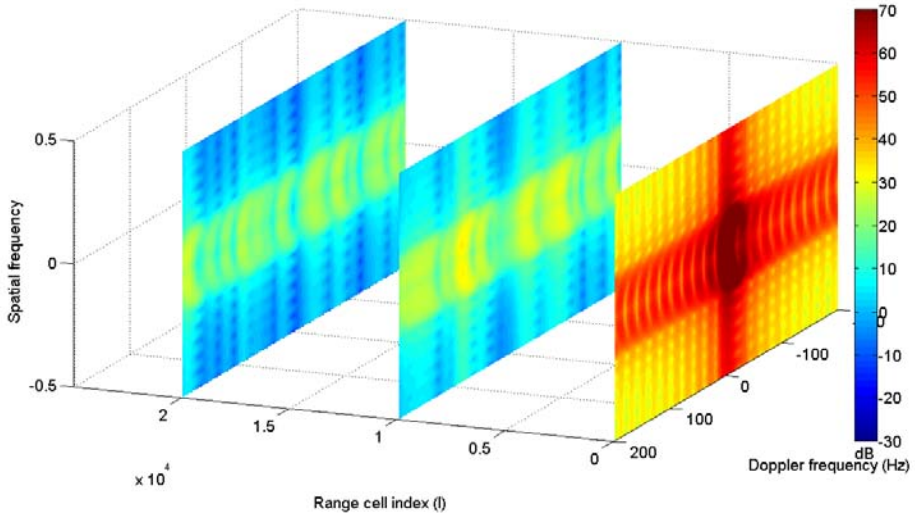

Fig. 4.15: Power spectrum of the strong clutter at range cell $l = 9$ and its sidelobes snapshots along different range cells.

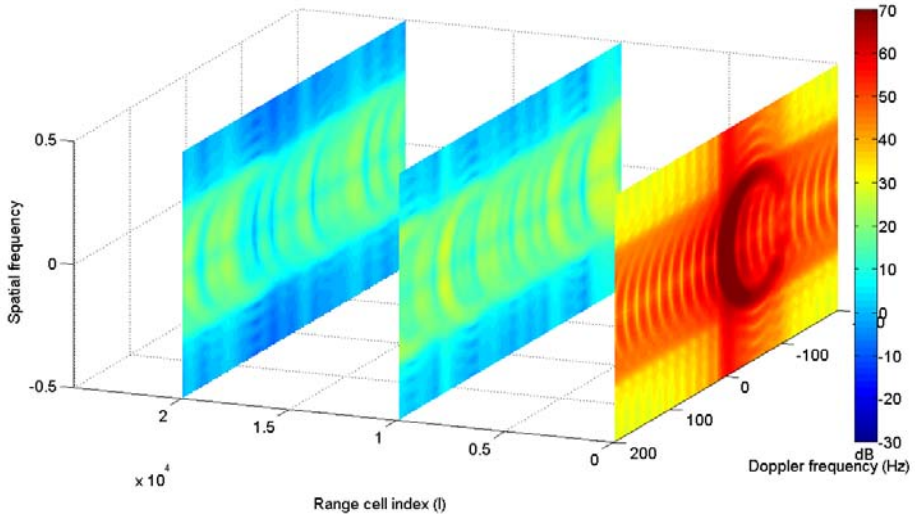

Fig. 4.16: Power spectrum of the strong clutter at range cell $l = 19$ and its sidelobes snapshots along different range cells.

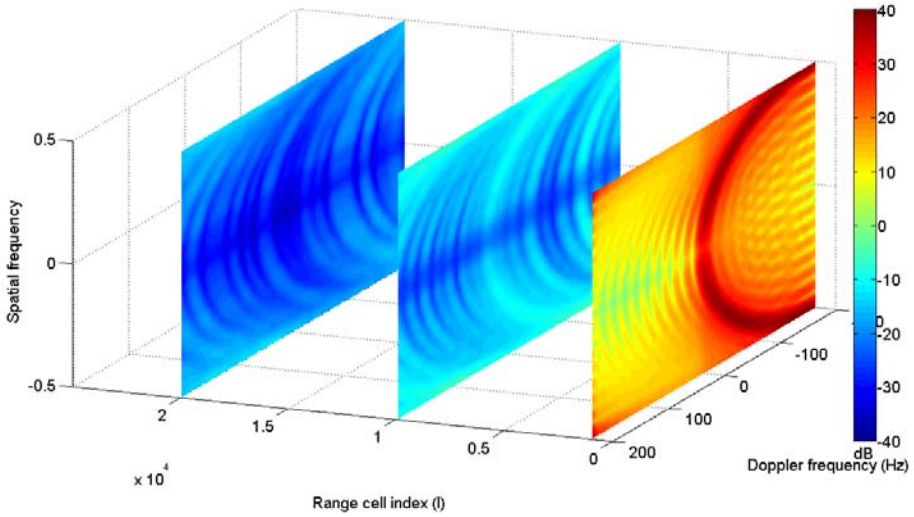

Fig. 4.17: Power spectrum of the clutter at range cell $l = 999$ and its sidelobes snapshots along different range cells.

As in the side-looking configuration, $2MN$ interference snapshots estimates centered at the range sum of 50 Km (detection range cell $l_d = 999$) are averaged and used to form the SCM estimate $\widehat{\mathbf{R}}_u$ of the interference scenario for the forward-looking airborne passive radar. Fig. 4.18 depicts the MVDR spectrum for the interference scenario of the forward-looking airborne passive radar. It is clear that Fig. 4.18 shows a severe interference scenario for the forward-looking configuration with the non-cooperative transmitter located at the array broadside. The semicircle ridge on the negative Doppler frequencies corresponds to the relative Doppler frequency of the stationary clutter in $\widehat{\mathbf{R}}_u$ after matched filter processing. The ridge along the Doppler frequency axis ($\vartheta = 0$) represents the random range sidelobes coupling of the direct path into $\widehat{\mathbf{R}}_u$. The spectrum shows a much higher pedestal on all spatial frequencies attributed by the random range sidelobes of the $N_{sc} = 139$ strong clutter (sidelobes coupling higher than thermal noise at l_d) where these undesirable couplings are close to overwhelming the clutter in $\widehat{\mathbf{R}}_u$. Similarly, the random range sidelobes of the strong clutter will be concentrated around the spatial frequency of the non-cooperative transmitter where its span increases with increasing range sum. Thus, the pedestal of the random range sidelobes of the strong clutter signal is elevated around the spatial frequency of the direct path random range sidelobes as Fig. 4.18 illustrates. Fig. 4.19 depicts the MVDR spectrum for the same interference scenario as in Fig. 4a but simulated using the LFMCW signal. As before, due to the coherent range sidelobes of the LFMCW signal, the sidelobes of the direct path exhibit a single peak (unique Doppler frequency of 0 Hz) as shown. Short range clutter (clutter at range sum $\leq$ 30 Km for the forward-looking geometry) are non-stationary due to the misaligned angle (90°) of the antenna array with respect to the passive radar velocity vector. Thus the corresponding sidelobes of these strong clutter will not be embedded within the clutter that is present in $\widehat{\mathbf{R}}_u$. Fortunately, the sidelobes of these short range non-stationary strong clutter are much lower in level and therefore the corresponding range sidelobes coupling are not very noticeable in the power spectrum. However, these effects will be more apparent in the eignespectrum as shown next.

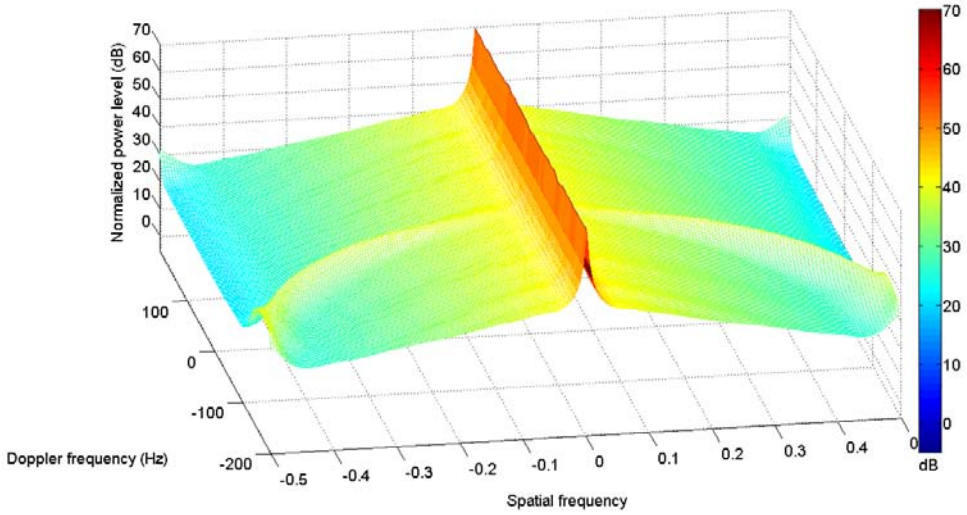

Fig. 4.18: MVDR spectrum for forward-looking airborne passive radar (centered at R_{sum} = 50 Km) using the random signal for the interferences scenario in Fig. 4.2.

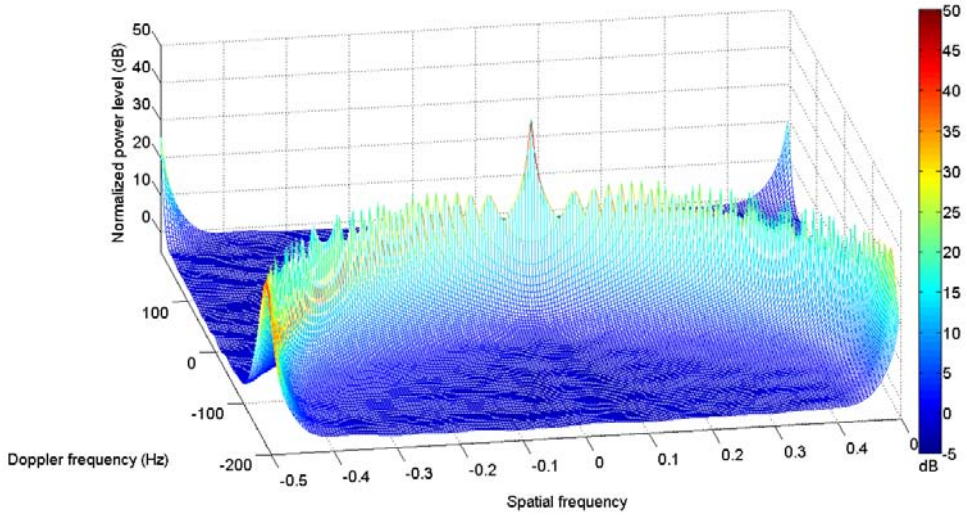

Fig. 4.19: MVDR spectrum for forward-looking airborne passive radar (centered at R_{sum} = 50 Km) using the LFMCW signal for the interference scenario in Fig. 4.2.

Fig. 4.20 depicts the interference eigenspectrum for the forward-looking configuration for both the random and LFMCW signals yielding the MVDR spectra of Fig. 4.18 and 4.19 respectively. For the LFMCW signal, its eigenspectrum exhibit a gradual decrease as opposed to the sharp cutoff for the same LFMCW signal in the side-looking configuration. As mentioned, this is due to the random range sidelobes couplings of the strong non-stationary clutter which are not buried within the clutter in $\widehat{\mathbf{R}}_u$. Nevertheless, these eigenvalues are extremely small given the much lower level of the range sidelobes of the LFMCW signal at range cells around l_d. For the case utilizing the random signal, the number of eigenvalues above the noise floor increases dramatically with the coupling of the direct path and strong clutter random range sidelobes into $\widehat{\mathbf{R}}_u$. Again, the first M eigenvalues correspond to that of the direct path sidelobes, making MTI at the array broadside a big challenge. The clutter and strongest clutter random range sidelobes also exhibit similar power level and thus its corresponding eigenvalues cannot be prominently separated in the eigenspectrum. The strong clutter sidelobes cause a severe increase of nonzero eigenvalues with span across all the

spatial frequencies. Thus, its covariance matrix is of full rank. The increase of pedestal in $\widehat{\mathbf{R}}_u$ for the forward-looking configuration is slightly worse off than in the side-looking configuration. This is due to the higher level of random range sidelobes coupling of the short range clutter (stronger CNR) in the forward-looking configuration.

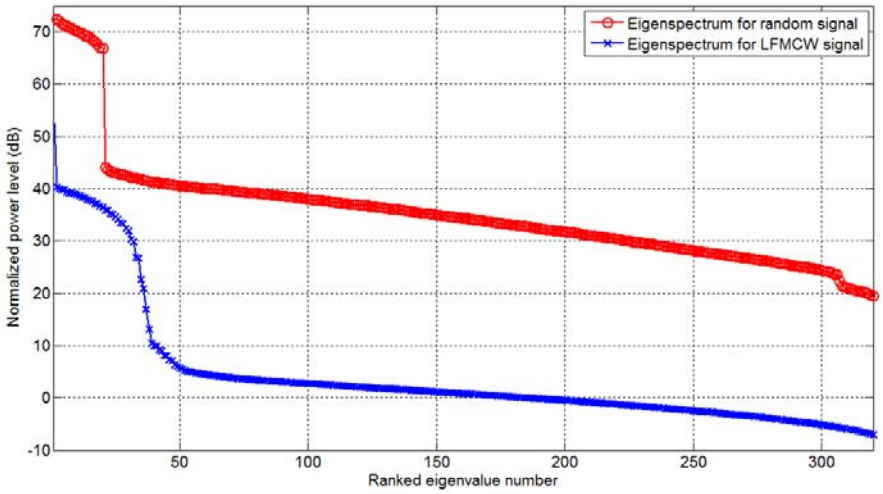

Fig 4.20: Eigenspectrum for forward-looking airborne passive radar (centered at R_{sum} = 50 Km) using the random and LFMCW signal.

4.3.2 Results summary and discussions

The random range sidelobes couplings of the direct path and of the strong clutter and the passive signal attributes are important considerations on moving target detection performance for the airborne passive radar. For both the side-looking and forward-looking configurations, these undesirable random range sidelobes seriously exacerbate the interference covariance matrix of $\widehat{\mathbf{R}}_u$. First, the direct path random range sidelobes coupling cause the formation of a spatial frequency dependent Doppler ridge that is well above the level of the clutter in $\widehat{\mathbf{R}}_u$. Secondly, due to the severe random range sidelobes coupling of the strong clutter that spanned over all spatial frequencies, the pedestal of $\widehat{\mathbf{R}}_u$ is seriously elevated. These undesired sidelobes coupling effects of the direct path and of the strong clutter into further range cells for the passive signal are in stark contrast to that of a coherent signal which does not possess such sidelobes coupling issues. From the eigenspectrum, it is clearly evident that both the random range sidelobes of the direct path and of the strong clutter exhibit severe coupling effects which induce strong eigenvalues in the eigenspectrum. The undesirable increase of pedestal in $\widehat{\mathbf{R}}_u$ for the forward-looking configuration is worse off than in the side-looking configuration since its short range clutter exhibit stronger CNR as calculated. In both side-looking and forward-looking scenarios, if nothing is done to suppress these strong clutter (which equates to suppressing its associated random range sidelobes couplings), target detection at range cell l_d will be random range sidelobes limited instead of the noise limited case of the typical active airborne Doppler radar. Thus, the airborne passive radar performance will be severely degraded.

4.4 Signal processing overview for moving target detections

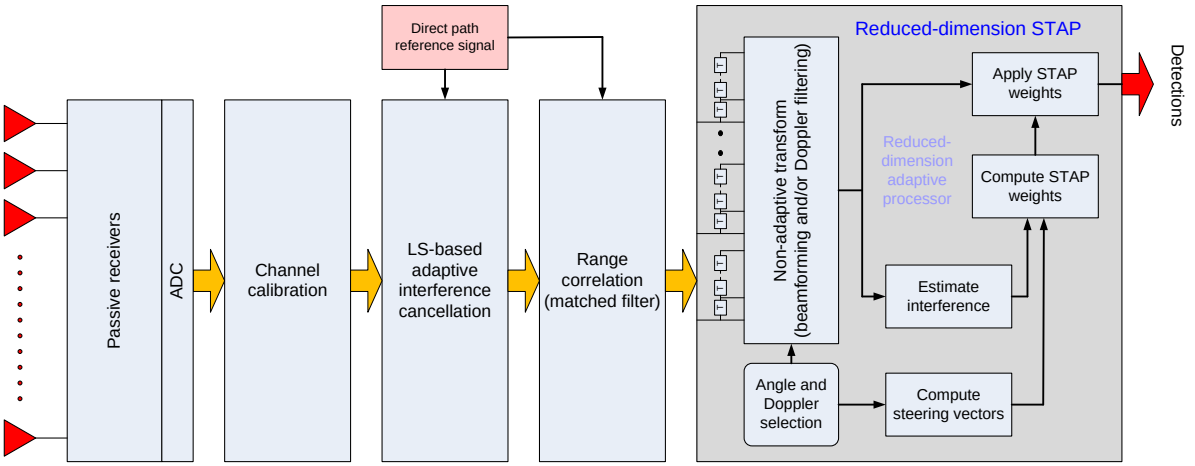

Fig. 4.21: Signal processing for the airborne passive radar.

Recall that the major attributes of the airborne passive radar are its flexible sub-CIT repetition frequency (unambiguous in Doppler), operation in VHF/UHF band and a moderate size antenna array mounted in the side-looking and forward-looking configurations. The interference environment for the airborne passive radar is always severely characterized by the high levels of direct path and clutter against the thermal noise background. The random range sidelobes couplings of these interfering signals will seriously exacerbate the background interference. Simulations in the preceding Sections envisage the degree of severity of the random range sidelobes couplings of the direct path and of the strong clutter on the spatial-Doppler spectrum and eigenspectrum profiles of both the side-looking and forward-looking airborne passive radar. These severe interference are in addition to the spatial-Doppler dependent clutter that are present at range cell l_d which if not mitigated, target detection would be virtually impossible. Effective signal processing schemes that are able to suppress these interfering signals for improved MTI performance in the airborne passive radar are detailed and investigated in Chapter 3. As such, the overall signal processing schemes associated with the airborne passive radar is illustrated in Fig. 4.21. The N-elements antenna array, together with the N-channel airborne passive radar receiver system, convert the RF passive signal received at each element to an IF suitable for complex sampling where the ADC digitizes and stores the complex baseband samples. The data from each channel are then unpacked and reformatted for subsequent digital signal processing. In order to fully realize the potential of the N-channels receiver system requires effective channel calibration to compensate for various non-ideal and dissimilar practical effects among the receiving channels. This includes amplitude and phase mismatch between physical receiving channel components and amplitude and phase mismatch between connections and cablings in the different channels. A correction matrix, to be calculated in the signal frequency-domain, is generally used to encapsulate all these non-ideal effects (components, connections, cablings, etc.) in the system and eventually used to compensate for these errors. The correction matrix between a reference and the other channels are estimated from a common signal (split using a power splitter) collected at each of the channel output where the amplitude and phase weightings are computed in the signal frequency-domain to form the matrix for compensation. It should be pointed out that the mismatch errors due to the antenna element are not considered in the calibration process and the insignificant errors induced by the power splitter are ignored. Following that will be the two main signal processing blocks

for MTI for the airborne passive radar; namely the LS-based adaptive interference cancellation and reduced-dimension STAP. The adaptive interference cancellation is used to suppress the direct path, zero-Doppler strong clutter as well as the Doppler shifted strong clutter signals so that its corresponding random range sidelobes that manifest into $\widehat{\mathbf{R}}_u$ will also be suppressed by the same amount. Subsequently, any residual random range sidelobes couplings that remains and that of the spatial-Doppler dependent stationary clutter at the detection range cell l_d will be suppressed by reduced-dimension STAP prior to detections. Simulations and results analyses for both the side-looking and forward-looking configuration will be discussed in the remaining part of this Chapter.

4.5 Adaptive interference cancellation results and analyses

After the N received signals at the output of the passive receiver channels had been calibrated where the amplitude and phase errors/mismatches between channels compensated, adaptive FIR filtering will be implemented to estimate the weight coefficients for interference cancellation of the direct path and strong clutter signals prior to matched filter processing. Both the direct path reference signal and the received signal are the inputs of the adaptive FIR filter where the LS-based adaptive cancellation algorithm is able to suppress the direct path, zero-Doppler strong clutter as well as the Doppler shifted strong clutter signals present in the received signal. In mitigating these interfering signals, its corresponding random range sidelobes that manifest into $\widehat{\mathbf{R}}_u$ will also be suppressed by the same amount, diminishing these undesirable coupling effects on the target. The concept and formulation of the adaptive interference cancellation algorithm had been detailed in Chapter 3. Its cancellation performance on the signals received by the airborne passive radar for the interference scenario on both the side-looking and forward-looking configuration will be analyzed and discussed in this Section.

4.5.1 Side-looking configuration

The passive signal received from any given element for the side-looking airborne passive radar according to the interference scenario as computed in the preceding Section is depicted in Fig. 4.22 as the cross-ambiguity function coherent processing plot and corresponding Doppler cell cuts. Fig. 4.22 shows the result without the application of the adaptive interference cancellation processing. Only $N_{sc} = 298$ strong clutter are included in the received signal since it is computed that the random range sidelobes coupling for $N_{sc} > 298$ strong clutter are trivial (below thermal noise at the detection range cell l_d) for the side-looking configuration. In addition, for ease of performance analysis, clutter at further range cells $l \geq 298$ are not added to the received signal so that the pedestal level (around l_d) before and after the application of the adaptive interference cancellation will be clearly evident for the purpose of performance analysis. On the ambiguity surface, the direct path (0 Hz at origin range cell) has a peak value of 111 dB (DNR per element per sub-CIT of 98 dB + $10\log_{10} M$ dB) where surrounding it are the strong clutter and Doppler-shifted strong clutter spread across all 20 Doppler cells and in range cell index up to $l = 297$. Most of these strong clutter are all seemingly buried by the random range sidelobes of the direct path. Thus, the pedestal (due to sidelobes of the direct path) is approximately $10\log_{10}\left(1/(BT_{sub}M)\right)$ dB lower than the peak value of the DNR. On the spatial-Doppler spectrum, this pedestal that is associated with the random range sidelobes of the direct path will be localized in a single spatial frequency of the direct path ($\vartheta_{dp} = -0.5$) as a parallel ridge along the Doppler frequency axis. However, the pedestal that is associated to the random range sidelobes of the

strong clutter will occupy the entire span of spatial frequencies, severely degrading moving target detection performance. Next, Fig. 4.23 depicts the resultant cross-ambiguity function coherent processing plot and corresponding Doppler cell cuts where the adaptive interference cancellation algorithm is used to suppress the direct path, strong clutter and Doppler-shifted strong clutter components in the received signal of Fig. 4.22. Ideally, the adaptive FIR filtering should be performed with a 298^{th}-order (at least) filter across all 20 Doppler cells. However, due to reasons of computational and memory load processing issues, this requirement cannot be satisfied. Thus, only a 220^{th}-order adaptive FIR filter across 17 Doppler cells is used since the Doppler-shifted clutter in the last 3 Doppler cells are relatively weaker. As shown, nulls can be prominently seen over the range and Doppler cells that the algorithm operates on which demonstrate that all these interfering components present in these cells ($l \leq 219$ and across 17 Doppler cells) had been effectively suppressed. Residual clutter at the further range cells ($l > 219$) are not suppressed and remains. The resulting pedestal is now due to that of the remaining clutter and comparing with Fig. 4.22, this pedestal is significantly lower.

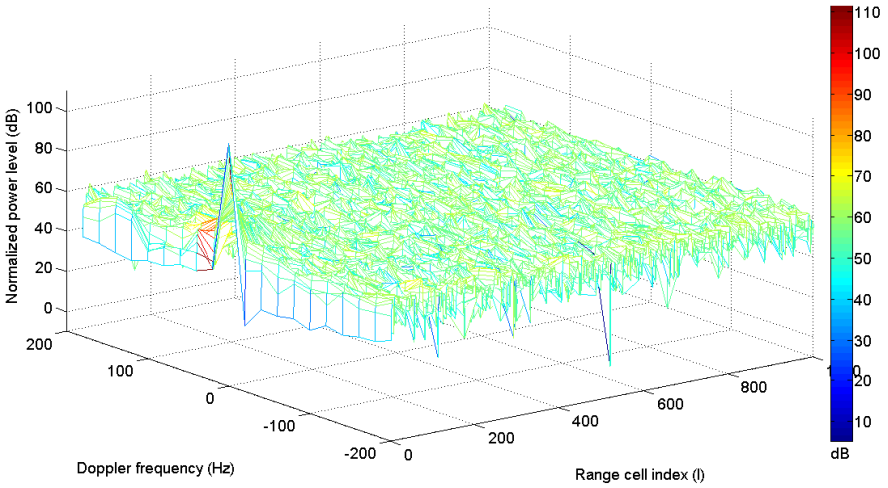

(a)

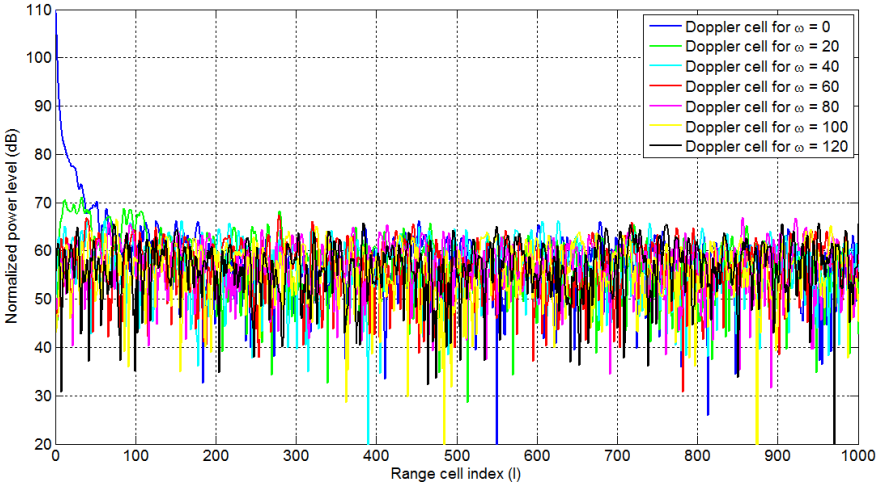

(b)

Fig. 4.22: (a) Ambiguity function plot and corresponding (b) Doppler cell cuts for a single element without adaptive interference cancellation.

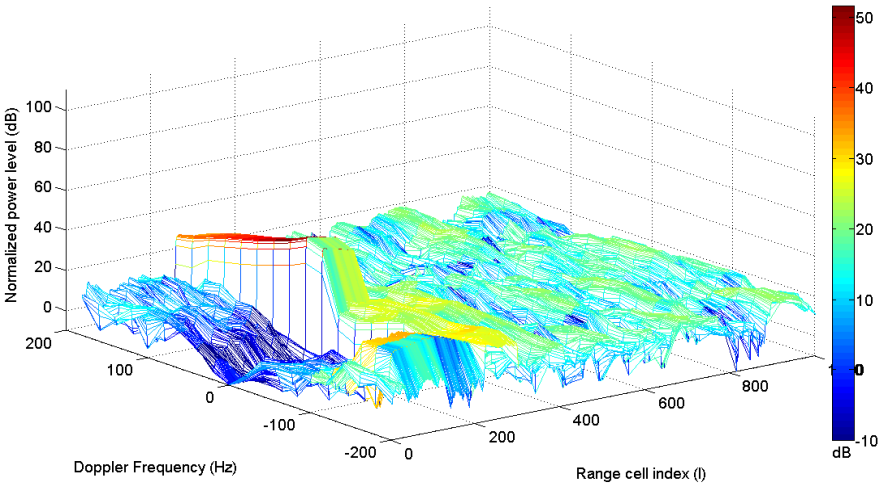

(a)

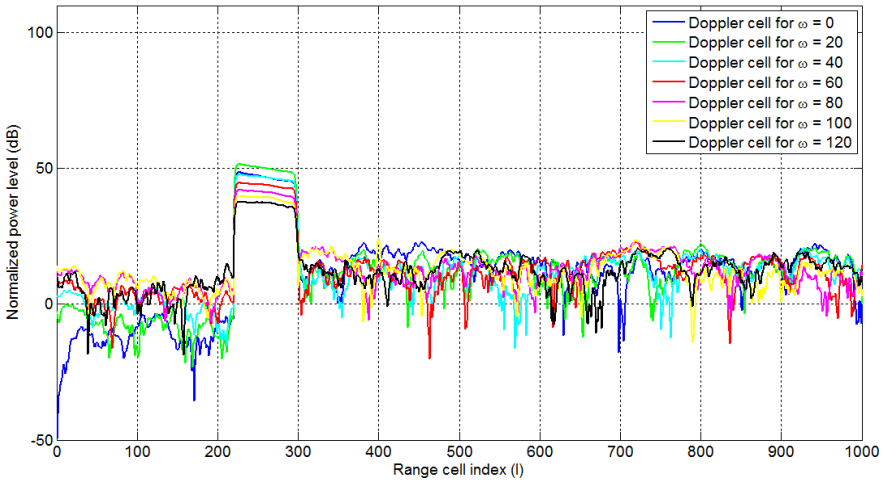

(b)

Fig. 4.23: (a) Ambiguity function plot and corresponding (b) Doppler cell cuts for a single element after applying the 220th-order adaptive interference cancellation.

4.5.2 Forward-looking configuration

Fig. 4.24 depicts the forward-looking airborne passive radar resultant cross-ambiguity function coherent processing plot and corresponding Doppler cell cuts for the passive signal received from any given element. It shows the result without the application of the adaptive interference cancellation processing. As before, only $N_{sc} = 139$ strong clutter are included since the random range sidelobes coupling for $N_{sc} > 139$ strong clutter are trivial (below thermal noise at the detection range cell l_d) in the forward-looking configuration. Most of the strong clutter and Doppler-shifted strong clutter spread across all 20 Doppler cells and in range cell index up to $l = 138$ are all seemingly buried by the random range sidelobes of the direct path. Thus, the pedestal (due to sidelobes of the direct path) is approximately $10\log_{10}\left(1/(BT_{sub}M)\right)$ dB lower than the peak value of the DNR. Similarly, pedestal that is associated with the random range sidelobes of the direct path will be localized as a parallel ridge (single spatial frequency, $\vartheta_{dp} = 0$) along the Doppler frequency axis and pedestal associated with the strong clutter random range sidelobes occupy the entire span of spatial frequencies. Next, Fig. 4.25 depicts the resultant cross-ambiguity function coherent

processing plot and corresponding Doppler cell cuts where the 150th-order adaptive FIR filter across all Doppler cells is used to completely suppress the direct path, strong clutter and Doppler-shifted strong clutter components in the received signal of Fig. 4.24. As shown, nulls can be prominently seen over the range and Doppler cells that the algorithm operates on which demonstrated that all these interfering components that are present in the received signal had been effectively suppressed. The resulting pedestal is now due to that of thermal noise.

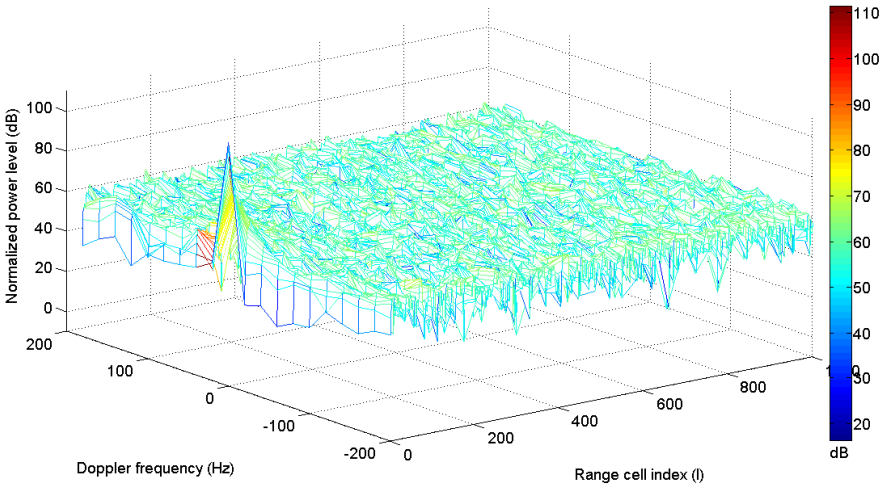

(a)

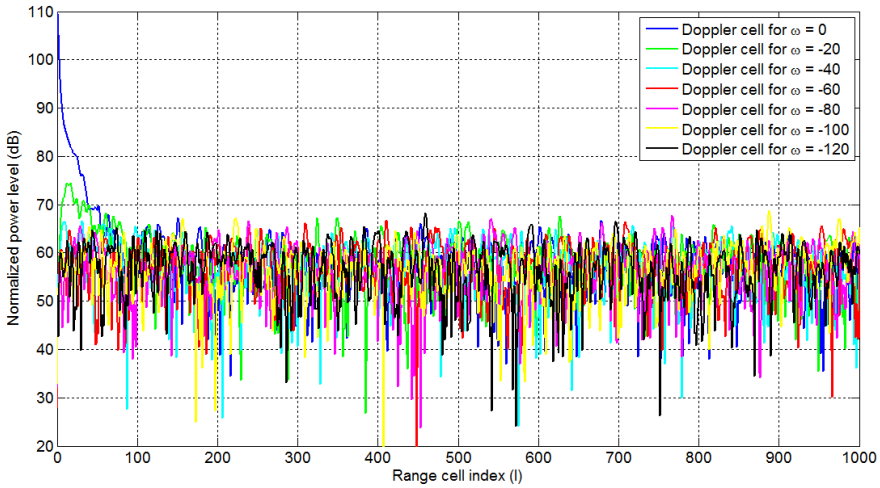

(b)

Fig. 4.24: (a) Ambiguity function plot and corresponding (b) Doppler cell cuts for a single element without adaptive interference cancellation.

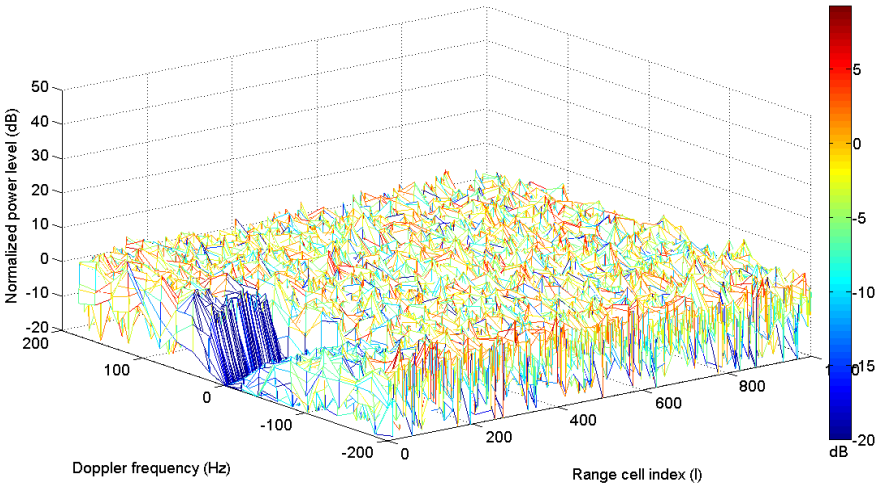

(a)

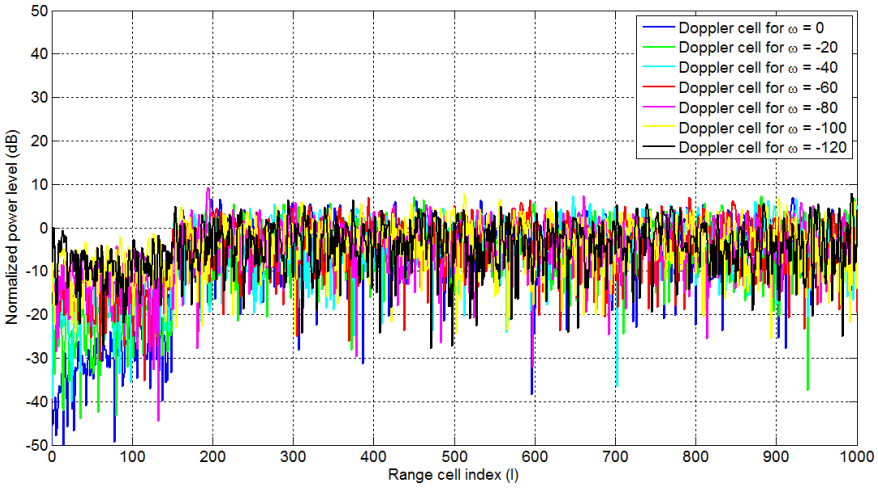

(b)

Fig. 4.25: (a) Ambiguity function plot and corresponding (b) Doppler cell cuts for a single element after applying the 150th-order adaptive interference cancellation.

4.5.3 Results summary and discussions

Without assimilating computational and memory load as a limiting factor, the results for the adaptive interference cancellation applied to the received signal for both side-looking and forward-looking configuration demonstrated the capabilities and effectiveness of the technique. The LS-based adaptive interference cancellation algorithm is able to effectively suppress the direct path, clutter and Doppler-shifted clutter signals received at each element which subsequently lower its corresponding random range sidelobes that manifest into detection range cell l_d by the same amount. This drastically decreases the significant eigenvalues of the interference covariance matrix. For the algorithm to operate effectively, the number of cancellation weights (FIR filter order) must be at least the number of N_{sc} strong clutter and across the Doppler cells where these N_{sc} strong clutter lies. Accordingly to the airborne passive radar simulations for the side-looking and forward-looking configurations, the dimension of the weights vector must be at least 5980×1 ($QP \times 1$ where $Q = 299$ and $P = 20$) and 2800×1 ($QP \times 1$ where $Q = 140$ and $P = 20$) respectively. Computing the weight vector requires inversion of the matrix $\mathbf{S}^H\mathbf{S}$ (dimension $QP \times QP$)

which requires on the order of $(5980)^3$ and $(2800)^3$ operations for the side-looking and forward-looking configurations respectively. Thus, the main drawback is such that the entail computational and memory load for the adaptive interference cancellation processing might not be within acceptable time necessary for real-time airborne passive radar operations. Another issue for the adaptive interference cancellation concerns the suppression of near range targets. As a matter of fact, near range targets that fall within the range and Doppler cells where the adaptive FIR filtering algorithm operates will be suppressed as well. For the airborne passive radar, this is more of less trivial since near range targets that are visible from the airborne passive platform are not of utmost importance in any case.

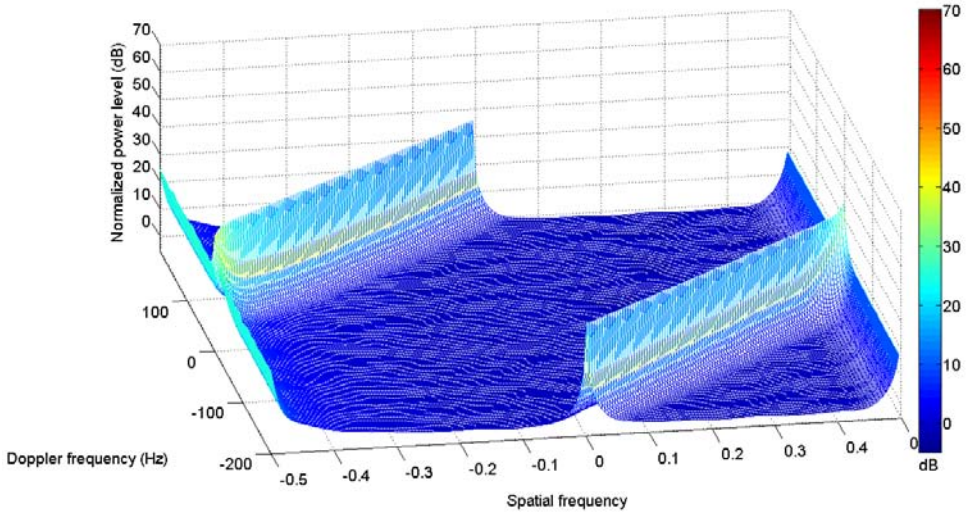

Fig 4.26: MVDR spectrum for side-looking airborne passive radar (centered at R_{sum} = 50 Km) using the random signal after adaptive interference cancellation.

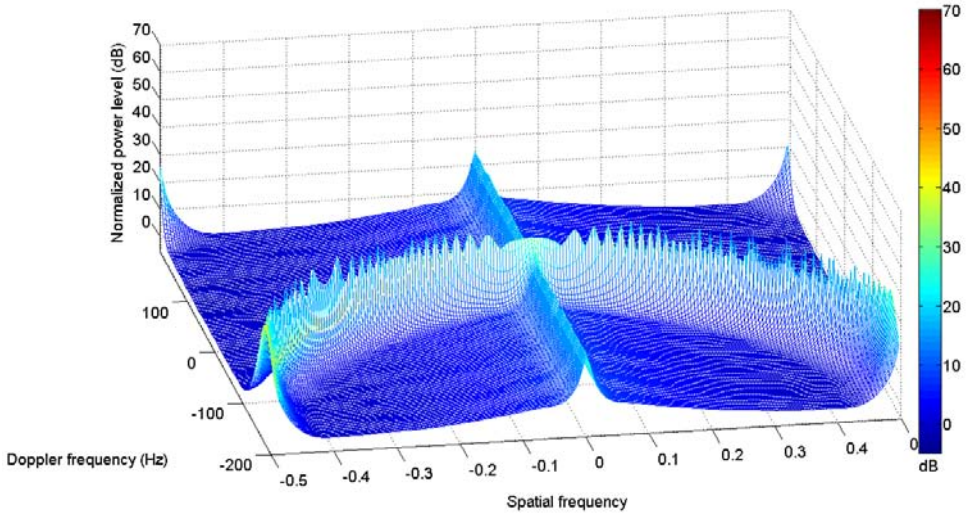

Fig 4.27: MVDR spectrum for forward-looking airborne passive radar (centered at R_{sum} = 50 Km) using the random signal after adaptive interference cancellation.

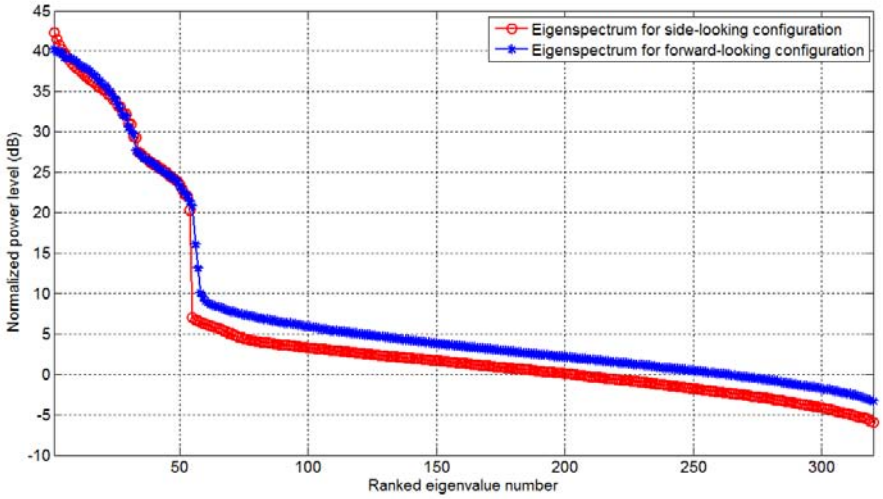

Fig 4.28: Eigenspectrum for side-looking and forward-looking airborne passive radar (centered at R_{sum} = 50 Km) after adaptive interference cancellation.

For the adaptive interference cancellation, the direct path reference signal serves as one of the two inputs for the adaptive FIR filter. As mentioned, the direct path reference signal is available to the processor either by beamforming or collected with an auxiliary antenna and is assumed to be ideal. In a practical scenario, the direct path reference signal will be corrupted due to various reasons such as a strong multipath environment, non-LOS to the non-cooperative transmitter, etc. Therefore, it is inevitable that the adaptive interference cancellation processing will suffer some degradation in performance where the interfering signals will not be fully cancelled. Hence, its associated random range sidelobes couplings will also not be completely suppressed at range cell l_d. In view of that, a practical concession will be made on the performance of the adaptive interference cancellation for the side-looking and forward-looking airborne passive radar. It is assumed that the LS-based adaptive interference cancellation algorithm is able to suppress the direct path coupling in the received signal at each element by 45 dB, and the strong clutter and Doppler-shifted strong clutter signals by an amount of 35 dB. In this case, their corresponding random range sidelobes coupling at further range cells will also be decreased by the same level. Thus, Fig. 4.26 depicts the MVDR spectrum of $\widehat{\mathbf{R}}_u$ for the side-looking configuration after applying the adaptive clutter cancellation algorithm where the direct path and all of the strong clutter (Doppler-shifted strong clutter included) are suppressed by 45 dB and 35 dB respectively. Similarly, Fig. 4.27 depicts the MVDR spectrum of $\widehat{\mathbf{R}}_u$ for the forward-looking configuration after applying the adaptive clutter cancellation algorithm where the interfering signals are seemingly suppressed by the same amount as the side-looking scenario. In both configurations, as prominently seen, the random range sidelobes of the direct path and of the strong clutter coupling in $\widehat{\mathbf{R}}_u$ had been significantly reduced. The direct path sidelobes coupling are significantly lowered (by 45 dB) to below the clutter level. In addition, a great amount of the random range sidelobes of the strong clutter had been suppressed to below thermal noise level. Fig. 4.28 illustrates the corresponding interference eigenspectra of Figs. 4.26 and 4.27. Both configurations exhibit similar eigenspectrum after applying the adaptive clutter cancellation algorithm. The eigenvalues due to the respective interference is now better separated with the strongest 35 eigenvalues corresponding to that of clutter followed by the subsequent 20 (M) eigenvalues corresponding to that of the direct path random range sidelobes. Some residual random range sidelobes of the strong clutter remains but these eigenvalues are rather small. In summary, it can be said that the adaptive interference

cancellation algorithm is able to effectively suppress the direct path and strong clutter components (Doppler-shifted clutter included) and this drastically decreases the significant eigenvalues of the interference covariance matrix which in turn lower the DOFs requirements for subsequent reduced-dimension STAP.

4.6 Reduced-dimension space-time adaptive processing results and analyses

For both side-looking and forward-looking airborne passive radar, the adaptive interference cancellation prior to matched filtering is able to effectively suppress the interfering signals where their corresponding random range sidelobes couplings will also be suppressed by the same amount. Subsequently, the resultant interference components in $\widehat{\mathbf{R}}_u$ will be the residual random range sidelobes couplings that remains and that of the spatial-Doppler dependent stationary clutter. As the next signal processing step for the airborne passive radar, these interference will be suppressed by reduced-dimension STAP prior to detections. The 'whitened then filter' approach where sub-optimum STAP is performed before Doppler filtering is known as the pre-Doppler processing and sub-optimum adaptive processing after Doppler processing refers to the 'filter then adapt' approach of post-Doppler processing. Element-space pre-Doppler and post-Doppler reduced-dimension STAP adaptively combine signals from all the elements through adaptive processing only a few sub-CITs at a time or by adaptively combining a small number of filtered outputs on each element respectively. Spatial filtering may also be performed on the element outputs of each sub-CIT prior to adaptation and these algorithms are referred to as beam-space STAP algorithms.

Section 3.4 has been devoted to detailed discussions of each of the reduced-dimension STAP approach where the characteristics/properties of a large number of variations (depending on the bin or beam selection) have been thoroughly analyzed. There is no 'best' approach for all airborne passive radar scenarios but rather each has some specific advantages as well as disadvantages over others in certain scenario. Thus, the most superior performance algorithm from each of the four classes will be used for interference suppression in the airborne passive radar and subsequently having their results analyzed and discussed. The algorithms applied to the side-looking and forward-looking airborne passive radar that will be examined are:

- element-space pre-Doppler STAP,
- element-space sub-CIT-staggered post-Doppler STAP,
- beam-space displaced-beam pre-Doppler STAP and
- beam-space displaced-filter post-Doppler STAP.

All beamformers and Doppler filters that are used are designed with a 30 dB Chebyshev taper. For the algorithms performance analyses, the snapshots used in the computation of $\widehat{\mathbf{R}}_u$ will be twice the DOFs centered at l_d. Obviously, this is the main advantage of reduced-dimension STAP in having less computational complexity and IID data support for training requirements. In addition to SINR loss, the MDV will also be tabulated where this quantity is computed at 12 dB cutoff point, representing values of SINR loss that would cause a loss in range sum coverage of 50 % against the thermal noise limited detection range sum.

4.6.1 Side-looking configuration

For the side-looking airborne passive radar, the performance of the four algorithms in terms of SINR loss for the detection range sum of 50 Km ($l_d = 999$) is depicted from Figs. 4.29 to 4.32. The 0 spatial frequency cut, overlaid with the SINR loss of optimum fully adaptive STAP, is also shown in each plot. The SINR loss performances of element-space pre-Doppler STAP for $K = 2$ and element space sub-CIT-staggered post-Doppler STAP for

$K = 2$ are shown in Figs. 4.29 and 4.30 respectively. The element-space algorithms make use of all spatial channels (maintain full spatial adaptivity) and require at least two temporal DOFs (two sub-CITs or two Doppler filters) in its implementation. Figs. 4.31 and 4.32 depict the SINR loss of beam-space displaced-beam pre-Doppler STAP for $K_t = 2$ and $K_s = 3$ and beam-space displaced-filter post-Doppler STAP for $K_{tm} = 3$ and $K_{sm} = 3$ respectively. For the beam-space algorithms, both approaches need the dimensionality of at least three spatial beams ($K_s = 3$ for displaced-beam pre-Doppler and $K_{sm} = 3$ for displaced-filter pre-Doppler) to achieve acceptable interference cancellation due to the direct path random range sidelobes and spatial-Doppler dependent clutter that are present. In addition, Tab. 4.2 tabulates the MDV for each of the algorithm.

The pre-Doppler reduced-dimension STAP approaches are able to provide reasonable performance while the post-Doppler techniques (MDV of 4.94 m/s for element-space and 4.85 m/s for beam-space) has performance very close to that of the optimum fully adaptive algorithm (MDV of 2.39 m/s). As shown, significant SINR loss (null) that is formed along the disjointed diagonal clutter ridge and that of the parallel ridge ($\vartheta = -0.5$) of the direct path random range sidelobes demonstrated the excellent performance of these algorithms. As shown in the Figs. and calculated in Tab. 4.2, post-Doppler approaches have better MDV, resulting in a better UDSF. By definition, the beam-space approaches are lower dimension than element-space approaches with the same number of temporal DOFs. For the same level of performance, the beam-space approaches have the advantage of less computational complexity and training requirements. In this case, beam-space approaches with only six (pre-Doppler) and nine (post-Doppler) DOFs perform as well as (if not better than) their element-space counterparts that is of significantly higher dimension.

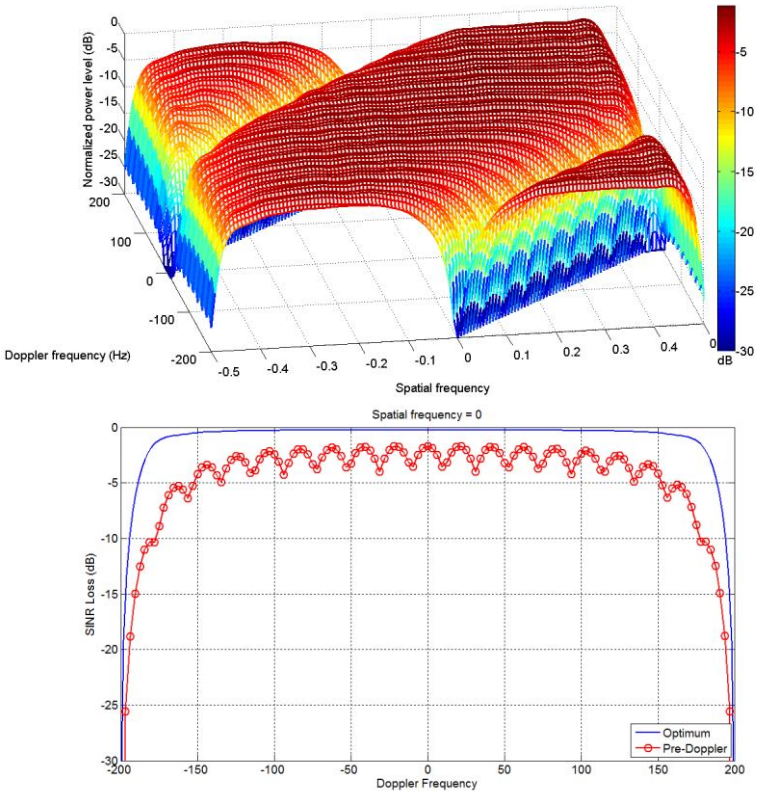

Fig. 4.29: SINR loss and spatial frequency cut for element-space pre-Doppler STAP, $K = 2$.

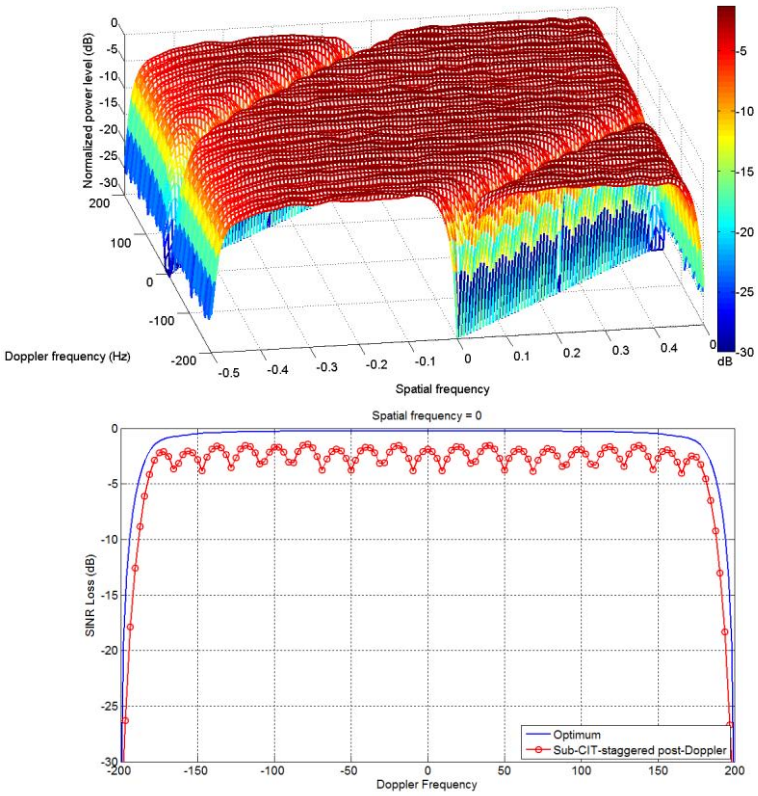

Fig. 4.30: SINR loss and spatial frequency cut for element-space sub-CIT-staggered post-Doppler STAP, $K = 2$.

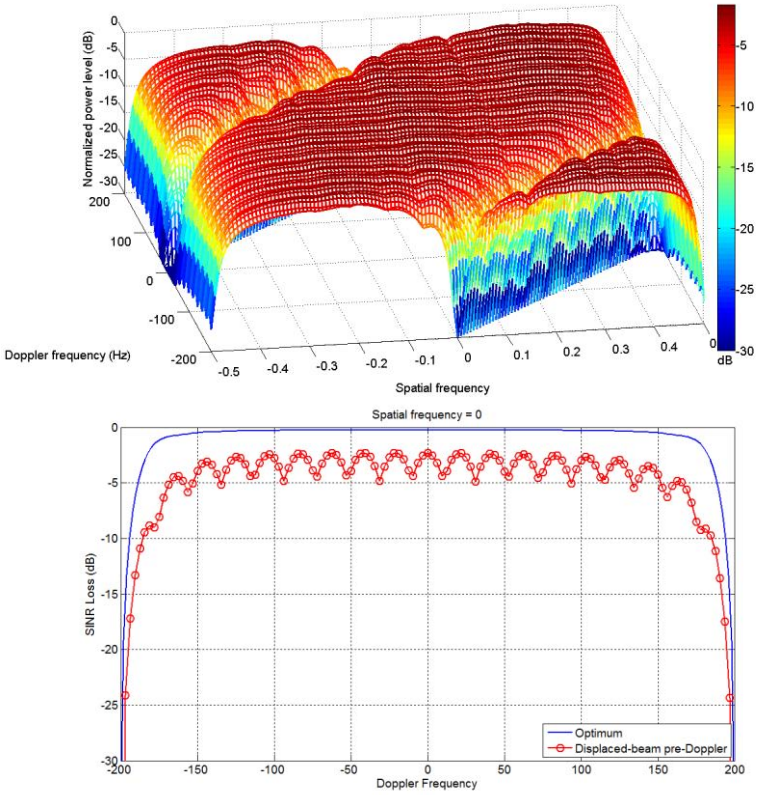

Fig. 4.31: SINR loss and spatial frequency cut for beam-space displaced-beam pre-Doppler STAP, $K_t = 2$ and $K_s = 3$.

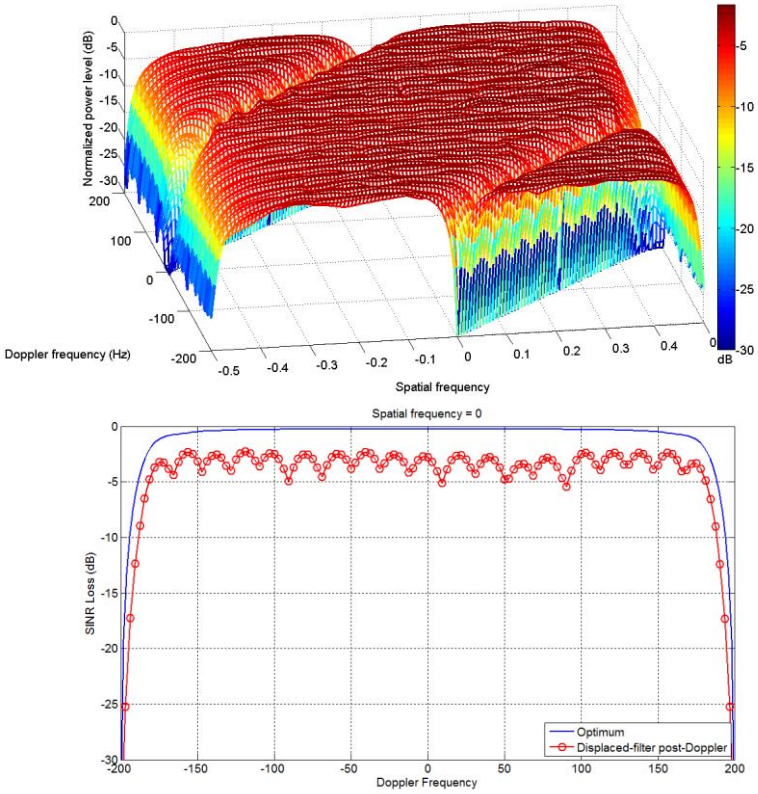

Fig. 4.32: SINR loss and spatial frequency cut for beam-space displaced-filter post-Doppler STAP, $K_{tm} = 3$ and $K_{sm} = 3$.

Tab. 4.2: MDV for side-looking configuration for various algorithms.

Algorithm	*Number of DOFs*	*MDV (m/s)*
Optimum	320	2.39
Element-space pre-Doppler	32	6.79
Element-space post-Doppler	32	4.94
Beam-space pre-Doppler	6	5.53
Beam-space post-Doppler	9	4.85

4.6.2 Forward-looking configuration

The performance of the four algorithms for the forward-looking airborne passive radar at the detection range sum of 50 Km ($l_d = 999$) is depicted from Figs. 4.33 to 4.36. In this forward-looking configuration, the non-cooperative transmitter is located at the array broadside (0 spatial frequency) to replicate a severe direct path and strong clutter coupling interference scenario. Thus, after the adaptive interference cancellation, the random range sidelobes coupling of the direct path can still be seen above thermal noise as a parallel ridge (along the Doppler frequency axis) at 0 spatial frequency and similarly, the strong clutter random range sidelobes will cause an elevation of the pedestal that is also concentrated around 0 spatial frequency as explained in Section 4.5.3. In this case, the spatial frequency cut that is associated to each SINR loss mesh plot for exact performance comparison between algorithms will be at a spatial frequency of 0.2 instead. The overlaid SINR loss of the optimum fully adaptive STAP for the same spatial frequency of 0.2 exhibits a small loss in

the clutter free Doppler region due to the residual random range sidelobes of the strong clutter that remains at this spatial frequency. The SINR loss performances of element-space pre-Doppler STAP for $K = 2$ and element space sub-CIT-staggered post-Doppler STAP for $K = 2$ are shown in Figs. 4.33 and 4.34 respectively. The element-space algorithms make use of all spatial channels (maintain full spatial adaptivity) and require at least two temporal DOFs (two sub-CITs or two Doppler filters) in its implementation. Due to the forward-looking configuration, the clutter has a semicircle profile which occupies several Doppler cells near to the array endfire. Thus, the SINR loss performance around the spatial frequencies of –0.5 and 0.5 is extremely poor when two temporal DOFs are used. Figs. 4.35 and 4.36 depict the SINR loss for beam-space displaced-beam pre-Doppler STAP for $K_t = 2$ and $K_s = 4$ and beam-space displaced-filter pre-Doppler STAP for $K_{tm} = 4$ and $K_{sm} = 4$ respectively. For beam-space STAP approaches applied to the forward-looking configuration, three spatial beams are insufficient to achieve acceptable interference cancellation due to both the positive and negative spatial frequency clutter and the direct path sidelobes that are present at a given Doppler frequency. At least four spatial beams ($K_s = 4$ for displaced-beam pre-Doppler and $K_{sm} = 4$ for displaced-filter post-Doppler) are needed to restore the performance to nearly that of the element-space approaches. Again, Tab. 4.3 tabulates the MDV for each of the algorithm.

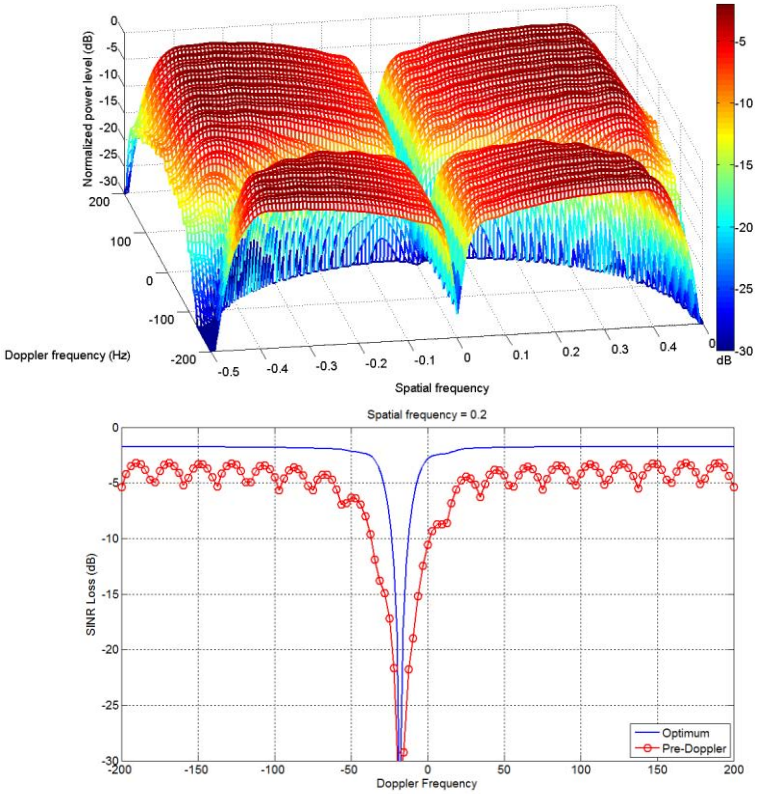

Fig. 4.33: SINR loss and spatial frequency cut for element-space pre-Doppler STAP, $K = 2$.

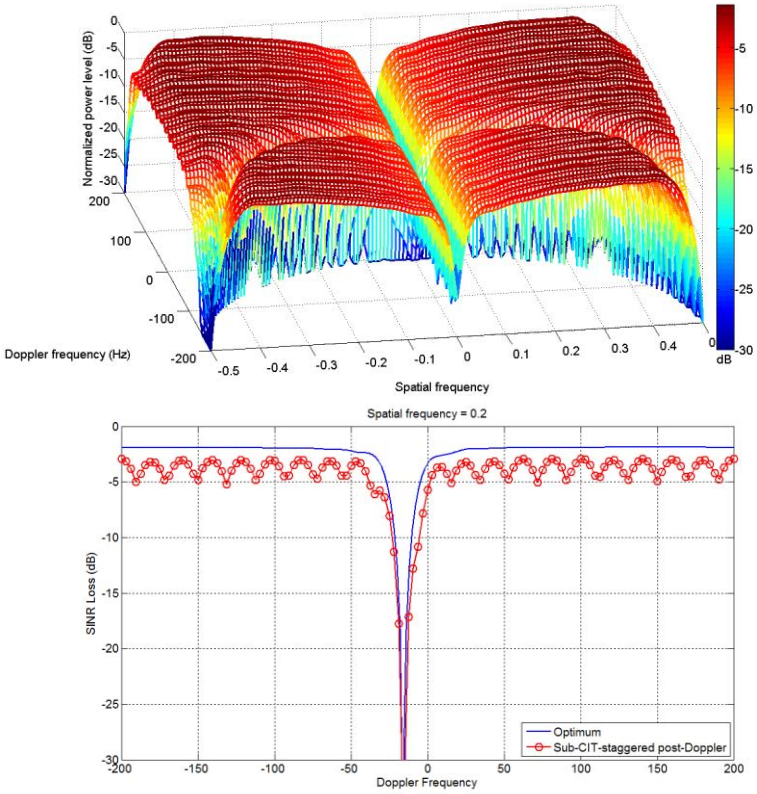

Fig. 4.34: SINR loss and spatial frequency cut for element-space sub-CIT-staggered post-Doppler STAP, $K = 2$.

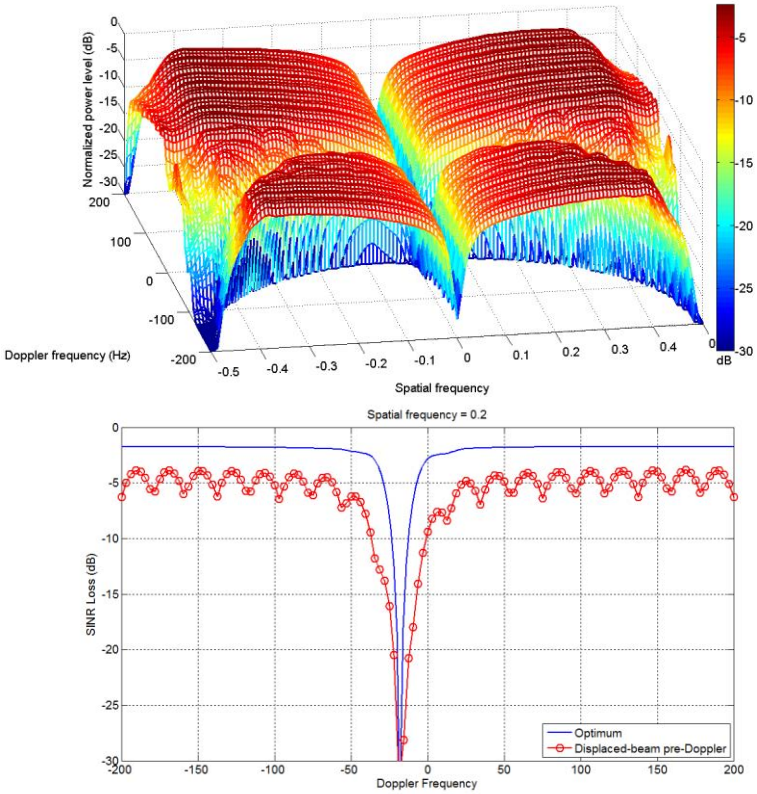

Fig. 4.35: SINR loss and spatial frequency cut for beam-space displaced-beam pre-Doppler STAP, $K_t = 2$ and $K_s = 4$.

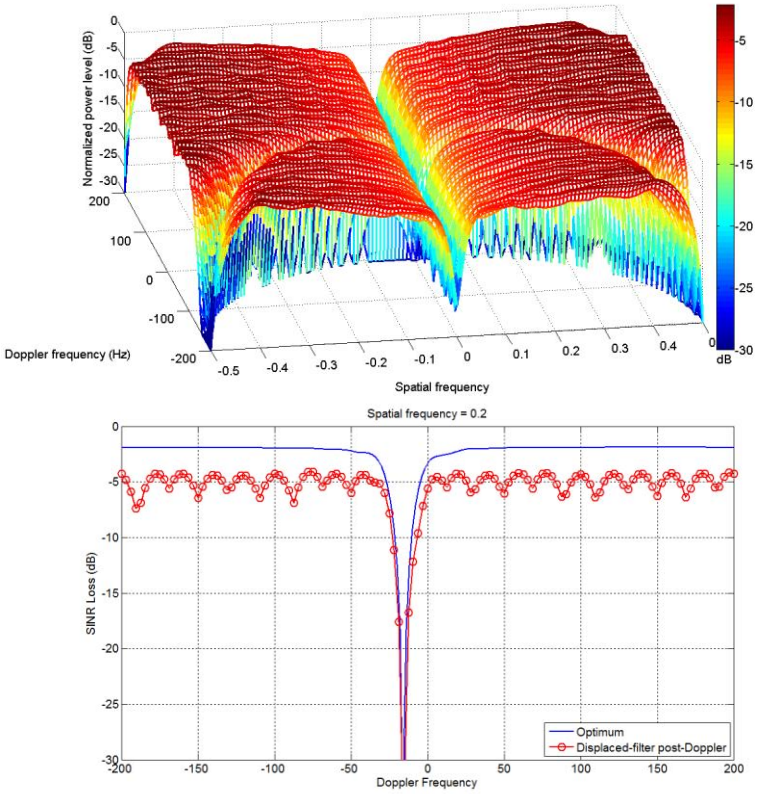

Fig. 4.36: SINR loss and spatial frequency cut for beam-space displaced-filter post-Doppler STAP, $K_{tm} = 4$ and $K_{sm} = 4$.

The pre-Doppler reduced-dimension STAP approaches are able to provide reasonable performance while the post-Doppler techniques (MDV of 3.95 m/s for element-space and 3.44 m/s for beam-space) has performance very close to that of the optimum fully adaptive algorithm (MDV of 2.10 m/s). Significant SINR loss (null) that is formed along the semicircle clutter profile and that of the parallel ridge ($\vartheta = 0$) of the direct path random range sidelobes demonstrated the performance capabilities of these algorithms. As in the side-looking configuration, post-Doppler approaches will have a better UDSF. In addition, the beam-space approaches with only eight (pre-Doppler) and sixteen (post-Doppler) DOFs perform slightly better than their element-space counterparts that is of significantly higher dimension.

Tab. 4.3: MDV for forward-looking configuration for various algorithms.

Algorithm	*Number of DOFs*	*MDV (m/s)*
Optimum	320	2.10
Element-space pre-Doppler	32	7.82
Element-space post-Doppler	32	3.95
Beam-space pre-Doppler	8	7.05
Beam-space post-Doppler	16	3.44

4.6.3 Results summary and discussions

In a practical airborne passive radar, due to the power budget and the narrowband passive signal bandwidth, the number of range cells collected may be limited. In addition, the often heterogeneous and non-stationary clutter will limit the amount of secondary data which can be assumed IID. These concerns, together with the issues of computational complexity, lead naturally to reduced-dimension STAP which enables localized training, and thus can be used to advantage in the airborne passive radar. The most superior performance algorithm from each class of reduced-dimension STAP approach is used for interference suppression in the airborne passive radar scenario. For the side-looking and forward-looking airborne passive radar operating in a practical environment and interference scenario, the simulation results demonstrated the performance of the various reduced-dimension STAP techniques. The element-space pre-/post-Doppler and beam-space pre-/post-Doppler STAP algorithms with varying dimensionality is able to effectively suppress the clutter ridge and the direct path random range sidelobes and random range sidelobes of the strong clutter that has a limited spatial frequency span. Reduced-dimension STAP will not be useful in suppressing the residual random range sidelobes of the strong clutter that spanned the full spatial frequency range as the properties of this interference is similar to that of thermal noise which is of full rank. Element-space approaches are inherently more flexible because full spatial adaptively is retained. This provides a large number of spatial DOFs to cancel the direct path random range sidelobes, random range sidelobes of the strong clutter that has a limited spatial frequency span and clutter simultaneously. Thus, the element-space STAP techniques can be suitable for the airborne passive radar operation which usually has a small or moderately sized antenna arrays. Pre-Doppler approaches provide a more rapid adaption capability than post-Doppler techniques where the weights are recomputed for every sub-CIT and is desirable in a rapidly varying environment. However, the main drawback is that the sidelobe response of each weighting vector may vary across sub-CIT-to-sub-CIT and Doppler spreading will be evident upon Doppler integration over the full CIT. For post-Doppler approaches, the Doppler frequency of the clutter depends on beam direction (spatial frequency) and low sidelobe Doppler filtering can localize the clutter in angle. It should therefore require fewer spatial DOFs to remove clutter from returns in a particular Doppler bin than from returns at a particular sample time (clutter is present in all sub-CITs). Thus, post-Doppler algorithms can provide slightly better Doppler space coverage than pre-Doppler algorithms. However, when the CIT length is relatively short, the spatial angle (frequency) extent corresponding to a Doppler bin becomes large, thus putting a heavier burden on the spatial adaptive processing. Even for the severe interference scenario of the forward-looking configuration, these algorithms are able to perform well. It had been shown that the post-Doppler implementation of reduced-dimension STAP outperformed the pre-Doppler approaches with better MDV and exhibit SINR loss performance close to that of the optimum fully adaptive STAP algorithm. Post-Doppler technique is also more robust in the forward-looking scenario where there is backlobe clutter. In fact, pre-Doppler techniques have relatively poor gain for target returns with Doppler frequency close to the mainlobe clutter. For the beam-space implementation, at least three spatial beams for the side-looking configuration and at least four spatial beams for the forward-looking configuration are required to achieve acceptable interference cancellation performance. The beam-space pre- and post-Doppler approaches are able to provide comparable (if not better) SINR loss performance to their element-space counterparts with significantly fewer DOFs. Thus, the requirement for lesser secondary data support for weights training which is a definite advantage in the airborne passive radar.

4.7 Summary

Simulations on the power profile for the side-looking and forward-looking airborne passive radar in a practical and realistic interference scenario had demonstrated the undesired random range sidelobes coupling effects of the direct path and of the strong clutter into further range cells. For both configurations, the direct path sidelobes coupling cause the formation of a spatial frequency dependent Doppler ridge that is well above the level of the clutter present at the range cell of interest. The severe sidelobes couplings of the strong clutter that spanned over all spatial frequencies caused the significant elevation of the pedestal in the spatial-Doppler power spectrum. Thus, target detections at this range cell will be random range sidelobes limited. If not mitigated, the effects of these undesirable couplings and together with the spatial-Doppler dependent clutter will make target detections virtually impossible. The signal processing flow for the airborne passive radar to mitigate the undesirable interfering signals had been graphically illustrated. Channel calibration compensates for the amplitude and phase errors/mismatches between the received passive signals at the output of each channel. The next signal processing scheme calls for the suppression of the strong interfering signals where the adaptive FIR filtering is implemented to estimate the weight coefficients for interference cancellation. Simulations showed that the LS-based adaptive interference cancellation algorithm is able to effectively suppress the direct path, zero-Doppler strong clutter and Doppler-shifted strong clutter signals received at each element. This lowers its corresponding random range sidelobes couplings into further range cells by the same amount. The cancellation algorithm is able to completely suppress the strong interfering signals but the main drawback is such that the entail computational and memory load for the processing might not be within acceptable time necessary for real-time airborne passive radar operations. In addition, its performance will suffer some degradation where the interfering signals will not be fully cancelled if the direct path reference signal becomes corrupted. Following that, the passive signals are then formatted into a $N \times M \times L$ CIT datacube where the range profile is obtained by matched filter processing (range correlation) that is carried out separately on a sub-CIT-by-sub-CIT basis. Subsequently, any residual random range sidelobes couplings that remains and that of the spatial-Doppler dependent stationary clutter at the detection range cell of interest will be suppressed by reduced-dimension STAP.

The main benefit of reduced-dimension techniques is in the significant reduction of the adaptive weights dimensionality where the performance and statistical convergence with a limited amount of data available for the airborne passive radar can be dramatically improved and also the computational load eased. Simulation results demonstrated the effective performance of the reduced-dimension STAP techniques for the side-looking and forward-looking airborne passive radar. The element-space pre-/post-Doppler and beam-space pre-/post-Doppler STAP algorithms are able to effectively suppress the clutter, direct path random range sidelobes and the random range sidelobes of the strong clutter that has a limited spatial frequency span to improve slow moving target detections. These algorithms perform well under the side-looking and the severe interference environment of the forward-looking configuration. For the beam-space implementation, more spatial beams are required for the forward-looking configuration to achieve comparable interference cancellation performance to the side-looking configuration. It had been shown that the post-Doppler implementation of reduced-dimension STAP outperformed the pre-Doppler approaches with better MDV where the beam-space approach is able to provide excellent SINR loss performance with significantly fewer DOFs.

Chapter 5

Ground-Based Moving Passive Radar Experimental Trials

5.1. Introduction

It has been outlined that the airborne passive radar must detect targets in severe environments consisting of clutter and random range sidelobes couplings of the direct path and of the strong clutter. Chapter 4 explains the overall signal processing schemes for moving target detection in the airborne passive radar. A comprehensive study and simulations demonstrated the performance capabilities to improve slow moving target detection for the airborne passive radar through effective signal processing schemes. However, further development and performance evaluation of these schemes has been limited due to a lack of real world data. The absence of measured airborne passive data has also hindered progress towards fielding an operational airborne passive radar. Experimental trials need to be conducted to collected real airborne passive data which is essential for the performance evaluation and verification of the airborne passive radar signal processing in the real world interference scenario. Firstly, the trust of this effort is the assessment of the passive signals collected by the multi-channel airborne passive radar test-bed to validate against the theoretical models that were derived. Subsequently, the performance verification and evaluation of the signal processing algorithms will be performed on these data. Another objective of this effort is also to demonstrate the impact of non-homogenous environments on the airborne passive radar signal processing performance. It will not be possible within the means and the time frame of the research thesis to accomplish measurement experiments based on airborne campaigns representative of the airborne passive radar. Instead, simplified ground-based moving passive radar trials will be conducted to mimic as close as possible the airborne scenario and provide data for the validation of the airborne passive radar signal processing on moving target detections. The experimental details of the ground-based moving passive radar trials together with the signal processing results and analyses will be presented in this Chapter.

5.2. Overview of multi-channel passive radar test-bed

For the purpose of the ground-based moving passive radar experimental trials, a low-cost experimental passive radar receiver test-bed has been designed and developed in Nanyang Technological University, Singapore. Upon implementation, the performance of the test-bed (which is based mostly on COTS components), is successfully appraised and evaluated. The portable passive radar receiver test-bed consists of a 4-element horn antenna array, each having its own receiver which can be easily mounted on a ground moving platform. An arbitrary signal generator (R&S SMBV100A) is used to generate the DVB-T format signal at the carrier frequency of 4.44 GHz which is transmitted with a separate antenna to replicate the non-cooperative transmit signal from a DVB-T transmitter. Using a

scaled-up RF carrier DVB-T signal as opposed to existing non-cooperative transmission of opportunity that operates mainly below L-band takes into consideration two factors. First, the high carrier signal that was used compensates (to a certain effect) for the differences in Doppler frequency of the ground clutter due to the decrease in the differences of velocity between the ground-moving platform and the actual airborne platform that the passive radar is modeled and based upon. Secondly and more importantly, the COTS components for the passive radar test-bed and antenna array (at this RF frequency band) are readily available.

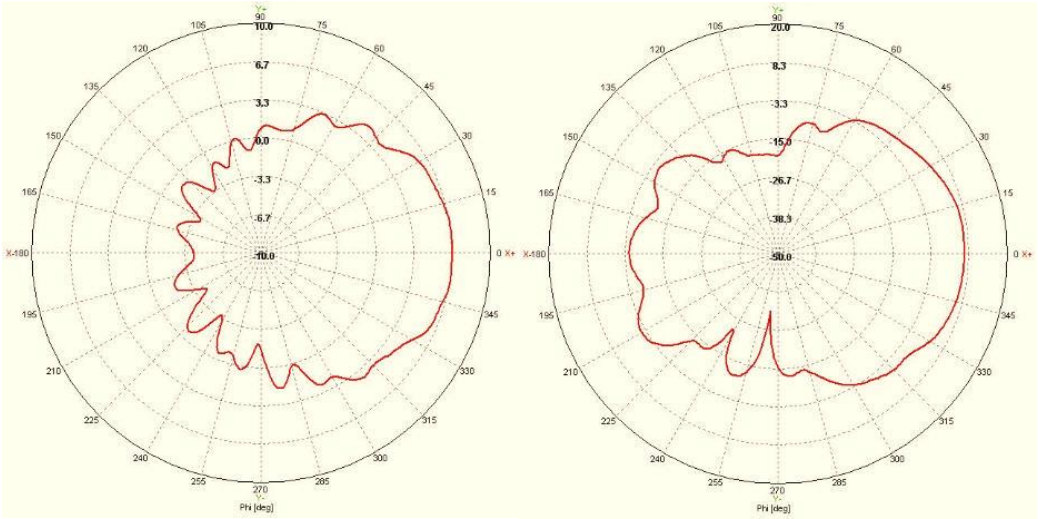

(a) (b)

Fig. 5.1: (a) Azimuth and (b) elevation radiation pattern of the horn antenna at 4.44 GHz.

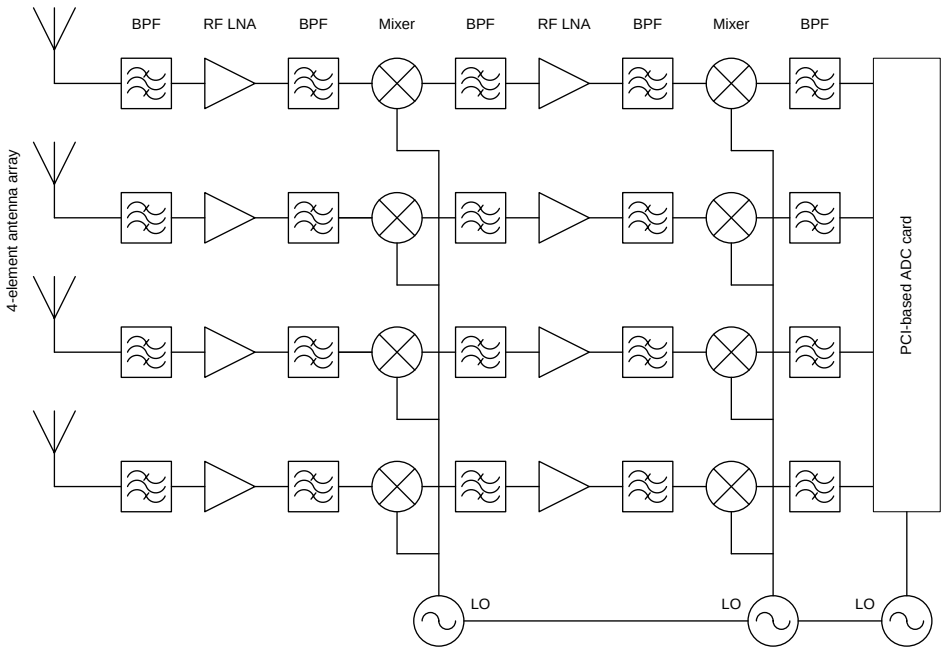

Fig. 5.2: Architecture of the 4-channel passive radar receiver test-bed.

Four commercial horn antennas with frequency range from 3.5 GHz to 5 GHz were used to implement the 4-element antenna array for the receiver test-bed to achieve high gain with limited dimension. Each horn antenna has a physical aperture dimension of

approximately 25×50 mm and 150 mm in length. The azimuth and elevation radiation pattern of a horn antenna, where each has been individually measured in an anechoic chamber, are depicted in Figs. 5.1(a) and 5.1(b) respectively. The half-power azimuth and elevation beamwidth for each horn antenna element at 4.44 GHz were measured to be $90°$ and $65°$ respectively, with a gain of approximately 7 dBi. For the 4-channel passive radar receiver, each channel has identical architecture based on a double conversion superheterodyne receiver with IF sampling and is constructed using COTS components. Fig. 5.2 depicts the architecture of the 4-channel passive receiver test-bed. In each channel, first, the RF low-noise amplifier (with RF BPFs before and after the amplifier) amplifies the DVB-T signal received by the antenna. This is followed by a mixer for down-conversion to the first IF stage of 1445 MHz. The double conversion superheterodyne architecture makes use of a relatively high first IF stage to easily achieve high levels of image rejection at the RF front end. The filtered and amplified DVB-T signal after the first IF stage is then passed through a second mixer for conversion to a lower IF for IF sampling. The low second IF stage provides the levels of performance required for the adjacent channel selectivity where narrowband filtering removed adjacent channel signals. Thus, the DVB-T signal is duly narrowband filtered prior to signal digitization. The data acquisition system used to digitize the 4-channel DVB-T is a PCI-based ADC card with DDC and external clock synchronization capability to allow the sampling to be fully coherent with the 4-channel passive radar test-bed. Once sampled, using the DDC, the 4 channels of digital IF signals are translated to baseband and saved continuously into the computer harddisk.

5.3 Experimental trials setup, results and analysis

This Section first describes the ground-based moving passive radar experimental trials geometrical configuration. This is followed by the results of the signal processing for moving target indication, namely on the results of the adaptive interference cancellation and reduced-dimension STAP. In addition, comprehensive discussions and analysis on all results are provided.

5.3.1. Geometrical configuration and setup

The selected experimental trial site is located at the south-western part of Singapore. The site is a large plot of grass patch which offers a surface clutter measurement scenario having a swath of approximately 600 m. Fig. 5.3 depicts the map and photograph of the clutter measurement scenario for the experimental trials. The ground-based moving passive radar experimental trials are to be conducted such that the entire passive radar test-bed is installed and operates on the moving lorry vehicle platform as illustrated in the photographs in Fig. 5.4. As prominently seen, both the transmit horn antenna and 4-element receive horn antenna array are mounted on the same elevated mounting stand of approximately 3.5 m in height from the ground where they are spaced about 1 m apart. Then, the mounting stand is safely secured parallel to the side of the back compartment railing of the lorry. Due to the special physical dimension of the horn antenna (having a small aperture in the azimuthal axis), even operating at such short carrier wavelength of 4.44 GHz, the inter-element spacings for the receive antenna array can still be half λ ($\lambda = 6.75$ cm) apart. The antenna array axis is parallel to the moving platform velocity vector to mimic a monostatic sidelooking array configuration. The look angle in elevation for both the transmit antenna and receive antenna array is roughly a few degrees so that the antenna elevation center points approximately to the center of the whole swath width of the clutter measurement scenario. Data are recorded and processed for platform velocity of approximately 7 m/s (lorry speed of 25 Km/h).

Fig. 5.3: Map and photograph of the clutter measurement experimental trials site.

Fig. 5.4: Photographs of the ground-based passive
radar test-bed on the moving lorry vehicle platform.

5.3.2. Signal processing results and analyses

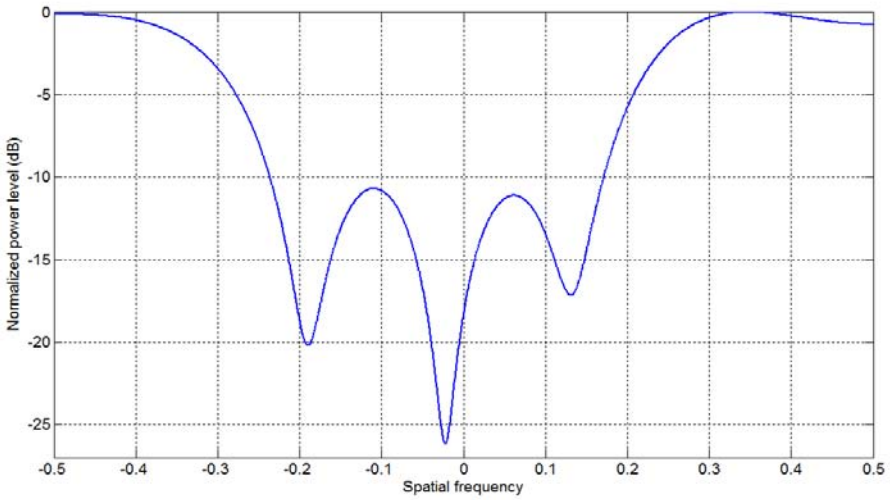

Fig. 5.5: DOA of received DVB-T signals from the antenna array.

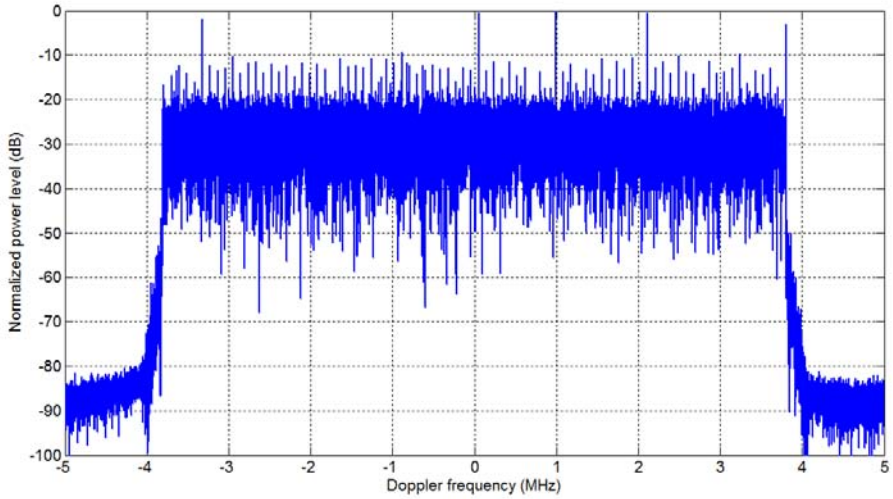

Fig. 5.6: Power spectrum of DVB-T direct path reference signal.

For the ground-based moving passive radar experimental trials, 4-channels of complex-valued baseband data are recorded. Using the channel calibration procedures as outlined in Section 4.4, the 4-channel ground-based moving passive radar test-bed is duly calibrated prior to the subsequent signal processing. Fig. 5.5 depicts the spatial spectrum (DOA) of the received DVB-T signals from the antenna array when the platform is stationary. It illustrates the output power estimated from the signals received from different channels as a function of DOA. As anticipated, the direct path will be the strongest signal that is coupled from the sidelobe of the transmit antenna into the end-fire of the antenna array. Thus, it is clearly evident that the spatial spectrum exhibits the highest power level at the spatial frequency of –0.5. Consequently, the direct path reference signal used for match filtered processing is obtained via digital beamforming to the direction (end-fire) of the transmit antenna. Fig. 5.6 depicts the power spectrum of the beamformed DVB-T direct path reference signal. Tab. 5.1 tabulates the geometrical parameters for the ground-based moving passive radar experimental trials and other parameters used for processing the received signals where the passive CIT datacube of 0.2 sec consists of 4 channels, 100 sub-CITs and 20000 range cells.

Tab. 5.1: Parameters for the ground-based moving passive radar experimental trials.

Geometrical parameters	
Non-cooperative transmitter height	3.5 m
Ground-based passive radar height	3.5 m
Ground-based passive radar velocity	7 m/s
Passive signal parameters	
DVB-T signal carrier frequency	4.44 GHz
DVB-T signal bandwidth	8 MHz
Complex sampling bandwidth	10 MHz
Effective radiated power	10 dBm at output of signal generator
Passive datacube parameters	
Number of elements	4
Sub-CIT repetition frequency	500 Hz
Sub-CIT repetition interval	2 ms
Number of sub-CITs	100

To illustrate the practical severe interfering environment for the ground-based passive radar scenario, Figs. 5.7 to 5.10 depict the angle-Doppler Fourier power spectrum of the received passive signal snapshots along incremental range cell without the adaptive interference cancellation. For ease of comparison, all these Fourier power spectrum plots will be normalized to the peak power level of the direct path at the origin range cell. Doppler resolution will be much more superior than the cross-range spatial resolution due to the vast differences between the number of sub-CITs and the number of elements used. First, Fig. 5.7 shows the power spectrum (mesh and image plot) at the origin range cell $l = 0$. Accordingly, the direct path enters the passive radar at the array endfire (ϑ_{dp} = –0.5) with a neutralized Doppler frequency (0 Hz after matched filter processing). For the experimental trial geometrical configuration, the 3.5 m in height for the passive radar signifies that clutter will also be present at the origin range cell since each range cell occupies a distance of 15 m. Using the parameters in Tab. 5.1, it can be calculated that the Doppler spectrum of the ground clutter spanned approximately from $-205\ Hz$ to $205\ Hz$ where Fig. 5.7 clearly illustrated. Figs. 5.8 to 5.10 depict the power spectrum for range cell $l = 5$ (75 m), $l = 15$ (225 m) and $l = 25$ (375 m) respectively where these power profiles mainly consist of the strong random range sidelobes of the direct path. As anticipated, the direct path random range sidelobes appear as an irregular ridge spread across all Doppler frequencies having the same normalized spatial frequency as the direct path. The average value of the random range sidelobes is approximately –62.5 dB which is about $10\log_{10}(1/MBT_{sub}) = 62$ dB lower than the peak value of the direct path at the origin range cell. A relatively high level of 0 Hz Doppler frequency components can be in seen in Figs. 5.8 and 5.9. This is due to the fact that the coherency of the correlation function across sub-CIT-to-sub-CIT at near range are still quite apparent. Explicitly, this shows that the DVB-T signal is not totally noise-like. From these power spectrum of the received passive signal snapshots for the ground-based moving passive radar, clutter is only visible up to the 11th range cell where subsequently, the clutter will be embedded by the FFT sidelobes of the direct path random range sidelobes. The low clutter power is also due to the fact that grass patch for the trials measurement exhibit low reflectivity for the return signal. The power spectrum plots attain from the experimental trials data exhibit random range sidelobes coupling of the direct path and the angle-Doppler dependent stationary clutter ridge accordingly to the measurement parameters. More importantly, these results from the collected data accurately coincide with that from the theoretical derivations and simulations in the preceding Chapters. As mentioned, if these interfering signals (undesirable random range sidelobes couplings and spatial-Doppler dependent clutter) are not mitigated, target detection would be virtually impossible.

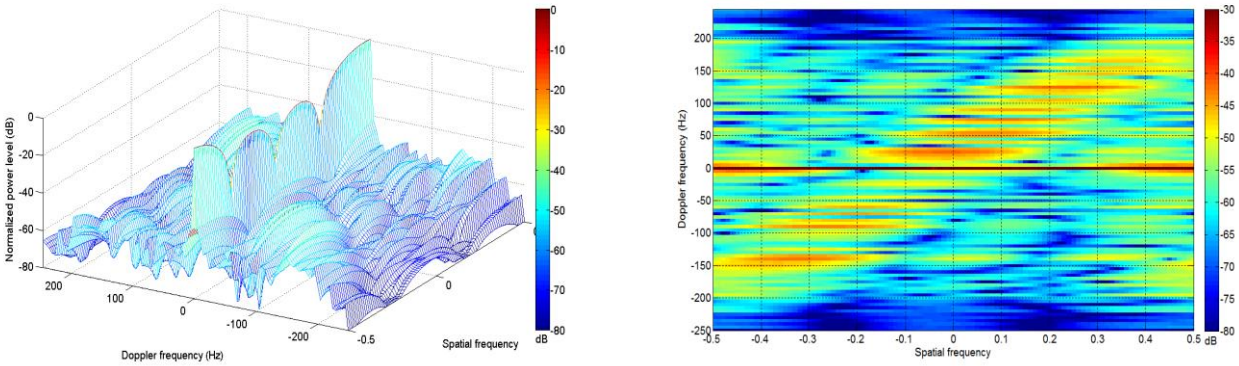

Fig. 5.7: Power spectrum at the origin range cell $l = 0$.

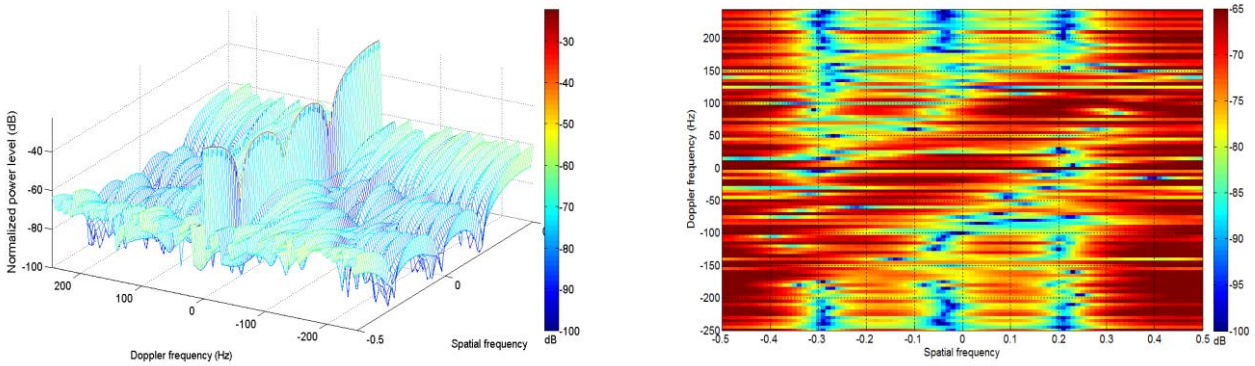

Fig. 5.8: Power spectrum at range cell $l = 5$.

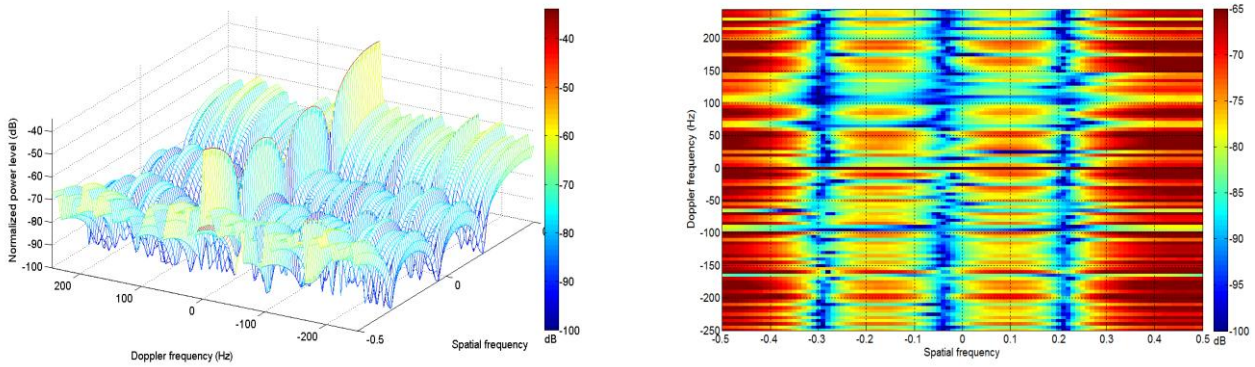

Fig. 5.9: Power spectrum at range cell $l = 15$.

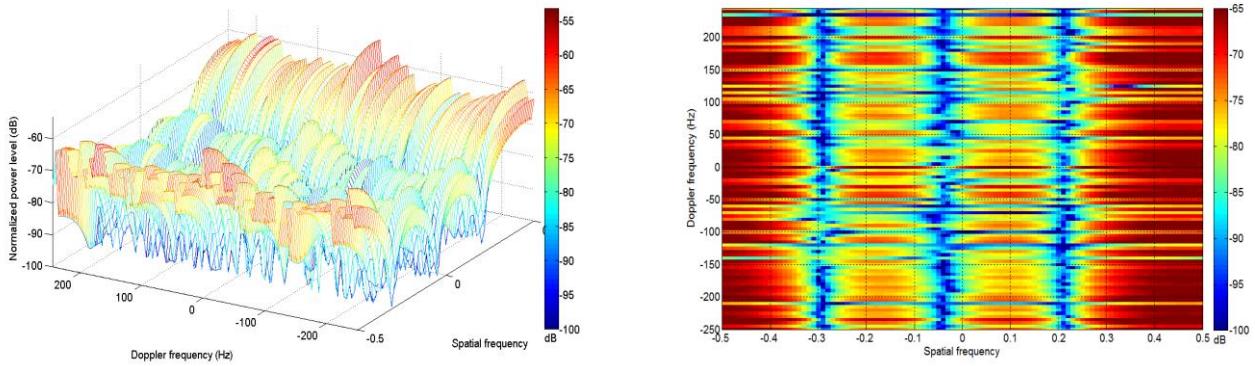

Fig. 5.10: Power spectrum at range cell $l = 25$.

With reference to Fig. 4.21, the initial signal processing block calls for interference suppression to overcome the random range sidelobes coupling effects of the direct path and of the strong clutter in the ground-based moving passive radar prior to matched filter processing. In cancelling the direct path, zero-Doppler strong clutter and the Doppler shifted strong clutter signals, their corresponding random range sidelobes that manifest into further range cells will also be suppressed by the same amount. In-depth analyses of the measurement data indicate that only the random range sidelobes coupling of the direct path and none from the near range strong clutter random range sidelobes (as will be explain later) is higher than thermal noise at further range cells. In this case, in order to suppress the direct path and the coherency of its correlation function (zero-Doppler components) at near range, a 50^{th}-order adaptive FIR filter for the adaptive interference cancellation algorithm will be employed. Figs. 5.11 to 5.15 depict the angle-Doppler power spectrum of the received

passive signal snapshots along incremental range cell after applying the adaptive interference cancellation algorithm. First, Fig. 5.11 shows the power spectrum at the origin range cell $l = 0$. As shown, a deep null can be prominently seen over 0 Hz Doppler frequency (over all spatial frequency) that the algorithm operates on which demonstrate that the 0 Hz components had been effectively suppressed. What remains is the clutter that is present at this range cell and having the same power level as in Fig. 5.7. Figs. 5.12 to 5.14 depict the power spectrum (mesh and image plot) for range cell $l = 5$ (75 m), $l = 15$ (225 m) and $l = 25$ (375 m) respectively where these power profiles show the clutter present at the particular range cell and free of the undesirable couplings of the direct path random range sidelobes. Comparing Fig. 5.12 to 5.8, Fig. 5.13 to 5.9 and Fig. 5.14 to 5.10, the former shows a much more visible clutter ridge as compared to the latter Figs. for each respective range cell. Applying the adaptive interference cancellation algorithm, the random range sidelobes of the direct path that couple into further range cells had been effectively suppressed and now clutter can be prominently seen up to at least the 48th range cell as depicted in Fig. 5.15. From range cell $l = 49$ to 62, pale image of clutter ridge can still be visibly seen but having a high degree of non-homogeneity. At further range cells $l \geq 63$, the clutter ridge is no longer visible and the power level of the angle-Doppler spectrum stays at an almost consistent level of approximately -102 dB as illustrated in Fig. 5.16 where the average power is plotted against range cell index.

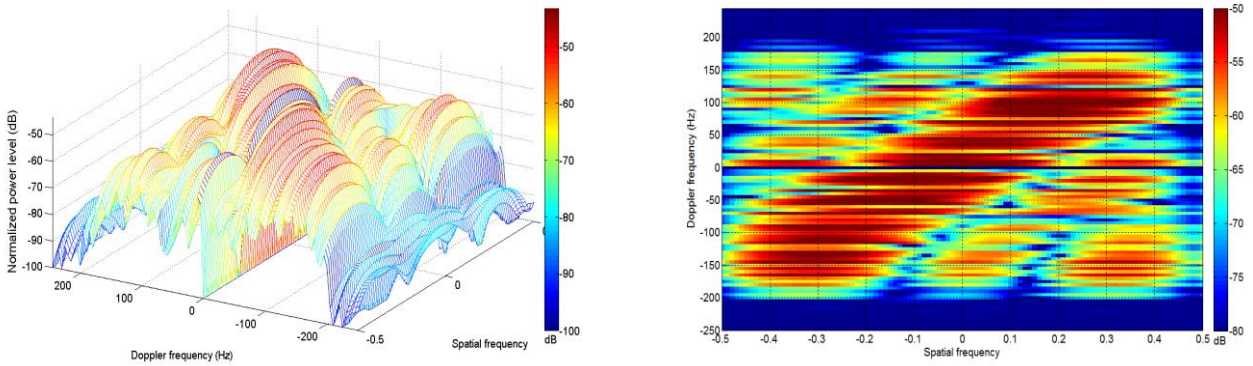

Fig. 5.11: Power spectrum at the origin range cell $l = 0$ after adaptive interference cancellation.

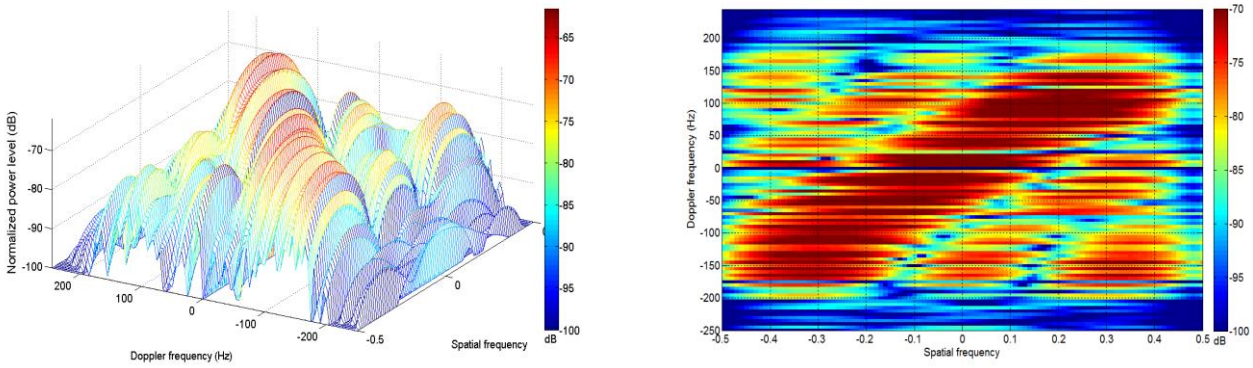

Fig. 5.12: Power spectrum at range cell $l = 5$ after adaptive interference cancellation.

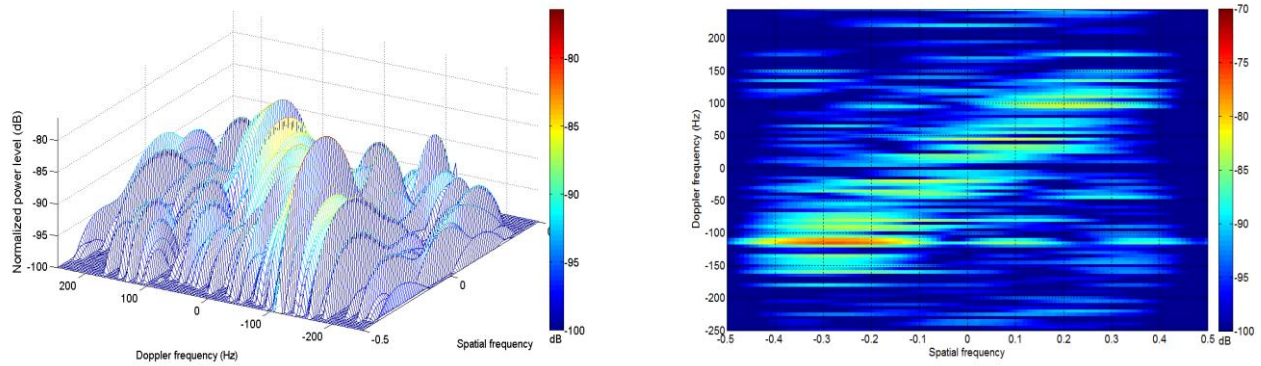

Fig. 5.13: Power spectrum at range cell $l = 15$ after adaptive interference cancellation.

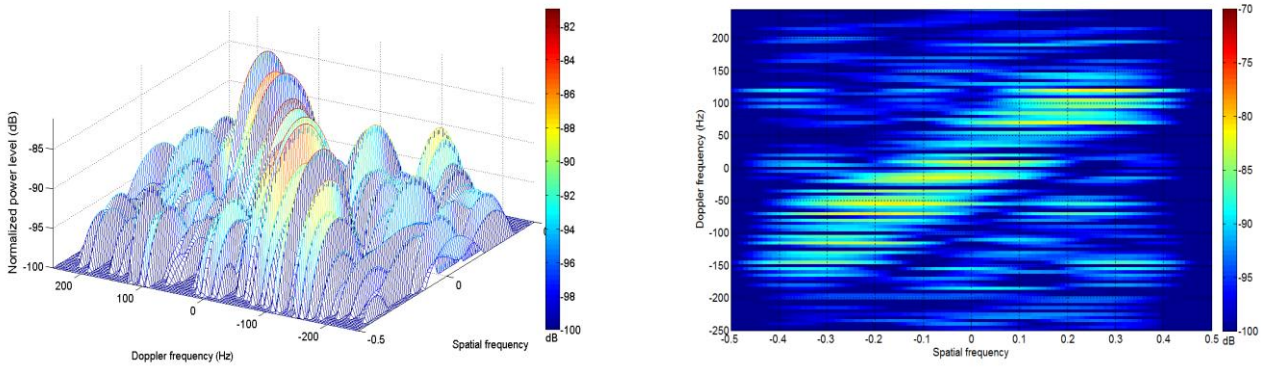

Fig. 5.14: Power spectrum at range cell $l = 25$ after adaptive interference cancellation.

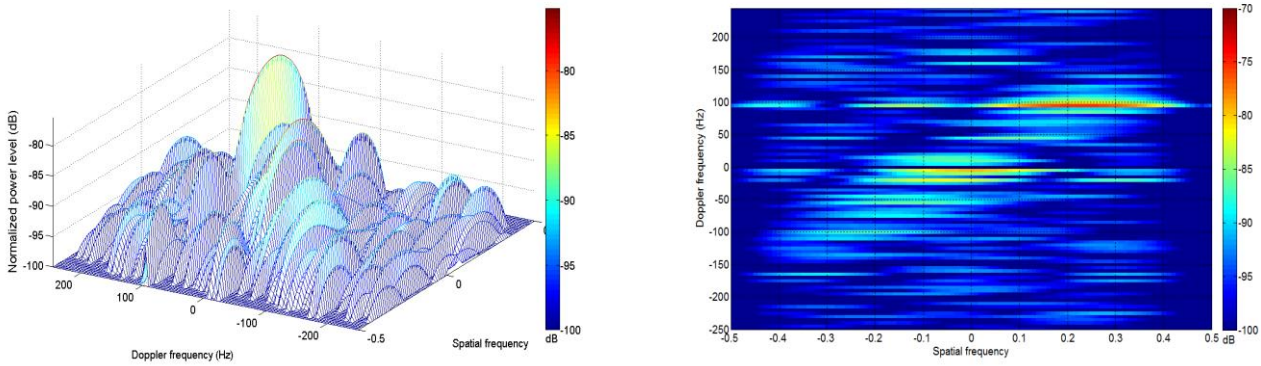

Fig. 5.15: Power spectrum at range cell $l = 48$ after adaptive interference cancellation.

Fig. 5.17 depicts the power spectrum of range cell $l = 90$ (1350 m) which represents the noise-only snapshot having an average normalized power level of -102 dB. Analysis ascertain that the contributing signal at this range cell is that of thermal noise and not of the random range sidelobes of the strongest clutter which exhibit similar properties. As in Fig. 5.11, the clutter ridge at the origin range cell represents the strongest clutter return having a peak value of -43.5 dB and the average value of approximately -52 dB. Thus, the corresponding random range sidelobes of this strongest clutter with be approximately -114 dB ($-52 - 62$ dB) that couples into further range cells (including for $l = 90$). By contrast, the random range sidelobes of the strongest clutter exhibit a lower level compared to the consistent average power level of the spectrum from range cell $l = 65$ and beyond. This establishes the thermal noise power level to be at -102 dB. Finally, Figs. 5.18 and 5.19 depict the power spectrum of the SCM estimate $\widehat{\mathbf{R}}_u$ for $K_e = 16$ snapshots and $K_e = 24$

snapshots respectively and centered at range cell $l = 20$. These results show a less fluctuating clutter ridge response as compared to the power spectrum plotted for a single range cell (snapshot).

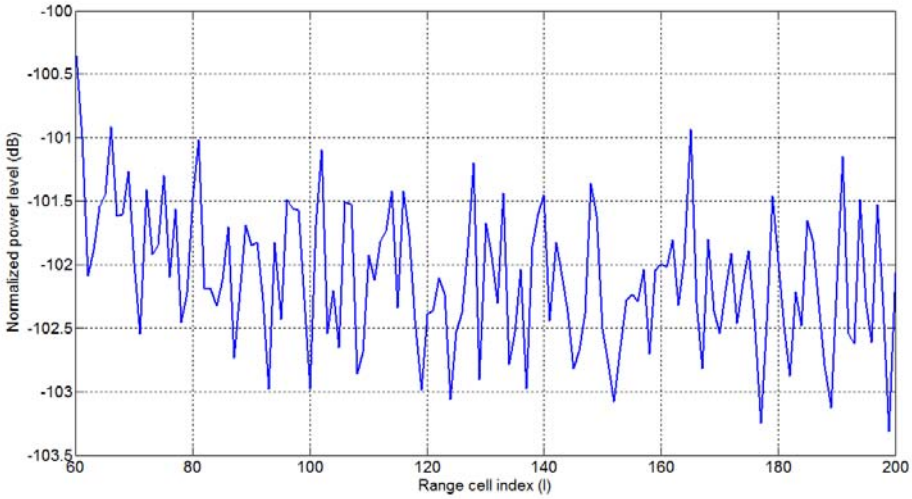

Fig. 5.16: Average power level of angle-Doppler power spectrum against range cell index.

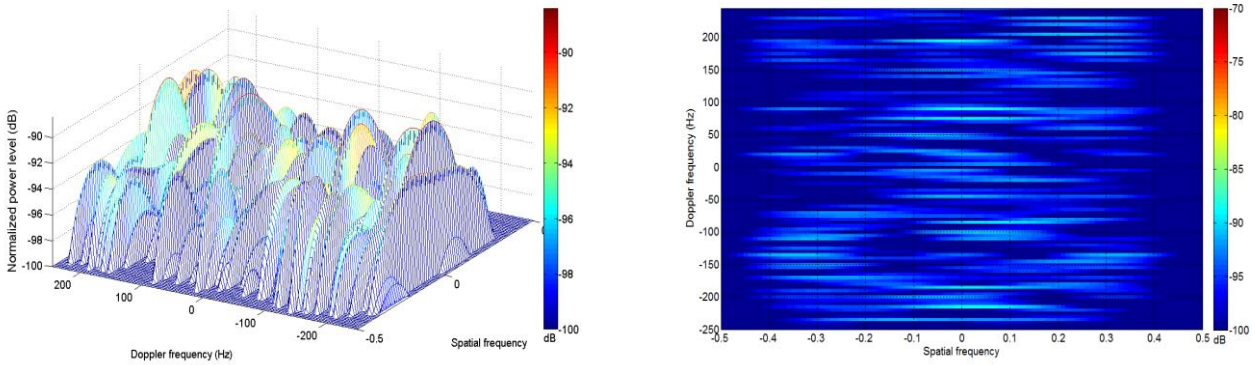

Fig. 5.17: Power spectrum at range cell $l = 90$ after adaptive interference cancellation.

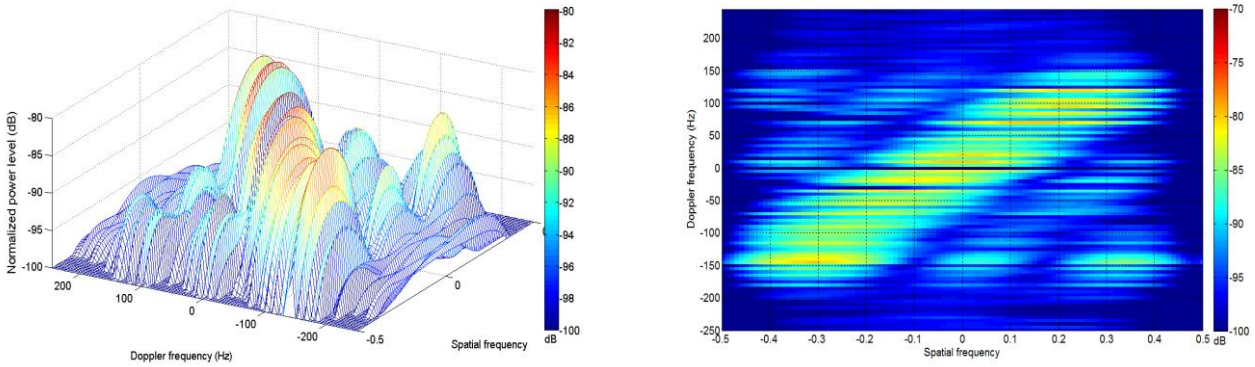

Fig. 5.18: Power spectrum of averaged covariance matrix
(16 range cells) after adaptive interference cancellation.

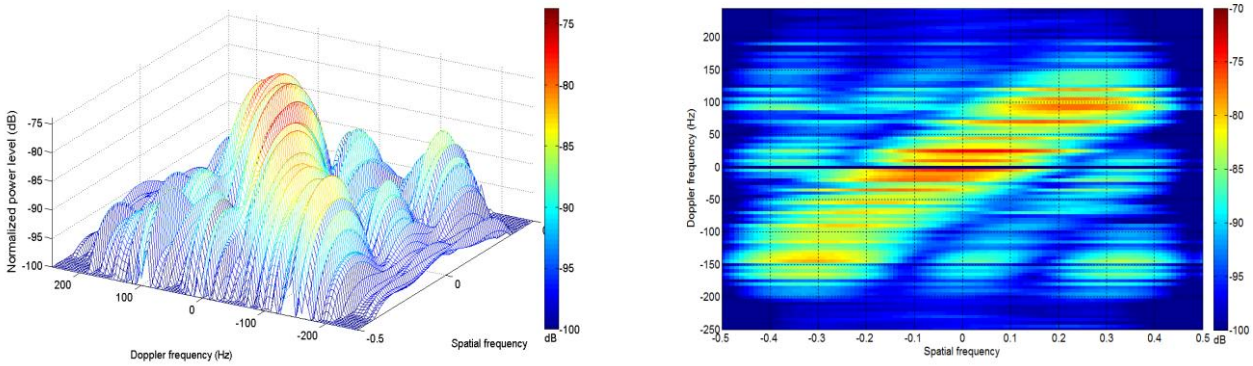

Fig. 5.19: Power spectrum of averaged covariance matrix
(24 range cells) after adaptive interference cancellation.

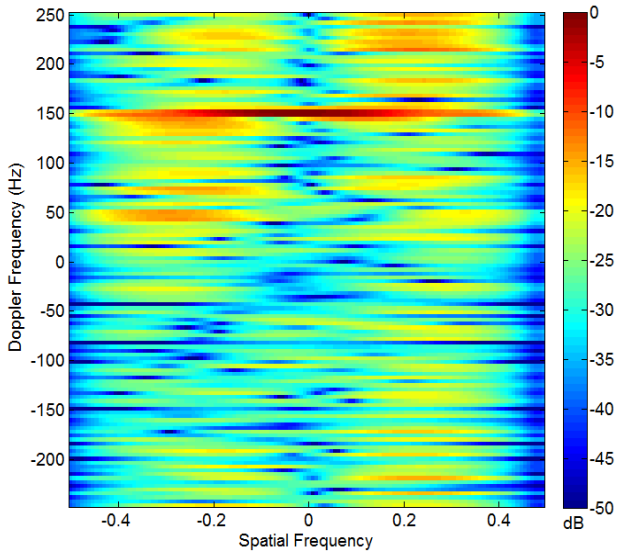

Fig. 5.20: Composite adapted pattern for element-space
pre-Doppler STAP, Doppler bin 30 (151.5 Hz).

The adaptive interference cancellation prior to matched filter processing is able to effectively suppress the direct path where its corresponding random range sidelobes coupling had been suppressed completely. In the subsequent signal processing scheme, the spatial-Doppler dependent clutter will be suppressed by reduced-dimension STAP prior to detections. For the side-looking ground-based moving passive radar experimental trials, due to the power budget and the narrowband passive signal bandwidth, the number of range cells collected is limited. In total, clutter is more prominent for approximately 49 range cells ($l = 0$ to 48) with some degree of heterogeneity at further range cells. With these considerations and the motivation to achieve good cancellation performance, element-space STAP will be used on the 4-channels measurement data to suppress the remaining spatial-Doppler dependent clutter. Element-space STAP that uses all four spatial DOFs enables localized training (small amount of secondary data) by adaptively combining signals from all the 4 elements. Dimensionality reduction is achieved through adaptive processing only a few sub-CITs at a time or by adaptively combining a small number of filtered outputs on each element which greatly reduce the number of adaptive DOFs. In processing the measurement data using element-space pre-/post-Doppler STAP, Doppler filters are designed with a 30 dB

Chebyshev taper and the training data will be twice the DOFs taken from the range cells centered at $l = 20$.

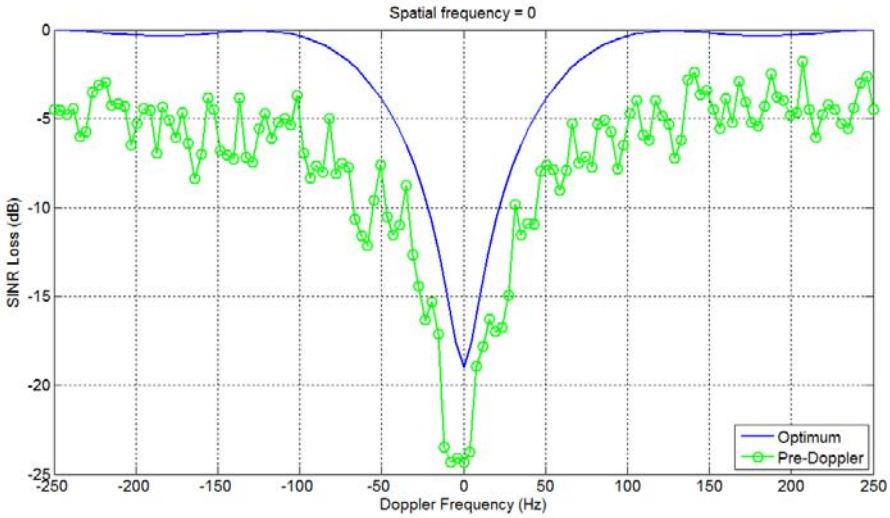

Fig. 5.21: SINR loss for element-space pre-Doppler STAP, $K = 2$.

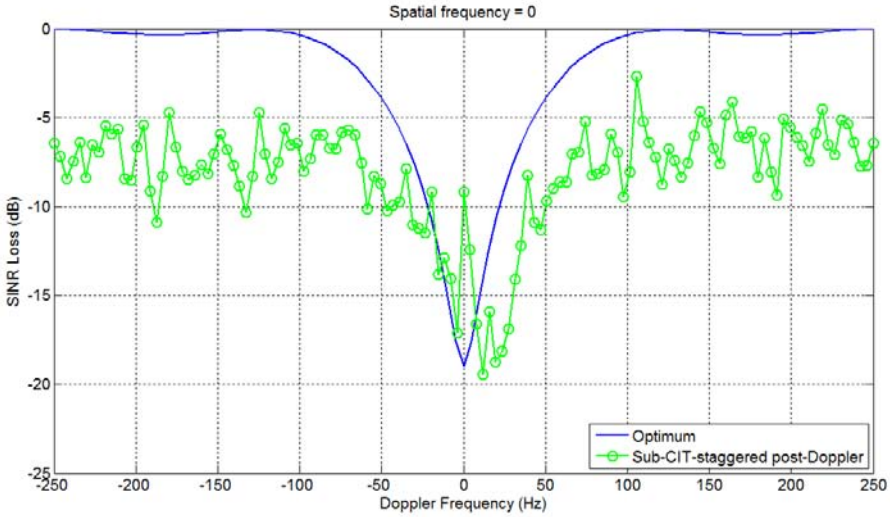

Fig. 5.22: SINR loss for element-space sub-CIT-staggered post-Doppler STAP, $K = 3$.

For element-space pre-Doppler STAP with $K = 2$, the composite adapted pattern for spatial frequency of 0 and Doppler bin 30 (151.5 Hz) and is plotted in Fig. 5.20. As shown, the response has its maximum focused at both the spatial frequency and normalized Doppler frequency of a potential target. Resolution in spatial frequency domain is poor since only four elements are used. As expected, a visible null is formed along the clutter ridge contour. Next, the SINR loss is depicted in Fig. 5.21 where the SINR loss for optimum fully adaptive STAP is also included for reference. As anticipated, both SINR losses have a high degree of resemblance (shape of the SINR loss against Doppler frequency) where the additional loss for the measurement data against the optimum case is very obvious. In theory, it requires a significant amount of secondary data to support where the number of $K_e \geq 2KN$ IID secondary data is required to confine the SINR loss to within 3 dB. As shown, the SINR loss in the clutter free regions amounts to approximately -5 dB. Significant SINR loss that is formed around the 0 Hz Doppler frequency demonstrated the effective performance of the

element-space pre-Doppler algorithm. The losses are excessive relative to the optimal performance and the broaden null are always the resulting effect when dealing with measurement data where $\widehat{\mathbf{R}}_u$ used to compute the weight vector is not exactly IID in nature. Thus, estimating the interference covariance matrix represents another practical concern when processing measured data. With the MDV computed at 12 dB cutoff point, targets must have a Doppler frequency less than -32 Hz or greater than 29.5 Hz to be detected. Using a mean value, the MDV is calculated to be 2.08 m/s which is slightly less than twice of the MDV for optimum fully adaptive STAP of 1.11 m/s. For element-space pre-Doppler STAP with $K = 3$, a significantly poorer MDV results due to a wider notch at the mainlobe clutter Doppler.

Fig. 5.22 depicts the SINR loss for element-space sub-CIT-staggered post-Doppler STAP using $K = 3$ where the performance using $K = 3$ is marginally better than using $K = 2$. 30 dB Chebyshev Doppler filter tapers are used and the MDV performance does not improve with heavier Doppler tapering. The SINR loss for optimum fully adaptive STAP is also included for reference. As shown, the SINR loss in the clutter free regions amounts to approximately -6.5 dB which is slightly worse off than the element-space pre-Doppler STAP algorithm. As anticipated, significant SINR loss that is formed around the 0 Hz Doppler frequency demonstrated the effective performance of the element-space post-Doppler algorithm. By comparison, the resultant SINR loss for post-Doppler STAP exhibits smaller SINR loss in the clutter region but the computed losses have a higher degree of variation across different Doppler frequencies (bins) than for the pre-Doppler STAP algorithm. More importantly, a better MDV can be achieved with sub-CIT-staggered post-Doppler STAP but at the expense of higher secondary data support ($K = 3$). For the MDV computed at 12 dB cutoff point, targets must have a Doppler frequency less than -17 Hz or greater than 35.5 Hz to be detected. Using a mean value between the two, the MDV is calculated to be will be 1.77 m/s which is approximately more than 1.5 times that of the optimum MDV of 1.11 m/s. Thus, for the ground-based moving passive radar experimental trials, sub-CIT-staggered post-Doppler STAP ($K = 3$) has a slender improved MDV performance as compared to pre-Doppler STAP ($K = 2$). This somewhat validate the simulation results that post-Doppler approaches have better MDV, resulting in a better UDSF.

The results in an airborne passive radar signal processing for MTI is the scalar output of the space-time processor that combines all the data from the range gate of interest using a single weight vector that is optimized for a specific angle and Doppler. Then, this output signal is given to a detector to determine the presence or absence of a target at the specific range cell. Thus, for the ground-based moving passive radar measurement data, the most direct and practical method to validate the effectiveness of space-time adaptive processor will be to compute its scalar output. For this purpose, a target will be injected at a conveniently chosen range cell where the space-time processor output will be computed using element-space pre-Doppler STAP and element-space sub-CIT-staggered post-Doppler STAP to envisage the benefits provide by adaptive space-time filtering. A target with a spatial frequency of 0 and Doppler frequency of -150 Hz (no range migration) will be inserted into the interference snapshot at range cell $l = 20$ having two different value of SNR per element per sub-CIT of -6 dB (target X) and -26 dB (target Y). Thus, on the power spectrum at this range cell, the level of these two targets (after a gain of $10\log_{10}(1/MN) = 26$ dB) will have a normalized value of -82 dB and -102 dB where thermal noise power level is previously computed as -102 dB. Correspondingly, the output SNR is 20 dB for target X and 0 dB for target Y respectively. In addition, the clutter profile at this range cell has an average power of approximately -85 dB. In this case, conventional processing will not be able to detect these two targets. Fig. 5.23 depicts the normalized output across all the Doppler frequencies using

element-space pre-Doppler STAP ($K = 2$) for the two target scenarios. As clearly illustrated, target X can be detect at approximately 8.5 dB above the pedestal level while target Y cannot be detected. Using element-space sub-CIT-staggered post-Doppler STAP ($K = 3$) for the two target scenarios, Fig. 5.24 depicts the normalized output across different Doppler frequencies. Again as anticipated, target X can be detected at approximately 8 dB above the pedestal level and target Y is not strong enough to be detected. These processing results using the experimental trial measurement data clearly demonstrated that reduced-dimension STAP is able to effectively suppress the spatial-Doppler dependent clutter, leading to improve moving target detections.

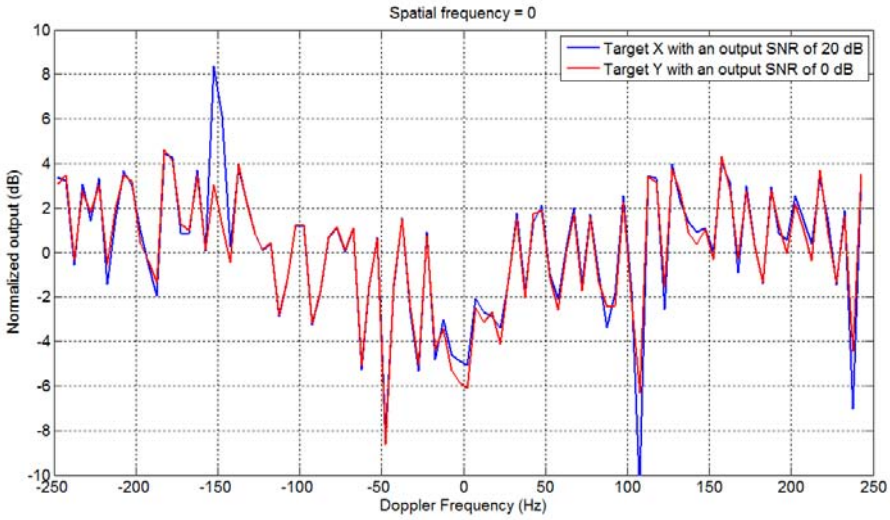

Figs. 5.23: Normalized output for element-space pre-Doppler STAP ($K = 2$) for the two target scenarios.

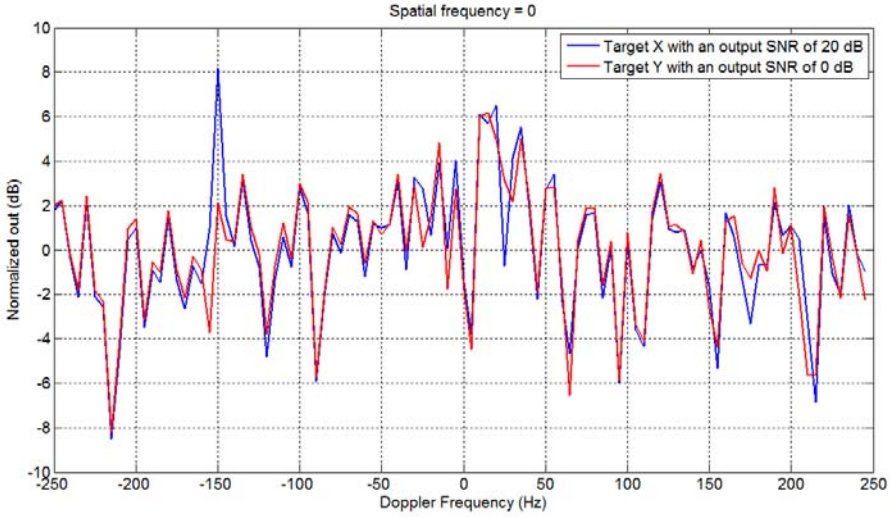

Figs. 5.24: Normalized output for element-space sub-CIT-staggered post-Doppler STAP ($K = 3$) for the two target scenarios.

5.4. Summary

A 4-channel low-cost experimental passive radar test-bed with a 4-element horn antenna array that can be easily mounted on a moving platform to mimic an airborne passive radar had been designed and implemented. The objectives are to collect real measurement data to firstly assess the passive signals in order to validate against the theoretical models that were derived. These data are also essential for the performance evaluation and verification of the proposed airborne passive radar signal processing for moving target detection in the real world interference scenario. For this purpose, a ground-based moving passive radar experimental trials, where both the transmit antenna and receive antenna array are installed on the same elevated mounting stand on the lorry vehicle platform in a monostatic side-looking array, had been conducted. The experimental trial site is a large plot of grass patch which offers a surface clutter measurement scenario having a swath of approximately 600 m. 4-channels of complex-valued baseband data are recorded for platform velocity of approximately 7 m/s. The results of the angle-Doppler power spectrum of the received passive signal without any interference cancellation signal processing schemes (neither adaptive interference cancellation nor reduced-dimension STAP) clearly illustrated the severe interfering environment for a practical passive radar scenario with a ground-moving passive radar receiver. For the experimental trials, the direct path that couples into the antenna array is the strongest signal received by the passive radar. Correspondingly, its random range sidelobes that acted as a severe spatial interference have power level higher than the spatial-Doppler dependent clutter at further range cells ($l \geq 5$). These results accurately concurred with of the theoretical models and simulations in the preceding Chapters.

The initial signal processing block calls for interference suppression to overcome the random range sidelobes coupling effects of the direct path and of the strong clutter in the ground-based moving passive radar prior to matched filter processing. In the experimental trials, the random range sidelobes coupling of the strong clutter are trivial. Applying the adaptive interference cancellation algorithm, the random range sidelobes of the direct path that interfere into further range cells had been completely suppressed and what remains is the spatial-Doppler dependent clutter that is to be effectively suppressed by element-space STAP prior to detections. Both the element-space pre-Doppler STAP ($K = 2$) and sub-CIT-staggered post-Doppler STAP ($K = 3$) for spatial-Doppler dependent clutter suppression have results that demonstrated the effective performance of the algorithms. SINR loss in the clutter free regions amounts to approximately -5 dB and -6.5 dB for the pre-Doppler and post-Doppler algorithm respectively. In the clutter region, the post-Doppler STAP exhibits smaller SINR loss compared to the pre-Doppler STAP algorithm but the computed losses have a higher degree of variation across different Doppler frequencies. This slender improved MDV performance for the sub-CIT-staggered post-Doppler STAP as compared to pre-Doppler STAP somewhat validated the theoretical and simulation results that post-Doppler approaches have better a MDV. Further signal processing where the space-time processor output had been computed clearly demonstrated that reduced-dimension STAP is able to effectively suppress the spatial-Doppler dependent clutter, thus, improving moving target detection performance. Overall, the ground-based moving passive radar experiment trials does indeed provide real measurement data to validate the theoretical passive signal models that are derived and against simulations results. More importantly, it necessitate the validation and evaluation of the signal processing schemes for interference suppression in the airborne passive radar to improve moving target detections.

Chapter 6

Conclusions and Perspectives

6.1. Conclusions

The research thesis considers the novel concept of the passive radar on an airborne platform which has multiple passive receiving arrays (side-looking and forward-looking configurations) to cover a 4π steradian angle around the airborne passive platform. This challenging airborne passive radar configuration, which makes use of the ground-based stationary transmitter as the illuminator of opportunity, offers application for near range (up to tens of Km) covert surveillance around the airborne platform. Being highly mobile and deployable, the additional benefit for the airborne passive radar is such that target detections are made easier by the increase in visible range due to the elevated position of airborne platform which also implies a reduction of the terrain masking effect and more favourable wave propagation conditions. However, the airborne passive radar is a not without any shortcomings. The severe interfering environment for the airborne passive radar is usually characterized by the high levels of direct path and clutter against the thermal noise background. Due to the CW, random and aperiodic nature of the passive signals and given that the power of direct path and strong clutter signals are much stronger than the target power, the random range sidelobes coupling of these interfering signals into further range cells will seriously exacerbate the background interference, making moving target detections a big challenge. For the airborne passive radar utilizing a ground-based stationary transmitter, the received ground clutter is spread over a region in Doppler frequency where the Doppler shift of each individual clutter patch is proportional to the angle of arrival relative to the velocity vector of the airborne passive platform. This spatial-Doppler dependent clutter can be effectively suppressed by two-dimensional filters, i.e. space-time filters. In conclusion, these pressing issues concerning the random range sidelobes of the direct path and of the strong clutter coupling and the spatial-Doppler dependent clutter ridge at the range cell of interest need to be thoroughly analyzed and fully addressed for the airborne passive radar to be feasible and practical.

The research thesis is devoted to the study of signal processing schemes and techniques for interference suppression to improve moving target detections in the airborne passive radar. The focuses are on identifying and analyzing the critical issues faced by the airborne passive radar in order to propose effective signal processing schemes/techniques to address and overcome these issues. Importantly to derived the models for the passive signals received by the airborne passive radar and the effects of these signals on the detection range cell of interest. Consequently, effective signal processing schemes associated to the airborne passive radar will be studied and proposed to address and mitigate these challenging problems for improving the moving target detection performance in the airborne passive radar.

The theoretical signal modeling for the airborne passive radar had been methodically studied and analyzed in Chapter 2. A generic bistatic geometry of the airborne passive radar utilizing a stationary ground-based non-cooperative transmitter is first introduced in order to establish the passive CIT datacube model and key parameters used to define the generalized

space-time steering vector. The statistical properties of the passive signal which is necessary in the snapshots development for the signals received by the airborne passive radar are studied. The vital property is in the correlation function of the passive signal which exhibits a single peak at the origin surrounded by pedestal of energy which is on average lower than the peak by the reciprocal of its time-bandwidth product. With that, the space-time snapshot models for each of the received passive signal are derived and presented. In a typical target present scenario, a snapshot at the detection range cell of interest will also contains undesired components which include clutter returns, random range sidelobes contributions of the direct path and of the strong clutter, and the background thermal noise. Subsequently, the spatial-Doppler properties of the clutter profile and on the random range sidelobes of the direct path and of the strong clutter are analyzed where the efficiency of the interference suppression depends significantly on these properties. Theoretical studies ascertain that the random range sidelobes couplings of the direct path and of the strong clutter and the passive signal attributes are important considerations on moving target detection performance for the airborne passive radar. Simulations on the power budget profile for the airborne passive radar (side-looking and forward-looking) in a practical environment and interference scenario had demonstrated the undesired sidelobes coupling effect of the direct path and of the strong clutter into further range cells. For both configurations, the direct path sidelobes coupling cause the formation of a spatial frequency dependent Doppler ridge that is well above the level of the spatial-Doppler dependent clutter present at the range cell of interest. The severe random range sidelobes couplings of the strong clutter that spanned over all spatial frequencies caused the significant elevation of the pedestal in the spatial-Doppler power spectrum. Thus, target detections at this range cell will be random range sidelobes limited. These undesirable coupling effects, together with the spatial-Doppler dependent clutter, drastically increase the significant eigenvalues of the interference covariance matrix and thus the requirement for more degrees of freedom for effective interference rejection.

The overall block diagram of the signal processing schemes that are able to mitigate the undesirable interfering signals in the airborne passive radar is depicted in Chapter 4. The two main signal processing blocks are the LS-based adaptive interference cancellation and reduced-dimension STAP. The adaptive interference cancellation where adaptive FIR filtering is implemented to estimate the weight coefficients for interference cancellation prior to matched filter processing is used to suppress the direct path, zero-Doppler strong clutter as well as the Doppler shifted strong clutter signals at each array element. Simulations showed that the LS-based adaptive interference cancellation algorithm is able to effectively suppress these interfering signals, which subsequently lowers their corresponding random range sidelobes that manifest into further range cells by the same amount. The cancellation algorithm works well but the main drawback is such that the entail computational and memory load for the processing might not be within acceptable time necessary for real-time airborne passive radar operations. In addition, its performance will suffer some degradation where the interfering signals will not be fully suppressed if the direct path reference signal becomes corrupted. Following the adaptive interference cancellation, the passive signals are then formatted into a $N \times M \times L$ CIT datacube where the range profile is obtained by matched filter processing (range correlation) that is carried out separately on a sub-CIT-by-sub-CIT basis. Subsequently, any residual random range sidelobes couplings that remain and that of the spatial-Doppler dependent clutter at the detection range cell of interest will be suppressed by reduced-dimension STAP.

For the airborne passive radar, due to the power budget and the narrowband passive signal bandwidth, the number of range cells collected may be limited. In addition, the clutter is often heterogeneous which limits the amount of secondary data which can be assumed IID. These concerns, together with the issues of computational complexity, lead naturally to

reduced-dimension STAP which enables localized training and thus can be used to advantage in the airborne passive radar. The main benefit of reduced-dimension techniques is in the significant reduction of the adaptive weights dimensionality where the performance and statistical convergence with a limited amount of data available for the airborne passive radar can be dramatically improved. Reduced-dimension STAP algorithms are classified by the type of non-adaptive transformation on the datacube where the four main types are the element-space pre-/post-Doppler and beam-space pre-/post-Doppler algorithms. Simulation results (in a practical environment and interference scenario for both side-looking and forward-looking configurations) for the various reduced-dimension STAP techniques (with varying dimensionality) demonstrated their ability to effectively suppress the spatial-Doppler dependent clutter ridge and the residual direct path random range sidelobes and random range sidelobes of the strong clutter that has a limited spatial frequency span to improve moving target detections. Beam-space architectures result in lower DOF processors than element-space approaches. Element-space approaches are inherently more flexible because full spatial adaptively is retained where spatial adaptivity provide a large number of spatial DOFs to cancel the random range sidelobes couplings simultaneously. Thus, the element-space STAP techniques can be suitable for the airborne passive radar operation where moderate sized antenna array are used. Post-Doppler implementation of reduced-dimension STAP outperformed the pre-Doppler approaches with better MDV and exhibit SINR loss performance close to that of the optimum fully adaptive STAP algorithm. However, when the CIT length is relatively short, the spatial angle (frequency) extent corresponding to a Doppler bin becomes large, thus putting a heavier burden on the spatial adaptive processing. Comparison of the simulation results showed that beam-space pre- and post-Doppler approaches are able to provide comparable (in not better) SINR loss performance to their element-space counterparts with significantly fewer DOFs. Thus, the requirement for lesser secondary data support for weights training which is a definite advantage in the airborne passive radar. The post-Doppler implementation outperformed the pre-Doppler approaches with a better MDV. For the airborne passive radar, the main difficulty concerns the residual random range sidelobes of the strong clutter which is not completely eliminated by the adaptive interference cancellation. Reduced-dimension STAP will not be useful in suppressing the strong clutter sidelobes that spanned the full spatial frequency range as the properties of this interference is similar to that of thermal noise which is of full rank.

Chapter 5 outlines the ground-based moving passive radar experimental trials where a 4-channel low-cost experimental passive radar test-bed had been designed and implemented. The objectives are to collect real measurement data to assess the passive signals against the theoretical models that were derived. These data are also essential for the performance evaluation and verification of the proposed airborne passive radar signal processing in the real world interference scenario. The raw results of the angle-Doppler power spectrum (without any interference cancellation schemes) clearly illustrated the severe interfering environment for a practical passive radar scenario on a ground-moving platform. These results accurately concurred with that of the theoretical models and simulations in the preceding Chapters and if these undesirable random range sidelobes couplings and spatial-Doppler dependent clutter are not mitigated, target detection would be virtually impossible. As a result of applying the adaptive interference cancellation algorithm in the measurement data, the random range sidelobes of the direct path that interfere into further range cells had been completely suppressed and what remains is the spatial-Doppler dependent clutter that need to be effectively suppressed by element-space STAP prior to detections. Subsequently, the results of the element-space pre- and post-Doppler STAP algorithms demonstrated their effective performance. The resultant SINR loss for sub-CIT-staggered post-Doppler STAP exhibits lower SINR loss in the clutter region as well as having a higher degree of variation

across different Doppler frequencies than for the pre-Doppler STAP algorithm. For both algorithms, the excessive SINR losses in the clutter free regions (relative to the optimal performance) and the broaden null are always the resulting effect when dealing with measurement data. Thus, estimating the interference covariance matrix represents another practical concern when processing measured data. Overall, the ground-based moving passive radar experiment trials does indeed provide real data to validate and evaluate the airborne passive radar signal processing schemes for interference suppression to improve moving target detections.

In summary, the research thesis analyzed the critical challenges faced by the airborne passive radar when operating in a typical and yet severe interfering environment. Efficient and effective signal processing schemes/techniques are proposed to address and mitigate these issues for improving moving target detections performance. Finally, the ground-based moving passive radar experiment trials were conducted to provide real measurement data to validate against the theoretical models that were derived and more importantly, to ascertain the performance of the signal processing schemes for the airborne passive radar.

6.2. Perspectives

For suppressing the spatial-Doppler dependent clutter as received by the airborne passive radar, reduced-dimension STAP algorithms are proposed to address the issues of computational complexity and sample support for covariance estimation. There might be no single algorithm that consistently performs best for all scenarios. Detection strategies might be utilized in such a way where various detectors are to be used in different scenarios, depending on the computation power and the data resource available to the passive airborne radar. During a stable and level flight, if clutter environment is relatively homogeneous and there are sufficient training data, reduced-dimension STAP may be employed. The element-space and beam-space approaches to the reduced-dimension STAP algorithms had been thoroughly investigated and analyzed in this thesis. During a highly maneuvering flight by the airborne passive radar, it might not be desirable to use secondary data (range samples) to compute the weights. Deterministic approach that utilizes only one space-time snapshot of data (primary range cell) such as direct data domain algorithms [81] may be introduced to solve the problem. If the passive radar is in a routine cruise mission, conducting surveillance in a pre-identified and/or repeating routes and where the radar and platform parameters are well-known, knowledge based STAP [82] may be used in the scenario. Future work as a continuation of this thesis will be to look into these approaches to fully understand the characteristics for each type of algorithm in order to comprehend their merits and drawbacks and then apply them to advantage.

The ground-based moving passive radar experimental trials that were conducted to validate the proposed signal processing schemes in the real world interference scenario use a non-cooperative DVB-T format signal that is generated from an arbitrary signal generator. As the next and most important step closer to fielding an operational airborne passive radar, the non-cooperative DVB-T signal from an operational DVB-T transmitter should be used. This enables a more accurate analysis on the practical performance of the associated signal processing schemes with a truly non-cooperative signal in a bistatic configuration. Furthermore, it is ascertain that with the operational DVB-T transmitter that is considerably some distance away, the direct path reference signal that is either beamformed or collected with an auxiliary antenna will be corrupted. Thus, the level of performance degradation on MTI due to the corrupted direct path reference signal for the adaptive interference cancellation can also be analyzed and quantified.

Appendix A

Moments of the auto-correlation function of random signal

Section 2.5.1 gives two statistical properties of the auto-correlation function when the signal of interest is random: the function's mean and variance. The auto-correlation function for the random signal is defined by Equation (2.20) and properties of the model $s(n)$ are given in Equation (2.19). From these, it can be shown that

$$E[r(\tau)] = \frac{1}{\mathcal{N}} \sum_{n=1}^{\mathcal{N}} E[s(n)s^*(n+\tau)] = \begin{cases} \sigma^2, \text{ for } \tau = 0 \\ 0, \text{ otherwise} \end{cases} \tag{A.1}$$

where $\mathcal{N}$ is the number of samples in the passive signal. Consequently

$$\begin{aligned} E[|r(\tau)|^2] &= \frac{1}{\mathcal{N}^2} \sum_{n_1=1}^{\mathcal{N}} \sum_{n_2=1}^{\mathcal{N}} E\left[s(n_1)s^*(n_1+\tau)\left(s(n_2)s^*(n_2+\tau)\right)^*\right] \\ &= \frac{1}{\mathcal{N}^2} \sum_{n_1=1}^{\mathcal{N}} \sum_{n_2=1}^{\mathcal{N}} E[s(n_1)s^*(n_1+\tau)]E[s^*(n_2)s(n_2+\tau)] \\ &+ \frac{1}{\mathcal{N}^2} \sum_{n_1=1}^{\mathcal{N}} \sum_{n_2=1}^{\mathcal{N}} E[s(n_1)s^*(n_2)]E[s^*(n_1+\tau)s(n_2+\tau)]. \end{aligned} \tag{A.2}$$

When $\tau = 0$, this simplifies to

$$E[|r(0)|^2] = \frac{1}{\mathcal{N}^2} \sum_{n_1=1}^{\mathcal{N}} \sum_{n_2=1}^{\mathcal{N}} \sigma^2\sigma^2 + \frac{1}{\mathcal{N}^2} \sum_{n=1}^{\mathcal{N}} \sigma^2\sigma^2 = \left(1 + \frac{1}{\mathcal{N}}\right)\sigma^4. \tag{A.3}$$

For $\tau \neq 0$ (away from origin),

$$E[|r(\tau)|^2] = \frac{1}{\mathcal{N}^2} \sum_{n_1=1}^{\mathcal{N}} \sum_{n_2=1}^{\mathcal{N}} 0 + \frac{1}{\mathcal{N}^2} \sum_{n=1}^{\mathcal{N}} \sigma^2\sigma^2 = \frac{1}{\mathcal{N}}\sigma^4. \tag{A.4}$$

Therefore

$$E[|r(\tau)|^2] = \begin{cases} \left(1 + \frac{1}{\mathcal{N}}\right)\sigma^4, \text{ for } \tau = 0 \\ \frac{1}{\mathcal{N}}\sigma^4, \text{ otherwise} \end{cases}. \tag{A.5}$$

Bibliography

[1] M.I. Skolnik, *Introduction to Radar Systems*, 3rd Edition, McGraw-Hill, Inc., New York, NY, 2001.

[2] D.K. Barton, *Modern Radar System Analysis*, Artech House, Norwood, MA, 1988.

[3] H.L. Van Trees, *Detection, Estimation and Modulation Theory, Part III*, John Wiley and Sons, Inc., New York, NY, 1971.

[4] J.M. Hawkins, "An Opportunistic Bistatic Radar", *International Conference on Radar*, No. 449, October 1997, pp. 318-322.

[5] N.J. Willis, *Bistatic Radar*, Artech House, Norwood, MA, 1991.

[6] S. Herman, P. Moulin, "A Particle Filtering Approach to FM-Band Passive Radar Tracking and Automatic Target Recognition", *IEEE Proceedings Aerospace Conference*, Vol. 4, March 2002, pp. 1789-1808

[7] H.D. Griffiths and C.J. Baker, "Passive Coherent Location Radar Systems. Part 1: Performance Prediction", *IEE Proceedings Radar, Sonar & Navigation*, Vol. 152, No. 3, June 2005, pp. 153-159.

[8] N.J. Willis and H.D. Griffiths, *Advances in Bistatic Radar*, SciTech, Raleigh, NC, 2007.

[9] M. Cherniakov, *Bistatic Radar: Emerging Technology*, John Wiley & Sons Ltd., West Sussex, UK, 2008.

[10] (2010, March) Silent Sentry®, Lockheed Martin. [Online]. Available: http://www.lockheedmartin.com/products/silent-sentry/index.html

[11] (2007, May) Silent Sentry®, Innovative Technology for Passive, Persistent Surveillance. Lockheed Martin. [Online]. Available: http://www.lockheedmartin.com/data/assets/10644.pdf

[12] J. Ferrier, M. Klein, and S. Allam, "Frequency and Waveform Complementarities for Passive Radar Applications", *International Radar Symposium 2009*, September 2009.

[13] C.L. Zoeller, M.C. Budge Jr. and M.J. Moody, "Passive Coherent Location Radar Demonstration", *Proceedings of the Thirty-Fourth Southeastern Symposium on System Theory*, March 2002, pp. 358-362.

[14] C.C. Zhou, "*Application And Extension Of Space-Time Adaptive Processing To Passive FM Radar*", Dissertation for Ph.D. Degree, University of Washington, Seattle, WA, 2003.

[15] H.D. Griffiths and N.R.W. Long, 'Television-Based Bistatic Radar", *IEE Proceedings*, Vol. 133, No. 7, Pt. F, December 1986, pp. 649-657.

[16] P.E. Howland, "Target Tracking Using Television-Based Bistatic Radar", *IEE Proceedings Radar, Sonar & Navigation*, Vol. 146, No. 3, June 1999, pp. 166-174.

[17] D. Poullin, "Passive Detection Using Digital Broatcasters (DAB, DVB) with CODFM Modulation", *IEE Proceedings Radar, Sonar & Navigation – Special Issue on Passive Radar System*, Vol. 152, No. 3, June 2005, pp. 143-152.

[18] R. Saini and M. Cherniakov, "DTV Signal Ambiguity Function Analysis For Radar Applications", *IEE Proceedings Radar, Sonar & Navigation – Special Issue on Passive Radar System*, Vol. 152, No. 3, June 2005, pp.133-142.

[19] D.K.P. Tan, H.B. Sun, Y. Lu, M. Lesturgie and H.L. Chan, "Passive Radar Using Global System for Mobile Communication Signals – Theory, Implementation and Measurements", *IEE Proceedings Radar, Sonar & Navigation – Special Issue on Passive Radar System*, Vol. 152, No. 3, June 2005, pp. 116-123.

[20] Roke Manor Research, "*Celldar - Cellphone Radar System*", http://www.roke.co.uk/sensors/stealth/celldar.asp

[21] D. Petri, F. Berizzi, M. Martorella, E. Dalle Mese, A. Capria, "A Software Defined UMTS Passive Radar Demostrator", *11th International Radar Symposium (IRS)*, Vilnius, Lithuania, June 2010, pp. 1-4.

[22] Q. Wang, C. Hou, Y. Lu, "An Experimental Study of WiMAX-Based Passive Radar", *IEEE Transactions on Microwave Theory and Techniques*, Vol. 58, No. 12, December 2010 Date: Dec. 2010, pp. 3502-3510.

[23] V. Koch and R. Westphal, "A New Approach To A Multistatic Passive Radar Sensor For Air Defense", *IEEE International Radar Conference*, Washington DC, USA, May 2000, pp. 22-28.

[24] M. Cherniakov, D. Nezlin and K. Kubik, "Air Target Detection Via Bistatic Radar Based On LEOs Communication Signals", *IEE Proceedings Radar, Sonar, & Navigation*, Vol. 149, No. 1, February 2002, pp. 33-38

[25] D. Cristallini, M. Caruso, P. Falcone, D. Langellotti, C. Bongioanni, F. Colone, S. and P. Lombardo, "Space-based passive radar enabled by the new generation of geostationary broadcast satellites", *IEEE Aerospace Conference*, March 2010, pp. 1-11.

[26] D.K.P. Tan, H. Sun and Y. Lu, "Sea and Air Moving Target Measurements Using a GSM Based Passive Radar", *IEEE Radar Conference*, Arlington, Virginia, USA, May 2005, pp. 783-786.

[27] D.K.P. Tan, H. Sun and Y. Lu, "Ground Moving Target Measurements Using a GSM Based Passive Radar", *IEEE International Conference on Radar*, Toulouse, France, October 2004, pp. 18-22.

[28] J.D. Sahr and E.D. Lind, "The Manastash Ridge Radar: A Passive Bistatic Radar for Upper Atmospheric Radio Science", *Radio Science*, Vol. 32, No. 6, 1997, pp. 2345-2358.

[29] D. Trizna and J. Gordon, "Results of a Bistatic HF Radar surface Wave Sea Scatter Experiment", *Proceedings International Geoscience and Remote Sensing Symposium*, Vol. 3, June 2008, pp. 1902-1904.

[30] V.P. Yakubov, V. B. Antipov, D.N. Losev, and I.A. Yuriev, "Passive Radar Detection of Radioactive Pollution", Application of the Conversion Research Results for International Cooperation, SIBCONVERS. *The Third International Symposium*, 2, May 1999, pp. 397-399.

[31] D.K.P. Tan, M. Lesturgie, H. Sun, W. Li and Y. Lu, "GSM Based Through-the-Wall Passive Radar Demonstrator for Motion Sensing", *IEEE Workshop and Exhibition on New Trends for Environmental Monitoring Using Passive Systems (Passive'08)*, Hyères, France, October 2008.

[32] H.B. Sun, D.K.P. Tan, Y.L. Lu and M. Lesturgie, "Applications of Passive Surveillance Radar System using Cell Phone Base Station Illuminators", *IEEE Aerospace and Electronic Systems Magazine*, Vol. 25, Issue 3, March 2010, pp. 10-18.

[33] J. Raout, X. Neyt and P. Rischette, "Bistatic STAP Using DVB-T Illuminators of Opportunity", *IET International Conference on Radar Systems*, Edinburgh, UK, October 2007.

[34] J. Raout, A. Santori and E. Moreau, "Space-Time Clutter Rejection and Target Passive Detection Using the APES Method", *IET Signal Processing*, Vol. 4, Issue 3, June 2010, pp. 298-304.

[35] J. Raout, A. Santori and E. Moreau, "Passive Bistatic Noise Radar Using DVB-T Signals", *IET Proceedings Radar, Sonar & Navigation*, Vol. 4, Issue 3, June 2010, pp. 403-411.

[36] J. Brown, K. Woodbridge, A. Stove and S. Watts, "Air Target Detection Using Airborne Passive Bistatic Radar", *Electronics Letters*, Vol. 46, No. 20, September 2010, pp. 1396-1397.

[37] K. Kulpa, M. Malanowski, P. Samczynski and B. Dawidowics, "The Concept of Airborne Passive Radar", *Microwaves, Radar and Remote Sensing Symposium*, Kiev, Ukraine, August 2011, pp. 267-270.

[38] B. Dawidowicz and K. Kulpa, Airborne Passive Radar System – First Study. *Proc. International Radar Symposium IRS7*, Cologne, Germany, 2007, pp. 443-447.

[39] M. Malanowski, K. Kulpa and J. Misiurewicz, PaRaDe – Passive Radar Demonstrator Family Development at Warsaw University of Technology. *MRRS – 2008 Symposium Proceedings*, Kiev, Ukraine, 2008, pp. 75-78.

[40] B. Dawidowicz and K. Kulpa, "Experimental Results from PCL Radar on Moving Platform", *Proceedings of the International Radar Symposium*, Wroclaw, Poland, May 2008, pp. 305-308.

[41] C.J. Baker, H.D. Griffiths and I. Papoutsis, "Passive Coherent Location Radar Systems. Part 2: Waveform Properties", *IEE Proceedings Radar Sonar & Navigation – Special Issue on Passive Radar System*, Vol. 152, No.3, June 2005, pp. 160-168.

[42] M.A. Ringer and G.J. Frazer, "Waveform Analysis of Transmissions of Opportunity for Passive Radar", *Fifth International Symposium on Signal Processing and its Applications*, Brisbane, Australia, August 1999, pp. 511-514.

[43] A.W. Rihaczek, *Principles of High-Resolution Radar*, Peninsula Publishing, 1985.

[44] S. Stein, "Algorithms for Ambiguity Function Processing", *IEEE Transactions Acoustic Speech Signal Processing*, Vol. 29, No. 3, 1981, pp. 588-599.

[45] D.K.P. Tan, M. Lesturgie, H. Sun and Y. Lu, "Target Detection Performance Analysis for Airborne Passive Bistatic Radar", *IEEE International Geoscience and Remote Sensing Symposium*, Honolulu, HI, USA, July 2010, pp. 3553-3556.

[46] R. Klemm, *Principles of Space-Time Adaptive Processing*, 3rd Edition, The Institution of Engineering and Technology, London, UK, 2006.

[47] W. Bürger, "Space-Time Adaptive Processing: Fundamentals", *Advanced Radar Signal and Data Processing*, Educational Notes RTO-EN-SET-086, Neuilly-sur-Seine, France, 2006. pp. 6-1 to 6-14.

[48] W. Melvin, "A STAP Overview", *IEEE Aerospace and Electronic Systems Magazine*, Vol. 19, No. 1, January 2004, pp. 19-35.

[49] J. Ward, "*Space-Time Adaptive Processing for Airborne Radar*", Technical Report 1015, MIT Lincoln Laboratory, Lexington, MA, December 1994.

[50] S.D. Yakov, *Computer Simulation of Aerial Target Radar Scattering, Recognition, Detection, and Tracking*, Artech House, Norwood, MA, 2006.

[51] D.K.P. Tan, M. Lesturgie, H. Sun and Y. Lu, "Signal Analysis of Airborne Passive Radar using Transmissions of Opportunity", *International Conference on Radar*, Chengdu, China, October 2011, pp. 169-172.

[52] T.B. Hale, "*Airborne Radar Interference Suppression Using Adaptive Three-Dimensional Techniques*", Dissertation for Ph.D. Degree, Air Force Institute of Technology, May 2002.

[53] R. Klemm, "Doppler Properties of Airborne Clutter," *Proceeding Research and Technology Organization, North Atlantic Treaty Organization (RTO-NATO) Lecture Series 228 on Military Applications of Space-Time Adaptive Processing*, RTO-ENP-027, September 2002, pp. 2-12 to 2-24.

[54] R. Klemm, "Adaptive Clutter Suppression for Airborne Phased Array Radar", *IEE Proceedings*, Vol. 130, No. 1, February 1983, pp. 125-132.

[55] J. Guerci, *Space-time Adaptive Processing*, Artech House, House, Norwood, MA, 2003.

[56] L. Brennan, J. Mallett and I. Reed, "Adaptive Arrays in Airborne MTI Radar", *IEEE Transactions on Antennas and Propagation*, Vol. 24, Issue 5, September 1976, pp. 607-615.

[57] G.K. Borsari, "Mitigating Effects on STAP Processing Caused by an Inclined Array", *IEEE National Radar Conference*, Dallas, TX, USA, May 1998, pp. 135-140.

[58] R. Klemm, *Space-Time Adaptive Processing - Principles and Applications*, The Institution of Engineering and Technology, London, UK, 1998.

[59] S.M. Kogan and M.A. Zatman, "Bistatic STAP for Airborne Radar Systems", *Proceedings of the IEEE SAM 2000*, Lexington, MA, March 2000.

[60] S.D. Hayward, "Adaptive Beamforming for Rapidly Moving Arrays", *Proceedings of the CIE International Conference on Radar*, Beijing, China, October 1006, pp. 480-483.

[61] F. Pearson and G. Borasari, "Simulation and Analysis of Adaptive Interference Suppression for Bistatic Surveillance Radars", *Proceedings of the 2001 ASAP Symposium*, Lexington, MA, March 2001.

[62] B. Himed, Y. Zhang and A. Hajjari, "STAP with Angle-Doppler Compensation for Bistatic Airborne Radars", *Proceedings of the 2002 IEEE Radar Conference*, Long Beach, CA, April 2002.

[63] O. Kreyenkamp and R. Klemm, "Doppler Compensation in Forward-Looking STAP Radar", *IEE Proceedings Radar, Sonar & Navigation*, Vol. 148, No. 5, October 2001, pp. 252-258.

[64] W. Melvin, B. Himed and M.E. Davis, "Doubly-Adaptive Bistatic Clutter Filtering", *Proceedings of the 2003 IEEE Radar Conference*, Huntville, AL, May 2003, pp. 171-178.

[65] F. Colone, R. Cardinali and P. Lombardo, "Cancellation of Clutter and Multipath in Passive Radar using a Sequential Approach", *IEEE Conference on Radar*, Verona, NY, USA, April 2006, pp. 393-398.

[66] P.E. Howland, D. Maksimiuk and G. Reitsma, "FM Radio Based Bistatic Radar", *IEE Proceedings Radar, Sonar & Navigation – Special Issue on Passive Radar System*, Vol. 152, No. 3, June 2005, pp. 107-115.

[67] S. Haykin, *Adaptive Filter Theory*, 4th Edition, Prentice Hall, Upper Saddle River, NJ, 2002.

[68] R. Cardinali, F. Colone, C. Ferretti and P. Lombardo, "Comparison of Clutter and Multipath Cancellation Techniques for Passive Radar", *IEEE Radar Conference*, Boston, MA, April 2007, pp. 469-474.

[69] R.A. Monzingo and T.W. Miller, *Introduction to Adaptive Arrays*, John Wiley and Sons, Inc., New York, NY, 1980.

[70] R.T. Compton Jr., *Adaptive Antennas – Concepts and Performances*, Prentice Hall, Englewood Cliffs, New Jersey, 1980.

[71] L.E. Brennan and I.S. Reed, "Theory of Adaptive Radar", *IEEE Transactions on Aerospace and Electronic Systems*, Vol. AES-9, March 1973, pp. 237-252.

[72] I.S. Reed, J.D. Mallet and L.E. Brennan, "Rapid Convergence Rate in Adaptive Arrays", *IEEE Transactions on Aerospace and Electronic Systems*, Vol. AES-10, No. 6, November 1974.

[73] D.M. Boroson, "Sample Size Considerations for Adaptive Arrays", *IEEE Transactions on Aerospace and Electronic Systems*, Vol. AES-16, No. 4, 1974, pp. 446-451.

[74] Y. Dong, "*Overview of STAP Algorithms*", Electronic Warfare and Radar Division, Defence Science and Technology Organisation, 2011.

[75] B. Himed, "STAP Techniques and Applications (Tutorial)", *IEEE International Radar Conference*, Adelaide, Australia, 2008.

[76] J. Ward and A. Steinhardt, "Multiwindow Post-Doppler Space-Time Adaptive Processing", *IEEE Seventh SP Workshop on Statistical Signal and Array Processing*, 1994 pp. 461-464.

[77] L.E. Brennan and F.M. Staudaher, "*Subclutter Visibility Demonstartion*", Technical Report RL-TR-92-21, Adaptive Sensors Incorporated, March 1992.

[78] R. DiPietro, "Extended Factored Space-Time Processing for Airborne Radar System", *Proceedings of the 26th Asilomar Conference on Signals, Systems and Computing*, Pacific Grove, CA, October 1992, pp. 425-430.

[79] H. Wang and L. Cai, "On Adaptive Spatial-Temporal Processing for Airborne Surveillance Radar Systems", *IEEE Transactions on Aerospace and Electronic Systems*, Vol. 30, No. 3, July 1994, pp. 660-669.

[80] M. Wicks and H. Wang, "Adaptive Array Technology for Clutter Rejection in Airborne Radar", *Proceedings of the 1993 National Radar Conference*, March 1993.

[81] R. Dong and Z Bao, "Direct Data Domain STAP Algorithm for Airborne Radar Applications", *CIE International Conference on Radar*, Beijing, China, October 2001.

[82] R.S. Adve, T.B. Hale, M.C. Wicks and P.A. Antonik, "Ground Moving Target Indication using Knowledge Based Space-Time Adaptive Processing," *IEEE International Radar Conference*, Washington, DC, May 2000, pp. 735–740.